Title
Surface, Interface, and Defect Dynamics of Metal Halide Perovskites

Author
Tan, Shaun

Publication Date
2022

Peer reviewed|Thesis/dissertation

UNIVERSITY OF CALIFORNIA

Los Angeles

Surface, Interface, and Defect Dynamics of Metal Halide Perovskites

A dissertation submitted in partial satisfaction of the

requirements for the degree Doctor of Philosophy

in Materials Science and Engineering

by

Shaun Qi En Tan

2022

ABSTRACT OF THE DISSERTATION

Surface, Interface and Defect Dynamics of Metal Halide Perovskites

by

Shaun Qi En Tan

Doctor of Philosophy in Materials Science and Engineering

University of California, Los Angeles, 2022

Professor Yang Yang, Chair

In contrast with conventional inorganic semiconductors such as silicon, defects in ionic metal halide perovskite materials are charged. The migration and redistribution of charged defects under a potential gradient (e.g. electrical bias) are known to underly a myriad of detrimental performance- and stability-limiting phenomena in perovskite-based optoelectronic devices. Crucially, the long-term instability issues remain the major bottleneck towards practical usage and commercialization of perovskite-based optoelectronics. Simultaneously, progress in compositional and crystal growth engineering have made possible the controlled fabrication of perovskite thin films with minimized bulk trap density, and it is becoming apparent that defects are predominantly located at the surface and interfaces.

In chapter 2, we observed that shallow iodine interstitial defects (I_i) can be generated unintentionally during commonly used post-fabrication treatments. We show that I_i can lower the cubic-to-hexagonal phase transformation activation energy barrier of $FAPbI_3$-based perovskites to accelerate its degradation. We demonstrate that concurrently avoiding the generation of I_i and the

more effective passivation of iodine vacancy defects (V_I) improve the thermodynamic phase stability and operational stability of the perovskite films and devices.

In chapter 3, we investigate the mechanistic reconstruction processes occurring at the perovskite surface during post-fabrication treatments. Through complementary surface-sensitive techniques, we observed the generation of defects and a reconstruction towards a more PbI_2-rich surface as isopropyl alcohol (IPA) is spun onto the surface. We show that this reconstruction has important implications on the thermodynamics and energetics of the perovskite surface.

In chapter 4, we study the consequences of the altered heterointerface energetics on carrier extraction, trap passivation, charge accumulation, and ion migration. We show that a negative work function change (ΔW) accumulates charges in a potential well, which lowers the halide migration activation energy to limit PSC stability.

In chapter 5, we investigate the effect of 'A' cation size mismatch on the ion migration energetics and operational stability of PSCs. Partially substituting small MA with a larger 'A' site cation is expected to locally distort the perovskite lattice in order to fit the larger cation. The effect of this on the perovskite ion migration energetics has not been independently studied before due to the difficulty in separating the contributions of 'A' cation hydrogen bonding vs size.

In chapter 6, we present here a route to induce kinetic-controlled epitaxial crystal growth of formamidinium lead tri-iodide ($FAPbI_3$) perovskite thin films by using layered perovskite templates. The local epitaxial growth of the $FAPbI_3$ perovskite crystal was observed during its solid-state phase transformation from the hexagonal non-perovskite $FAPbI_3$ when it is heterostructured with layered perovskite, whereby the growth kinetics was dependent on strain energy originating from the heterointerface.

The dissertation of Shaun Qi En Tan is approved.

Richard B. Kaner

Jaime Marian

Aaswath Raman

Yang Yang, Committee Chair

University of California, Los Angeles

2022

Table of Contents

List of Figures

perovskite films as a function of exposure time to iodine vapour. **b**, 3D atomic force microscopy topography images of the control and treated perovskite films after different exposure times to iodine vapour, showing the surface root-mean-square roughness (R_q). Scale bar is 1 μm. **c,** Simulated energy pathway for the cubic-to-hexagonal phase transition with or without I_i defect. The activation energy barriers are included on the right. Evolution of the atomic arrangements for the **d**, defect-free, and **e**, with iodine interstitial (green spheres) lattices during the α-$FAPbI_3$-to-δ-$FAPbI_3$ transformation. Only one unit cell is shown. Atoms are expressed by spheres; iodine (purple), lead (grey), carbon (brown), and nitrogen (blue).

Figure 2.3. Device performance and photoluminescence properties of the control and treated perovskites. Top view of the slab models used for the **a**, V_I - I^- and **b**, V_I - TFA^- interaction energy (E_{int}) calculations. Only the first and second (blurred) layers of the slab are shown. Atoms are expressed by spheres; iodine (purple), carbon (grey), nitrogen (blue), oxygen (red), and fluorine (green). **c**, Power conversion efficiency (PCE) distribution of the control and treated devices. **d**, Current density and voltage (*J*-*V*) curves of the champion devices in reverse (1.2 V to -0.1 V) and forward (-0.1 V to 1.2 V) scan. Inset is the stabilized power output (SPO) of the champion devices. **e**, Steady-state photoluminescence (PL) spectra of the perovskite films on glass probed with an excitation wavelength of 532 nm. **f**, Normalized time-resolved PL spectra of the perovskite films on glass. Solid white lines are the fitted profiles using a mono-exponential decay function.

Figure 2.4. α-phase stability of the control and treated perovskite films. a, Hexagonal δ(010)-to-cubic α(100) X-ray diffraction (XRD) peak intensity ratio of the control and treated perovskite films as a function of exposure time to iodine vapour. **b**, Photographs and **c**, absorbance at 600 nm of the perovskite films exposed to RH 75 ± 10 % with time. **d**, XRD diffractograms of the perovskite films after exposure to RH 75 ± 10 % for 32 h.

Figure 2.5. Operational stability of the perovskite devices. a, Normalized stabilized power output (SPO) of encapsulated control and treated devices under continuous illumination (90 ± 10 mW cm^{-2}) under open-circuit condition. **b**, Normalized SPO of best-performing device with PATFA treatment. Dashed lines are linear fits to extract the device T_{90} lifetime. Shaded areas mark the 'burn-in decay' regime.

Figure 3.1. Defect generation by IPA treatment. (a) Schematic of the *in situ* PL measurement during IPA post-treatment. (b) *In situ* PL contour plot of a perovskite film undergoing surface

treatment with IPA dropped at around 53 s. (c) Evolution of the PL parameters extracted from fitting (b). (d) PAS depth-profiling of the perovskite films.

Figure 3.2. Characterizations of the perovskite films. (a) High-resolution XPS spectra of the Pb 4f and I $3d_{5/2}$ peaks of the perovskite films. Inset includes the calculated I:Pb ratios of the films. Solid lines are fitted plots. Dashed vertical lines demarcate the peak positions for the control film. Intensities are normalized to Pb 4f peak. (b) UPS spectra of the perovskite films. Inset includes a schematic band diagram of the energy levels based on the UPS measurements. GIXRD diffraction patterns of the perovskite films measured with an incident angle of (c) $\omega = 0.2°$ and (d) $\omega = 1.0°$.

Figure 3.3. Surface reconstruction and its implications. (a), (b) Theoretical slab models for first-principles DFT calculations. Atoms are colored black (lead), red (iodine), gray (nitrogen), and blue (hydrogen). (c) Calculated surface physiochemical properties. The asterisk indicates that surface energy is in units of eV nm^{-2}. (d) Enthalpy of adsorption of either PEAI or OAI on the surfaces. (e) Current density-voltage curves of devices treated with 10 mM OABr in CF. Inset includes the measured photovoltaic parameters. Brackets indicate parameters measured in forward bias. *In situ* PL contour plots of perovskite films undergoing surface treatment with (f) 10 mM OAI or (g) 10 mM PEAI in IPA.

Figure 4.1. Perovskite surface and heterointerface dynamics. a, b, UPS secondary electron cut-offs of various surface-treated perovskite films. Labels are BA: butylammonium, OA: octylammonium, DA: dodecylammonium. KPFM surface potential maps of the **c,** Reference, **d,** OAI-treated, and **e,** OATsO-treated films. Insets include the corresponding AFM topography images. All scale bars are 2 μm. **f,** Work function distributions and **g,** RMS surface roughness (R_q) of the films measured by KPFM and AFM, respectively. Charge density distribution profiles of the complete **h,** OATsO-treated and **i,** OAI-treated device cross-sections measured by cross-sectional KPFM. The devices were illuminated under open-circuit condition. Red error bars demarcate the estimated spatial resolution of ~30 nm.[8,28]

Figure 4.2. **Charge carrier dynamics, performance, and photostability. a,** Steady-state and **b,** time-resolved PL spectra of the glass/perovskite films. **c,** Steady-state and **d,** time-resolved PL spectra of the glass/perovskite/spiro-MeOTAD films. Included are the extracted lifetimes fitted with a mono-exponential decay function for (b) and bi-exponential decay function for (d). **e,** Histogram showing the PCE distributions of the devices. **f,** Photostability evolution with time of encapsulated devices aged under continuous illumination at maximum power point. P_0 denotes

the initial PCE. **g,** Photostability evolution with time of encapsulated devices aged under continuous illumination in open-circuit condition. Error bars represent the standard deviation of four devices for each condition. **h,** Photostability PCE evolution of the most stable OATsO-treated device aged under open-circuit condition. Included are the PCE retentions in approximately 500 h intervals.

Figure 4.3. STEM and EDX analyses of the aged devices. STEM bright field images of the aged **a,** OAI-treated and **b,** OATsO-treated device cross-sections. The OAI-treated device is seen to have a rougher heterointerface contacting spiro-MeOTAD. EDX elemental maps of bromine for the **c,** OAI-treated and **d,** OATsO-treated device cross-sections, and iodine for the **e,** OAI-treated and **f,** OATsO-treated device cross-sections. All scale bars in the STEM and EDX images represent 200 nm. Elemental distributions of bromine for the **g,** OAI-treated and **h,** OATsO-treated devices, and iodine for the **i,** OAI-treated and **j,** OATsO-treated devices.

Figure 4.4. **Physical origins of the experimental observations.** Activation energy for the **a,** intra-lattice and **b,** extra-lattice migrations of iodine or bromine calculated using first-principles NEB simulations. The forward migration pathways are indicated by the red arrows in the example simulated supercells. Charge displacement with **c,** $[OA]^+$ or **d,** $[TsO]^-$ on the surface, superimposed on the defect-free slab models, and **e,** corresponding charge displacement profiles. Blue and yellow volumes on the slab models correspond to electron-depleted or electron-enriched regions, respectively.

Figure 5.1. Decoupling size versus hydrogen bonding effect. Chemical structures of a) acetamidinium, b) methylammonium, and c) guanidinium. Density functional theory (DFT) modelled effective hydrogen bonds between the 'A' cations and perovskite lattice for d) acetamidinium, e) methylammonium, and f) guanidinium. Black numbers are the bond lengths (in angstroms) and blue numbers are the bond angles (in degrees).

Figure 5.2. Computational study of ion migration energetics. Density functional theory (DFT) modelled a) side view and b) top view iodide ion migration pathway for $MAPbI_3$ perovskite and c) side view and d) top view iodide ion migration pathway for $Ace_{0.25}MA_{0.75}PbI_3$ perovskite, showing only the unit cell containing the Ace cation. e) Iodide ion migration activation energy for $MAPbI_3$ and $Ace_{0.25}MA_{0.75}PbI_3$ calculated using DFT. Included are the transition states corresponding to the maximum energy states, showing the hydrogen bond length between the migrating iodide ion (highlighted in green) and the nearest neighbouring hydrogen atom.

Figure 5.3. Size-mismatch-induced lattice expansion and optical properties of the films. a) X-ray diffraction (XRD) spectra of the $Ace_xMA_{1-x}PbI_3$ films with different values of x. b) High-resolution XRD spectra of the perovskite films showing the (100) perovskite diffraction peak. The PbI_2 and secondary phase (*) diffraction peaks are labelled. Inset shows the magnified normalized (100) perovskite peak. c) Variation of the *a* (or b) and *c* unit cell lattice parameters of the $Ace_xMA_{1-x}PbI_3$ films with different values of x. d) Absorption and normalized photoluminescence spectra of the $Ace_xMA_{1-x}PbI_3$ films with different values of x.

Figure 5.4. Device photovoltaic performance, charge carrier lifetimes and diode characteristics. a) Box plot showing the power conversion efficiency (PCE) distribution of the $MAPbI_3$ and $Ace_{0.03}MA_{0.97}PbI_3$ devices. b) Current density and voltage (*J-V*) curves of the champion devices. Inset includes the stabilized PCEs. c) Time-resolved photoluminescence spectra of the MA and AceMA films. Solid lines are the fitted profiles using a bi-exponential decay function. Inset includes the steady-state PL spectra. d) Transient photovoltage decay of the MA and AceMA devices. Solid lines are the fitted profiles using a mono-exponential decay function.

Figure 5.5. Ion migration and operational stability. Temperature-dependant conductivity of the a) $MAPbI_3$ and b) $Ace_{0.03}MA_{0.97}PbI_3$ lateral devices. c) Operational stability testing of encapsulated $MAPbI_3$ and $Ace_{0.03}MA_{0.97}PbI_3$ devices under continuous 1 sun illumination under open-circuit condition in ambient air. d) Thermal stability testing of the $MAPbI_3$ and $Ace_{0.03}MA_{0.97}PbI_3$ devices heated continuously at 85 °C in a nitrogen atmosphere.

Figure 6.1. Phase conversion kinetics of formamidinium lead tri-iodide ($FAPbI_3$) perovskite with a hetero-interface at the grain boundaries. a, Photographs of $FAPbI_3$ films on SnO_2-coated ITO substrates with different annealing times at 150 °C. Control: bare $FAPbI_3$, 1P: $FAPbI_3$ with 1.67 mol% PEA_2PbI_4, 3P: $FAPbI_3$ with 3.33 mol% PEA_2PbI_4, and 3F: $FAPbI_3$ with 3.33 mol% $FPEA_2PbI_4$. **b**, *In-situ* grazing incident wide angle X-ray scattering (GIWAXS) measurements of corresponding films deposited on silicon wafer substrates. **c**, Isothermal transformation diagrams showing the evolution of the α-$FAPbI_3$ phase proportion in the films as a function of annealing time at 150 °C on silicon wafers (upper panel) and on SnO_2-coated ITO substrates (lower panel).

Figure 6.2. Transmission electron microscopy (TEM) images and density functional theory (DFT) calculations. a-d, *In-situ* TEM images of the δ-$FAPbI_3$ film annealed at the phase conversion temperature for different times. The relatively bright spots are the cubic phase nuclei transformed from the hexagonal phase. High-resolution TEM images of $FAPbI_3$ films incorporated

with 3.33 mol% $FPEA_2PbI_4$ **e**, **f**, before and **h**, **i**, after the phase conversion process. **f** and **i** show magnified TEM images of the regions highlighted with yellow dashed boxes in **e** and **h**, respectively. **g** and **j** show corresponding fast Fourier transform (FFT) analysis of images **f** and **i**, respectively. Figure 6.2e-j are from samples prepared by scratching off the films from the substrate. **k**, DFT-calculated free energy barriers (ΔG_cs) for phase conversion from cubic to hexagonal (α→δ), from hexagonal to cubic (δ→α), and formation enthalpy of the cubic phase (ΔH) with respect to that of the hexagonal phase. Dashed lines and solid lines indicate ΔG_c without and with strain, respectively. The interlayer spacing of the strain-free hexagonal phase, layered perovskite and cubic phase are indicated with gray colored dashed vertical lines (d-spacings of DFT optimized structures). **l**, Schematic free energy diagrams for the hexagonal and cubic phased $FAPbI_3$ at different temperatures and strain condition. T is temperature and T_c is the temperature for phase conversion.

Figure 6.3. Crystallographic analyses before and after the phase conversion. X-ray diffraction (XRD) patterns of the films **a**, before and **b**, after the phase conversion process. **c**, High-resolution X-ray diffraction (XRD) patterns of the films after the phase conversion process. Inset shows the normalized (002) orientation peaks. **d**-**g**, XRD pole figure measurements along the (001) orientation of the **d**, control, **e**, 1P, **f**, 3P, and **g**, 3F films **h.** Composition-dependent strain before phase conversion and crystallite size of the films before and after the phase conversion process. The strain was calculated using the Williamson-Hall method from δ-$FAPbI_3$ films. The δ-$FAPbI_3$ crystallite sizes were calculated by the Williamson-Hall method, while the α-$FAPbI_3$ crystallite sizes were extracted from the AFM images. **i**, Steady-state photoluminescence (PL) and **j**, time-resolved PL decay profile measurements of the corresponding films. Insets of I show peak intensity (left) and normalized PL spectra (right).

Figure 6.4. Proof-of-concept devices. a, Device structure schematics and corresponding cross-sectional scanning electron microscopy (SEM) images of the solar cell devices based on the $FAPbI_3$ film with nano heteroepitaxy (NHE, with 3.33 mol% $FPEA_2PbI_4$). **b**, Current density-voltage (J-V) and **c**, external quantum efficiency (EQE) curves of solar cell devices based on a bare $FAPbI_3$ film (control) and a $FAPbI_3$ film with NHE. Inset of **b** shows steady-state power conversion efficiencies (SSPCEs) measured at maximum power points. **d**, Voltage-radiance curves of the light emitting diode (LED) devices, and **e**, corresponding EQE curves of the LED devices based on the control and NHE films. Inset of **d** shows the electroluminescence spectra of the LED

devices. Operational stability measurements of the **f**, solar cell (normalized SSPCE) and **g**, LED devices (normalized radiance) based on the control and NHE films.

List of Tables

Acknowledgments

This Ph.D. and the work described in this dissertation would not have been possible without the support, mentorship, and collaborative effort of many. I would like to express my deepest gratitude to all who have accompanied me through this journey.

First, I would like to offer my sincerest thanks to my advisor, Prof. Yang Yang, for his guidance and supervision across the 4.5 years of my Ph.D. studies at UCLA. Prof. Yang was kind enough to take me in as his graduate student back in 2017, despite my relative lack of research experience. He has always encouraged me to pursue my own interests, to consistently challenge myself and to think outside the box, and to never be afraid of failing. I am grateful for Prof. Yang for entrusting me with many responsibilities beyond just pure research, which I believe has adequately prepared me for a life and career in academia. I am thankful for every discussion and conversation we have had together over the last 4.5 years, which I have learned a lot from, both in terms of research and academia, and also more generally in life. I am sure that my connections with Prof. Yang will persist even long after I have left UCLA.

I would also like to thank the committee members for their mentorship: Prof. Richard B. Kaner, Prof. Jaime Marian, and Prof. Aaswath Raman. In particular, Prof. Marian also offered me my first teaching assistant opportunity during my first year at UCLA, and I am grateful for the trust he had in me since near the very beginning.

I would like to especially thank Dr. Jin-Wook Lee and Dr. Tae-Hee Han, who were both postdocs in Prof. Yang's group back when I first joined in 2017. I was assigned by Prof. Yang to be mentored by Dr. Lee and Dr. Han, and they taught me everything I needed to know to make the leap and transformation from an inexperienced undergraduate student to an independent graduate

researcher. Dr. Lee and Dr. Han devoted their time and effort to mentor me despite my many shortcomings, and I am sincerely grateful for their guidance and support. Dr. Lee and Dr. Han are now both faculty members themselves in South Korea, at Sungkyunkwan University and Hanyang University, respectively. Despite them having left Prof. Yang's group more than 3 years ago, we have all kept in close contact and collaboration, and I look forward to many more fruitful and productive endeavors to come in the near future.

In addition, I would also like to especially thank my seniors at Prof. Yang's lab: Dr. Nicholas De Marco, Mr. Oliver Lin, Mr. Zhenghong Dai, Dr. Sheng-Yung Chang, and Dr. Yao-Tsung Hsieh. They have all contributed tremendously and profoundly in shaping my nascent years when I first joined UCLA.

I am glad to have had the chance to share the joys and endure through the challenging times together with my fellow colleagues in Prof. Yang's lab. In addition to my colleagues already mentioned above, I would also like to thank, in no particular order: Dr. Pei Cheng, Dr. Dong Meng, Prof. Yu Duan, Prof. Zhao-Kui Wang, Dr. Guangwei Xu, Dr. Le Cai, Dr. Hangbo Yang, Dr. Rui Wang, Dr. Jingjing Xue, Dr. Zhengxu Wang, Dr. Yu-Che Lin, Dr. Yuqiang Liu, Dr. Haowen Cheng, Dr. Tianyi Huang, Dr. Hao-Cheng Wang, Dr. Chung-Hao Chen, Dr. Minhuan Wang, Dr. Jiahui Zhu, Dr. Yepin Zhao, Dr. Selbi Nuryyeva, Ms. Elizabeth Zhang, Mr. Ran Zheng, Mr. Qiyu Xing, Mr. Bin Chang, and Mr. Zongqi Li. I wish them all the best in their life and career, and I sincerely look forward to the chance for us to meet in person again, wherever and whenever.

I would also like to especially single out and thank Dr. Tianyi Huang, who also joined UCLA at the same time as me in 2017. We have toughed it out together through countless hard and difficult times across our Ph.D. studies. He has been a great friend over the last 4.5 years, both inside and outside the lab. It is no coincidence that we have co-first authored the most publications together. I am sure that our friendship will last long beyond our times at UCLA.

My research projects have majorly involved collaborative efforts with research groups outside of Prof. Yang's lab. I would like to especially thank: Prof. Ilhan Yavuz (Marmara University), Dr. Carolin M. Sutter-Fella (LBNL), Dr. Marc H. Weber (Washington State University), Mr. Tae Woong Yoon (Sungkyunkwan University), Dr. Mingjie Xu (UC Irvine), Dr. Maged Abdelsamie (LBNL), Mr. Keonwoo Park (Sungkyunkwan University), Dr. Sung-Joon Lee (UCLA), Dr. Jeong Hoon Ko (Caltech), Dr. Finn Babbe (LBNL), Mr. Michael E. Liao (UCLA), Mr. Kenny Huynh (UCLA), Dr. Kootak Hong (LBNL), Dr. Chenhui Zhu (LBNL), Prof. Kendall N. Houk (UCLA), Prof. Young Jae Song (Sungkyunkwan University), Prof. Xiaoqing Pan (UC Irvine), Prof. Sang Il Seok (UNIST), and Prof. Nam-Gyu Park (Sungkyunkwan University). It is fair to say that my research projects would not have turned out the way they did without the joint effort and contributions of all these collaborators. I look forward to continue working with them even after my time at UCLA ends.

I am thankful to my parents, sister, and extended family. This journey to obtain a Ph.D. began long before I joined UCLA, and I would not have reached this stage in my life and career without their support and belief in me through all these years.

Lastly, but perhaps most importantly, I would like to offer my greatest thanks to my fiancé, girlfriend, and best friend, Ms. Jinju Chun. She has been beside me through the highest of highs and the lowest of lows in life. Many people, incidents, and events in my life have come and gone, but her unwavering support and companionship have been the constants that have kept me pushing forward. This is just the beginning, and I look forward to spending the rest of my life together with her.

Chapter 1 is a version of *Advanced Materials*, **2019**, 31, 1803515; Chapter 2 is a version of *Joule*, **2020**, 4, 2426-2442; Chapter 3 is a version of *Journal of the American Chemical Society*, **2021**, 143, 6781-6786; Chapter 4 is a version of *Nature*, **2022**, https://doi.org/10.1038/s41586-022-04604-5; Chapter 5 is a version of *Advanced Materials*, **2020**, 32, 1906995; Chapter 6 is a version of *Nature Communications*, **2020**, 11, 5514. All the permissions have been granted by the publishers.

VITA

2013-2017	Master of Engineering, Department of Materials Science and Engineering, The University of Manchester, Manchester, United Kingdom
2015	Research intern, Institute of Materials Research and Engineering, Agency for Science, Technology and Research (A*STAR), Singapore
2017-2022	Graduate Student Researcher, Department of Materials Science and Engineering, University of California Los Angeles, Los Angeles CA, United States
2020-2022	Research affiliate, Chemical Sciences Division, Lawrence Berkeley National Laboratory, Berkeley CA, United States

Selected Publications

1. Shaun Tan†, Tianyi Huang†, Ilhan Yavuz†, Rui Wang, Tae Woong Yoon, Mingjie Xu, Qiyu Xing, Keonwoo Park, Do-Kyoung Lee, Chung-Hao Chen, Ran Zheng, Taegeun Yoon, Yepin Zhao, Hao-Cheng Wang, Dong Meng, Jingjing Xue, Young Jae Song, Xiaoqing Pan, Nam-Gyu Park, Jin-Wook Lee, and Yang Yang. Stability-limiting heterointerfaces of perovskite photovoltaics, *Nature*, 2022, https://doi.org/10.1038/s41586-022-04604-5 (†Contributed equally)
2. Shaun Tan†, Tianyi Huang†, Ilhan Yavuz†, Rui Wang, Marc H. Weber, Yepin Zhao, Maged Abdelsamie, Jingjing Xue, Finn Babbe, Jin-Wook Lee, Carolin M. Sutter-Fella, and Yang Yang. Surface Reconstruction of Halide Perovskites during Post-treatment, *Journal of the American Chemical Society*, 2021, 143, 6781-6786. (†Contributed equally)
3. Shaun Tan, Ilhan Yavuz, Marc H. Weber, Tianyi Huang, Chung-Hao Chen, Rui Wang, Hao-Cheng Wang, Jeong Hoon Ko, Selbi Nuryyeva, Jingjing Xue, Yepin Zhao, Kung-Hwa Wei, Jin-

Wook Lee, and Yang Yang. Shallow iodine defects accelerate the degradation of α-phase formamidinium perovskite, *Joule*, 2020, 4, 2426-2442.

4. Shaun Tan, Ilhan Yavuz, Nicholas De Marco, Tianyi Huang, Sung-Joon Lee, Christopher S Choi, Minhuan Wang, Selbi Nuryyeva, Rui Wang, Yepin Zhao, Hao-Cheng Wang, Tae-Hee Han, Bruce Dunn, Yu Huang, Jin-Wook Lee, and Yang Yang. Steric Impediment of Ion Migration Contributes to Improved Operational Stability of Perovskite Solar Cells, *Advanced Materials*, 2020, 32, 1906995.
5. Shaun Tan†, Tianyi Huang†, and Yang Yang. Defect passivation of perovskites in high efficiency solar cells, *Journal of Physics: Energy*, 2021, 3, 042003. (†Contributed equally)
6. Jin-Wook Lee†, Shaun Tan†, Sang Il Seok, Yang Yang, and Nam-Gyu Park. Rethinking the A Cation in Halide Perovskites, *Science*, 2022, 375, eabj1186. (†Contributed equally)
7. Jin-Wook Lee†, Shaun Tan†, Tae-Hee Han†, Rui Wang, Lizhi Zhang, Changwon Park, Mina Yoon, Chungseok Choi, Mingjie Xu, Michael E. Liao, Sung-Joon Lee, Selbi Nuryyeva, Chenhui Zhu, Kenny Huynh, Mark S. Goorsky, Yu Huang, Xiaoqing Pan, and Yang Yang. Solid-phase hetero epitaxial growth of α-phase formamidinium perovskite, *Nature Communications*, 2020, 11, 5514. (†Contributed equally)
8. Tianyi Huang†, Shaun Tan†, Selbi Nuryyeva†, Ilhan Yavuz, Finn Babbe, Yepin Zhao, Maged Abdelsamie, Marc H. Weber, Rui Wang, K. N. Houk, Carolin M. Sutter-Fella, and Yang Yang. Performance-Limiting Formation Dynamics in Mixed-Halide Perovskites, *Science Advances*, 2021, 7, eabj1799 (†Contributed equally)
9. Tae-Hee Han†, Shaun Tan†, Jingjing Xue, Lei Meng, Jin-Wook Lee, and Yang Yang. Interface and Defect Engineering for Metal Halide Perovskite Optoelectronic Devices, *Advanced Materials*, 2019, 31, 1803515. (†Contributed equally)

Chapter 1. Introduction to the Interface and Defect Engineering of Metal Halide Perovskites

Within the past decade, metal halide perovskites have attracted tremendous interest from the optoelectronics community, owing to their unique combination of properties, which have enabled the versatile functionality of metal halide perovskites, being applied to photovoltaics[1–3], light emitting diodes (LEDs)[4–6], lasers[7], photodetectors[8,9] and thin film transistors.[10] External quantum efficiencies (EQEs) over 20% have been achieved for perovskite-based LEDs, while the certified record power conversion efficiency (PCE) for perovskite solar cells currently stand at an astounding 25.7%. Perovskite-based optoelectronic devices already rival that of commercially available conventional devices such as silicon, CIGS and organic LEDs fabricated via high temperature vacuum processes.

Metal halide perovskites have the general formula ABX_3 (**Figure 1.1a**), where A is a monovalent cation, commonly organic methylammonium (MA, $CH_3NH_3^+$) or formamidinium (FA, $(NH_2)_2CH^+$), or inorganic cesium or rubidium; B is a divalent metal cation, possibly lead, tin or germanium; and X is a halide anion. By varying either of the A, B or X site ions, or utilizing multicomponent A, B or X site ions, the optoelectronic properties of metal halide perovskites can be modified (**Figure 1.1b-d**) to fit a specific application. Considering the standard iodide-based perovskite, $CH_3NH_3PbI_3$ ($MAPbI_3$), for instance, the bandgap can be increased from 1.59 eV to 2.31 eV by substituting I for Br.[11]

Cubic symmetry of the *Pm*3*m* space group is the most ideal for metal halide perovskites, with octahedra of corner-sharing BX_6 surrounding A cations with 12-fold coordination.[12] However, perovskites with too small A cations or too large B cations will deviate towards either a tetragonal, orthorhombic or rhombohedral structure. The Goldschmidt tolerance factor, *t*, defined by the ratio $t = (R_A + R_X) / [\sqrt{2}\,(R_B + R_X)]$, and the octahedral factor, μ, where $\mu = R_B / R_X$, where R_A, R_B, R_X are the ionic radii of the A, B, X species, respectively, quantify this deviation. It is observed that metal halide perovskites have $0.8 < t < 1.0$ and $0.44 < \mu < 0.90$, and that the ideal cubic structure occurs at $t = 1.0$.[13] Calculated theoretical *t* and μ values for some common metal halide perovskites are shown in **Figure 1.1e**.[14]

Regarding photophysical properties, high absorption coefficients ($> 10^5$ cm^{-1}) throughout the visible spectrum (**Figure 1.2a**) because of a direct bandgap enable submicron functional film thickness.[15] $MAPbI_3$ and $MAPbI_2Cl$ exhibits sharp absorption onsets at approximately 800 nm,

compared to the 700 nm of $MAPbI_2Br$.[16] The Urbach energy of $MAPbI_3$ is as low as 15 meV.[17] Electronic structure studies on $MAPbI_3$ revealed that the conduction band minimum (CBM) is formed from the non-bonding 6p orbitals of Pb while the valence band maximum (VBM) consists of antibonding hybrid states between the s orbitals of Pb and the p orbitals of I.[18] Exciton binding energy was measured to be only a few tens of millielectronvolts, comparable to ambient thermal energy and thus free carriers are generated spontaneously upon photoexcitation.[19] Metal halide perovskites are also ambipolar charge transporters.[20] Time-resolved terahertz spectroscopy on $MAPbI_3$ observed that photogeneration of electron-hole pairs occur almost instantaneously and dissociate in 2 ps into free carriers (**Figure 1.2b**). Carrier diffusion lengths around 100 nm for $MAPbI_3$ for both electrons and holes and exceeding 1 micrometer for a mixed halide $MAPbI_{3-x}Cl_x$ perovskite were measured by time-resolved photoluminescence studies (**Figure 1.2c-d**).[21] In terms of fabrication, metal halide perovskites are solution-processable at low temperatures with relative ease using abundant precursor materials. All in all, metal halide perovskites possess an advantageous set of photophysical properties for optoelectronics applications.

The main loss mechanism undermining the performance of perovskite optoelectronic devices is nonradiative recombination induced by heterointerfaces and defects. Surface defects along the heterointerfaces between the perovskite layer and the adjacent contact layers have been shown to be detrimental to the functionality and operation of perovskite optoelectronic devices. Interfacial recombination loss is minimized by reducing the defect density and promoting a more favorable energy level alignment between the perovskite layer and its contacts. Within the bulk of the perovskite, solution processing inevitably introduces structural disorders in the form of grain boundaries, which were found to have a significant impact on both the optoelectronic properties and stability of the perovskite film and device. Dislocations and dangling bonds at grain boundaries constitute trap states that impede charge carrier transport and induce non-radiative recombination losses. Consequently, charge carrier diffusion lengths in perovskite single crystals with trap densities as low as 10^9-10^{10} cm^{-3} exceed 100 μm, whereas that of polycrystalline thin films with trap densities between 10^{16}-10^{18} cm^{-3} are lower than 10 μm.[22–25] Defective grain boundaries are also known to be vulnerable to environmental degradation. Heat- and moisture-induced decomposition initiates at grain boundaries and propagates into the bulk perovskite, while charged defects migrate through the grain boundaries under an electrical bias.

The small exciton binding energies (E_b ~30 meV for $CH_3NH_3PbI_3$, ~76 meV for

$CH_3NH_3PbBr_3$), long carrier diffusion lengths (~1 μm) and also a high density of surface defects of perovskite polycrystalline films induce severe exciton quenching in the bulk or at the interfaces of devices, limiting the electroluminescent properties of LEDs.[21,26–28] In addition, perovskite LEDs are usually plagued by an unbalanced charge transport from each of the two metal electrodes, a consequence of the difficulty and associated problems with depositing multiple functional layers via solution-processing, such as the carrier or exciton blocking layers. Unbalanced charge transport in perovskite LEDs results in the formation of narrow recombination zones close to the heterointerfaces, which causes a severe efficiency drop, operational instability, and a large efficiency roll-off. Therefore, interface engineering and the manipulation of defective grain boundaries to achieve high EL are essential before perovskite LEDs can be applied to display technologies.

For perovskite photovoltaics, the best devices already boast short-circuit current density (J_{SC}) values near the theoretical limit for a given bandgap.[29] Thus maximizing the open-circuit voltage (V_{OC}) and consequently fill factor (FF) is necessary to further improve the record achievable PCE of perovskite photovoltaics. Nonradiative recombination losses along the interfaces and within the bulk are responsible for reducing the V_{OC} and FF. In this context, interface and defect engineering prove crucial to mitigate nonradiative recombination in a bid to further push the PCE towards its thermodynamic Shockley-Queisser limit.

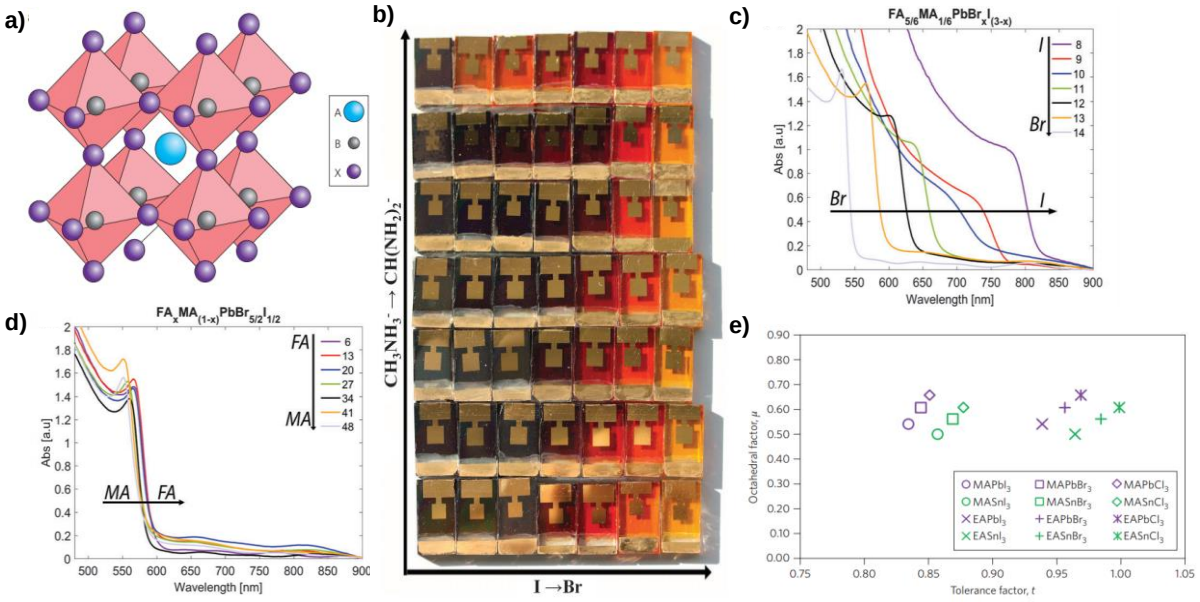

Figure 1.1. Crystal structure and compositional breadth of metal halide perovskites. a) Cubic

crystal structure of perovskite. Reproduced with permission.[13] Copyright 2014, Macmillan Publishers Limited. b) Colour tuning of devices with varying MA/FA and/or Br/I compositions; absorption spectra of c) $FA_{5/6}MA_{1/6}PbBr_xI_{3-x}$ and d) $FA_xMA_{1-x}PbBr_{5/2}I_{1/2}$ perovskites as x is varied. Reproduced with permission.[11] Copyright 2016, Royal Society of Chemistry. e) Calculated tolerance factors, *t*, of some metal halide perovskites. MA = Methylammonium (CH_3NH_3), FA = formamidinium ($NH_2CH{=}NH_2$) and EA = ethylammonium ($CH_3CH_2NH_3$). Reproduced with permission.[13] Copyright 2014, Macmillan Publishers Limited.

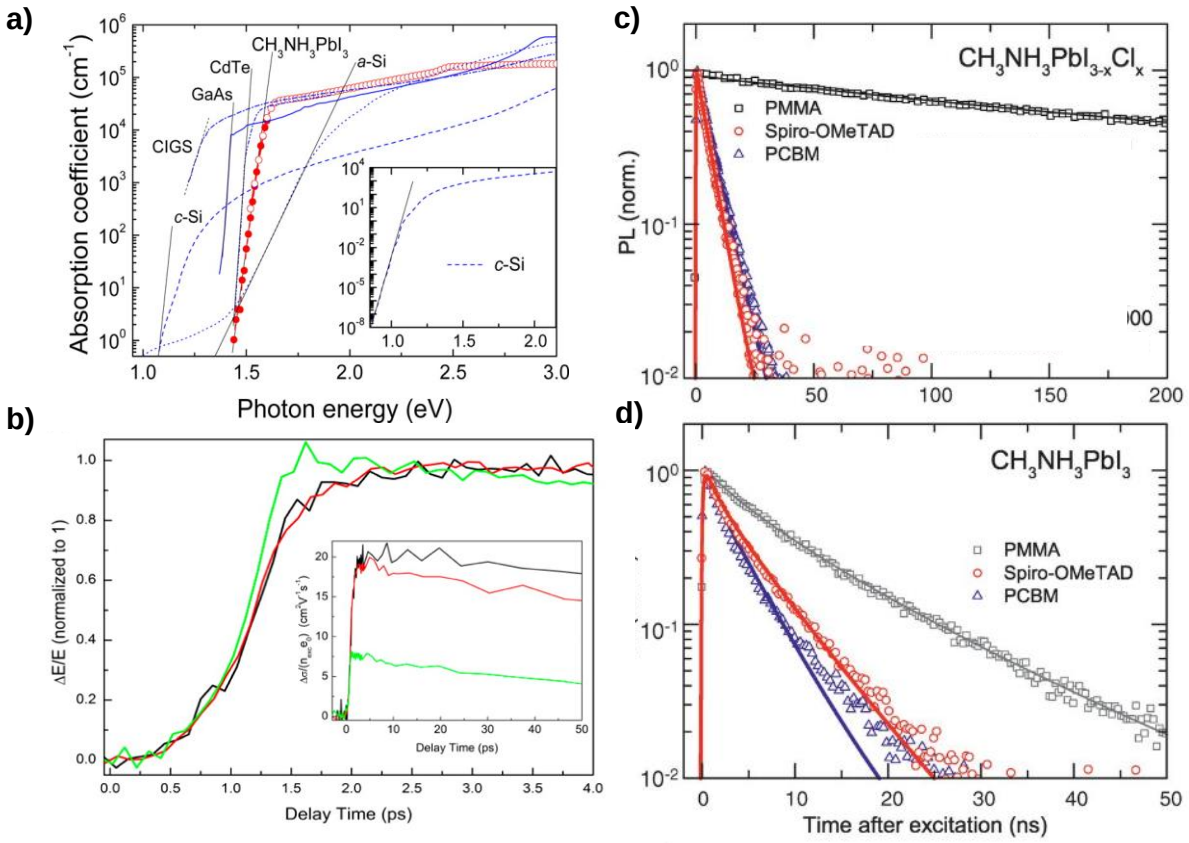

Figure 1.2. Optoelectronic properties of metal halide perovskites. a) Absorption coefficient of $MAPbI_3$ versus other optoelectronic materials. The slope of the Urbach tails are also included, with the inset image showing the data for *c*-Si (crystalline Si) down to low absorption values. Reproduced with permission.[17] Copyright 2014, American Chemical Society. b) THz kinetics of $MAPbI_3$ (black), $MAPbI_3/TiO_2$ (green) and $MAPbI_3/Al_2O_2$ (red). Inset shows THz photoconductivity kinetics normalized to $n_{exc}e$ for the first 50s. Reproduced with permission.[14] Copyright 2014, American Chemical Society. Time-resolved photoluminescence studies on b) $MAPbI_{3-x}Cl_x$ c) $MAPbI_3$ on PCBM (blue) or spiro-MeOTAD (red) with fits to the PMMA data (black). The perovskite films were

encapsulated with PMMA. Reproduced with permission.[18] Copyright 2013, American Association for the Advancement of Science.

References

1. Yang, W. S. *et al.* Iodide management in formamidinium-lead-halide–based perovskite layers for efficient solar cells. *Science* **356**, 1376–1379 (2017).
2. Lee, J.-W., Kim, H.-S. & Park, N.-G. Lewis Acid-Base Adduct Approach for High Efficiency Perovskite Solar Cells. *Acc. Chem. Res.* **49**, 311–319 (2016).
3. Ahn, N. *et al.* Highly Reproducible Perovskite Solar Cells with Average Efficiency of 18.3% and Best Efficiency of 19.7% Fabricated via Lewis Base Adduct of Lead(II) Iodide. *J. Am. Chem. Soc.* **137**, 8696–8699 (2015).
4. Lei, M. *et al.* Pure Formamidinium-Based Perovskite Light-Emitting Diodes with High Efficiency and Low Driving Voltage. *Adv. Mater.* **29**, 1603826 (2016).
5. Kim, D. Bin *et al.* Improved performance of perovskite light-emitting diodes using a PEDOT:PSS and MoO3 composite layer. *J. Mater. Chem. C* **4**, 8161–8165 (2016).
6. Dai, X. *et al.* Solution-processed, high-performance light-emitting diodes based on quantum dots. *Nature* **515**, 96 (2014).
7. Xing, G. *et al.* Low-temperature solution-processed wavelength-tunable perovskites for lasing. *Nat. Mater.* **13**, 476–480 (2014).
8. Dong, R. *et al.* High-Gain and Low-Driving-Voltage Photodetectors Based on Organolead Triiodide Perovskites. *Adv. Mater.* **27**, 1912–1918 (2015).
9. Dou, L. *et al.* Solution-processed hybrid perovskite photodetectors with high detectivity. *Nat. Commun.* **5**, 5404 (2014).
10. Senanayak, S. P. *et al.* Understanding charge transport in lead iodide perovskite thin-film field-effect transistors. *Sci. Adv.* **3**, (2017).
11. Jesper Jacobsson, T. *et al.* Exploration of the compositional space for mixed lead halogen perovskites for high efficiency solar cells. *Energy Environ. Sci.* **9**, 1706–1724 (2016).
12. Chen, Q. *et al.* Under the spotlight: The organic-inorganic hybrid halide perovskite for optoelectronic applications. *Nano Today* **10**, 355–396 (2015).
13. Green, M. A., Ho-Baillie, A. & Snaith, H. J. The emergence of perovskite solar cells. *Nat.*

Photonics **8**, 506–514 (2014).

14. Ponseca, C. S. *et al.* Organometal halide perovskite solar cell materials rationalized: Ultrafast charge generation, high and microsecond-long balanced mobilities, and slow recombination. *J. Am. Chem. Soc.* **136**, 5189–5192 (2014).
15. Kim, H.-S. *et al.* Lead Iodide Perovskite Sensitized All-Solid-State Submicron Thin Film Mesoscopic Solar Cell with Efficiency Exceeding 9%. *Sci. Rep.* **2**, 1–7 (2012).
16. Mosconi, E., Amat, A., Nazeeruddin, M. K., Grätzel, M. & De Angelis, F. First-principles modeling of mixed halide organometal perovskites for photovoltaic applications. *J. Phys. Chem. C* **117**, 13902–13913 (2013).
17. De Wolf, S. *et al.* Organometallic Halide Perovskites: Sharp Optical Absorption Edge and Its Relation to Photovoltaic Performance. *J. Phys. Chem. Lett.* **5**, 1035–1039 (2014).
18. Frost, J. M. *et al.* Atomistic origins of high-performance in hybrid halide perovskite solar cells. *Nano Lett.* **14**, 2584–2590 (2014).
19. Miyata, A. *et al.* Direct measurement of the exciton binding energy and effective masses for charge carriers in organic-inorganic tri-halide perovskites. *Nat. Phys.* **11**, 582–587 (2015).
20. Ball, J. M., Lee, M. M., Hey, A. & Snaith, H. J. Low-temperature processed meso-superstructured to thin-film perovskite solar cells. *Energy Environ. Sci.* **6**, 1739–1743 (2013).
21. Stranks, S. D. *et al.* Electron-Hole Diffusion Lengths Exceeding 1 Micrometer in an Organometal Trihalide Perovskite Absorber. *Science* **342**, 341–344 (2013).
22. Stranks, S. D. *et al.* Recombination Kinetics in Organic-Inorganic Perovskites: Excitons, Free Charge, and Subgap States. *Phys. Rev. Appl.* **2**, 1–8 (2014).
23. Draguta, S. *et al.* Spatially Non-uniform Trap State Densities in Solution-Processed Hybrid Perovskite Thin Films. *J. Phys. Chem. Lett.* **7**, 715–721 (2016).
24. Angelis, F. De & Petrozza, A. Clues from defect photochemistry. *Nat. Mater.* **17**, 377–384 (2018).
25. Haughn, C. R. *et al.* Quantification of trap state densities in GaAs heterostructures grown at varying rates using intensity-dependent time resolved photoluminescence. *Appl. Phys. Lett.* **102**, (2013).
26. Xing, G. *et al.* Long-Range Balanced Electron- and Hole-Transport Lengths in Organic-Inorganic CH 3 NH 3 PbI 3. *Science* **342**, 344–347 (2013).

27. Liu, D. & Kelly, T. L. Perovskite solar cells with a planar heterojunction structure prepared using room-temperature solution processing techniques. *Nat. Photonics* **8**, 133 (2013).
28. Young-Hoon, K. *et al.* Multicolored Organic/Inorganic Hybrid Perovskite Light-Emitting Diodes. *Adv. Mater.* **27**, 1248–1254 (2014).
29. Correa-Baena, J.-P. *et al.* Promises and challenges of perovskite solar cells. *Science* **358**, 739–744 (2017).

Chapter 2 Shallow Iodine Defects Accelerate the Degradation of α-Phase Formamidinium Perovskite

The record power conversion efficiencies (PCEs) of single-junction metal halide perovskite solar cells (PSCs) have catapulted to over 25 % in just over a decade.[1–5] With attainable PCEs now rivalling that of matured photovoltaic technologies based on conventional inorganic semiconductors, the attention of the community has turned to addressing the notorious instability issues of PSCs.

Shallow defects, by definition, do not constitute non-radiative recombination centers due to their low transition energies, and are therefore considered mostly benign and of less importance in inorganic covalent semiconductors like silicon or gallium arsenide. In contrast, due to the characteristic ionic nature of metal halide perovskites, intrinsic point defects are charged,[6–8] and this has significant implications on its defect physics. Particularly, the migration of charged defects in response to a potential gradient is known to seriously degrade the long-term operational stability of PSCs.[9–12] Notably, several shallow defects are theoretically predicted to have low formation and migration activation energies.[6,7,9,12,13] This implies the possible generation of shallow defects during film fabrication and post-treatment processes. Although the initial device photovoltaic performance is mostly unaffected by the generated defects due to their shallow nature, the long-term operational stability of the PSCs can potentially be impacted. Therefore, systematic investigations on the effects of shallow defects are required.

In particular, fewer studies have been done on the formamidinium lead triiodide ($FAPbI_3$) perovskite as compared to the prototypical methylammonium lead triiodide ($MAPbI_3$),[14–17] whilst the vast majority of high-performance PSCs are based on a $FAPbI_3$ dominant composition.[3,4] This is significant because of the different degradation mechanisms between the two – $FAPbI_3$, for instance, phase degrades from the photoactive cubic α-$FAPbI_3$ perovskite phase to the hexagonal non-perovskite δ-$FAPbI_3$ phase, whereas the $MAPbI_3$ perovskite phase degrades into PbI_2.[14,16,18] Point defects disrupt the original lattice arrangement, and thus may affect the thermodynamic energetics of the perovskite,[19,20] especially relevant for $FAPbI_3$ due to its metastable nature. Therefore, it is of critical importance to understand the effects of the intrinsic point defects to mitigate the instability issues of $FAPbI_3$-based PSCs.

In this study, we observed that shallow iodine interstitial defects (I_i) can be generated unintentionally during commonly used post-fabrication treatments. We show that I_i can lower the

cubic-to-hexagonal phase transformation activation energy barrier of $FAPbI_3$-based perovskites to accelerate its degradation. We demonstrate that concurrently avoiding the generation of I_i and the more effective passivation of iodine vacancy defects (V_I) improve the thermodynamic phase stability and operational stability of the perovskite films and devices. Consequently, our most stable PSC devices demonstrated a more than five-fold increased average lifetime over the control devices under continuous illumination operational stability testing. The champion device retained 92.1 % of its initial performance after nearly 1,000 h of testing.

2.1 Identification of iodine interstitial defects

Iodine-related shallow defects are theoretically predicted to have relatively low (bulk) formation energies.[6–8] Recently, post-fabrication surface treatment strategies using organic iodides have been reported by many groups. The iodide anion (I^-) has been reported to passivate V_I defects.[21–23] However, we speculated that excessive I^- coated on the perovskite surface possibly generates shallow iodine-related defects, so we tried to investigate this by mimicking the surface environments while excluding the organic cation.

All control samples for this study are based on a $FAPbI_3$ composition with 5 mol% of added $MAPbBr_3$ fabricated by a one-step antisolvent quenching method. The as-fabricated perovskite films were then post-treated with different concentrations of pure iodine (I_2) dissolved in isopropanol[3] (hereafter, concentrations given in terms of equivalent concentration of atomic iodine) at 5000 rpm, followed by annealing at 100°C for 5 min. The concentrations and deposition conditions were set to be comparable to those commonly reported for organic iodide salts (**Table B2.1**). The control films were treated with blank (pure) isopropanol, and underwent the same annealing. PSC devices of architecture ITO/SnO_2/perovskite/spiro-MeOTAD/Au were fabricated without or with surface treatment. We observed that the device photovoltaic parameters, including the open-circuit voltage (V_{OC}), measured in reverse current density-voltage (*J-V*) scan, changed marginally with surface treatment (**Figure A2.1**), while the scan direction dependent *J-V* hysteresis (**Figure 2.1a**, **Figure A2.1** and **Figure A2.2**) of the devices became increasingly more pronounced. This hints at the formation of shallow iodine related defects, given that defect migration is responsible for the hysteresis behavior in perovskites.[10,11,24] Particularly, on the longer timescales of the stabilized power output (SPO) measurements (insets of **Figure 2.1a**), where defects have sufficient time to migrate and screen the applied bias,[10,25] the SPO is seen to stabilize slower and decays to a lower value with

increased surface treatment concentration.

First-principles density functional theory (DFT) calculations were performed to identify the probable defect species. The surface formation energies (**Figure 2.1b**) of iodine-related neutral point defects were computed for $FAPbI_3$ grown in stoichiometric conditions for a FAI terminated surface (most thermodynamically stable, see **Figure A2.3** for details), and compared to the bulk formation energies reproduced from a previous report.[7] **Figure 2.1b** shows that the bulk formation energies of V_I, I_i, FA-I antisite defects (FA_I), and I-FA antisite defects (I_{FA}) are approximately comparable at ~1 eV. The trend however changes dramatically at the surface. The calculated formation energies increased from their bulk values for V_I (1.16 to 2.71 eV), FA_I (1.27 to 4.56 eV), and I_{FA} (1.37 to 2.78 eV), but decreased for I_i (1.13 to 0.97 eV). The Fermi level (E_F) dependence of the formation energies at the surface was further computed for ${I_i}^q$, where q denotes the defect charge state (**Figure A2.4**). Negatively charged ${I_i}^-$ has the lowest formation energy across the bandgap among the different ${I_i}^q$ charged states. Near the valence band maximum, the formation energies for ${I_i}^0$ and ${I_i}^-$ are comparable and relatively low at ~1 eV. The position of the (q/q') transitions (transition levels) relative to the bandgap determine the susceptibility of the defect to trap or release charge carriers, i.e. the depth of the (shallow or deep) trap state. The (0/-1) transition occurs 0.03 eV above the valence band edge, whereas the (+1/0) and (+1/-1) transitions occur within the valence band, indicating that I_i is a shallow hole trap with low formation energy. The theoretical results suggest that I_i, predominantly in its ${I_i}^-$ charged state (due to its relatively lower formation energy) is the likely generated species. Additionally, ${I_i}^-$ has a low migration activation energy,[9,13,25] and is thus a plausible candidate to induce the *J-V* hysteresis. We further note that additional concurrent phenomena reported for $MAPbI_3$ may perhaps also explain the benign nature of ${I_i}^-$, including kinetic deactivation due to a fast hole trapping/detrapping process.[26]

We further probed the perovskite films using positron annihilation spectroscopy (PAS) to investigate the existence of the defects. A basic schematic of the measurement mechanism is shown in **Figure A2.5**. Positively charged positrons (antiparticle to the electron) are implanted from the perovskite surface and annihilate with electrons from a free lattice site or after trapping at negatively charged or neutral (but not positive) vacancies and/or interstitial defects to emit two gamma photons.[27–29] The shape (S) parameter is then extracted from the doppler broadening of the gamma spectrum at each implantation depth. The S parameter increases with increasing density of defect

sites.[27,28] Here, we varied the implantation depth of the positron by changing its kinetic energy (E_k) to investigate the depth dependent defect density. The results show that the S parameter of the films near the top surface (mean depth <10 nm, shaded in yellow in **Figure 2.1c**) is higher with increasing surface treatment concentration, indicating a higher density of negatively charged or neutral defects at the surface region. Notably, an inverse uptick (**Figure 2.1c**) right at the top surface (mean depth <0.2 nm) is observed for the treated films, but not the control film. The selective enhancement in defect density and thus S parameter at the top surface (E_k <0.8 keV, mean depth <0.24 nm) compared to the bulk region (0.8 keV<E_k <6 keV, 6.73 nm<mean depth <170 nm) is more obviously seen in **Figure 2.1d**.

Together with the theoretical and device results, the selectivity of PAS to detect *only* negatively charged or neutral defects supports the generation of I_i^-, i.e. I^-occupying an interstitial site. I_3^- occupying an interstitial site is equivalent to the I_i^+point defect,[26,30] since I_i^+ consists of one central I^+ bounded by two I^- (coordinating with Pb) on both sides,[30] i.e. the trimer structure of I_3^-. The dripping solution consists of I_3^- in dynamic equilibrium:[3]

$$I_2 + I^- \leftrightarrow I_3^-$$

We thus speculate that the I^- can possibly be generated from 1) the evaporation of I_2 upon post-treatment annealing shifts the dynamic equilibrium towards the reactants to form I^- according to *Le Chatelier*`s principle, and/or 2) the thermal decomposition of I_3^- into I^- from the annealing.[31] Further PAS measurements on samples surface treated without annealing (**Figure A2.6**) support this, in that I^- must have been generated from some back reaction, and that I_3^- (I_i^+) cannot be detected by positrons. We can further exclude any post-treatment induced damage (discussed below). Regardless of the source of I^-, the results suggest that surface treatment with organic iodide salts can unintentionally generate shallow I_i^- defects.

2.2 Accelerated phase degradation due to iodine interstitial defects

Although the generated I_i seem to not act as non-radiative electronic traps, we speculated that the intrinsic stability of the perovskite may be affected.[32,33] Specifically, it was shown that excess I_2 added to $MAPbI_3$ accelerated its degradation into PbI_2 due to an intrinsic degradation pathway whereby the excess I^- in the perovskite undergoes an autocatalytic chain reaction with self-generated

I_2 vapor.[32] Similar degradation by I_2 vapor was also observed for $FAPbI_3$. I_2 vapor inevitably and readily self-forms from within the perovskite[32,33] during PSC operation due to the effect of illumination,[14,33] oxygen,[15] heat,[14,16,33] or even applied bias.[17,34] Importantly, PSC encapsulation cannot fully resolve this intrinsic self-degradation. To test whether surface I_i defects has a similar detrimental role on $FAPbI_3$, we intentionally exposed the perovskite films to I_2 vapor in a nitrogen glovebox as with the previous study.[32]

The phase and morphology evolution of the films were monitored by X-ray diffraction (XRD) and atomic force microscopy (AFM) measurements in **Figure 2.2**. The crystallinity, phase purity, morphology, and surface roughness of the fresh films were essentially the same irrespective of surface treatment as seen in **Figure 2.2a**, **Figure 2.2b** and **Figure A2.7**. The fresh films were dominated by the cubic α-$FAPbI_3$ phase with its characteristic peaks at ~14.1° and ~28.2° corresponding to the (001) and (002) diffraction planes. A small peak at ~12.6° corresponding to the (001) plane of PbI_2 is visible with comparable intensities for all films. After 5 min exposure to I_2 vapor, the intensity of the α-$FAPbI_3$ peaks decreased with emergence of a new peak at ~11.8° corresponding to the (010) plane of the hexagonal δ-$FAPbI_3$ non-perovskite phase. With increased exposure to I_2 vapor, the α-$FAPbI_3$ phase incrementally degraded into the δ-$FAPbI_3$ phase. The PbI_2 peak intensity remained approximately unchanged, highlighting a different degradation pathway compared to $MAPbI_3$.[32] Notably, the PbI_2 peak intensity is comparable for all films even after the 35 min exposure. **Figure 2.2a** plots the evolution of the δ(010):α(100) peak ratios for the films with exposure time. We observed that the films degraded more rapidly with increased surface treatment concentration. This is supported by the 3D AFM topography images of **Figure 2.2b**. All the fresh films were compact and uniform with grain sizes on the order of ~1 μm. The surface root-mean-square roughness (R_q) of the fresh films were comparable (~30 nm). With increased exposure, R_q of the 30 mM treated film was observed to increase more rapidly than the control film, likely due to an accelerated recrystallization (phase transition) into the δ-$FAPbI_3$ phase: R_q of the treated film increased to 71.0 nm and 137.0 nm after 15 min and 35 min exposure, respectively. In contrast, R_q of the control film increased from 29.7 nm to 39.3 nm to 79.7 nm over the same time period.

The accelerated degradation of cubic α-$FAPbI_3$ without forming PbI_2 suggests that the activation energy barrier for the α-$FAPbI_3$-to-δ-$FAPbI_3$ phase transformation is lowered by the presence of I_i. Since the phase transformation rate is exponentially proportional to the negative of

the activation barrier,[35,36] we performed first-principles calculations to check for any changes in the transition energetics for the α-to-δ phase transformation of $FAPbI_3$ (**Figure 2.2c**). Indeed, the results show that the activation barrier nearly halves from 689 meV to 354 meV with I_i as compared to the defect-free case, correlating with the experimental observations. Therefore, the surface I_i defects probably acted as preferred initiation points for the nucleation of the δ-$FAPbI_3$ phase, which then propagate into the perovskite bulk to accelerate its degradation. A possible origin for the lowered transition barrier can be seen in the intermediate bond reconstruction processes between the defect-free and defected structures (**Figure 2.2d** and **Figure 2.2e**), where I_i diffuses to participate in the active breakage/reformation of the lattice. This is further seen in the transition states in **Figure 2.2e** and **Figure A2.8**, where I_i coordinates with Pb in a face-sharing configuration, which is characteristic of the hexagonal crystal structure.[37]

2.3 A possible mitigation strategy

In addition to the accelerated phase degradation, although shallow defects (e.g. I_i) by nature do not trap charges, the migration and accumulation of shallow defects at the opposite contact layers can screen the built-in electric field to negatively impact the device performance.[38,39] In the longer term, shallow defects can possibly penetrate into the adjacent contact layers to induce irreversible chemical reactions.[40,41] Given the possible generation of I_i from depositing I^- at the perovskite surface during typical surface treatments, a solution would be to replace I^- with an alternative anion. Ammonium iodide salts are usually synthesized via the neutralization reaction between an amine and hydroiodic acid. An alternative acid, which would be deprotonated to its conjugate base on neutralization, is thus the obvious choice. Our initial screening identified trifluroacetate (TFA^-) as a possible choice, given that the pK_a of trifluroacetic acid (0.23) is sufficiently low to ensure that it reacts completely with most common amines.[42] I^- as a counter anion functions to passivate iodine vacancy (V_I) defects.[21–23] Thus, the most crucial requirement for TFA^- is to fulfill the same role.

To assess this possibility, the density of states (DOS) of the defect-free, defected, and passivated surfaces are calculated as in **Figure A2.9**. With TFA^-, the electronic states formed by V_I is almost completed eliminated to restore the DOS profile of the defect-free case. The V_I – TFA^- interaction energy was calculated to be -4.01 eV, higher than the $V_I - I^-$ interaction energy of -3.41 eV (**Figure 2.3a** and **3b**), suggesting that TFA^- likely passivates V_I more effectively.

To verify our theoretical results, PSC devices were fabricated where the perovskite was post-

treated with different ammonium cations. To generalize our approach, an aliphatic (octylammonium, OA), aromatic (phenylammonium, PEA) and zwitterionic (phenylalanine, PA) cation were chosen. The average photovoltaic parameters of the devices are summarized in **Table B2.2**. Overall, all treated devices showed superior performance compared to the control, with all TFA^- treated devices demonstrating higher PCEs attributed to an improved V_{OC} and FF relative to their corresponding I^- counterparts.

Since the PA treated devices demonstrated the best photovoltaic performance, we focused on them to further investigate the differences between I^- and TFA^-. Given that the perovskite surface chemistry may differ when an organic cation capping layer is present,[43] we further probed the perovskite films on glass treated with either PAI or PATFA with Positron Annihilation Spectroscopy (**Figure A2.10)**. The results show that the S parameter beyond the passivation layer/perovskite interface is higher with PAI treatment, supporting the generation of I_i. Further computational calculations (**Figure A2.11)** like before on $FAPbI_3$ slabs with PA^+ as a top capping layer[44] indicate that the formation energy for I_i^- (and I_i^0) are more negative (relative to the pristine surface in **Figure A2.3**) across the bandgap, indicating that its formation is even more energetically favorable. Furthermore, all transition levels occur within the VBM, confirming its shallow nature.

Subsequently, additional devices were fabricated, and the distribution of their photovoltaic parameters are plotted in **Figure 2.3c** and **Figure A2.12**, and summarized in **Table 2.1**. The average PCE of the control devices was increased from 20.32 ± 0.35 % to 21.23 ± 0.36 % with PAI treatment and 21.84 ± 0.35 % with PATFA treatment. The performance enhancement of the treated devices is attributed to an improved V_{OC} (1.073 ± 0.012 V to 1.103 ± 0.009 V with PAI treatment to 1.120 ± 0.013 V with PATFA treatment) and FF (0.774 ± 0.012 to 0.786 ± 0.014 with PAI treatment to 0.796 ± 0.019 with PATFA treatment). The J_{SC} of the devices were essentially the same at ~24.5 mA cm^{-2}, and well-matched with the external quantum efficiency spectra of the devices with <4 % discrepancy (**Figure A2.13**).[45] *J-V* curves of the champion devices are displayed in **Figure 2.3d**, with individual photovoltaic parameters summarized in parenthesis in **Table 2.1**. The champion PATFA treated device attained a reverse scan PCE of 22.98 % (J_{SC} of 24.61 mA cm^{-2}, V_{OC} of 1.127 V, and FF of 0.829), higher than that of the PAI treated device at 21.86 % (J_{SC} of 24.62 mA cm^{-2}, V_{OC} of 1.101 V, and FF of 0.806). The champion control device had a PCE of 20.95 % (J_{SC} of 24.67 mA cm^{-2}, V_{OC} of 1.079 V, and FF of 0.787). The stabilized power outputs (SPOs) are included in the inset of **Figure 2.3d** and **Table 2.1**. The PATFA treated device achieved a champion SPO of 22.4 %, relative to the

21.4 % and 20.3 % of the PAI treated and control devices, respectively.

We subsequently measured the steady-state photoluminescence (PL) of the perovskite films on glass to study their carrier recombination dynamics. Excitation wavelengths of 640 nm and 532 nm were separately used, with the beam incident on the perovskite side. The excitation wavelength-dependent penetration depths were calculated using the Beer-Lambert law and the perovskite absorption coefficients (**Figure A2.14**). Using the 640 nm excitation source (**Figure A2.15**), with an estimated absorption depth of ~200 nm, the steady-state PL peak intensity was minimally enhanced from 1.04×10^7 for the control film to 1.08×10^7 (3.8 % increase) and 1.14×10^7 (9.6 % increase) for the PAI and PATFA treated films, respectively. In contrast, using the 532 nm excitation source (**Figure 2.3e**), with an estimated absorption depth of ~80 nm and therefore more surface sensitive,[46] the peak intensity increased from 8.40×10^5 for the control film to 1.49×10^6 for the PAI treated film (77.4 % increase) and 1.88×10^6 for the PATFA treated film (123.8 % increase). The excitation wavelength-dependent steady-state PL enhancement confirms that surface treatment of the perovskite films was responsible for their increased radiative recombination. Time-resolved photoluminescence (TRPL) of the films was then measured, with the decay profiles fitted with a mono-exponential decay function (**Figure 2.3f**). The extracted carrier lifetimes of the films increased from 871 ns to 1106 ns to 1447 ns for the control, PAI treated, and PATFA treated films, respectively. The elongated carrier lifetimes of the treated films indicate a suppression of defect-mediated non-radiative recombination, and likely contributed to the observed V_{OC} and FF improvements. High-resolution Pb 4*f* X-ray photoelectron spectroscopy (XPS) spectra of the films (**Figure A2.16**) indicate that the PATFA treated film has a stronger interaction with Pb as seen by the peak shifts to higher binding energy, corroborating its theoretically predicted stronger binding with V_I. It may also indicate that TFA^- passivates Pb-related deep traps such as Pb_I antisite defects and/or Pb clusters, which are known to form deep traps in perovskites.[47–49]

2.4 α-$FAPbI_3$ phase stability of the perovskite films

To examine the α-$FAPbI_3$ phase stability of the PA-treated perovskites, we exposed the films to I_2 vapor as with before, with the δ(010):α(100) peak ratios extracted from the XRD spectra of **Figure A2.17**. As presented in **Figure 2.4a**, both PAI or PATFA treatment enhances the α-$FAPbI_3$ phase stability upon exposure to I_2 vapor, but the PATFA treated film proved to be the most stable. After 80 min exposure, the δ(010):α(100) peak ratios of the control, PAI treated and PATFA treated

films were 5.04, 3.92, and 0.84, respectively.

To further verify the phase stability, we also exposed the films to a high relative humidity (RH) environment (RH 75 ± 10 %), where the α-to-δ phase transformation of $FAPbI_3$ is also expected to be the dominant degradation mechanism for $FAPbI_3$-based perovskites.[18,50] Photographs of the films with exposure time in eight-hour intervals are shown in **Figure 2.4b**, and their corresponding absorption spectra were monitored (**Figure 2.4c** and **Figure A2.18**). We sidenote that the bandgaps and absorption profiles of the films remained unchanged with surface treatment. The control film can be visibly seen to degrade completely to the yellow δ-$FAPbI_3$ phase within 24 h of exposure. After 32 h, the PAI treated film has almost completely degraded to δ-$FAPbI_3$, whereas the black α-$FAPbI_3$ phase of the PATFA treated film is mostly retained. The average absorbances at 600 nm after 32 h were 0.19, 0.45 and 1.22 for the control, PAI treated and PATFA treated films, respectively. This trend was also obvious in the XRD spectra of the films measured after the 32 h exposure, shown in **Figure 2.4d** and **Figure A2.19**. The characteristic α-$FAPbI_3$ peaks of the PATFA treated film is still dominant with a comparatively small trace of the δ(010) peak, whereas the α-$FAPbI_3$ peaks of the control film are barely visible. The improved phase stability with PAI treatment is probably due to the defect passivation effects by PA^+ and I^-, evidenced by the improved PL intensity.[46] We speculate that the more improved phase stability of the PATFA treated films is possibly due to 1) mitigating the unintentional generation of I_i, and 2) the more effective passivation of V_I due to its stronger interaction with TFA^-. We further observed that the average water contact angle, shown in **Figure A2.20**, of the PATFA treated films (73.4 ± 2.8°) is comparable to that of the PAI treated films (71.8 ± 2.0°). This indicates that the hydrophobicity of the treated films was similar despite the fluorine moiety of TFA^-, and as such is likely not the main contributor to the improved phase stability.

Additionally, we investigated the phase stability (and device performance) of the films as a function of PAI concentration (**Table B2.3**, **Figure A2.21**, and **Figure A2.22**). With increasing PAI concentration, the device performance decreases due to noticeable drops in FF and J_{SC}, likely due to a higher series resistance from the thicker (hydrophobic but resistive) capping layer. In contrast, at low PAI concentrations, the phase stability improves due to the thicker hydrophobic capping layer to impede moisture penetration. With even higher PAI concentrations however, we observed aggravated phase instability, which we speculate is due to the generated iodine interstitials outcompeting the thicker capping layer to result in a net worsening of the phase stability. The SPO decayed more

rapidly with increasing PAI concentration, likely due to both the thicker capping layer and generated iodine interstitials, but it is difficult to decouple both contributions.

2.5 Operational stability of the perovskite solar cells

To assess the operational stability of the PSCs, encapsulated devices were subjected to continuous illumination at a temperature of ~40°C and under open-circuit condition (see Experimental Procedures for details). In addition to the phase instability of $FAPbI_3$ based PSCs, the migration of ionic defects under the light-induced potential gradient is expected to be the major degradation mechanism during PSC operation.[9,10,50,51] Notably, shallow defects are theoretically predicted to have low migration activation energies.[9,12,25] Defect migration is most severe under open-circuit condition (versus maximum power point tracking) due to the uncompensated built-in potential induced by illumination.[52,53]

Figure 2.5a plots the evolution of the SPOs of the devices with time. The degradation profiles can be separated into two regimes, where an initial rapid 'burn-in' regime for the first ~80 h is subsequently followed by a slower near linear decay.[10,54,55] The rapid 'burn-in' decay was attributed to the redistribution of charged defects, while the slower decay was ascribed to irreversible chemical reactions due to the migration.[10] The control, PAI treated and PATFA treated devices retained 77.3 %, 84.3 % and 94.2 % of their initial SPOs after the 'burn-in' phase, indicating the most reduced defect density with PATFA treatment. Subsequently, the T_{90}, defined as the linearly extrapolated time taken for the SPO to degrade to 90 % of its post 'burn-in' value,[10,50,54] is obtained by fitting the post burn-in region with an almost linear degradation profile. The average T_{90} of the control devices was enhanced from 383 h to 866 h with PAI treatment (126 % increase). Even more impressively, the average T_{90} of the PATFA treated devices was 2,034 h, a 432 % and 135 % increase over the control and PAI treated devices, respectively. After 971 h, the devices retained 52.7 %, 73.7 % and 89.2 % of their initial SPOs for the control, PAI treated and PATFA treated devices, respectively. The most stable PATFA treated device (**Figure 2.5b**) retained 92.1 % of its initial SPO after the 971 h testing. The most improved operational stability of the PATFA treated devices is likely due to 1) avoiding the generation of I_i, and 2) more effectively passivating V_I – which are both theoretically predicted to have low migration activation energies,[9,12,13] and 3) their superior α-$FAPbI_3$ phase stability.

2.6 Conclusion

In this work, through a systematic series of experimental and theoretical results, we unraveled the possible generation of I_i defects at the perovskite surface from commonly used post-fabrication treatments. Regardless of its shallow nature, it was found that I_i accelerates the degradation of $FAPbI_3$-based perovskites by lowering the cubic-to-hexagonal transformation energy barrier. We further demonstrate that concurrently avoiding the generation of I_i and the more effective passivation of V_I by using TFA^- as an alternative counter anion can simultaneously improve the photovoltaic performance, thermodynamic phase stability, and operational stability under continuous illumination of the PSCs. Consequently, our champion PSC devices showed a more than five-fold increased average T_{90} lifetime over the control devices under operational stability testing. This work sheds light on the detrimental role of shallow defects on the long-term stability of PSCs, highlighting the need to be mindful of them to achieve further stability improvements.

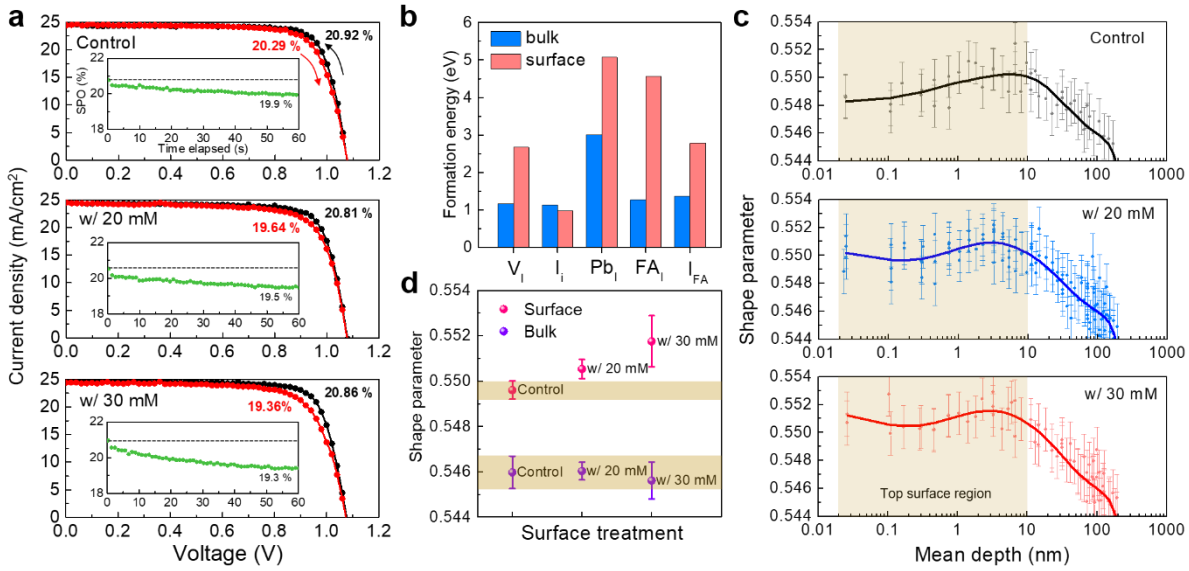

Figure 2.1. Experimental and theoretical indications of iodine interstitial defects. a, Current density and voltage (*J*-*V*) curves of the control and treated devices in reverse (1.2 V to -0.1 V) and forward (-0.1 V to 1.2 V) scans. Insets are the stabilized power output (SPO) measurements of the corresponding devices. Horizontal grey line marks the initial SPO. **b**, Bulk and surface formation energies of neutral iodine related point defects in $FAPbI_3$ perovskite. Bulk values reproduced from reference.[7] **c**, Positron Annihilation Spectroscopy (PAS) depth-profiling of the control and treated

perovskite films on glass. Solid lines are fitted plots. Yellow shaded areas indicate the top surface region of the films. **d**, Extracted surface and bulk shape parameters of the perovskite films. Yellow shaded areas demarcate the upper and lower bounds for the control.

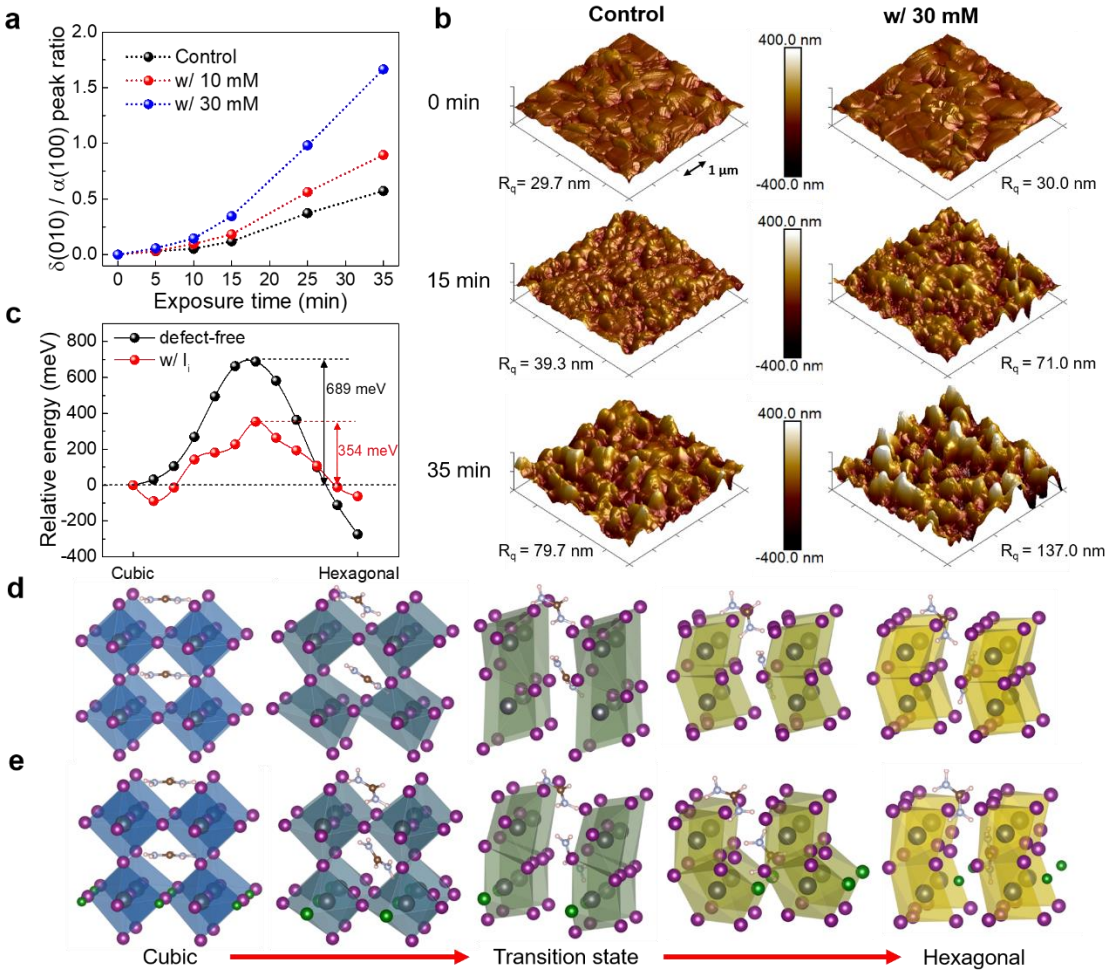

Figure 2.2. Accelerated phase instability of the treated perovskite films. a, Hexagonal δ(010)-to-cubic α(100) X-ray diffraction (XRD) peak intensity ratio of the control and treated perovskite films as a function of exposure time to iodine vapour. **b**, 3D atomic force microscopy topography images of the control and treated perovskite films after different exposure times to iodine vapour, showing the surface root-mean-square roughness (R_q). Scale bar is 1 μm. **c,** Simulated energy pathway for the cubic-to-hexagonal phase transition with or without I_i defect. The activation energy barriers are included on the right. Evolution of the atomic arrangements for the **d**, defect-free, and **e**, with iodine interstitial (green spheres) lattices during the α-$FAPbI_3$-to-δ-$FAPbI_3$ transformation.

Only one unit cell is shown. Atoms are expressed by spheres; iodine (purple), lead (grey), carbon (brown), and nitrogen (blue).

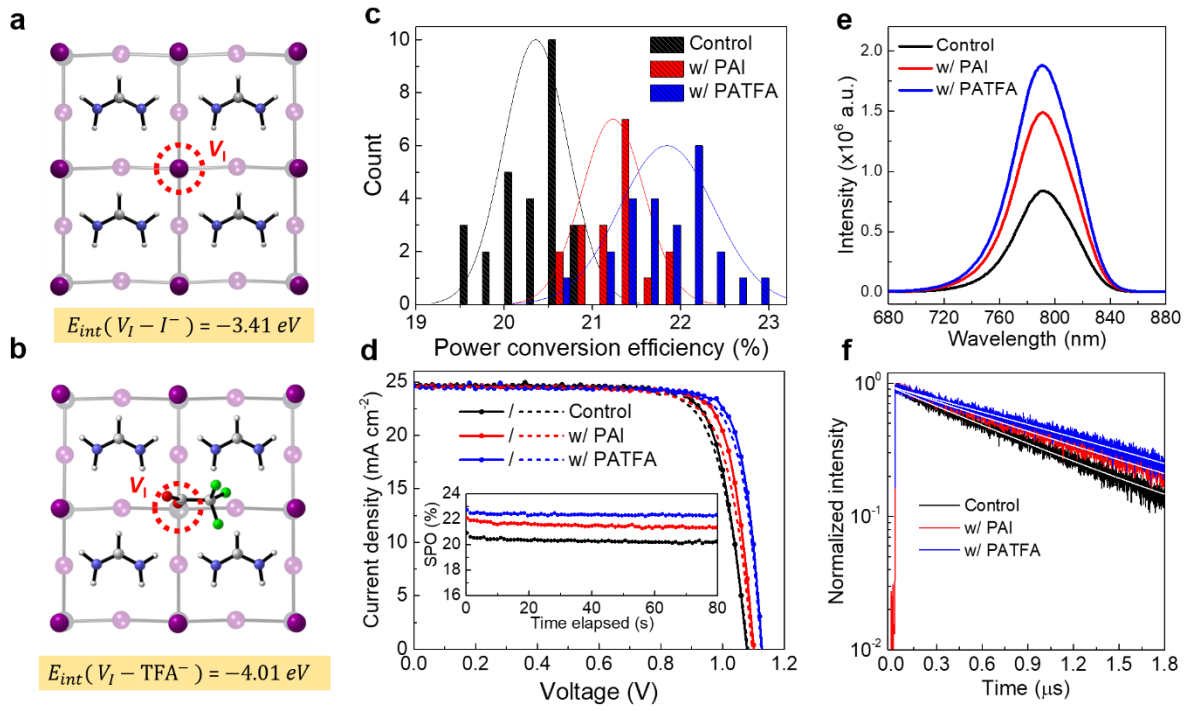

Figure 2.3. Device performance and photoluminescence properties of the control and treated perovskites. Top view of the slab models used for the **a**, V_I - I^- and **b**, V_I - TFA^- interaction energy (E_{int}) calculations. Only the first and second (blurred) layers of the slab are shown. Atoms are expressed by spheres; iodine (purple), carbon (grey), nitrogen (blue), oxygen (red), and fluorine (green). **c**, Power conversion efficiency (PCE) distribution of the control and treated devices. **d**, Current density and voltage (*J*-*V*) curves of the champion devices in reverse (1.2 V to -0.1 V) and forward (-0.1 V to 1.2 V) scan. Inset is the stabilized power output (SPO) of the champion devices. **e**, Steady-state photoluminescence (PL) spectra of the perovskite films on glass probed with an excitation wavelength of 532 nm. **f**, Normalized time-resolved PL spectra of the perovskite films on glass. Solid white lines are the fitted profiles using a mono-exponential decay function.

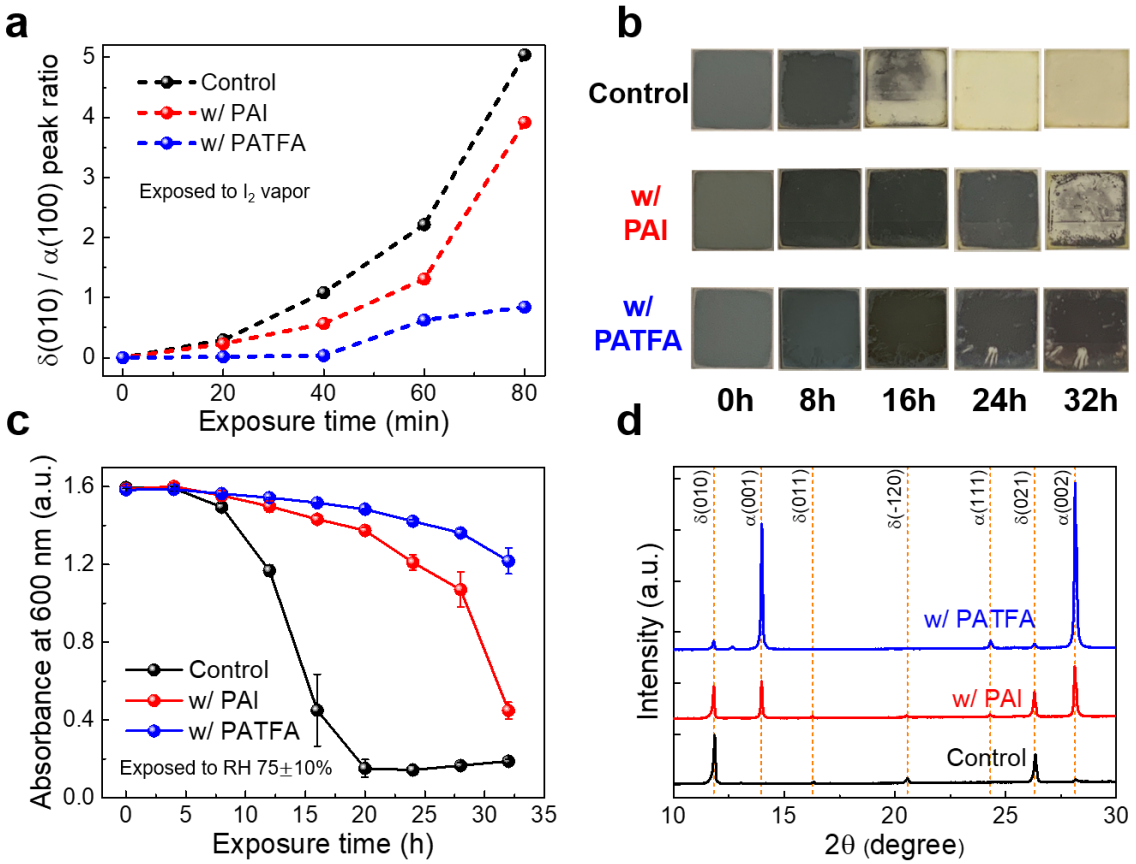

Figure 2.4. α-phase stability of the control and treated perovskite films. a, Hexagonal δ(010)-to-cubic α(100) X-ray diffraction (XRD) peak intensity ratio of the control and treated perovskite films as a function of exposure time to iodine vapour. **b**, Photographs and **c**, absorbance at 600 nm of the perovskite films exposed to RH 75 ± 10 % with time. **d**, XRD diffractograms of the perovskite films after exposure to RH 75 ± 10 % for 32 h.

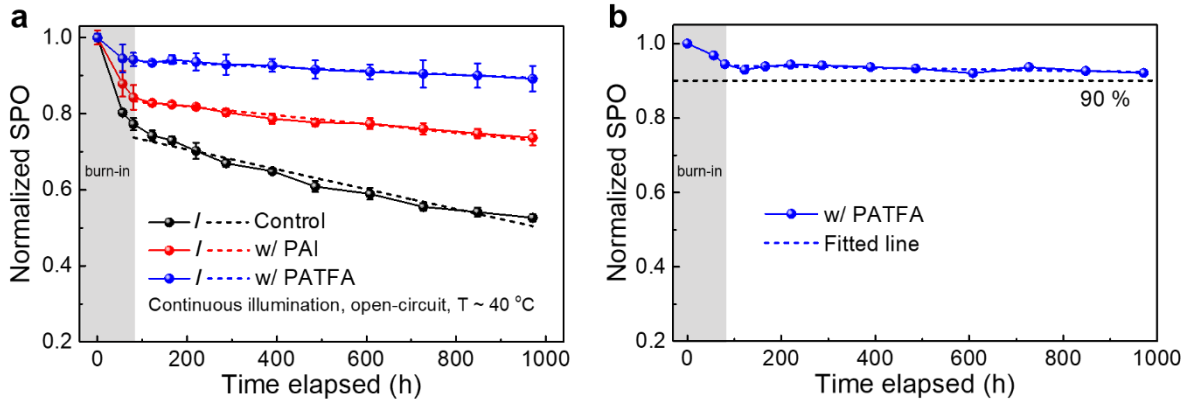

Figure 2.5. Operational stability of the perovskite devices. a, Normalized stabilized power output (SPO) of encapsulated control and treated devices under continuous illumination (90 ± 10 mW cm^{-2}) under open-circuit condition. **b**, Normalized SPO of best-performing device with PATFA treatment. Dashed lines are linear fits to extract the device T_{90} lifetime. Shaded areas mark the 'burn-in decay' regime.

Table 2.1. Distribution of the device photovoltaic parameters. Average photovoltaic parameters of the control and treated devices. Parenthesis indicate parameters measured from champion devices for each condition. Abbreviations are open-circuit voltage (V_{OC}), short-circuit current density (J_{SC}), fill factor (FF), power conversion efficiency (PCE), and stabilized power output (SPO).

	V_{OC} (V)	J_{SC} (mA cm^{-2})	FF	PCE (%)	SPO (%)
Control	1.073 ± 0.012 (1.079)	24.45 ± 0.12 (24.67)	0.774 ± 0.012 (0.787)	20.32 ± 0.35 (20.95)	20.3
w/ PAI	1.103 ± 0.009 (1.101)	24.49 ± 0.13 (24.62)	0.786 ± 0.014 (0.806)	21.23 ± 0.36 (21.86)	21.4
w/ PATFA	1.120 ± 0.013 (1.127)	24.51 ± 0.10 (24.61)	0.796 ± 0.019 (0.829)	21.84 ± 0.35 (22.98)	22.4

References

1. Kim, H.-S. *et al.* Lead Iodide Perovskite Sensitized All-Solid-State Submicron Thin Film Mesoscopic Solar Cell with Efficiency Exceeding 9%. *Sci. Rep.* **2**, 1–7 (2012).
2. Yang, W. S. *et al.* High-Performance Photovoltaic Perovskite Layers Fabricated through Intramolecular Exchange. *Science* **348**, 1234–1237 (2015).
3. Yang, W. S. *et al.* Iodide management in formamidinium-lead-halide–based perovskite

layers for efficient solar cells. *Science* **356**, 1376–1379 (2017).

4. Jiang, Q. *et al.* Surface passivation of perovskite film for efficient solar cells. *Nat. Photonics* **13**, 460–466 (2019).
5. Min, H. *et al.* Efficient, stable solar cells by using inherent bandgap of α-phase formamidinium lead iodide. *Science* **366**, 749–753 (2019).
6. Yin, W.-J., Shi, T. & Yan, Y. Unusual defect physics in CH 3 NH 3 PbI 3 perovskite solar cell absorber. *Appl. Phys. Lett.* **104**, 063903 (2014).
7. Liu, N. & Yam, C. First-principles study of intrinsic defects in formamidinium lead triiodide perovskite solar cell absorbers. *Phys. Chem. Chem. Phys.* **20**, 6800–6804 (2018).
8. Walsh, A., Scanlon, D. O., Chen, S., Gong, X. G. & Wei, S. Self-Regulation Mechanism for Charged Point Defects in Hybrid Halide Perovskites. *Angew. Chemie Int. Ed.* **54**, 1791–1794 (2015).
9. Azpiroz, J. M., Mosconi, E., Bisquert, J. & Angelis, F. De. Defect migration in methylammonium lead iodide and its role in perovskite solar cell operation. *Energy Environ. Sci.* **8**, 2118–2127 (2015).
10. Domanski, K. *et al.* Migration of cations induces reversible performance losses over day/night cycling in perovskite solar cells. *Energy Environ. Sci.* **10**, 604–613 (2017).
11. Lee, J.-W., Kim, S.-G., Yang, J.-M., Yang, Y. & Park, N.-G. Verification and mitigation of ion migration in perovskite solar cells. *APL Mater.* **7**, 1–12 (2019).
12. Aristidou, N. *et al.* Fast oxygen diffusion and iodide defects mediate oxygen-induced degradation of perovskite solar cells. *Nat. Commun.* **8**, 1–10 (2017).
13. Meloni, S. *et al.* Ionic polarization-induced current–voltage hysteresis in CH3NH3PbX3 perovskite solar cells. *Nat. Commun.* **7**, 1–9 (2016).
14. Juarez-Perez, E. J. *et al.* Photodecomposition and thermal decomposition in methylammonium halide lead perovskites and inferred design principles to increase photovoltaic device stability. *J. Mater. Chem. A* **6**, 9604–9612 (2018).
15. Aristidou, N. *et al.* The Role of Oxygen in the Degradation of Methylammonium Lead Trihalide Perovskite PhotoactiveLayers. *Angew. Chemie - Int. Ed.* **54**, 8208–8212 (2015).
16. Conings, B. *et al.* Intrinsic Thermal Instability of Methylammonium Lead Trihalide Perovskite. *Adv. Energy Mater.* **5**, 1–8 (2015).
17. Yuan, Y. *et al.* Electric-Field-Driven Reversible Conversion Between Methylammonium

Lead Triiodide Perovskites and Lead Iodide at Elevated Temperatures. *Adv. Energy Mater.* **6**, 1–7 (2016).

18. Lee, J.-W. *et al.* Formamidinium and Cesium Hybridization for Photo- and Moisture-Stable Perovskite Solar Cell. *Adv. Energy Mater.* **5**, 1501310 (2015).
19. Kapur, S. S., Prasad, M., Crocker, J. C. & Sinno, T. Role of configurational entropy in the thermodynamics of clusters of point defects in crystalline solids. *Phys. Rev. B* **72**, 1–12 (2005).
20. Bulyarskii, S. V. & Oleinikov, V. P. Thermodynamics of Defect Formation and Defect Interaction in Compound Semiconductors. *Phys. Status Solidi* **146**, 439–447 (1988).
21. Abdi-Jalebi, M. *et al.* Maximizing and stabilizing luminescence from halide perovskites with potassium passivation. *Nature* **555**, 497–501 (2018).
22. Li, N. *et al.* Cation and anion immobilization through chemical bonding enhancement with fluorides for stable halide perovskite solar cells. *Nat. Energy* **4**, 408–415 (2019).
23. Wu, W.-Q. *et al.* Reducing Surface Halide Deficiency for Efficient and Stable Iodide-Based Perovskite Solar Cells. *J. Am. Chem. Soc.* **142**, 3989–3996 (2020).
24. Tress, W. *et al.* Understanding the rate-dependent J–V hysteresis, slow time component, and aging in CH3NH3PbI3 perovskite solar cells: the role of a compensated electric field. *Energy Environ. Sci.* **8**, 995–1004 (2015).
25. Eames, C. *et al.* Ionic transport in hybrid lead iodide perovskite solar cells. *Nat. Commun.* **6**, 7497 (2015).
26. Angelis, F. De & Petrozza, A. Clues from defect photochemistry. *Nat. Mater.* **17**, 377–384 (2018).
27. Barthe, M.-F. *et al.* Positron annihilation characteristics in UO2: for lattice and vacancy defects induced by electron irradiation. *Phys. Status Solidi C* **10**, 3627–3632 (2007).
28. Wiktor, J., Jomard, G., Torrent, M. & Bertolus, M. First-principles calculations of momentum distributions of annihilating electron–positron pairs in defects in UO2. *J. Phys. Condens. Matter* **29**, 1–9 (2017).
29. Xue, J., Wang, R. & Yang, Y. The surface of halide perovskites from nano to bulk. *Nat. Rev. Mater.* (2020) doi:10.1038/s41578-020-0221-1.
30. Meggiolaro, D. *et al.* Iodine chemistry determines the defect tolerance of lead-halide perovskites. *Energy Environ. Sci.* **11**, 702–713 (2018).

31. Awtrey, A. D. & Connick, R. E. The Absorption Spectra of I2, I3-, I-, I03-, S406- and S203-. Heat of the Reaction I3- = I2 + I-. *J. Am. Chem. Soc.* **73**, 1842–1843 (1951).
32. Wang, S., Jiang, Y., Juarez-perez, E. J., Ono, L. K. & Qi, Y. Accelerated degradation of methylammonium lead iodide perovskites induced by exposure to iodine vapour ShenghaoWang†,. *Nat. Energy* **16195**, 1–8 (2016).
33. Fu, F. *et al.* I2 vapor-induced degradation of formamidinium lead iodide based perovskite solar cells under heat–light soaking conditions. *Energy Environ. Sci.* **12**, 3074–3088 (2019).
34. Frolova, L. A., Dremova, N. N. & Troshin, P. A. The chemical origin of the p-type and n-type doping effects in the hybrid methylammonium-lead iodide (MAPbI3) perovskite solar cells. *Chem. Commun.* **51**, 14917–14920 (2015).
35. Han, T.-H. *et al.* Perovskite-polymer composite cross-linker approach for highly-stable and efficient perovskite solar cells. *Nat. Commun.* **10**, 520 (2019).
36. Zhao, Y. *et al.* A Polymerization-Assisted Grain Growth Strategy for Efficient and Stable Perovskite Solar Cells. *Adv. Mater.* **32**, 1907769 (2020).
37. Chen, T. *et al.* Entropy-driven structural transition and kinetic trapping in formamidinium lead iodide perovskite. *Sci. Adv.* **2**, 1–6 (2016).
38. Calado, P. *et al.* Evidence for ion migration in hybrid perovskite solar cells with minimal hysteresis. *Nat. Commun.* **7**, 1–10 (2016).
39. Weber, S. A. L. *et al.* How the formation of interfacial charge causes hysteresis in perovskite solar cells. *Energy Environ. Sci.* **11**, 2404–2413 (2018).
40. Carrillo, J. *et al.* Ionic Reactivity at Contacts and Aging of Methylammonium Lead Triiodide Perovskite Solar Cells. *Adv. Energy Mater.* **6**, 1502246 (2016).
41. Besleaga, C. *et al.* Iodine Migration and Degradation of Perovskite Solar Cells Enhanced by Metallic Electrodes. *J. Phys. Chem. Lett.* **7**, 5168–5175 (2016).
42. Milne, J. B. & Parker, T. J. Dissociation Constant of Aqueous Trifluoroacetic Acid by Cryoscopy and Conductivity. *J. Solution Chem.* **10**, 479–487 (1981).
43. Yoo, J. J. *et al.* An interface stabilized perovskite solar cell with high stabilized efficiency and low voltage loss. *Energy Environ. Sci.* **12**, 2192–2199 (2019).
44. Zheng, X. *et al.* Defect passivation in hybrid perovskite solar cells using quaternary ammonium halide anions and cations. *Nat. Energy* **2**, 17102 (2017).
45. Wang, H.-C. *et al.* Engineering the core units of small-molecule acceptors to enhance the

performance of organic photovoltaics. *Sol. RRL* (2020) doi:10.1002/solr.202000253.

46. Yang, S. *et al.* Tailoring Passivation Molecular Structures for Extremely Small Open-Circuit Voltage Loss in Perovskite Solar Cells. *J. Am. Chem. Soc.* **141**, 5781–5787 (2019).
47. Na Quan, L. *et al.* Edge stabilization in reduced-dimensional perovskites. *Nat. Commun.* **11**, 170 (2020).
48. Han, T.-H. *et al.* Interface and Defect Engineering for Metal Halide Perovskite Optoelectronic Devices. *Adv. Mater.* **31**, 1803515 (2019).
49. Wang, R. *et al.* Constructive molecular configurations for surface-defect passivation of perovskite photovoltaics. *Science* **366**, 1509–1513 (2019).
50. Lee, J.-W. *et al.* 2D perovskite stabilized phase-pure formamidinium perovskite solar cells. *Nat. Commun.* **9**, 1–10 (2018).
51. Bai, S. *et al.* Planar perovskite solar cells with long-term stability using ionic liquid additives. *Nature* **571**, 245–250 (2019).
52. Domanski, K., Alharbi, E. A., Hagfeldt, A., Grätzel, M. & Tress, W. Systematic investigation of the impact of operation conditions on the degradation behaviour of perovskite solar cells. *Nat. Energy* **3**, 61–67 (2018).
53. Nie, W. *et al.* Light-activated photocurrent degradation and self-healing in perovskite solar cells. *Nat. Commun.* **7**, 1–9 (2016).
54. Wang, Z. *et al.* Efficient ambient-air-stable solar cells with 2D–3D heterostructured butylammonium-caesium-formamidinium lead halide perovskites. *Nat. Energy* **2**, 17135 (2017).
55. Tan, S. *et al.* Steric Impediment of Ion Migration Contributes to Improved Operational Stability of Perovskite Solar Cells. *Adv. Mater.* **32**, 1906995 (2020).

Chapter 3 Surface Reconstruction of Halide Perovskites during Post-treatment

The record performance of single-junction halide perovskite solar cells (PSCs) have now exceeded 25 %.[1] Important breakthroughs on defect passivation strategies have contributed to the rapid performance improvements in recent years.[2,3] However, achievable voltage losses are still short of the theoretical limit. More importantly, it has become apparent that the migration and redistribution of charged point defects by a potential gradient is known to underly the operational instability of PSCs,[4–6] and this remains one of the major challenges of perovskite photovoltaics.

It has been reported that defect states causing non-radiative losses are dominantly located towards the top surface of halide perovskites.[7,8] This has motivated the development of surface passivation strategies by post-treatment of the perovskite film surface.[9] However, understanding of the complex reconstruction processes that can occur during the surface treatment procedures and any resulting changes to the interfacial charge dynamics are still lacking. This is urgently needed for targeted surface treatment strategies to minimize trial-and-error approaches. For this purpose, *in situ* spectroscopy is suited to monitor occurring changes on relevant time and length scales.[10–13]

In this study, we investigate the mechanistic reconstruction processes occurring at the perovskite surface during post-fabrication treatments. Through complementary surface-sensitive techniques, we observed the generation of defects and a reconstruction towards a more PbI_2-rich surface as isopropyl alcohol (IPA) is spun onto the surface. We show that this reconstruction has important implications on the thermodynamics and energetics of the perovskite surface. Importantly, our observations suggest that IPA assists in the anchoring process of organic ammonium salts to the perovskite surface.

IPA is ubiquitously used as the solvent to dissolve organic ammoniums for surface treatments, but formamidinium iodide (FAI), itself with the amidinium functional group, is also soluble in IPA. It is unclear what effects (if any) IPA has on the perovskite surface, given the short exposure timescales (~ms) at high rotation speeds (>4000 rpm). Conflicting results on the macroscopic bulk device/film properties have been reported. Beneficial improvements to film crystallinity, charge carrier dynamics, morphology, and device performance have been observed,[14,15] while detrimental effects to device stability were also reported.[16] To rationalize these contradictory results, we first attempted to explore the microscale phenomena occurring at the surface. Significantly, IPA remains perhaps a crucial solvent for post-treatment, since the most common surface passivating agents, such

as phenylethylammonium iodide (PEAI) and octylammonium iodide (OAI), are essentially insoluble in low polarity solvents such as chloroform (CF) (**Figure A3.1**).

The control perovskite is based on a $FAPbI_3$ composition with 5 mol% of added $MAPbBr_3$ fabricated by a one-step antisolvent quenching method. We monitored the photoluminescence (PL) of an as-fabricated perovskite film *in situ* with a 405 nm excitation wavelength (**Figure 3.1a**) in a nitrogen glovebox (<0.5 ppm O_2/H_2O). The laser penetration depth was estimated to be ~50 nm (**Figure A3.2**), and therefore sensitive to any potential changes in the surface charge carrier recombination behavior. The PL intensity abruptly decreased (23 % decrease) with a broadening and redshifting of the PL peak upon dropping IPA (**Figure 3.b, Figure 3.1c, Figure A3.3a**). In general, this is indicative of increased nonradiative carrier recombination, which implies the generation of charge-trapping defect states. Time-resolved PL (**Figure A3.3b**) of the perovskite films further support this, where the carrier lifetime fitted with a mono-exponential decay function decreased from 1,021 to 793 ns for the control and IPA treated films, respectively. The PL intensity (and FWHM) is observed to gradually recover with time, possibly due to trap-filling by photo-generated carriers,[17] as also seen in the control film without treatment (**Figure A3.3c, Figure A3.3d**).

We further investigated the distribution and nature of the generated defects using Positron Annihilation Spectroscopy (PAS). Positrons are implanted from the film surface and annihilate with electrons after trapping at negatively charged (or neutral) defects to emit two gamma photons. The incident kinetic energy is controlled to vary the positron implantation depth (**Figure 3.1d, Figure A3.4**), from which the depth-resolved defect density of the film can be investigated. The treated film had a higher Shape parameter within ~40 nm from the film surface, implying the generation of negatively charged (or neutral) defects at the top surface region. We speculate that the formed defect is possibly FA vacancy (V'_{FA}), given the solubility of FAI in IPA.

The implied existence of V'_{FA} suggests that iodine vacancy ($V_I^{\bullet}$) was likely generated concurrently, but PAS is unable to ascertain this due to its insensitivity to positively charged defects (i.e. $V_I^{\bullet}$).[18,19] We therefore further probed the films with high-resolution X-ray Photoelectron Spectroscopy (XPS). The I:Pb ratio, calculated from the integrated areas of the Pb 4f doublet and I $3d_{5/2}$ peak (**Figure 3.2a**), was 2.45 for the control film, and decreased to 2.04 for the treated film to approach that of stoichiometric PbI_2. We note that the ultra-high vacuum environment of the XPS instrument (~10^{-7}-10^{-8} torr) may have accelerated the outgassing of the volatile halide,[20,21] and therefore only relative comparisons would be reliable. Closer inspection of

the XPS spectra further showed that all of the Pb $4f_{5/2}$ (143.19 eV to 143.13 eV), Pb $4f_{7/2}$ (138.32 eV to 138.25 eV), and I $3d_{5/2}$ (619.15 eV to 619.08 eV) characteristic peaks shifted to lower binding energies for the treated film when compared to the control, suggesting a change in the surface chemical environment. Together with the observed change in the I:Pb ratios, the shift direction and final peak positions is consistent with the formation of PbI_2 for the treated film.[22] The existence of PbI_2 was directly detected by Grazing Incidence X-ray Diffraction (XRD) at an incident angle of $\omega = 0.2°$ (penetration depth ~60 nm, see Methods for estimation) (**Figure 3.2c**, **Figure 3.2d**). Moreover, the PbI_2:$FAPbI_3$ peak intensity ratio was observed to decrease at an incident angle of $\omega = 1.0°$ (penetration depth ~310 nm), suggesting that the PbI_2 is located more towards the top perovskite region. Combining the experimental observations together, we thus propose the following reconstruction of the perovskite film surface during post-treatment, by a dissolution reaction process induced by IPA:

$$FAPbI_3\ (s) \xrightarrow{\text{IPA}} FAI\ (in\ IPA) + PbI_2\ (s) + V_{FA}' + V_I^{\bullet}$$

We now discuss some possible implications of this inferred surface reconstruction. Ultraviolet Photoelectron Spectroscopy (UPS) was used to investigate any band structure changes at the surface. The fermi level was observed to downshift from -4.68 eV for the control film to -4.77 eV for the film treated with IPA (**Figure 3.2b**), indicating a more p-doped surface for the latter relative to the bare perovskite surface. The overall band structure of the treated surface further downshifted relative to the vacuum level due to the deeper valence band maximum (inset of **Figure 3.2b**), consistent with a relatively more FAI deficient surface.[23] This possibly creates a more beneficial band bending going from the perovskite bulk to the surface contacting a hole-transporting material (**Figure A3.5a**). The surface PbI_2 for the treated film may additionally contribute to interfacial passivation.[24] In reality, however, we observed that the treated device performance was inferior to the control with a more pronounced current-voltage hysteresis (**Figure A3.5b, Figure A3.5c**), likely due to the generated vacancy defects, given that defect migration (due to the bias potential) is known to underly the hysteric behavior.[4,9]

First-principles density functional theory (DFT) calculations were performed on slabs based on the deduced reconstruction to compare their thermodynamics and energetics. We note that realistically, the perovskite surface is expected to be a complex amalgamation of exposed atoms, local atomic pairing/reorientation, and defected.[25] However, simplified slab models are necessarily

required to reduce computational complexity. Nevertheless, *relative* comparisons can be made based on the predicted results. Experimental investigations have observed that the pristine perovskite surface (without treatment) is terminated mostly by organic halides,[26,27] which is also supported by computational results.[28] Our results imply that IPA reconstructs the surface towards a *relatively more* PbI_2-rich surface. We chose the two extreme cases of complete FAI termination (**Figure 3.3a**) and PbI_2 termination (**Figure 3.3b**) to model the pristine (control) and reconstructed (treated) surfaces, respectively, again noting that the models are used to predict *relative trends*.

The predicted bandgap decreased while the ionization energy increased for the PbI_2 termination surface (**Figure 3.3c**), matching the *in situ* PL and UPS observations discussed. The surface energy more than doubled (1.54 to 3.24 eV nm^{-2}) for the PbI_2 termination surface, indicating that the surface became more thermodynamically unstable with treatment. This likely contributed to the observed aggravated instability of the treated films (**Figure A3.6**). The generated defects might additionally lower the $FAPbI_3$ cubic-to-hexagonal phase transformation activation energy barrier to also accelerate the degradation.[29] Given the increased surface energy, we postulated that organic ammonium salts may preferentially adsorb onto the treated surface. We further calculated the formation enthalpy to attach the widely used passivation agents OAI or PEAI to the surfaces (**Figure 3.3d**). The adsorption enthalpies for both were significantly more negative on the PbI_2 termination surface – for OAI, -0.78 versus -1.88 eV (141% increase), and -0.9 versus -3.75 eV for PEAI (317% increase), suggesting that the surface reconstruction plays a vital role in the passivation process.

The more negative adsorption enthalpies imply that ammonium salts are thermodynamically more favored to adsorb onto the treated surface. We investigated this with a modified 2-step surface post-treatment process (**Figure A3.7**). Initially treating a perovskite film with pure IPA before subsequently depositing octylammonium bromide (OABr) in CF (at the same concentration) further improved the device photovoltaic performance (**Figure 3.3e**). The champion device surface treated with the modified 2-step approach reached a power conversion efficiency of 22.9 % in reverse bias (**Figure 3.3e**) with negligible current-voltage hysteresis, relative to the 22.4 % of the conventionally treated device. The improved performance was attributed to increases in the device open-circuit voltage (1.129 V to 1.146 V) and fill factor (79.1 % to 79.6 %), which is indicative of an enhanced defect passivation effect with the modified 2-step treatment. Therefore, the observations support the theoretical predictions that IPA assists in the adsorption process of ammonium salts to the surface and thus the passivation of defects. The surface is first reconstructed

by removing FAI to expose the undercoordinated Pb^{2+} (i.e. $V_I^{\bullet}$) for the ammonium groups to bond with by electrostatic coulomb interactions and/or hydrogen bonding.

We speculated that the PL evolution as OAI or PEAI (in IPA) is deposited on the surface may be related to their adsorption enthalpies. Further measurements show that although both treatments led to instantaneous PL enhancements immediately upon deposition (**Figure 3.3f, Figure 3.3g, Figure A3.8**), the PL intensity subsequently decayed ~10 s after deposition only for the OAI treated film. With the PbI_2 termination surface, the computed adsorption enthalpies imply a significantly weaker interaction of OAI (relative to PEAI) with the perovskite surface, which may possibly be correlated with the differing PL dynamics. On the other hand, the adsorption enthalpies are negligibly different when calculated using the FAI termination surface, which may be challenging to reconcile with the experimental observation. We also monitored the recombination dynamics with further *in situ* PL measurements during annealing (**Figure A3.9a, Figure A3.9b**). A rapid initial exponential decay in PL intensity was observed for both films due to increased phonon scattering at elevated temperatures.[10,12] However, only the OAI treated film counteracted the initial drop to eventually increase its PL intensity due to the activated defect passivation effect. The evolution and emission characteristics of the wide bandgap phases notably differ between the OAI and PEAI treated films, and will be the subject of future investigations (**Figure A3.9c, Figure A3.9d, Figure A3.9e**).

In summary, we observed a reconstruction of the perovskite top surface induced by IPA, which is ubiquitously used as the solvent for surface treatment with organic ammonium salts. We discussed several implications of this reconstruction on the perovskite surface energetics and thermodynamics. Importantly, given the profound differences between the reconstructed surface and the perovskite bulk/pristine surface, these results will guide further experimental and theoretical investigations of the perovskite surface and surface passivation strategies.

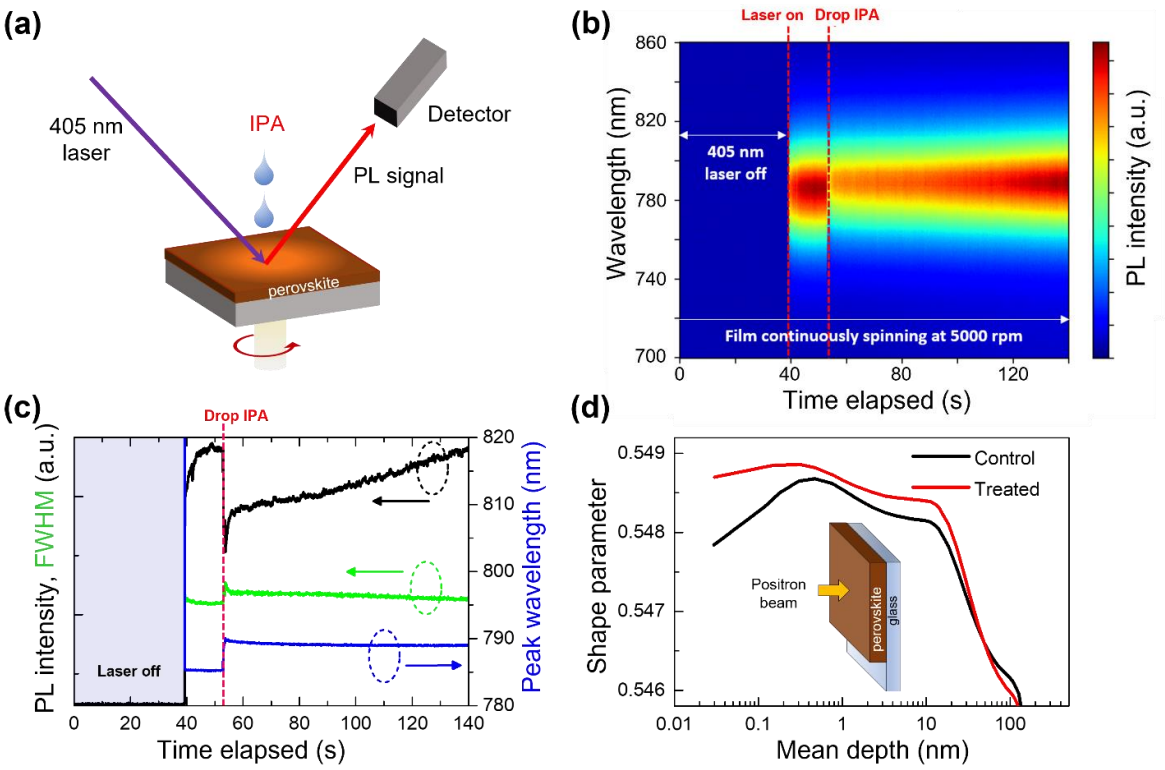

Figure 3.1. Defect generation by IPA treatment. (a) Schematic of the *in situ* PL measurement during IPA post-treatment. (b) *In situ* PL contour plot of a perovskite film undergoing surface treatment with IPA dropped at around 53 s. (c) Evolution of the PL parameters extracted from fitting (b). (d) PAS depth-profiling of the perovskite films.

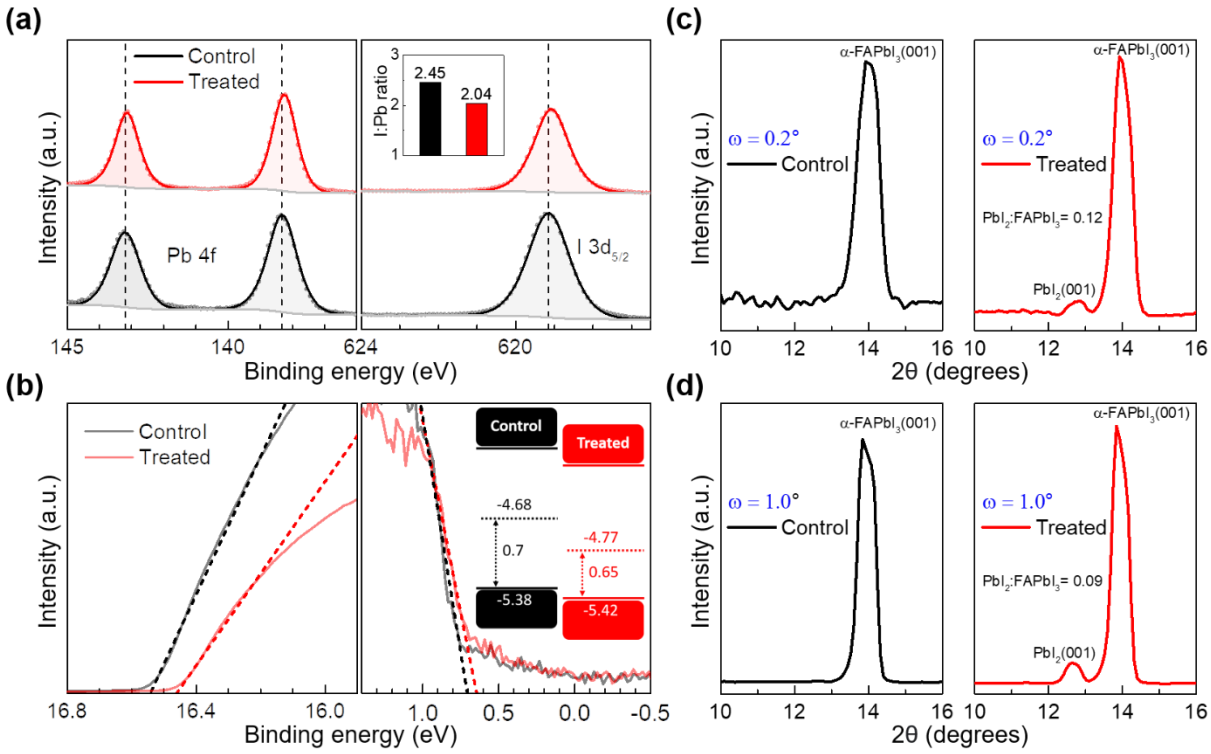

Figure 3.2. Characterizations of the perovskite films. (a) High-resolution XPS spectra of the Pb 4f and I $3d_{5/2}$ peaks of the perovskite films. Inset includes the calculated I:Pb ratios of the films. Solid lines are fitted plots. Dashed vertical lines demarcate the peak positions for the control film. Intensities are normalized to Pb 4f peak. (b) UPS spectra of the perovskite films. Inset includes a schematic band diagram of the energy levels based on the UPS measurements. GIXRD diffraction patterns of the perovskite films measured with an incident angle of (c) ω = 0.2° and (d) ω = 1.0°.

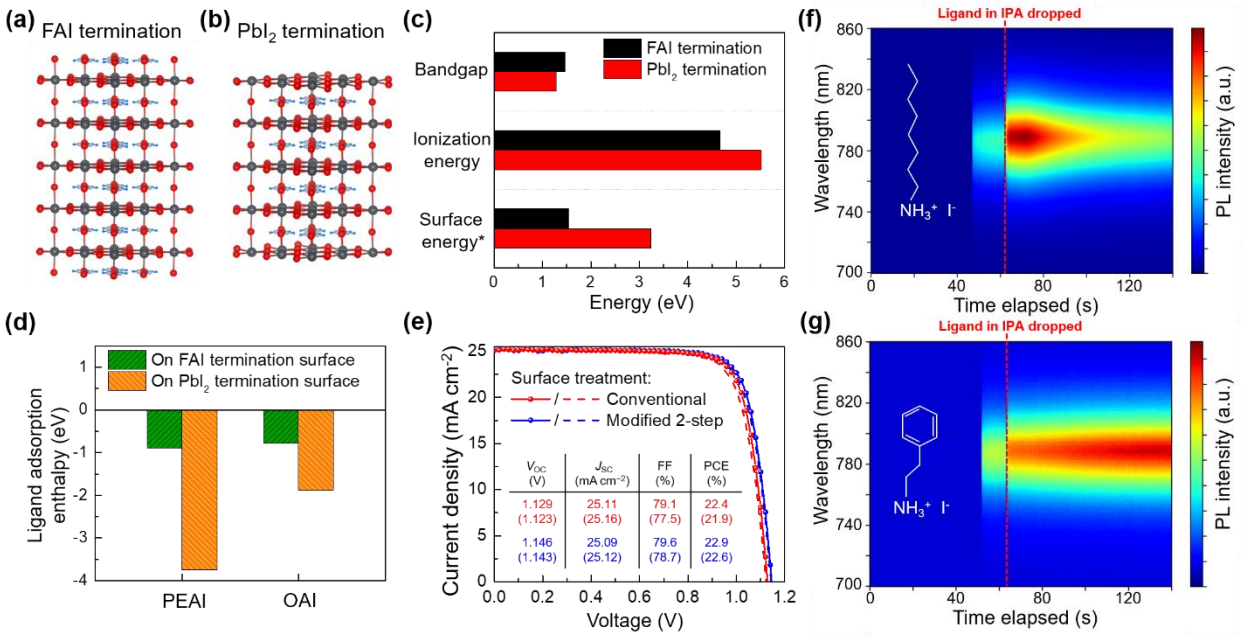

Figure 3.3. Surface reconstruction and its implications. (a), (b) Theoretical slab models for first-principles DFT calculations. Atoms are colored black (lead), red (iodine), gray (nitrogen), and blue (hydrogen). (c) Calculated surface physiochemical properties. The asterisk indicates that surface energy is in units of eV nm^{-2}. (d) Enthalpy of adsorption of either PEAI or OAI on the surfaces. (e) Current density-voltage curves of devices treated with 10 mM OABr in CF. Inset includes the measured photovoltaic parameters. Brackets indicate parameters measured in forward bias. *In situ* PL contour plots of perovskite films undergoing surface treatment with (f) 10 mM OAI or (g) 10 mM PEAI in IPA.

References

1. Best Research-Cell Efficiency Chart (2020). NREL.
2. Jiang, Q., Zhao, Y., Zhang, X., Yang, X., Chen, Y., Chu, Z., Ye, Q., Li, X., Yin, Z., and You, J. (2019). Surface passivation of perovskite film for efficient solar cells. Nat. Photonics *13*, 460–466.
3. Kim, G., Min, H., Lee, K.S., Lee, D.Y., Yoon, S.M., and Seok, S. Il (2020). Impact of strain

relaxation on performance of α-formamidinium lead iodide perovskite solar cells. Science *370*, 108–112.

4. Tan, S., Yavuz, I., De Marco, N., Huang, T., Lee, S., Choi, C.S., Wang, M., Nuryyeva, S., Wang, R., Zhao, Y., et al. (2020). Steric Impediment of Ion Migration Contributes to Improved Operational Stability of Perovskite Solar Cells. Adv. Mater. *32*, 1906995.
5. Ball, J.M., and Petrozza, A. (2016). Defects in perovskite-halides and their effects in solar cells. Nat. Energy *1*, 1–13.
6. Lee, J.-W., Kim, S.-G., Yang, J.-M., Yang, Y., and Park, N.-G. (2019). Verification and mitigation of ion migration in perovskite solar cells. APL Mater. *7*, 1–12.
7. Ni, Z., Bao, C., Liu, Y., Jiang, Q., Wu, W.-Q., Chen, S., Dai, X., Chen, B., Hartweg, B., Yu, Z., et al. (2020). Resolving spatial and energetic distributions of trap states in metal halide perovskite solar cells. Science *367*, 1352–1358.
8. Yang, Y., Yang, M., Moore, D.T., Yan, Y., Miller, E.M., Zhu, K., and Beard, M.C. (2017). Top and bottom surfaces limit carrier lifetime in lead iodide perovskite film. Nat. Energy *2*, 1–7.
9. Han, T.-H., Tan, S., Xue, J., Meng, L., Lee, J.-W., and Yang, Y. (2019). Interface and Defect Engineering for Metal Halide Perovskite Optoelectronic Devices. Adv. Mater. *31*, 1803515.
10. Babbe, F., and Sutter-Fella, C.M. (2020). Optical Absorption-Based In Situ Characterization of Halide Perovskites. Adv. Energy Mater. *10*, 1903587.
11. Song, T.-B., Yuan, Z., Babbe, F., Nenon, D.P., Aydin, E., De Wolf, S., and Sutter-Fella, C.M. (2020). Dynamics of Antisolvent Processed Hybrid Metal Halide Perovskites Studied by In Situ Photoluminescence and Its Influence on Optoelectronic Properties. ACS Appl. Energy Mater. *3*, 2386–2393.
12. Song, T., Yuan, Z., Mori, M., Motiwala, F., Segev, G., Masquelier, E., Stan, C. V., Slack, J.L., Tamura, N., and Sutter-Fella, C.M. (2020). Revealing the Dynamics of Hybrid Metal Halide Perovskite Formation via Multimodal In Situ Probes. Adv. Funct. Mater. *30*, 1908337.
13. Lee, J.-W., Tan, S., Han, T.-H., Wang, R., Zhang, L., Park, C., Yoon, M., Choi, C., Xu, M., Liao, M.E., et al. (2020). Solid-phase hetero epitaxial growth of α-phase formamidinium perovskite. Nat. Commun. *11*, 5514.
14. Prochowicz, D., Tavakoli, M.M., Solanki, A., Goh, T.W., Pandey, K., Sum, T.C., Saliba, M.,

and Yadav, P. (2018). Understanding the effect of chlorobenzene and isopropanol anti-solvent treatments on the recombination and interfacial charge accumulation in efficient planar perovskite solar cells. J. Mater. Chem. A *6*, 14307–14314.

15. Wang, X., Li, X., Tang, G., Zhao, L., Zhang, W., Jiu, T., and Fang, J. (2015). Improving efficiency of planar hybrid CH3NH3PbI3-xClx perovskite solar cells by isopropanol solvent treatment. Org. Electron. *24*, 205–211.
16. Yoo, J.J., Wieghold, S., Sponseller, M.C., Chua, M.R., Bertram, S.N., Putri, T., Tresback, J.S., Hansen, E.C., Correa-Baena, J.-P., Bulović, V., et al. (2019). An interface stabilized perovskite solar cell with high stabilized efficiency and low voltage loss. Energy Environ. Sci. *12*, 2192–2199.
17. DeQuilettes, D.W., Zhang, W., Burlakov, V.M., Graham, D.J., Leijtens, T., Osherov, A., Bulović, V., Snaith, H.J., Ginger, D.S., and Stranks, S.D. (2016). Photo-induced halide redistribution in organic–inorganic perovskite film. Nat. Commun. *7*, 1–9.
18. Barthe, M.-F., Labrim, H., Gentils, A., Desgardin, P., Corbel, C., Esnouf, S., and Piron, J.P. (2007). Positron annihilation characteristics in UO2: for lattice and vacancy defects induced by electron irradiation. Phys. Status Solidi C *10*, 3627–3632.
19. Wiktor, J., Jomard, G., Torrent, M., and Bertolus, M. (2017). First-principles calculations of momentum distributions of annihilating electron–positron pairs in defects in UO2. J. Phys. Condens. Matter *29*, 1–9.
20. Jiang, Y., Yang, S.-C., Jeangros, Q., Pisoni, S., Moser, T., Buecheler, S., Tiwari, A.N., and Fu, F. (2020). Mitigation of Vacuum and Illumination-Induced Degradation in Perovskite Solar Cells by Structure Engineering. Joule *4*, 1087–1103.
21. Das, C., Wussler, M., Hellmann, T., Mayer, T., and Jaegermann, W. (2018). In situ XPS study of the surface chemistry of MAPI solar cells under operating conditions in vacuum. Phys. Chem. Chem. Phys. *20*, 17180–17187.
22. Juarez-Perez, E.J., Ono, L.K., Maeda, M., Jiang, Y., Hawash, Z., and Qi, Y. (2018). Photodecomposition and thermal decomposition in methylammonium halide lead perovskites and inferred design principles to increase photovoltaic device stability. J. Mater. Chem. A *6*, 9604–9612.
23. Meggiolaro, D., Mosconi, E., Proppe, A.H., Quintero-Bermudez, R., Kelley, S.O., Sargent, E.H., and De Angelis, F. (2019). Energy Level Tuning at the MAPbI3 Perovskite/Contact

Interface Using Chemical Treatment. ACS Energy Lett. *4*, 2181–2184.

24. Chen, Q., Zhou, H., Song, T. Bin, Luo, S., Hong, Z., Duan, H.S., Dou, L., Liu, Y., and Yang, Y. (2014). Controllable self-induced passivation of hybrid lead iodide perovskites toward high performance solar cells. Nano Lett. *14*, 4158–4163.
25. Leblebici, S.Y., Leppert, L., Li, Y., Reyes-Lillo, S.E., Wickenburg, S., Wong, E., Lee, J., Melli, M., Ziegler, D., Angell, D.K., et al. (2016). Facet-dependent photovoltaic efficiency variations in single grains of hybrid halide perovskite. Nat. Energy *1*, 1–7.
26. She, L., Liu, M., and Zhong, D. (2016). Atomic structures of CH3NH3PbI3 (001) surfaces. ACS Nano *10*, 1126–1131.
27. Stecker, C., Liu, K., Hieulle, J., Ohmann, R., Liu, Z., Ono, L.K., Wang, G., and Qi, Y. (2019). Surface Defect Dynamics in Organic− Inorganic Hybrid Perovskites: From Mechanism to Interfacial Properties. ACS Nano *13*, 12127–12136.
28. Geng, W., Tong, C.-J., Tang, Z.-K., Yam, C., Zhang, Y.-N., Lau, W.-M., and Liu, L.-M. (2015). Effect of surface composition on electronic properties of methylammonium lead iodide perovskite. J. Mater. *1*, 213–220.
29. Tan, S., Yavuz, I., Weber, M.H., Huang, T., Chen, C.-H., Wang, R., Wang, H.-C., Ko, J.H., Nuryyeva, S., Xue, J., et al. (2020). Shallow Iodine Defects Accelerate the Degradation of α-Phase Formamidinium Perovskite. Joule *4*, 2426–2442.

Chapter 4 Stability-limiting heterointerfaces of perovskite photovoltaics

Optoelectronic devices consist of heterointerfaces formed between dissimilar semiconducting materials. The relative energy level alignment between contacting semiconductors determinately affects the heterointerface charge injection and extraction dynamics. For perovskite solar cells (PSCs), the heterointerface between the top perovskite surface and a charge-transporting material (CTM) is often treated for defect passivation[1–4] to improve PSC stability and performance. However, such surface treatments could also affect the heterointerface energetics.[1] Here we show that surface treatments may induce a negative work function shift (i.e. more n-type), which activates halide migration to aggravate PSC instability. Therefore, despite the beneficial effects of surface passivation, this detrimental side effect limits the maximum stability improvement attainable for PSCs treated in these ways. This trade-off between the beneficial and detrimental effects should guide further work on improving PSC stability via surface treatments.

Progress in compositional and crystal growth engineering have made possible the fabrication of halide perovskite thin films with minimized bulk trap density, such that defects are predominantly located at the surface.[5,6] This has motivated the development of defect passivation treatments applied onto the top perovskite surface.[1–4] However, such treatments could also change the heterointerface energetics and thus charge carrier dynamics between the perovskite and top CTM.[1] In this work, we study the consequences of the altered heterointerface energetics on carrier extraction, trap passivation, charge accumulation, and ion migration. We show that a negative work function change (ΔW) accumulates charges in a potential well, which lowers the halide migration activation energy to limit PSC stability. A negative ΔW is equivalently described as a negative vacuum level change (ΔE_{vac}) at a heterointerface, and hereafter, ΔW and ΔE_{vac} are used interchangeably.

4.1 Perovskite surface and heterointerface dynamics

The genesis of this study began with our investigations on the surface energetics of perovskite films, based on a $(FAPbI_3)_{0.95}(MAPbBr_3)_{0.05}$ composition. Ultraviolet photoelectron spectroscopy (UPS) measurements show that ubiquitously used iodide-based ammonium surface treatments generally result in a negative ΔW (**Figure 4.1a**, **Figure A4.1**, **Table B4.1**), successively increasing in magnitude with longer alkylammonium chain length. Given that a negative ΔW is

associated with a relatively more electron-enriched surface, we speculated initially that the negative ΔW can be modulated by increasing the electron-withdrawing ability of the counter-anion. Further UPS measurements (**Figure 4.1b**) showed that substitution of iodide $[I]^-$ with bromide $[Br]^-$, tetrafluoroborate $[BF_4]^-$, or trifluoroacetate $[TFA]^-$ progressively negated the negative ΔW of OAI treatment towards that of the Reference film, but only substitution with tosylate $[TsO]^-$ fully neutralized the negative ΔW. Particularly, among the counter-anions, $[TsO]^-$ has the strongest electron-withdrawing character,[7] which also justifies its ubiquitous use as the leaving group in synthetic heterolytic fission chemistry. The interaction of $[TsO]^-$ with the surface is further verified by XPS analysis (**Figure A4.2**).

Kelvin probe force microscopy (KPFM) measurements were performed to verify the work function distributions (**Figure 4.1c-f**). The mean work function of the OAI-treated film was decreased to 4.49 ± 0.09 eV, from 4.67 ± 0.08 eV of the Reference film, and in contrast with the 4.77 ± 0.11 eV of the OATsO-treated film. From the topographical atomic force microscopy (AFM) maps, the surface morphology and root-mean-square roughness of the treated films were negligibly different (**Figure 4.1g**), expected given the dilute (but common) solution concentration used for surface treatment. Further comparisons of the height depth distributions and scanning electron microscopy (SEM) images also suggest that the surface uniformity is relatively similar for the treated films (**Figure A4.3**, **Figure A4.4**).

4.2 Consequences of heterointerface energetics on charge carrier dynamics

Band alignments constructed from the UPS results predict that a negative ΔE_{vac} may create a potential well to trap charges at the heterointerface (**Figure A4.5**). Cross-sectional KPFM measurements under illumination in open-circuit condition were followed to investigate the real-time charge carrier distributions in complete devices of planar architecture ITO/SnO_2/perovskite/spiro-MeOTAD/Au (**Figure A4.6, Figure A4.7, Figure A4.8**). The measured device ΔE_{vac} values at the perovskite/spiro-MeOTAD heterointerface are consistent with those obtained from the films (**Figure A4.9**). Charge carriers are unextractable in open-circuit condition (split quasi Fermi level), and might accumulate at a contacting selective heterointerface of the opposite polarity.[8,9] This is observed as an accumulation of holes for both devices at the perovskite/SnO_2 heterointerface (**Figure 4.1h**, **i**). In contrast, a pronounced electron accumulation

exists at the perovskite/spiro-MeOTAD heterointerface for only the OAI-treated device. The electron accumulation is noted to be significantly more severe than the counterpart hole accumulation. In principle, the ideal photovoltaic device would have a homogenous electric field distribution with no charge accumulation across its heterojunctions,[10] which is seen for the OATsO-treated device at its perovskite/spiro-MeOTAD heterointerface. Both devices were relatively field-free (i.e. flat potential) along the active layer, indicative of a high-quality perovskite bulk, suggesting that the different behaviors were a consequence of the surface treatments. The results are consistent with those predicted based on the band diagrams (**Figure A4.5**), where the non-negative ΔE_{vac} of the OATsO-treated device avoided the potential well and charge accumulation.

Photoluminescence (PL) spectroscopy indicates an effective suppression of charge-trapping defect states in the surface-treated films, as evidenced by their enhanced PL intensities and carrier lifetimes with a glass/perovskite architecture (**Figure 4.2a**, **b**). The defect passivation efficacies of the surface-treated films are noted to be relatively comparable. Comparing their PL intensity distributions indicate again that the surface uniformity is similar between the films (**Figure A4.10**). Despite the beneficial passivation effects, charge extraction into spiro-MeOTAD is sacrificially impeded in all surface-treated films (**Figure 4.2c**, **Figure 4.2d**, **Table B4.2**), but to different extents, with the trend correlated with the magnitude of ΔE_{vac}. Compared to the Reference/spiro-MeOTAD film, the average carrier lifetime (τ_{ave}) more than doubled to 8.1 ns (from 3.0 ns) for the OAI-treated film and the steady-state PL intensity was 223% higher. In contrast, OATsO treatment simultaneously suppressed trap states while charge extraction is barely impeded, avoiding the trade-off seen for $OABF_4$ and OAI treatments. Further photo-transient measurements on complete devices complement the film PL results (**Figure A4.11**). We postulate that the charge obstruction and accumulation cannot be explained by the surface 2D phase, since the insulating large organic cation (OA^+) is kept unchanged (**Figure A4.12**).

4.3 Device performance and hysteresis behavior

For the surface-treated devices, the power conversion efficiency (PCE) trends as OATsO-treated > $OABF_4$-treated > OAI-treated devices, due primarily to an increasing fill factor (*FF*) (**Figure 4.2e**, **Figure A4.13**). The device open-circuit voltages (V_{OC}) are marginally different, reflective of the comparable PL results of the glass/perovskite films. The best OATsO-treated

device reached a PCE of 24.41% (**Figure A4.14**). We further verified the performance of encapsulated devices at an independent third-party laboratory, noting that the performance slightly decreased after the encapsulation procedure (**Figure A4.15**). Contrasting the surface-treated devices, the PCE trend can be explained as follows; firstly, a more negative ΔE_{vac} deepened the valence band offset with spiro-MeOTAD, which increased hole extraction resistance to sacrifice *FF*. Additionally, the heterointerface barrier observed from the KPFM profiling may also contribute to impede charge extraction.[9,11] Regardless, a negative ΔE_{vac} remains the cause that gave rise to both effects. Separate investigations on a $FAPbI_3$ composition further verified our observations (**Figure A4.16**).

Comparing the surface-treated devices, the hysteresis behavior generally improved as the negative ΔE_{vac} decreases in magnitude (**Figure A4.17**). This provided the first hint at a correlation between charge accumulation and ion migration, given that ion migration is responsible for PSC hysteresis.[12,13] On the other hand, the Reference devices exhibited the lowest performance and worst hysteresis, due to the abundant, unpassivated heterointerface traps. Overall, the device performance results provide evidence for the sacrificial trade-off of a negative ΔE_{vac} to limit PSC performance.

4.4 Device stability under continuous illumination

We assessed the photostability of encapsulated devices under continuous illumination without an ultraviolet filter. All devices were aged in ambient atmosphere at ~40 °C. We preserved the original device architecture with spiro-MeOTAD as the HTM, without applying further modifications (e.g. copper phthalocyanine (CuPC) or poly(triarylamine) (PTAA) were not used). Under maximum power point (MPP) testing (**Figure 4.2f**), the OATsO-treated device sustained its performance with negligible degradation after ~800 h. The $OABF_4$-treated device was also relatively stable, retaining 91.5% of their performance after ~500 h. Among the surface-treated devices, the OAI-treated device degraded the most rapidly to 84.8% of their performance after ~500 h.

Contrasting the device degradation under MPP versus open-circuit condition (OC) testing, all devices were generally less stable under OC testing (**Figure 4.2g**, **Figure A4.18**). However, the device degradation trends are identical, and correlated with the magnitude of ΔE_{vac}. Particularly, the

$OABF_4$-treated devices with an intermediate negative ΔE_{vac} exhibited stability between that of the OAI-treated and OATsO-treated devices. Near the approximate halfway point of 1,014 h, the devices retained 94.3% (OATsO-treated), 86.2% ($OABF_4$-treated), and 74.8% (OAI-treated) of their average PCEs. Ending after 2,092 h, the OATsO-treated devices retained 87.0% of their initial PCE on average. On the other hand, the average PCE (65.1% of initial) of the OAI-treated devices decreased dramatically over the 2,092 h aging duration. The most stable OATsO-treated device (**Figure 4.2h**) retained 94.9% and 88.5% of its initial PCE after 1,014 h and 2,092 h, respectively.

Analyzing the degradation trends, we postulated that the potential well and charge accumulation may have accelerated ion migration, considering that the KPFM profiling was also performed under illumination in open-circuit condition. Particularly, the more rapid "burn-in" decay of the OAI-treated and $OABF_4$-treated devices, observed in both the MPP (**Table B4.4**) and OC tests, strongly hints that ion migration has been aggravated by a negative ΔE_{vac}, given that transient ion migration underlies the "burn-in" regime.[12,14,15] The altered ion migration energetics was also hinted by the device hysteresis behavior. Moreover, the 2D interlayer of conventional OAI treatment likely contributed to impeding ion migration,[16] yet the $OABF_4$ and OATsO-treated devices still had superior photostability, indicating that the ion migration energetics have been dominantly affected.

4.5 Analyses of the degraded devices

To directly investigate the extent of ion migration, upon completion of the OC stability testing, the original OAI-treated and OATsO-treated devices (after 2,092 h illumination) were sent for scanning transmission electron microscopy (STEM) analysis. The encapsulation cover glasses were detached immediately prior to focused ion beam (FIB) milling to extract sample cross-sections. STEM bright field images of the planar device stacks reveal that the micron-scale grain sizes are still visibly intact even after the extended aging (**Figure 4.3a, Figure 4.3b, Figure A4.19**). The first significant difference between the two samples can be seen at the perovskite/spiro-MeOTAD heterointerface. The OAI-treated device had a rougher heterointerface morphology, which is in contrast with the negligibly different topography for the fresh films observed by AFM and SEM. This suggests that the roughening is inherent to the aging process, possibly associated with heterointerface degradation by ion migration-induced compositional loss.

The elemental distributions were compared by X-ray energy-dispersive (EDX) mapping in STEM (**Figure 4.3c-f, Figure A4.20**). On close inspection, large accumulations of both bromine (green arrows) and iodine (yellow arrows) can be seen for the OAI-treated device along the top gold/platinum region. This is verified by quantitative analysis of the elemental distributions (**Figure 4.3g-j**). In consideration of the nominal stoichiometry of the perovskite, both bromine and iodine accumulation were approximately similar in order magnitude (**Figure A4.21**). We note that despite progress to completely rid the need for bromine in $FAPbI_3$-based compositions,[17,18] it was shown that bromine might remain necessary to stabilize the α-$FAPbI_3$ phase in state-of-the-art devices.[19] The bulk devices that underwent FIB milling were further recovered and characterized by ω-2θ XRD (**Figure A4.22**). The δ-$FAPbI_3$ peak supposedly at ~11.8° was not detected for both devices, and the α-$FAPbI_3$ phase remained dominant, ruling out possible aggravation of the perovskite phase metastability by iodine interstitial generation.[20]

4.6 Aggravated ion migration and device instability

We further simulated the ion migration pathways using the first principles nudged elastic band (NEB) methodology. To model the charge accumulation at the perovskite/spiro-MeOTAD heterointerface, we calculated the activation energy for halide migration in either a neutral uncharged, or negatively charged environment. Two independent pathways were explored; 1) migration within a unit cell of a supercell (intra-lattice), and 2) migration escaping a supercell (extra-lattice) (**Figure A4.23**, **Table B4.5**). The intra-lattice migration (vacancy mediated) investigates possible coulombic screening effects by a charged environment to alter the bonding affinities and thus migration energetics,[21,22] while the extra-lattice migration is defect-independent. For intra-lattice migration (**Figure 4.4a**), the energy barriers for both iodine (-38.7%) and bromine (-29.4%) decreased substantially in the negatively charged environment. Similarly observed for the extra-lattice scenario (**Figure 4.4b**), the activation energy for iodine migration (-13.3%) and bromine migration (-17.8%) were both lower in the charged environment. Per the Arrhenius relationship, the rate constant has exponential dependance on the activation energy barrier.

Ion penetration can result in irreversible chemical reactions with spiro-MeOTAD to degrade its hole-transporting functionality,[23] and also chemical corrosion of the top electrode layer,[24] which potentially contributed to the V_{OC} and *FF* decays of the devices. The robust encapsulation

procedure ruled out environmental degradation factors, indicating that intrinsic mechanisms (i.e. ion migration) were responsible, and also excluded trapped charges catalyzing extrinsic degradation pathways by moisture and oxygen.[25] This is evidenced by the J_{SC} retention for the devices, demonstrating the excellent phase stability of the active layers. By excluding ion migration, half-device tests further indicate that the photostability of the surface-treated films are negligibly different (**Figure A4.24**). Tying together all results, we propose that the potential well and charge accumulation created by a negative ΔE_{vac} aggravated device instability, by detrimentally accelerating halide migration at the spiro-MeOTAD/perovskite heterointerface. More generally, the beneficial improvements of surface treatments are sacrificially limited by a negative ΔE_{vac}, but modulating the counter-anion presents a simple method to further improve PSC stability and performance.

Backtracking, we also preliminarily explored the possible mechanistic origins of ΔE_{vac} using first principles, summarized as follows: Ligand-induced ΔW originate from two independent contributions;[26,27] 1) the ligand intrinsic dipole moment (μ_{dipole}), and 2) a charge density displacement by ligand-surface interactions and bond formation (μ_{charge}). The dipole moments of $[OA]^+$ and $[TsO]^-$ were +20.3 D and -10.5 D, respectively (**Figure A4.25**, **26**). On the other hand, $[TsO]^-$ induces a striking negative surface charge displacement, $\bar{q}$, of -0.022 *e*, three-fold larger in magnitude than the positive $\bar{q}$ of $[OA]^+$ (+0.006 *e*) (**Figure 4.4c-e, Table B4.6**). The negative $\bar{q}$ sign of $[TsO]^-$ indicates a depletion of electrons from the surface, and is equivalent with a positive ΔW. This trend is reproducible even with defect states on the surface, or different surface concentrations and species (**Figure A4.27**, **Figure A4.28**, **Table B4.7**). Therefore, we speculate that simultaneous contributions from both μ_{charge} and μ_{dipole} for $[TsO]^-$ synergistically counterbalanced $[OA]^+$, to result in a net positive ΔE_{vac} for OATsO treatment. More broadly, this proposes design principles for the ideal perovskite/CTM heterointerface. We preliminarily tested pairing $[TsO]^-$ with alkylammoniums with different chain lengths, but OATsO treatment yielded the best performance (**Figure A4.29**).

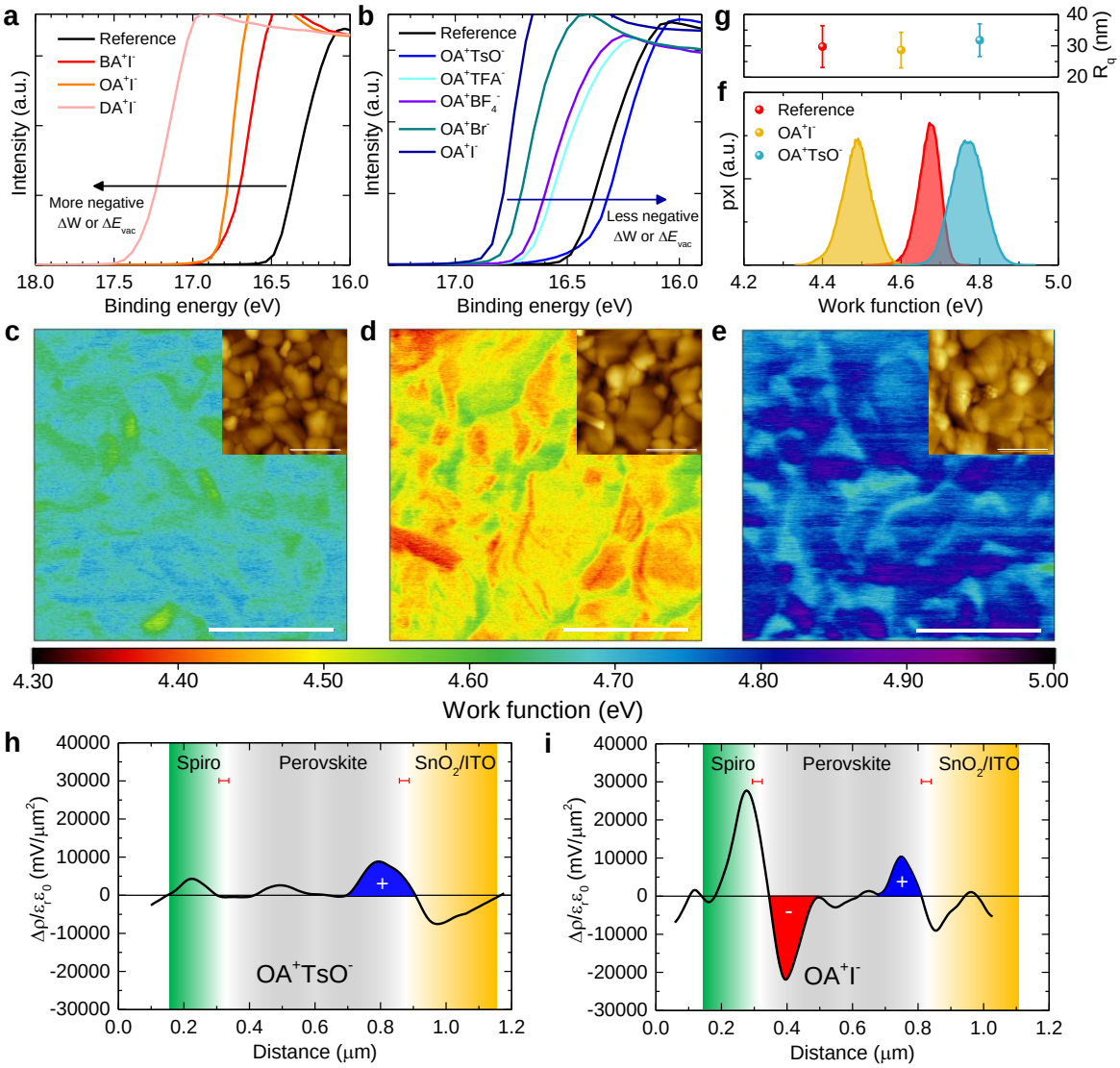

Figure 4.1. Perovskite surface and heterointerface dynamics. a, b, UPS secondary electron cut-offs of various surface-treated perovskite films. Labels are BA: butylammonium, OA: octylammonium, DA: dodecylammonium. KPFM surface potential maps of the **c,** Reference, **d,** OAI-treated, and **e,** OATsO-treated films. Insets include the corresponding AFM topography images. All scale bars are 2 μm. **f,** Work function distributions and **g,** RMS surface roughness (R_q) of the films measured by KPFM and AFM, respectively. Charge density distribution profiles of the complete **h,** OATsO-treated and **i,** OAI-treated device cross-sections measured by cross-sectional KPFM. The devices were illuminated under open-circuit condition. Red error bars demarcate the estimated spatial resolution of ~30 nm.[8,28]

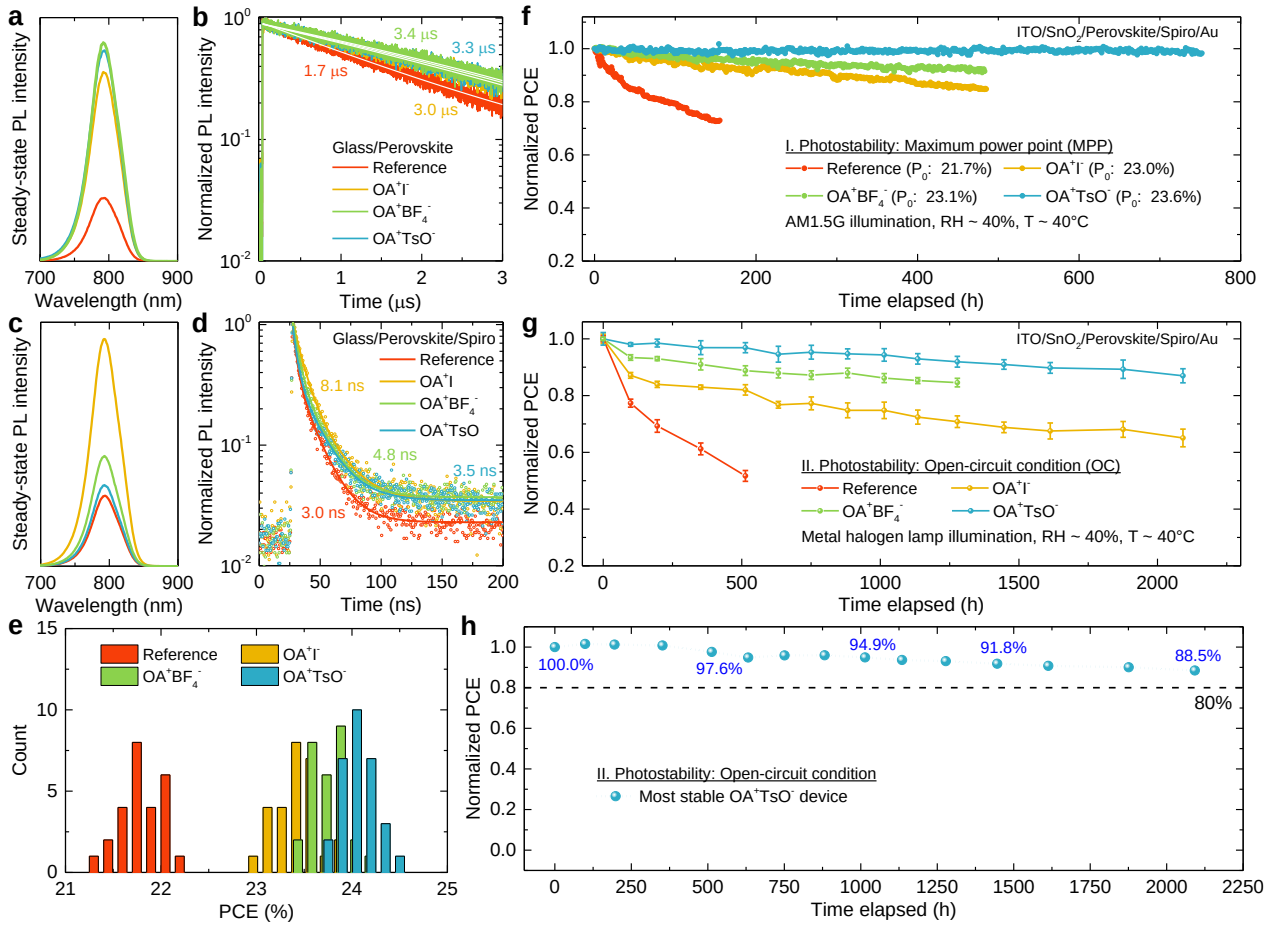

Figure 4.2. Charge carrier dynamics, performance, and photostability. a, Steady-state and **b,** time-resolved PL spectra of the glass/perovskite films. **c,** Steady-state and **d,** time-resolved PL spectra of the glass/perovskite/spiro-MeOTAD films. Included are the extracted lifetimes fitted with a mono-exponential decay function for (b) and bi-exponential decay function for (d). **e,** Histogram showing the PCE distributions of the devices. **f,** Photostability evolution with time of encapsulated devices aged under continuous illumination at maximum power point. P_0 denotes the initial PCE. **g,** Photostability evolution with time of encapsulated devices aged under continuous illumination in open-circuit condition. Error bars represent the standard deviation of four devices for each condition. **h,** Photostability PCE evolution of the most stable OATsO-treated device aged under open-circuit condition. Included are the PCE retentions in approximately 500 h intervals.

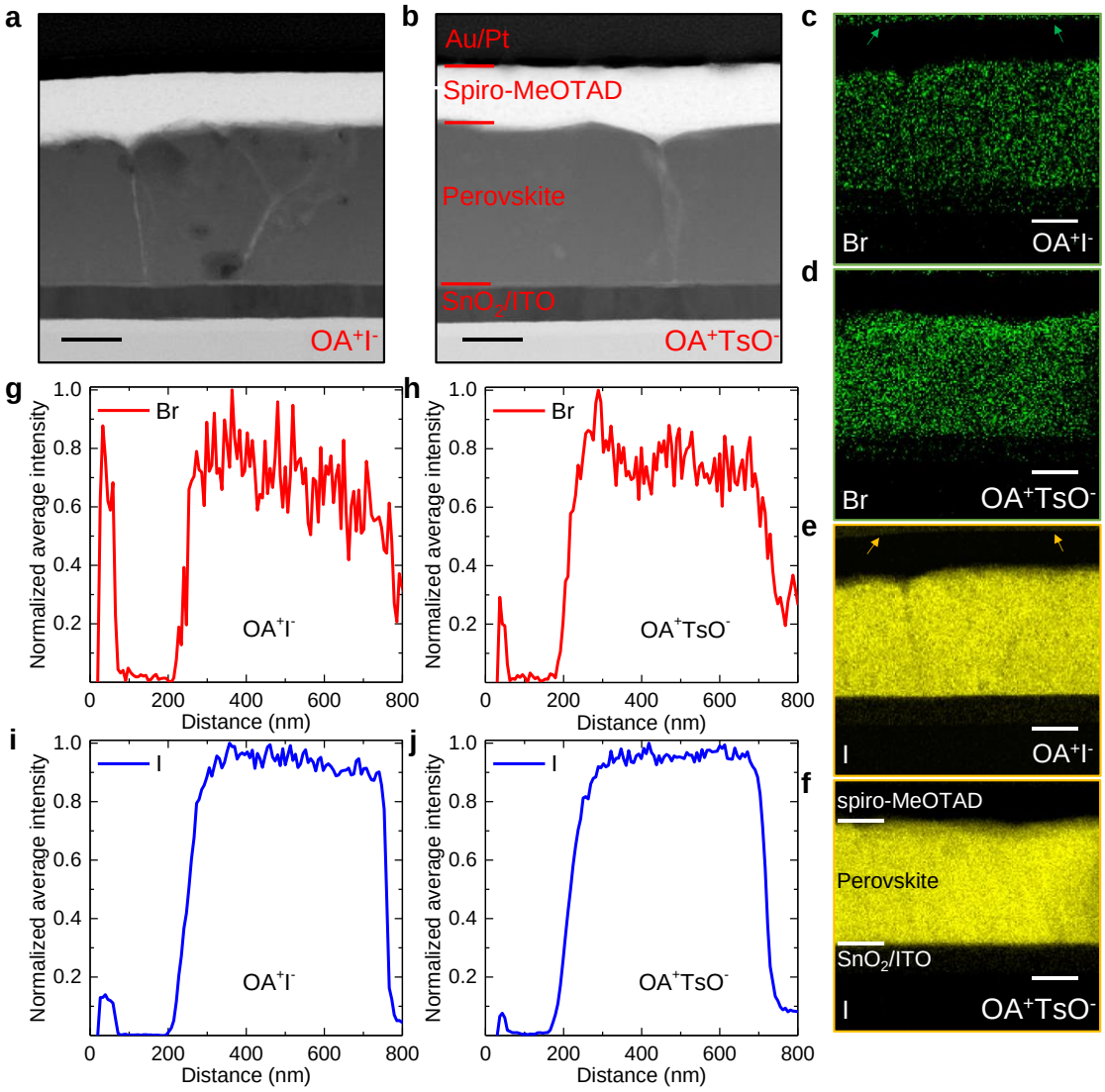

Figure 4.3. STEM and EDX analyses of the aged devices. STEM bright field images of the aged **a,** OAI-treated and **b,** OATsO-treated device cross-sections. The OAI-treated device is seen to have a rougher heterointerface contacting spiro-MeOTAD. EDX elemental maps of bromine for the **c,** OAI-treated and **d,** OATsO-treated device cross-sections, and iodine for the **e,** OAI-treated and **f,** OATsO-treated device cross-sections. All scale bars in the STEM and EDX images represent 200 nm. Elemental distributions of bromine for the **g,** OAI-treated and **h,** OATsO-treated devices, and iodine for the **i,** OAI-treated and **j,** OATsO-treated devices.

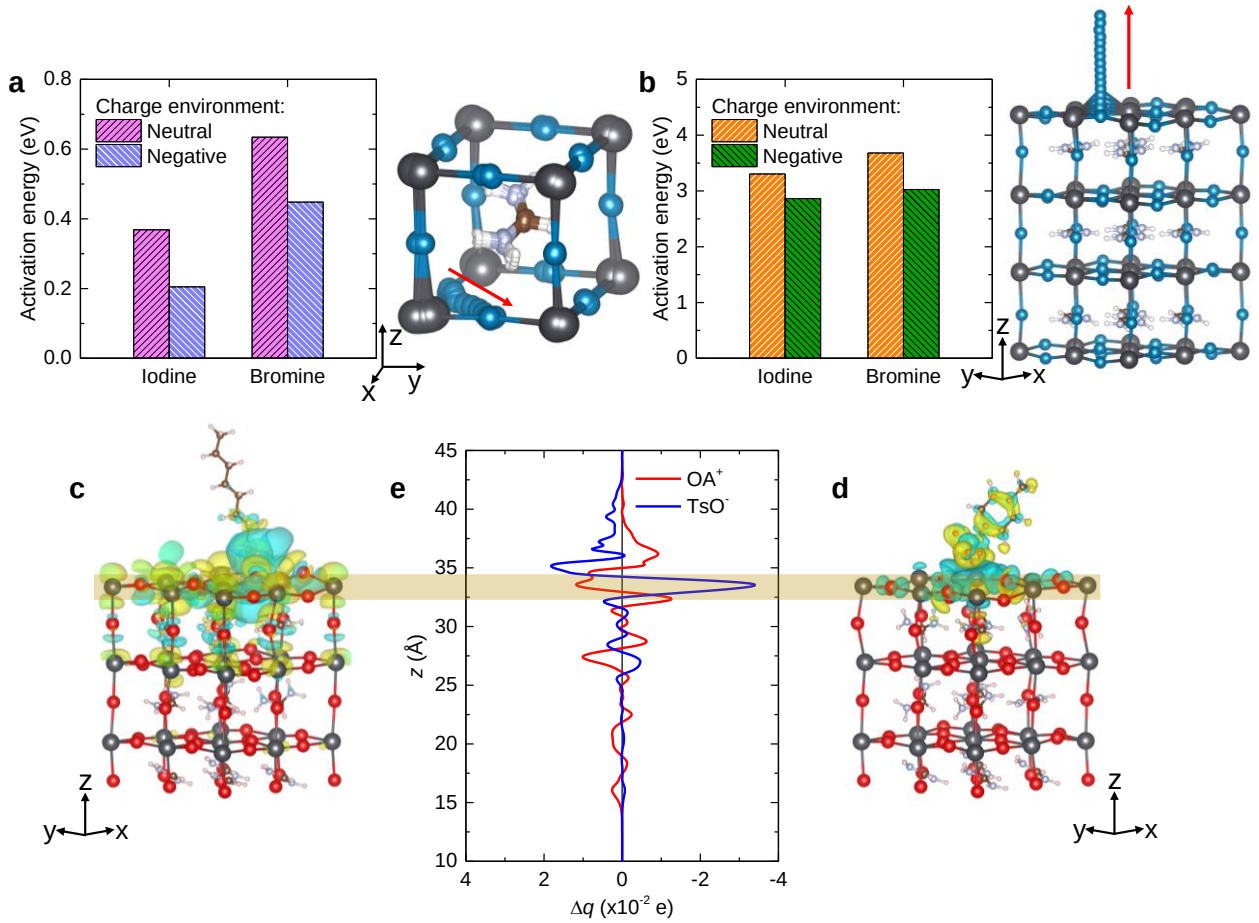

Figure 4.4. Physical origins of the experimental observations. Activation energy for the **a,** intra-lattice and **b,** extra-lattice migrations of iodine or bromine calculated using first-principles NEB simulations. The forward migration pathways are indicated by the red arrows in the example simulated supercells. Charge displacement with **c,** $[OA]^+$ or **d,** $[TsO]^-$ on the surface, superimposed on the defect-free slab models, and **e,** corresponding charge displacement profiles. Blue and yellow volumes on the slab models correspond to electron-depleted or electron-enriched regions, respectively.

References

1. Lee, J.-W., Tan, S., Seok, S. Il, Yang, Y. & Park, N.-G. Rethinking the A cation in halide perovskites. *Science* **375**, eabj1186 (2022).

2. Jung, E. H. *et al.* Efficient, stable and scalable perovskite solar cells using poly(3-

hexylthiophene). *Nature* **567**, 511–515 (2019).

3. Jiang, Q. *et al.* Surface passivation of perovskite film for efficient solar cells. *Nat. Photonics* **13**, 460–466 (2019).

4. Yoo, J. J. *et al.* An interface stabilized perovskite solar cell with high stabilized efficiency and low voltage loss. *Energy Environ. Sci.* **12**, 2192–2199 (2019).

5. Ni, Z. *et al.* Resolving spatial and energetic distributions of trap states in metal halide perovskite solar cells. *Science* **367**, 1352–1358 (2020).

6. Yang, Y. *et al.* Top and bottom surfaces limit carrier lifetime in lead iodide perovskite films. *Nat. Energy* **2**, 16207 (2017).

7. Smith, M. B. & March, J. *March's Advanced Organic Chemistry: Reactions, Mechanisms, and Structure, 6th Edition*. *John Wiley & Sons, Inc.*

8. Bergmann, V. W. *et al.* Local Time-Dependent Charging in a Perovskite Solar Cell. *ACS Appl. Mater. Interfaces* **8**, 19402–19409 (2016).

9. Cai, M. *et al.* Control of Electrical Potential Distribution for High-Performance Perovskite Solar Cells. *Joule* **2**, 296–306 (2018).

10. Söderström, T., Haug, F.-J., Terrazzoni-Daudrix, V. & Ballif, C. Optimization of amorphous silicon thin film solar cells for flexible photovoltaics. *J. Appl. Phys.* **103**, 114509 (2008).

11. Tsai, H. *et al.* Design principles for electronic charge transport in solution-processed vertically stacked 2D perovskite quantum wells. *Nat. Commun.* **9**, 2130 (2018).

12. Tan, S. *et al.* Steric Impediment of Ion Migration Contributes to Improved Operational Stability of Perovskite Solar Cells. *Adv. Mater.* **32**, 1906995 (2020).

13. Azpiroz, J. M., Mosconi, E., Bisquert, J. & Angelis, F. De. Defect migration in methylammonium lead iodide and its role in perovskite solar cell operation. *Energy Environ. Sci.* **8**, 2118–2127 (2015).

14. Domanski, K. *et al.* Migration of cations induces reversible performance losses over day/night cycling in perovskite solar cells. *Energy Environ. Sci.* **10**, 604–613 (2017).

15. Bai, S. *et al.* Planar perovskite solar cells with long-term stability using ionic liquid

additives. *Nature* **571**, 245–250 (2019).

16. Wang, Z. *et al.* Efficient ambient-air-stable solar cells with 2D–3D heterostructured butylammonium-caesium-formamidinium lead halide perovskites. *Nat. Energy* **2**, 17135 (2017).

17. Kim, M. *et al.* Methylammonium Chloride Induces Intermediate Phase Stabilization for Efficient Perovskite Solar Cells. *Joule* **3**, 2179–2192 (2019).

18. Min, H. *et al.* Efficient, stable solar cells by using inherent bandgap of α-phase formamidinium lead iodide. *Science* **366**, 749–753 (2019).

19. Yoo, J. J. *et al.* Efficient perovskite solar cells via improved carrier management. *Nature* **590**, 587–593 (2021).

20. Tan, S. *et al.* Shallow Iodine Defects Accelerate the Degradation of α-Phase Formamidinium Perovskite. *Joule* **4**, 2426–2442 (2020).

21. Zhao, J. *et al.* Strained hybrid perovskite thin films and their impact on the intrinsic stability of perovskite solar cells. *Sci. Adv.* **3**, eaao5616 (2017).

22. Lin, Y. *et al.* Excess charge-carrier induced instability of hybrid perovskites. *Nat. Commun.* **9**, 4981 (2018).

23. Carrillo, J. *et al.* Ionic Reactivity at Contacts and Aging of Methylammonium Lead Triiodide Perovskite Solar Cells. *Adv. Energy Mater.* **6**, 1502246 (2016).

24. Besleaga, C. *et al.* Iodine Migration and Degradation of Perovskite Solar Cells Enhanced by Metallic Electrodes. *J. Phys. Chem. Lett.* **7**, 5168–5175 (2016).

25. Ahn, N. *et al.* Trapped charge-driven degradation of perovskite solar cells. *Nat. Commun.* **7**, 13422 (2016).

26. Heimel, G., Rissner, F. & Zojer, E. Modeling the Electronic Properties of π-Conjugated Self-Assembled Monolayers. *Adv. Mater.* **22**, 2494–2513 (2010).

27. Brown, P. R. *et al.* Energy Level Modification in Lead Sulfide Quantum Dot Thin Films through Ligand Exchange. *ACS Nano* **8**, 5863–5872 (2014).

28. Zerweck, U., Loppacher, C., Otto, T., Grafström, S. & Eng, L. M. Accuracy and resolution

limits of Kelvin probe force microscopy. *Phys. Rev. B* **71**, 125424 (2005).

29. Kresse, G. & Furthmuller, J. Efficiency of ab-initio total energy calculations for metals and semiconductors using a plane-wave basis set. *Comput. Mater. Sci.* **6**, 15–50 (1996).

30. Perdew, J. P. *et al.* Restoring the Density-Gradient Expansion for Exchange in Solids and Surfaces. *Phys. Rev. Lett.* **100**, 1–4 (2008).

31. Grimme, S., Antony, J., Ehrlich, S. & Krieg, H. A consistent and accurate ab initio parametrization of density functional dispersion correction (DFT-D) for the 94 elements H-Pu. *J. Chem. Phys.* **132**, 154104 (2010).

32. Blöchl, P. E. Projector augmented-wave method. *Phys. Rev. B* **50**, 17953–17979 (1994).

33. Grimme, S., Bannwarth, C. & Shushkov, P. A Robust and Accurate Tight-Binding Quantum Chemical Method for Structures, Vibrational Frequencies, and Noncovalent Interactions of Large Molecular Systems Parametrized for All spd-Block Elements (Z = 1–86). *J. Chem. Theory Comput.* **13**, 1989–2009 (2017).

34. Bannwarth, C., Ehlert, S. & Grimme, S. GFN2-xTB—An Accurate and Broadly Parametrized Self-Consistent Tight-Binding Quantum Chemical Method with Multipole Electrostatics and Density-Dependent Dispersion Contributions. *J. Chem. Theory Comput.* **15**, 1652–1671 (2019).

35. Grimme, S. *et al.* Fully Automated Quantum-Chemistry-Based Computation of Spin-Spin-Coupled Nuclear Magnetic Resonance Spectra. *Angew. Chemie Int. Ed.* **56**, 14763–14769 (2017).

36. Grimme, S., Ehrlich, S. & Goerigk, L. Effect of the damping function in dispersion corrected density functional theory. *J. Comput. Chem.* **32**, 1456–1465 (2011).

37. Hirshfeld, F. L. Bonded-atom fragments for describing molecular charge densities. *Theor. Chim. Acta* **44**, 129–138 (1977).

Chapter 5 Steric Impediment of Ion Migration Contributes to Improved Operational Stability of Perovskite Solar Cells

In just a decade of unprecedented progress,[1–8] the record power conversion efficiencies (PCEs) of lead halide perovskite solar cells (PSCs) have propelled from an initial 3.8% to over 23%. Despite the impressive evolution, the notorious instability of PSCs remains a major challenge standing in the way of commercialization. Accelerated degradation upon exposure to external environmental factors including moisture, heat, oxygen, or ultraviolet illumination have been well documented.[9–13] More importantly, due to the ionic nature of perovskite materials, and the low formation[14] and migration activation energies[15,16] of the ionic species, a large number of the ions are mobile in the presence of a potential gradient, and this has been shown to have significant negative repercussions on the long-term operational stability of PSCs since mobile ions can migrate towards and into the adjacent contact layers to rupture the perovskite lattice and degrade the charge extracting/transporting functionality of the contacting layers.[15,17–19]

Various strategies have been reported to enhance the stability of PSCs. Particularly, compositional engineering involves substituting or replacing the 'A' site cation or 'X' site anion in the $APbX_3$ (X is one of or a mixed of I^-, Cl^- or Br^-) perovskite lattice.[20–22] Compositional engineering of the 'X' site anion by substitution of I^- to create mixed halide compositions have been reported to enhance the chemical and environmental stability of PSCs,[23–25] For instance, substitution of I^- with the more electronegative Br^- increases the bonding strength with the perovskite lattice to enhance its stability,[26] but halide substitution increases the optical bandgap of the perovskite to sacrifice its photocurrent. Furthermore, mixed halide PSCs suffer from poor operational stability due to phase segregation of the halide anions under illumination.[24,27]

On the other hand, modulation of the 'A' site cation has proven to be effective to enhance both the performance and stability without significantly altering the optoelectronic properties of the original perovskite composition. Compositional engineering of the 'A' site cation to incorporate formamidinium ($(NH_2)_2CH^+$, FA), guanidinium ($CH_6N_3^+$, GA), Cs and/or Rb have delivered high efficiencies as well as significantly improved stability over the commonly used pure methylammonium ($CH_3NH_3^+$, MA) composition.[28–30] However, the improved operational stability of mixed 'A' site compositions has yet been fully elucidated. For example, the substitution of MA for GA was previously shown to enhance the stability of the mixed MA/GA devices, attributed only to

the enhanced hydrogen bonding strength of GA with the lattice due to the two additional amine groups of GA.[28] However, the improved stability was not fully elucidated in terms of changes in the local lattice structure which might be more closely related to ion migration. Particularly, the possible change in the ion migration pathway and energetics as a result of localized lattice distortions caused by the much larger size of GA relative to MA was not investigated. It was recently suggested that 'A' cation compositional engineering can introduce localized distortions to the perovskite lattice structure in an attempt to control the energetics of ion migration.[31] However, it was challenging to decouple the steric impediment effect on ion migration due to the localized lattice distortions from the contribution of hydrogen bonding,[31] which was not further correlated with device stability. Understanding the relationship between 'A' cation size, hydrogen bonding, ion migration, and device operational stability would provide essential knowledge towards designing more operationally stable perovskite compositions.

In this work, we investigate the effect of 'A' cation size mismatch on the ion migration energetics and operational stability of PSCs. Partially substituting small MA with a larger 'A' site cation is expected to locally distort the perovskite lattice in order to fit the larger cation. The effect of this on the perovskite ion migration energetics has not been independently studied before due to the difficulty in separating the contributions of 'A' cation hydrogen bonding vs size. We systematically decoupled both effects by strategically choosing a suitable 'A' cation (acetamidinium (Ace), $CH_3C(NH_2)^{2+}$). Our work showcases a new strategy to utilize 'A' cation size mismatch to improve the operational stability of perovskites solar cells.

5.1 Decoupling size versus hydrogen bonding effect

We first had to find a suitable 'A' cation that will allow us to study only the 'A' cation size effect and decouple the hydrogen bonding effect. From our initial screening, we thought that Ace (**Figure 5.1a**) might be suitable due to its ionic radius (277 pm)[32] being considerably larger than MA (**Figure 5.1b**, 217 pm),[33] and being similar in size with GA (**Figure 5.1c**, 278 pm).[28] On the other hand, we speculated that Ace would probably have a weaker hydrogen bond interaction with the perovskite lattice due to its one less amine group compared to GA. The large size of Ace (or GA) means that the calculated tolerance factor (*t*) value of $AcePbI_3$ of 1.03 is above the theoretical range by which the cubic perovskite structure can form.[33] We confirmed that pure $AcePbI_3$ does not form

the perovskite phase using X-ray diffraction (XRD) on the as-prepared $AcePbI_3$ film (**Figure A5.1**). Conversely, $MAPbI_3$ (t=0.91) is known to crystallize in the less symmetrical tetragonal I4/*mcm* phase at room temperature[34] instead of the more ideal cubic phase since MA is too small. Partial substitution of MA with Ace to create a binary mixed cation $Ace_xMA_{1-x}PbI_3$ composition should compensate the two size extremes to tune the tolerance factor of $MAPbI_3$ upwards to within the desired cubic phase range. If so, the unit cell would have to expand to accommodate space to fit the larger Ace.

To empirically justify the choice of Ace for our study, we compared the hydrogen bonding interaction of MA, Ace and GA with the perovskite lattice using density functional theory (DFT) simulations. We modelled the ground state unit cell with the different 'A' cations and included the hydrogen bonds within a standard H-I bond length (2.5 – 3.5 Å)[35] and N-H-I bond angle > 110° (**Table 5.1**) in accordance with the recommended definition of a hydrogen bond by IUPAC[36] to arrive at the effective number of hydrogen bonds of Ace (3), MA (3), and GA (7), as shown in **Figure 5.1d-f**. The results show that MA and Ace have the same number of effective hydrogen bonds, and is less than half that of GA. This is supported by the thermogravimetric (TGA) results (**Figure A5.2**). As previously reported, the steps at approximately 100 °C, 300 °C and 450 °C are due to the sublimation of DMSO, MAI and PbI_2, respectively.[37] We observed from the first derivative weight loss curves that the sublimination peaks around 350 °C is comparable for pure $MAPbI_3$ and the Ace-containing perovskite, indicating that the hydrogen bond strengths of MA and Ace with the perovskite are comparable. Therefore, we assumed that a difference in ion migration energetics between Ace and MA, if any, should be due primarily to the size-mismatch-induced lattice distortions.

5.2 Computational study of ion migration energetics

We hypothesized that the localized lattice distortions caused by the size mismatch between Ace and MA might constitute a steric impediment effect to disrupt the pathways by which ions migrate. To study this effect theoretically, we performed further DFT simulations to model the ion migration pathway in the unit cell (**Figure 5.2a-d**) and to calculate the activation energy for the migration (**Figure 5.2e**). We chose to focus on the iodide ion transport since it was reported to have the lowest activation energy[15,16] and is thus the most prone to migrate/diffuse. **Figure 5.2a,c** (side view) and **Figure 5.2b,d** (top view) are overlays of 18 different structures corresponding to the 18 steps in **Figure 5.2e** used to define the initial and final positions of the iodide ion during the migration.

The calculated activation energy is 0.40 eV for $MAPbI_3$, consistent with previously reported values.[16,31,38] For the mixed $Ace_{0.25}MA_{0.75}PbI_3$ system, the activation energy is increased to 0.63 eV. The increased barrier height is probably due to steric impediment caused by the size-mismatch-induced lattice distortions, which can clearly be seen in the simulated migration pathway for the $Ace_{0.25}MA_{0.75}PbI_3$ system in **Figure 5.2d**, where the iodide ion should first curves inwards, then outwards, from the unit cell, as compared to the simple linear path of $MAPbI_3$ during the migration (**Figure 5.2b**). Importantly, we observe through the transition state structures in **Figure 5.2e** that the H-I bond length between the nearest neighboring hydrogen and the migrating iodide ion (highlighted in green) is significantly greater for $Ace_{0.25}MA_{0.75}PbI_3$ (3.10 Å) compared to $MAPbI_3$ (2.64 Å), indicating a much weaker H-I bond interaction between Ace and the mobile iodide. This, in addition to the overall weaker hydrogen bonding between Ace and the perovskite lattice discussed above, indicates that the steric impediment effect is mainly responsible for the increased activation energy barrier.

Since Ace (277 pm) and GA (278 pm) have almost identical ionic radii, we expect the lattice volume expansion by replacing MA with either to be similar. We calculated the unit cell volume from our simulated models of $Ace_{0.25}MA_{0.75}PbI_3$ and $GA_{0.25}MA_{0.75}PbI_3$ and found that both are identical at 253 $Å^3$ (for the Ace or GA containing unit cell), whereas pure $MAPbI_3$ has a unit cell volume of 248 $Å^3$. We then additionally simulated the energy barrier for $GA_{0.25}MA_{0.75}PbI_3$ (**Figure A5.3**) and expectedly found that the ion migration activation energy is the highest at 0.73 eV since for $GA_{0.25}MA_{0.75}PbI_3$, both steric impediment and hydrogen bonding contributes to impede ion migration. Therefore, comparing $MAPbI_3$ and $Ace_{0.25}MA_{0.75}PbI_3$ allows us to only study the effect of steric impediment (since Ace is larger than MA but has same number of effective hydrogen bonds). When comparing $MAPbI_3$ and $GA_{0.25}MA_{0.75}PbI_3$, both effects (since GA is larger and has higher number of effective hydrogen bonds than MA) influence the ion migration energetics, so it is not possible to distinguish one effect from the other.

5.3 Size-mismatch-induced lattice expansion and optical properties of the films

After justifying that the steric impediment effect can only be studied by comparing $MAPbI_3$ and $Ace_xMA_{1-x}PbI_3$, we subsequently fabricated $Ace_xMA_{1-x}PbI_3$ films to investigate the lattice distortions caused by the size mismatch between Ace and MA. XRD measurements were performed

on mixed composition $Ace_xMA_{1-x}PbI_3$ films, where x was varied from 0 ($MAPbI_3$) to 1.00 ($AcePbI_3$). As shown in **Figure 5.3a**, the tetragonal perovskite phase is retained without formation of any secondary phases up to x = 0.2. **Figure A5.4** displays the individual diffractograms in logarithmic scale for additional clarity. The (110) perovskite diffraction peak intensity was generally maintained except for x = 0.10, although the apparent grain size observed from the top surface scanning electron microscopy (SEM) images (**Figure A5.5** and **Figure A5.6**) of the films seemed to decrease, indicating that the bulk crystal quality might be improved with incorporation of Ace. We reasoned that the reduced apparent grain size is possibly due to the incorporated Ace acting as heterogenous nucleation sites to increase the nucleation rate, whereas the more ideal tolerance factor with incremental substitution of Ace is probably responsible for the improved bulk crystal quality as observed previously by the enhanced crystallinity of $FA_{1-x}Cs_xPbI_3$ and $FA_{1-x}MA_xPbI_3$ films relative to the pure $FAPbI_3$ film.[39–42] At x = 0.2, additional diffraction peaks at ~11.3° and ~25.3° began to emerge, which indicates that Ace can no longer incorporate into the perovskite lattice and thus formed the secondary $AcePbI_3$ phase. Additionally, X-ray photoelectron spectroscopy (XPS) measurements (**Figure A5.7**) on the $Ace_xMA_{1-x}PbI_3$ films further demonstrate the substitution of MA with Ace. The raw data was deconvoluted to reveal two constituent profiles attributed to the N 1s peaks originating from the NH_3^+ group in MA at ~402.3 eV and the NH_2^+ group in Ace at ~400.6 eV. The fitted profiles were used to calculate the Ace percentage in the films (**Figure A5.7b**), which closely match those of the nominal compositions in the precursor solutions.

High-resolution XRD measurements were carried out to investigate the lattice parameter changes, where the diffractograms were carefully calibrated with the constant PbI_2 peak at ~12.6° (**Figure 5.3b**). The results show that the (110) perovskite peak incrementally shifted towards lower 2θ angles with incorporation of Ace, indicating an expansion of the lattice due to the substitution of the smaller MA with the larger Ace. The *a* (or *b*) and *c* unit cell parameters for the films were extracted from the diffractograms as shown in **Figure 5.3c**, which shows that *a* (or *b*) increased with increasing incorporation of Ace from 8.867 Å for x = 0 to 8.913 Å for x = 0.2 (ca. 0.5% increment), whereas *c* increased marginally. We additionally measured the XRD diffractograms of $GA_xMA_{1-x}PbI_3$ (**Figure A5.8**) to compare the lattice volume expansions given by the ratio (unit cell volume of $Ace_xMA_{1-x}PbI_3$ or $GA_xMA_{1-x}PbI_3$)/(unit cell volume of $MAPbI_3$). The volume expansion is nearly identical (**Figure A5.9**) for $Ace_xMA_{1-x}PbI_3$ and $GA_xMA_{1-x}PbI_3$ due to the similarity in size between Ace and GA.

The absorption and normalized steady-state photoluminescence (PL) spectra of the $Ace_xMA_{1-x}PbI_3$ films are shown in **Figure 5.3d**. For x < 0.2, both the absorption profiles and the peak PL positions of the films were nearly identical with bare $MAPbI_3$ (x = 0), indicating that the films retained the optical properties of $MAPbI_3$ at relatively low levels of Ace incorporation. Further addition of Ace above x > 0.2 was seen to decrease the absorption of the films across all measured wavelengths, which can be attributed to the formation of the non-perovskite $AcePbI_3$ phase. Despite the substitution of MA with Ace, the absorption onsets were nearly unchanged (**Figure A5.10**), indicating that the bandgap of the mixed composition films remained roughly identical. The PL spectra redshifted and broadened asymmetrically, likely due to formation of the secondary phase that possibly introduced shallow defects at the band edges.

5.4 Device photovoltaic performance, charge carrier lifetimes and diode characteristics

To investigate the photovoltaic performance of the $Ace_xMA_{1-x}PbI_3$ perovskites, we fabricated planar n-i-p solar cell devices of structure ITO/SnO_2/perovskite/spiro-MeOTAD/Au. Based on tolerance factor considerations, pristine $MAPbI_3$ has a tetragonal crystal structure due to the small size of MA,[34] which implies that $MAPbI_3$ is intrinsically strained compressively. As previously reported, substitution of MA with a larger cation like FA or GA can compensate this intrinsic compressive strain and increase the tolerance factor towards 1 to improve the device photovoltaic performance.[28,39,43,44] Therefore, we speculated that the incorporation of Ace up to a certain limit should also improve the device performance. The photovoltaic parameters of the devices with different Ace substitution levels are summarized in **Table 5.2** and **Figure A5.11**. The average photovoltaic parameters (sample size, n = 25) of the reference $MAPbI_3$ devices (hereafter referred to as MA) are short-circuit current density (J_{SC}): 22.59 ± 0.14 mA cm^{-2}, open-circuit voltage (V_{OC}): 1.105 ± 0.007 V, fill factor (FF): 0.710 ± 0.012, and power conversion efficiency (PCE): 17.72 ± 0.34 %. Systematic variation of the Ace substitution level determined that $Ace_{0.03}MA_{0.97}PbI_3$ (henceforth denoted as AceMA) exhibited the best device performance, with an average (n = 43) J_{SC} of 22.67 ± 0.15 mA cm^{-2}, V_{OC} of 1.134 ± 0.009 V, FF of 0.750 ± 0.013, to yield a PCE of 19.28 ± 0.44 % (8.8% improvement over the average PCE of 17.72 ± 0.34 % for the MA devices). The PCE enhancement was due to the increased V_{OC} and FF, whereas the J_{SC} remained nearly identical. The distribution of the photovoltaic parameters of the MA and AceMA devices are compared in box plots

as shown in **Figure 5.4a** and **Figure A5.12**. We note that the devices were fabricated across multiple batches to demonstrate the reproducibility of the results.

The current density and voltage (*J-V*) curves of the champion devices are displayed in **Figure 5.4b**. Ultimately, the champion AceMA device attained a PCE of 20.30 % with a J_{SC} of 22.88 mA cm^{-2}, V_{OC} of 1.143 V, and FF of 0.776, while the champion MA device had a PCE of 18.49 % (J_{SC}: 22.80 mA cm^{-2}, V_{OC}: 1.108 V, FF: 0.732). The external quantum efficiency (EQE) spectra of the AceMA and MA devices are shown in **Figure A5.13**. The integrated J_{SC} calculated from the EQE spectra for the AceMA device was 22.02 mA cm^{-2}, within reasonable discrepancy (< 4%) from the measured J_{SC} from the *J-V* scans. However, the integrated J_{SC} for the MA device was 21.62 mA cm^{-2}, a comparatively large 5.5% discrepancy compared to the J_{SC} obtained from the *J-V* scans, which suggests an increased capacitive current effect due to more pronounced ion migration.[45] The stabilized PCEs were measured to be 19.5 % and 17.1 % for the champion AceMA and MA devices, respectively, as shown in inset **Figure 5.4b** and **Figure A5.14**. The smaller discrepancy between the stabilized PCE and the *J-V* scan obtained PCE for the AceMA device also implies suppressed hysteresis and ion migration, which is further evident in the scan direction dependent *J-V* curves of **Figure A5.15**.

To elucidate the origin of the improved photovoltaic performance of the mixed composition AceMA devices, we first measured the steady-state and time-resolved photoluminescence (PL) of the perovskite films deposited on glass substrates to study the charge recombination dynamics of the films (inset **Figure 5.4c**). The steady-state PL peak intensity increased by 43.7% from ~1.53 $\times 10^6$ for MA to ~2.20 $\times 10^6$ for AceMA, indicating an enhanced radiative recombination with substitution of 3 mol% MA for Ace. The time-resolved PL measurement showed that the improved radiative recombination is due to an enhanced PL lifetime, where the curves were fitted with a bi-exponential model (**Figure 5.4c**), with fitted parameters presented in **Table 5.3**. Two decay regimes are distinguishable from the fits, where the initial fast decay regime (A_1 and τ_1) is assigned to non-radiative carrier recombination induced by deep trap states such as structural disorders, whereas the subsequent slow decay regime (A_2 and τ_2) is ascribed to radiative recombination in the bulk perovskite.[46,47] For the AceMA film, we calculated that the fast decay carrier lifetime (τ_1) increased from 10.4 ns to 20.4 ns, and the proportion of fast decay (A_1) decreased from 83.6 % to 76 %, indicating reduced trap-mediated non-radiative recombination loss. τ_2 also increased from 180.7 ns for MA to 205.9 for AceMA. Resultantly, the average carrier lifetime was elongated from 38.3 ns to

64.9 ns for the MA and Ace films, respectively. We speculate that the enhanced steady-state PL and charge carrier lifetime for AceMA is a result of an improved bulk crystal quality due to the more ideal tolerance factor by replacing the too small MA with Ace.

The charge carrier lifetime within the complete device was also investigated with transient photovoltage (TPV) measurements at open-circuit condition, as shown in **Figure 5.4d**. Upon illumination with a pulsed light, electrons and holes are photogenerated to constitute the photovoltage, and subsequently recombine with elimination of the light source, which is observed as the decay in photovoltage. The rate with which the photovoltage decays is correlated with the charge carrier lifetime in the device. The decay time constants were extracted from the raw data using a mono-exponential decay function, with the fitted functions shown in **Figure 5.4d** as solid lines. The decay time constant was increased from 1.70 μs for the MA device to 2.28 μs for the AceMA device, indicating that the latter has much longer charge carrier lifetime in the device, consistent with the steady-state and time-resolved PL results.

Since the improved photovoltaic performance of the AceMA device is due to the increased V_{OC} and FF, we additionally measured the dark *J-V* response of the complete devices to extract the shunt (R_{sh}) and series (R_s) resistances, ideality factor (n) and reverse saturation current density (J_0), with results shown in **Figure A5.16** and **Table B5.1**, respectively. R_{sh} and R_s were calculated from the reciprocal of the slopes around the open-circuit and short-circuit regions, respectively. n and J_0 were obtained by fitting the dark *J-V* curves with the equation given by:[48]

$$\ln(J_D) = \ln(J_0) + \frac{1}{n}\frac{q}{k_B T}V_b \qquad (1)$$

where J_D is the dark current density, q is the elementary charge, k_B is Boltzmann's constant, T is temperature, and V_b is the applied bias. For the AceMA device, the lower n and J_0 indicates a reduced non-radiative trap-mediated recombination and explains the higher V_{OC}, whereas the higher R_{sh} and lower R_s is correlated with the higher FF. We further confirmed the reduced trap density of the AceMA devices using Thermal Admittance Spectroscopy (TAS), where the trap density of states (tDOS) can be calculated from the capacitance-angular frequency relationship using the equation:[49]

$$N_T(E_\omega) = -\frac{V_{bi}}{qW}\frac{dC}{d\omega}\frac{\omega}{kT} \qquad (2)$$

where C is the capacitance, ω is the angular frequency, q is the elementary charge, k is the Boltzmann constant, V_{bi} is the built-in potential, W is the depletion width, and T is the temperature. As shown in

Figure A5.17, the tDOS for the AceMA device was generally lower than that of the reference MA device, especially in the relatively deeper trap region (0.3 – 0.4 eV), where the minimum tDOS for the AceMA and MA devices reached ~5x10^{16} m^{-3} eV^{-1} and ~2x10^{17} m^{-3} eV^{-1}, respectively.

5.5 Ion migration and operational stability

In addition to the above discussed observations of reduced ion migration, we set out to directly investigate the ion migration properties of the films through direct current (DC) temperature-dependent conductivity measurements on lateral MA and AceMA devices with structure Au/perovskite (100 μm)/Au to experimentally determine the ion migration activation energies (**Figure 5.5a,b**). The activation energy (E_a) can be extracted by fitting the raw data points with the Nernst-Einstein equation given by:[17]

$$\sigma(T) = \frac{\sigma_0}{T} \exp\left(\frac{-E_a}{k_b T}\right) \qquad (2)$$

where $\sigma(T)$ is the conductivity as a function of temperature T, σ_0 is a constant, and k_b is Boltzmann's constant. Two linear regimes can be seen in the fitted plots of **Figure 5.5a,b**. In the low temperature regime, ion migration is essentially suppressed due to the insufficient thermal energy. Above a critical temperature, ion migration became activated and contributed to the exponential enhancement in conductivity. The extracted E_a is 0.542 eV for the AceMA lateral device, a 25% increase over the MA device (0.433 eV). This result complements our DFT calculations discussed before to further support our hypothesis that the lattice distortion caused by substituting MA with Ace resulted in a size-induced steric impediment effect to effectively obstruct the migration of ions in the perovskite.

To assess the operational stability of the AceMA devices, encapsulated solar cell devices were subjected to continuous illumination under 1 sun intensity (no ultraviolet filter) at open-circuit condition in ambient air to test their stability under operational conditions. Ion migration is most severe under open-circuit condition due to the uncompensated built-in potential under illumination.[50,51] In contrast, the applied bias during maximum power point (MPP) tracking is opposite in direction to the built-in voltage and reduces the effective potential gradient.[52] Upon the exclusion of external environmental factors such as moisture and oxygen by proper encapsulation or an inert atmosphere, the instability of PSCs under illumination should be largely due to the migration

of mobile ions due to the light-induced potential gradient to degrade the perovskite and adjacent contact layers.[17,19,52–54] For instance, migrating I^- can undergo an irreversible redox reaction to reduce spiro-OMeTAD$^+$ to its neutral state to degrade its p-doping character and thus degrade its hole conductivity and deteriorate the device performance.[53] It was also shown that I^- migrating out of the perovskite layer can deplete I^- from the perovskite layer to rupture its stoichiometry and lattice structure, in addition to reacting with Ag to form AgI to corrode the metal electrode.[54,55]

Figure 5.5c plots the evolution of the stabilized (steady-state) PCE of the MA and AceMA devices with time. The degradation profiles can be separated into two regimes, where an initial rapid decay is followed by a subsequent near linear decay, similar to what was obscaerved from previous reports.[17,45] From this, the T_{80} (time taken for device steady-state PCE to degrade to 80 % of its initial value) of the devices are obtained by fitting the linear degradation.[17,45] The T_{80} of the AceMA device was calculated to be 2,011 h, a considerable nine-fold improvement over the T_{80} of 222 h of the control MA device. After over 2,100 h of continuous illumination, the AceMA device retained over 55 % of its initial steady-state PCE, compared to only 6.9 % of the MA device after 700 h. The corresponding degradation of the photovoltaic parameters of the devices are also included in **Figure A5.18**, which show that the decline in device performance is mainly due to the drop in FF and V_{OC}, whereas the J_{SC} remained relatively constant, consistent with previous reports for devices aged under open-circuit condition.[50,52] Given that degradation of the encapsulated device under illumination at open-circuit condition is largely due to the migration of ionic defects and accumulated charge carriers,[45,52,56] the much improved stability of the AceMA device is probably due to the retarded ion migration as a result of the size-mismatch-induced steric impediment by the large Ace cation.

To assess the thermal stability of the devices, fabricated MA and AceMA devices were subjected to continuous heating at 85 °C in a nitrogen atmosphere and their reverse scan PCEs were measured periodically as shown in **Figure 5.5d**. Ag was used as the metal electrode, in which case the migration of I^- towards the electrode to deplete the stoichiometry of the perovskite and the corrosion of the electrode by AgI formation is expected to be the major cause of device degradation,[37,54,55] while the more thermally stable PTAA was used as the hole transporting layer (HTL) to replace spiro-MeOTAD.[8,30,37,57,58] The AceMA device was seen to have significantly improved thermal stability, and retained almost 92 % of its initial PCE after over 450 h of continuous heating. In contrast, the reference MA device degraded to just 1.6 % of its initial PCE over the same time period. **Figure A5.19** includes a breakdown of the evolution of the photovoltaic parameters of

the corresponding devices. For the AceMA device, the performance drop is due to the gradually decreasing FF, whereas the V_{OC} and J_{SC} changes negligibly with time. We speculate that the considerable thermal stability enhancement of the AceMA device is likely a result of the impeded migration of I^- due to the size-mismatch-induced lattice distortions. Particularly, we can deduce from the Nernst-Einstein equation above that ion migration is expected to be more severe at higher temperatures due to the supply of thermal energy.

We further exposed the MA and AceMA devices and bare films to controlled environments to investigate their moisture and ambient stabilities. However, we expected their environmental stabilities to be similar due to the comparable hydrogen bonding interaction between MA or Ace with the perovskite lattice. We monitored the X-ray diffractograms and normalized absorbance at 600 nm of the films (**Figure A5.20** and **Figure A5.21**) with time exposed to humidity or ambient, which showed that the degradation of AceMA was comparable or slightly enhanced compared to MA. The [(100) perovskite peak]/[PbI_2 peak] intensity ratio of the AceMA film degraded from 14.4 to 0.13 after 59 h exposure to the humid environment, and similarly the MA film degraded from 14.3 to 0.09. For the ambient exposure, the ratio decreased from 14.3 to 4.4 for the MA film and 14.6 to 4.5 for the AceMA film after 136 h exposure. For the devices, the reverse scan PCEs of both the MA and AceMA devices showed no apparent degradation after exposure to humidity or ambient, but the degradation of the devices was obvious through the stabilized PCEs of the devices. Combining the film and device results, we reason that the moisture-induced degradation (defect density generated) was comparable for MA and AceMA, and during the relatively short timescales of the reverse scan, the increased capacitive effects and hysteric behavior of the devices induced by the generated defects were not evident such that the reverse scan PCEs showed no obvious degradation.[17] However, during the longer timescales of the steady-state measurements, defects have sufficient time to migrate in response to the constant bias applied, but for the AceMA devices, due to the steric impediment effect which effectively obstructed defect migration, the capacitive effects was reduced and therefore the degradation of their stabilized PCEs was retarded.

Lastly, the formation enthalpies of the perovskites (**Figure A5.22**) were calculated using *ab initio* simulations to assess their intrinsic stability. The more negative formation enthalpy of the $Ace_{0.25}MA_{0.75}PbI_3$ composition demonstrates the improved thermodynamic stability due to the substitution of MA with Ace.

5.6 Generalizing the steric impediment of ion migration

To demonstrate the versatility of our proposed steric impediment approach, we generalized the strategy on the commonly used $FAPbI_3$ system. Unlike $MAPbI_3$, the tolerance factor of $FAPbI_3$ is thought to be slightly above the theoretical range to form the cubic phase due to the larger (253 pm) FA cation.[21] Therefore, opposite to the case with $MAPbI_3$, substitution of FA in $FAPbI_3$ for a relatively smaller cation such as MA (217 pm) or Cs (167 pm) can result in improved device operational stability.[22,29,43,59] Using the same procedure, we again measured the temperature-dependent conductivity of fabricated $FAPbI_3$, $MA_{0.05}FA_{0.95}PbI_3$ and $Cs_{0.05}FA_{0.95}PbI_3$ lateral devices to extract the ion migration activation energy. We observed that the activation energy increases in the order $FAPbI_3$ (0.259 eV) < $MA_{0.25}FA_{0.75}PbI_3$ (0.309 eV) < $Cs_{0.25}FA_{0.75}PbI_3$ (0.467 eV) (**Figure A5.23**), correlating with the increasing 'A' cation size mismatch. We additionally modelled the $FAPbI_3$, $MA_{0.25}FA_{0.75}PbI_3$ and $Cs_{0.25}FA_{0.75}PbI_3$ systems using DFT (**Figure A5.24**) as before and found that the simulated activation energy followed the trend of $FAPbI_3$ (0.37 eV) < $Cs_{0.25}FA_{0.75}PbI_3$ (0.72 eV) < $MA_{0.25}FA_{0.75}PbI_3$ (0.84 eV). Although both Cs and MA substitution into $FAPbI_3$ increases the energy barrier for iodide migration, the trend does not follow the experimental result. We note that the simulations consider only the iodide migration and do not account for other factors such as perovskite crystallinity, phase purity etc, which is probably the origin of the discrepancy with experimental data. We plan to further investigate this system for a future work.

5.7 Conclusions

In this work, we studied the effect of 'A' cation size mismatch induced lattice distortions on the ion migration energetics and operational stability of PSCs by partial substitution of small MA with the larger Ace cation. From our observations, we propose that the size mismatch between Ace and MA introduces localized lattice distortion in the perovskite lattice, which creates a steric effect to effectively impede the migration pathways of ions to increase the migration activation energy barrier. As a result, we observed that the optimized mixed composition $Ace_{0.03}MA_{0.97}PbI_3$ device had much improved thermal stability, retaining 92% of its initial PCE after 450 h under continuous heating at 85 °C, and also significantly elongated operational stability under continuous 1 sun illumination at open-circuit condition in ambient with an extrapolated T_{80} of 2,011 h, relative to the reference pure MA device with a T_{80} of 222 h. We believe our study on this steric engineering

strategy would provide essential knowledge to design more operationally stable perovskite compositions.

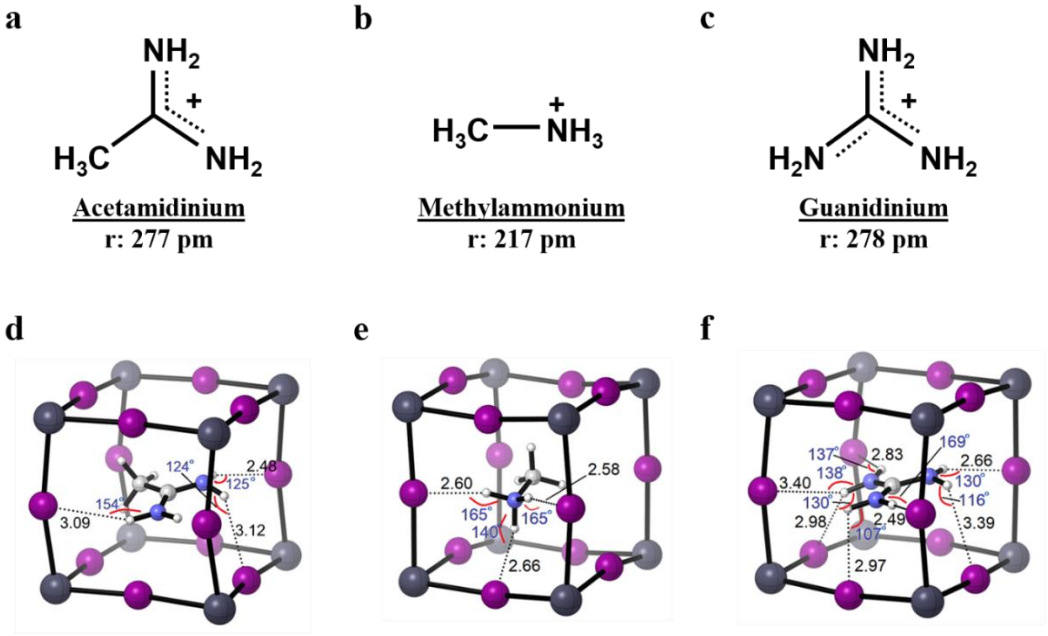

Figure 5.1. Decoupling size versus hydrogen bonding effect. Chemical structures of a) acetamidinium, b) methylammonium, and c) guanidinium. Density functional theory (DFT) modelled effective hydrogen bonds between the 'A' cations and perovskite lattice for d) acetamidinium, e) methylammonium, and f) guanidinium. Black numbers are the bond lengths (in angstroms) and blue numbers are the bond angles (in degrees).

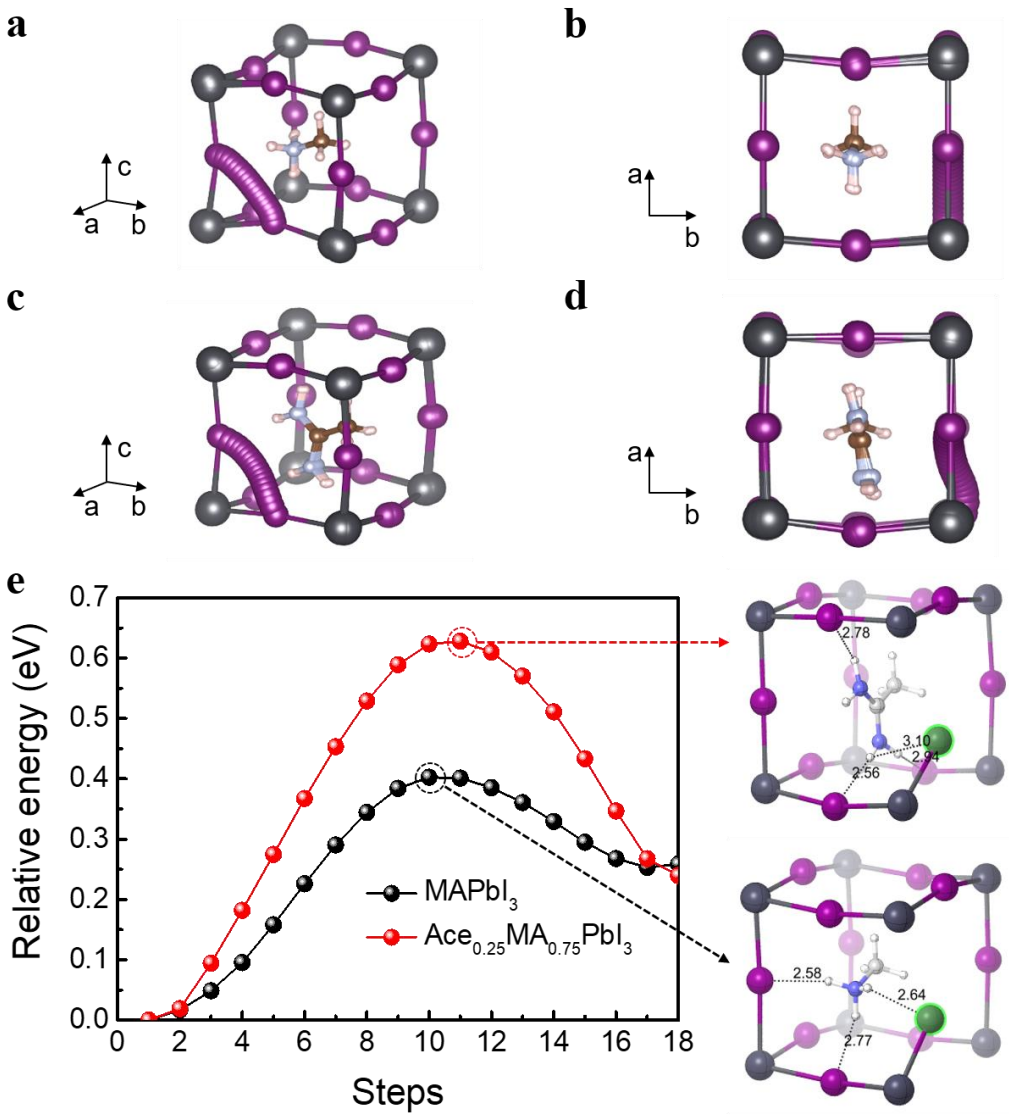

Figure 5.2. Computational study of ion migration energetics. Density functional theory (DFT) modelled a) side view and b) top view iodide ion migration pathway for $MAPbI_3$ perovskite and c) side view and d) top view iodide ion migration pathway for $Ace_{0.25}MA_{0.75}PbI_3$ perovskite, showing only the unit cell containing the Ace cation. e) Iodide ion migration activation energy for $MAPbI_3$ and $Ace_{0.25}MA_{0.75}PbI_3$ calculated using DFT. Included are the transition states corresponding to the maximum energy states, showing the hydrogen bond length between the migrating iodide ion (highlighted in green) and the nearest neighbouring hydrogen atom.

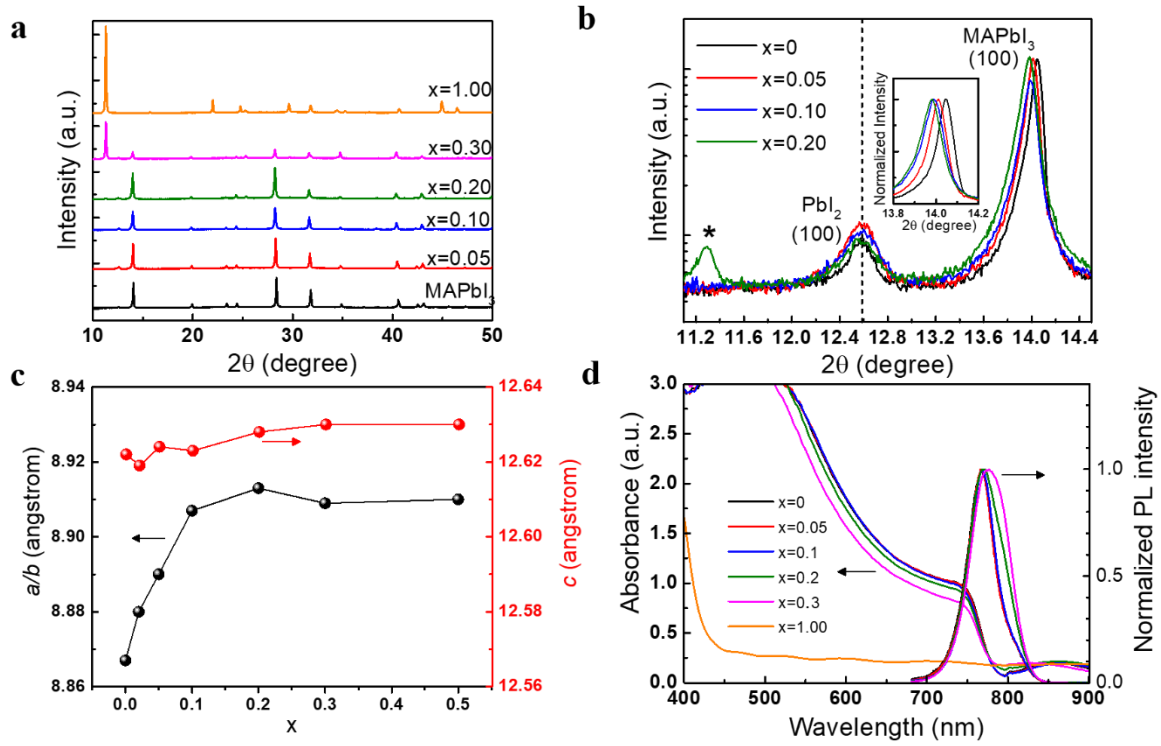

Figure 5.3. Size-mismatch-induced lattice expansion and optical properties of the films. a) X-ray diffraction (XRD) spectra of the $Ace_xMA_{1-x}PbI_3$ films with different values of x. b) High-resolution XRD spectra of the perovskite films showing the (100) perovskite diffraction peak. The PbI_2 and secondary phase (*) diffraction peaks are labelled. Inset shows the magnified normalized (100) perovskite peak. c) Variation of the *a* (or b) and *c* unit cell lattice parameters of the $Ace_xMA_{1-x}PbI_3$ films with different values of x. d) Absorption and normalized photoluminescence spectra of the $Ace_xMA_{1-x}PbI_3$ films with different values of x.

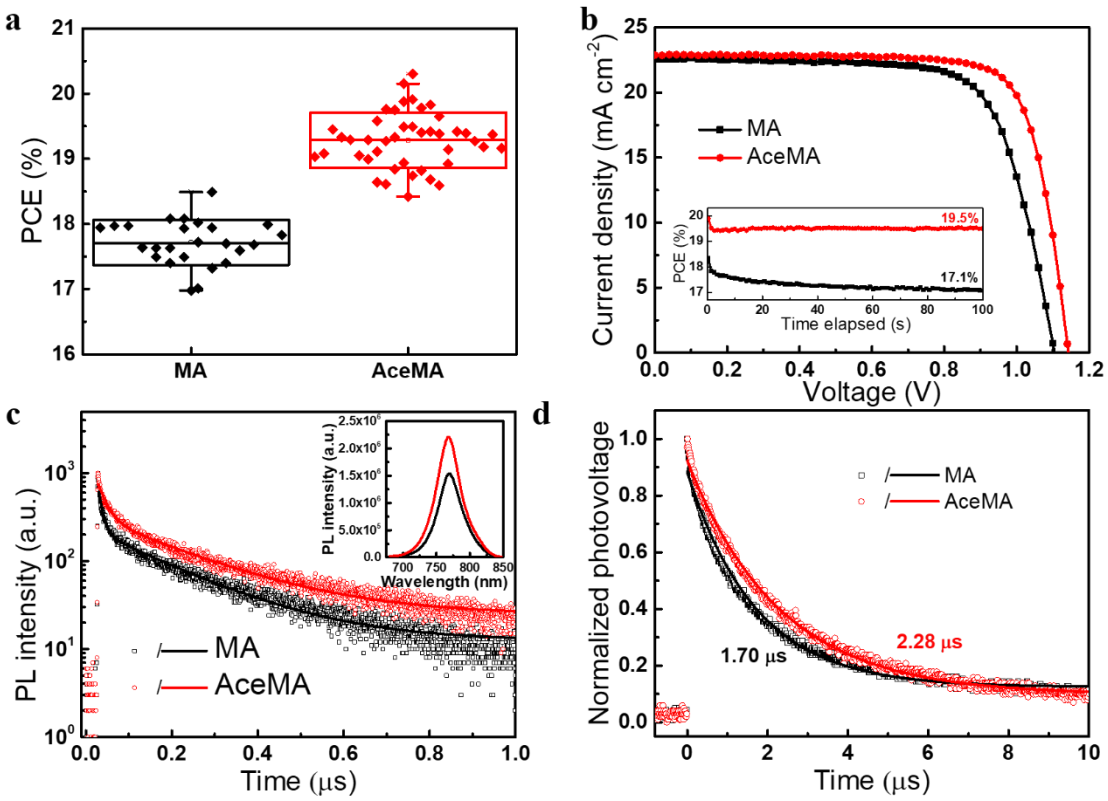

Figure 5.4. Device photovoltaic performance, charge carrier lifetimes and diode characteristics. a) Box plot showing the power conversion efficiency (PCE) distribution of the $MAPbI_3$ and $Ace_{0.03}MA_{0.97}PbI_3$ devices. b) Current density and voltage (*J*-*V*) curves of the champion devices. Inset includes the stabilized PCEs. c) Time-resolved photoluminescence spectra of the MA and AceMA films. Solid lines are the fitted profiles using a bi-exponential decay function. Inset includes the steady-state PL spectra. d) Transient photovoltage decay of the MA and AceMA devices. Solid lines are the fitted profiles using a mono-exponential decay function.

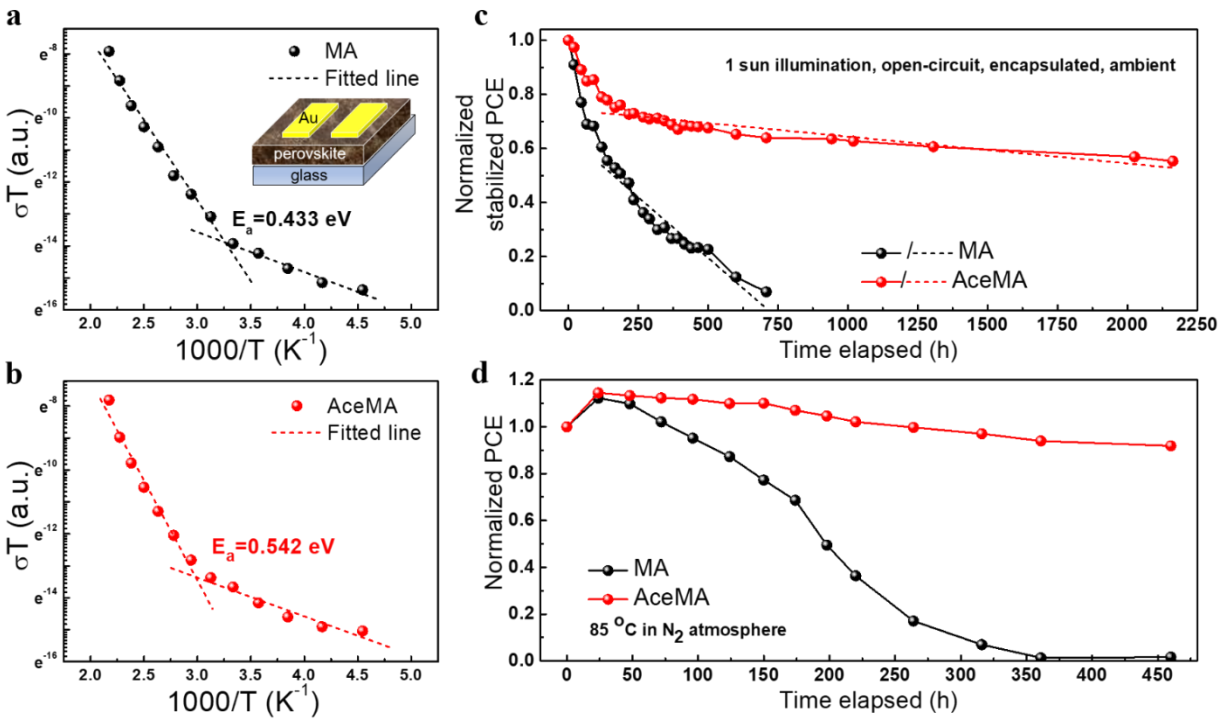

Figure 5.5. Ion migration and operational stability. Temperature-dependant conductivity of the a) $MAPbI_3$ and b) $Ace_{0.03}MA_{0.97}PbI_3$ lateral devices. c) Operational stability testing of encapsulated $MAPbI_3$ and $Ace_{0.03}MA_{0.97}PbI_3$ devices under continuous 1 sun illumination under open-circuit condition in ambient air. d) Thermal stability testing of the $MAPbI_3$ and $Ace_{0.03}MA_{0.97}PbI_3$ devices heated continuously at 85 °C in a nitrogen atmosphere.

Table 5.1. Density functional theory simulated effective bond lengths and bond angles of the 'A' cations with the perovskite lattice. Included are the average bond lengths and bond angles.

	Acetamidinium (Ace)		Methylammonium (MA)		Guanidinium (GA)	
Number	Bond length (Å)	Bond angles (°)	Bond length (Å)	Bond angles (°)	Bond length (Å)	Bond angles (°)
1	3.10	154	2.60	165	3.00	150
2	3.12	124	2.60	165	2.49	170
3	2.50	126	2.7	140	3.40	116
4					2.70	130
5					2.83	136
6					2.98	130
7					3.40	137
Average	2.91	135	2.63	157	2.97	138

Table 5.2. Average photovoltaic parameters of the $Ace_xMA_{1-x}PbI_3$ devices, summarizing the short-circuit current density (J_{SC}), open-circuit voltage (V_{OC}), fill factor (FF), power conversion efficiency (PCE), and best PCE.

	J_{SC} (mA cm^{-2})	V_{OC} (V)	FF	PCE (%)	Best PCE (%)
0	22.59 ± 0.14	1.105 ± 0.007	0.710 ± 0.012	17.72 ± 0.34	18.49
2	22.58 ± 0.13	1.134 ± 0.007	0.743 ± 0.006	19.03 ± 0.27	19.65
3	22.67 ± 0.15	1.134 ± 0.009	0.750 ± 0.013	19.28 ± 0.44	20.30
5	22.49 ± 0.15	1.143 ± 0.015	0.728 ± 0.015	18.60 ± 0.62	19.36
8	22.68 ± 0.25	1.136 ± 0.008	0.732 ± 0.008	18.86 ± 0.26	19.23
10	22.22 ± 0.46	1.132 ± 0.015	0.721 ± 0.004	18.16 ± 0.58	18.83

15	21.92 ± 0.23	1.124 ± 0.010	0.712 ± 0.007	17.53 ± 0.41	18.04
20	22.01 ± 0.25	1.128 ± 0.019	0.710 ± 0.014	17.63 ± 0.32	18.17

Table 5.3. Time-resolved photoluminescence decay parameters for the $MAPbI_3$ and $Ace_{0.03}MA_{0.97}PbI_3$ films on glass fitted using a bi-exponential decay model.

	A_1	**Proportion (%)**	τ_1 **(ns)**	A_2	**Proportion (%)**	τ_2 **(ns)**	τ_{ave} **(ns)**
MA	1065.0	83.6	10.4	208.5	16.4	180.7	38.3
AceMA	951.9	76.0	20.4	300.2	24.0	205.9	64.9

References

1. Kojima, A., Teshima, K., Shirai, Y. & Miyasaka, T. Organometal Halide Perovskites as Visible-Light Sensitizers for Photovoltaic Cells. *J. Am. Chem. Soc.* **131**, 6050–6051 (2009).
2. Kim, H.-S. *et al.* Lead Iodide Perovskite Sensitized All-Solid-State Submicron Thin Film Mesoscopic Solar Cell with Efficiency Exceeding 9%. *Sci. Rep.* **2**, 1–7 (2012).
3. Lee, M. M., Teuscher, J., Miyasaka, T., Murakami, T. N. & Snaith, H. J. Efficient Hybrid Solar Cells Based on Meso-Superstructured Organometal Halide Perovskites. *Science* **338**, 643–647 (2012).
4. Burschka, J. *et al.* Sequential deposition as a route to high-performance perovskite-sensitized solar cells. *Nature* **499**, 316–319 (2013).
5. Yang, W. S. *et al.* Iodide management in formamidinium-lead-halide–based perovskite layers for efficient solar cells. *Science* **356**, 1376–1379 (2017).
6. Tan, H. *et al.* Efficient and stable solution processed planar perovskite solar cell via contact passivation. *Science* **355**, 722–726 (2017).
7. Kim, M. *et al.* Methylammonium Chloride Induces Intermediate Phase Stabilization for Efficient Perovskite Solar Cells. *Joule* **3**, 2179–2192 (2019).

8. Jiang, Q. *et al.* Surface passivation of perovskite film for efficient solar cells. *Nat. Photonics* **13**, 460–466 (2019).
9. Song, Z. *et al.* Perovskite Solar Cell Stability in Humid Air: Partially Reversible Phase Transitions in the PbI2-CH3NH3I-H2O System. *Adv. Energy Mater.* **6**, 1–7 (2016).
10. Yang, J., Siempelkamp, B. D., Liu, D. & Kelly, T. L. Investigation of CH3NH3PbI3 Degradation Rates and Mechanisms in Controlled Humidity Environments Using in Situ Techniques. *ACS Nano* **9**, 1955–1963 (2015).
11. Christians, J. A., Herrera, P. A. M. & Kamat, P. V. Transformation of the Excited State and Photovoltaic Efficiency of CH3NH3PbI3 Perovskite upon Controlled Exposure to Humidified Air. *J. Am. Chem. Soc.* **137**, 1530–1538 (2015).
12. Bryant, D. *et al.* Light and oxygen induced degradation limits the operational stability of methylammonium lead triiodide perovskite solar cells. *Energy Environ. Sci.* **9**, 1655–1660 (2016).
13. Conings, B. *et al.* Intrinsic Thermal Instability of Methylammonium Lead Trihalide Perovskite. *Adv. Energy Mater.* **5**, 1–8 (2015).
14. Yin, W.-J., Shi, T. & Yan, Y. Unusual defect physics in CH 3 NH 3 PbI 3 perovskite solar cell absorber. *Appl. Phys. Lett.* **104**, 063903 (2014).
15. Azpiroz, J. M., Mosconi, E., Bisquert, J. & Angelis, F. De. Defect migration in methylammonium lead iodide and its role in perovskite solar cell operation. *Energy Environ. Sci.* **8**, 2118–2127 (2015).
16. Eames, C. *et al.* Ionic transport in hybrid lead iodide perovskite solar cells. *Nat. Commun.* **6**, 7497 (2015).
17. Domanski, K. *et al.* Migration of cations induces reversible performance losses over day/night cycling in perovskite solar cells. *Energy Environ. Sci.* **10**, 604–613 (2017).
18. Domanski, K. *et al.* Not All That Glitters Is Gold: Metal-Migration- Induced Degradation in Perovskite Solar Cells. *ACS Nano* **10**, 6306–6314 (2016).
19. Lee, J.-W., Kim, S.-G., Yang, J.-M., Yang, Y. & Park, N.-G. Verification and mitigation of ion migration in perovskite solar cells. *APL Mater.* **7**, 1–12 (2019).
20. Eperon, G. E. *et al.* Formamidinium lead trihalide: a broadly tunable perovskite for efficient planar heterojunction solar cells. *Energy Environ. Sci.* **7**, 982–988 (2014).
21. Lee, J.-W., Seol, D.-J., Cho, A.-N. & Park, N.-G. High-Efficiency Perovskite Solar Cells

Based on the Black Polymorph of HC(NH2)2PbI3. *Adv. Mater.* **26**, 4991–4998 (2014).

22. Lee, J.-W. *et al.* Formamidinium and Cesium Hybridization for Photo- and Moisture-Stable Perovskite Solar Cell. *Adv. Energy Mater.* **5**, 1501310 (2015).
23. Lin, C., Li, S., Zhang, W., Shao, C. & Yang, Z. Effect of Bromine Substitution on the Ion Migration and Optical Absorption in MAPbI3 Perovskite Solar Cells: The First-Principles Study. *ACS Appl. Energy Mater.* **1**, 1374–1380 (2018).
24. Ruess, R., Benfer, F., Bçcher, F., Stumpp, M. & Schlettwein, D. Stabilization of Organic–Inorganic Perovskite Layers by Partial Substitution of Iodide by Bromide in Methylammonium Lead Iodide. *ChemPhysChem* **17**, 1505–1511 (2016).
25. Noh, J. H., Im, S. H., Heo, J. H., Mandal, T. N. & Seok, S. Il. Chemical Management for Colorful, Efficient, and Stable Inorganic− Organic Hybrid Nanostructured Solar Cells. *Nano Lett.* **13**, 1764–1769 (2013).
26. Pont, S. *et al.* Tuning CH3NH3Pb(I1-xBrx)3 perovskite oxygen stability in thin films and solar cells. *J. Mater. Chem. A* **5**, 9553–9560 (2017).
27. Brennan, M. C., Draguta, S., Kamat, P. V & Kuno, M. Light-Induced Anion Phase Segregation in Mixed Halide Perovskites. *ACS Energy Lett.* **3**, 204–213 (2018).
28. Jodlowski, A. D. *et al.* Large guanidinium cation mixed with methylammonium in lead iodide perovskites for 19% efficient solar cells. *Nat. Energy* **2**, 972–979 (2017).
29. Saliba, M. *et al.* Cesium-containing triple cation perovskite solar cells: improved stability, reproducibility and high efficiency. *Energy Environ. Sci.* **9**, 1989–1997 (2016).
30. Saliba, M. *et al.* Incorporation of rubidium cations into perovskite solar cells improves photovoltaic performance. *Science* **354**, 206–209 (2016).
31. Ferdani, D. W. *et al.* Partial cation substitution reduces iodide ion transport in lead iodide perovskite solar cells. *Energy Environ. Sci.* **12**, 2264–2272 (2019).
32. Stoumpos, C. C. *et al.* Hybrid Germanium Iodide Perovskite Semiconductors: Active Lone Pairs, Structural Distortions, Direct and Indirect Energy Gaps, and Strong Nonlinear Optical Properties. *J. Am. Chem. Soc.* **137**, 6804–6819 (2015).
33. Kieslich, G., Sun, S. & Cheetham, A. K. Solid-state principles applied to organic – inorganic perovskites : new tricks for an old dog. *Chem. Sci.* **5**, 4712–4715 (2014).
34. Whitfield, P. S. *et al.* Structures, Phase Transitions and Tricritical Behavior of the Hybrid Perovskite Methyl Ammonium Lead Iodide. *Sci. Rep.* **6**, 1–15 (2016).

35. Amat, A. *et al.* Cation-Induced Band-Gap Tuning in Organohalide Perovskites: Interplay of Spin−Orbit Coupling and Octahedra Tilting. *Nano Lett.* **14**, 3608–3616 (2014).
36. Arunan, E. *et al.* Definition of the hydrogen bond (IUPAC Recommendations 2011)* Elangannan. *Pure Appl. Chem.* **83**, 1637–1641 (2011).
37. Xue, J. *et al.* A Small-Molecule "Charge Driver" enables Perovskite Quantum Dot Solar Cells with Efficiency Approaching 13%. *Adv. Mater.* **31**, 1900111 (2019).
38. Haruyama, J., Sodeyama, K., Han, L. & Tateyama, Y. First-Principles Study of Ion Diffusion in Perovskite Solar Cell Sensitizers. *J. Am. Chem. Soc.* **137**, 10048–10051 (2015).
39. Pellet, N. *et al.* Mixed-Organic-Cation Perovskite Photovoltaics for Enhanced Solar- Light Harvesting. *Angew. Chemie Int. Ed.* **53**, 3151–3157 (2014).
40. Li, Z. *et al.* Stabilizing Perovskite Structures by Tuning Tolerance Factor: Formation of Formamidinium and Cesium Lead Iodide Solid-State Alloys. *Chem. Mater.* **28**, 284–292 (2016).
41. Lee, J.-W., Lee, D.-K., Jeong, D.-N. & Park, N.-G. Control of Crystal Growth toward Scalable Fabrication of Perovskite Solar Cells. *Adv. Funct. Mater.* **1807047**, 1–18 (2018).
42. Qiao, H. W. *et al.* A Gradient Heterostructure Based on Tolerance Factor in High-Performance Perovskite Solar Cells with 0.84 Fill Factor. *Adv. Mater.* **31**, 1–6 (2019).
43. Zheng, X. *et al.* Improved Phase Stability of Formamidinium Lead Triiodide Perovskite by Strain Relaxation. *ACS Energy Lett.* **1**, 1014–1020 (2016).
44. Chen, H. *et al.* Efficient and Stable Inverted Perovskite Solar Cells Incorporating Secondary Amines. *Adv. Mater.* **31**, 1–9 (2019).
45. Lee, J.-W. *et al.* 2D perovskite stabilized phase-pure formamidinium perovskite solar cells. *Nat. Commun.* **9**, 1–10 (2018).
46. Shi, D. *et al.* Low trap-state density and long carrier diffusion in organolead trihalide perovskite single crystals. *Science* **347**, 519–522 (2015).
47. Son, D.-Y. *et al.* Self-formed grain boundary healing layer for highly efficient CH3NH3PbI3 perovskite solar cells. *Nat. Energy* **1**, 1–8 (2016).
48. Kang, H.-W., Lee, J.-W., Son, D.-Y. & Park, N.-G. Modulation of photovoltage in mesoscopic perovskite solar cell by controlled interfacial electron injection. *RSC Adv.* **5**, 47334–47340 (2015).
49. Lee, J. *et al.* A Bifunctional Lewis Base Additive for Microscopic Homogeneity in

Perovskite Solar Cells A Bifunctional Lewis Base Additive for Microscopic Homogeneity in Perovskite Solar Cells. *Chem* **3**, 290–302 (2017).

50. Domanski, K., Alharbi, E. A., Hagfeldt, A., Grätzel, M. & Tress, W. Systematic investigation of the impact of operation conditions on the degradation behaviour of perovskite solar cells. *Nat. Energy* **3**, 61–67 (2018).
51. Nie, W. *et al.* Light-activated photocurrent degradation and self-healing in perovskite solar cells. *Nat. Commun.* **7**, 1–9 (2016).
52. Khenkin, M. V., K.M., A., Katz, E. A. & Visoly-Fisher, I. Bias-Dependent Degradation of Various Solar Cells: Lessons for Stability of Perovskite Photovoltaics. *Energy Environ. Sci.* **12**, 550–558 (2019).
53. Carrillo, J. *et al.* Ionic Reactivity at Contacts and Aging of Methylammonium Lead Triiodide Perovskite Solar Cells. *Adv. Energy Mater.* **6**, 1502246 (2016).
54. Akbulatov, A. F. *et al.* Effect of Electron-Transport Material on Light-Induced Degradation of Inverted Planar Junction Perovskite Solar Cells. *Adv. Energy Mater.* **7**, 1–7 (2017).
55. Besleaga, C. *et al.* Iodine Migration and Degradation of Perovskite Solar Cells Enhanced by Metallic Electrodes. *J. Phys. Chem. Lett.* **7**, 5168–5175 (2016).
56. Ahn, N. *et al.* Trapped charge-driven degradation of perovskite solar cells. *Nat. Commun.* **7**, 13422 (2016).
57. Xue, J. *et al.* Crystalline Liquid-like Behavior: Surface-Induced Secondary Grain Growth of Photovoltaic Perovskite Thin Film. *J. Am. Chem. Soc.* **141**, 13948–13953 (2019).
58. Han, T.-H. *et al.* Interface and Defect Engineering for Metal Halide Perovskite Optoelectronic Devices. *Adv. Mater.* **31**, 1803515 (2019).
59. Yi, C. *et al.* Entropic stabilization of mixed A-cation ABX3 metal halide perovskites for high performance perovskite solar cells. *Energy Environ. Sci.* **9**, 656–662 (2016).
60. Kresse, G. & Furthmuller, J. Efficiency of ab-initio total energy calculations for metals and semiconductors using a plane-wave basis set. *Comput. Mater. Sci.* **6**, 15–50 (1996).
61. Kresse, G. & Furthmuller, J. Efficient iterative schemes for ab initio total-energy calculations using a plane-wave basis set. *Phys. Rev. B* **54**, 11169–11186 (1996).
62. Perdew, J. P., Burke, K. & Ernzerhof, M. Generalized Gradient Approximation Made Simple. *Phys. Rev. Lett.* **77**, 3865–3868 (1996).
63. Grimme, S. Semiempirical GGA-type density functional constructed with a long-range

dispersion correction. *J. Comput. Chem.* **27**, 1787–1799 (2006).

64. Grimme, S., Antony, J., Ehrlich, S. & Krieg, H. A consistent and accurate ab initio parametrization of density functional dispersion correction (DFT-D) for the 94 elements H-Pu. *J. Chem. Phys.* **132**, 154104 (2010).

65. Blöchl, P. E. Projector augmented-wave method. *Phys. Rev. B* **50**, 17953–17979 (1994).

Chapter 6 Solid-phase hetero epitaxial growth of α-phase formamidinium perovskite

Epitaxial growth is one of the most powerful ways to fabricate semiconducting thin films with low defect density and a desired orientation[1]. The technique has been widely adopted to form semiconducting thin films for optoelectronic applications for which the defect density should be minimized to promote carrier transport and thus device performance. Highly crystalline semiconducting films including silicon, gallium nitride, gallium arsenide, and two-dimensional materials have been successfully grown via epitaxial growth to be used in solar cells, light-emitting diodes (LEDs) and memory devices[2-6]. However, conventional epitaxy requires a compatible single crystalline substrate, and the growth process is performed in extremely controlled environments such as ultra-high vacuum and temperature. Often, the grown materials should be transferred from the templating substrate onto a desired substrate for device fabrication by delicate lift-off processes. These limit not only the price competitiveness and scalability, but also versatility of the process for various materials and devices.

For instance, the epitaxial growth of metal halide perovskite thin films for used in devices has not yet been achievable because of i) the absence of compatible substrates to template the growth of the perovskite film, and ii) the difficulty of inducing controlled nucleation and growth at the surface of a templating substrate. For the former, typical transparent oxide substrates and other charge transporting bottom contact layers used for devices cannot direct the growth of the perovskite film. Single crystalline chunks of halide perovskites and epitaxially grown thin films on single crystal substrate have been demonstrated[7-11], but thickness-controlled layer transfer of the grown materials onto a desired substrate has not been successful. For the latter, inherently fast reaction kinetics during the typical solution process causes numerous nuclei to form in the bulk solution, resulting in the growth of randomly oriented fine grains with a high density of defects. In light of these limitations, huge research efforts have been devoted to control the nucleation and growth kinetics[12,13], but accurate control over the kinetics in solution medium is still challenging.

Recently, strategies to incorporate layered perovskites into 3D perovskites have been extensively studied. Owing to their enhanced stability relative to 3D perovskites and favorable band alignment, layered perovskites effectively passivate the grain boundaries and surface of 3D perovskites, resulting in enhanced performance and stability of the perovskite solar cells and

LEDs.[14-17] We present here a route to induce kinetic-controlled epitaxial crystal growth of formamidinium lead tri-iodide ($FAPbI_3$) perovskite thin films by using layered perovskite templates. The local epitaxial growth of the $FAPbI_3$ perovskite crystal was observed during its solid-state phase transformation from the hexagonal non-perovskite $FAPbI_3$ when it is heterostructured with layered perovskite, whereby the growth kinetics was dependent on strain energy originating from the hetero-interface. Our first-principles calculations revealed a new mechanism to engineer the conversion energy barrier between the cubic and hexagonal phases by a synergistic effect between strain and entropy. The slow heteroepitaxy enabled the growth of 10-fold enlarged $FAPbI_3$ perovskite crystals with a reduced defect density and strong preferred orientation. This nano-heteroepitaxy (NHE) is applicable to various substrates used for devices. The proof-of-concept solar cell and light-emitting diode devices based on NHE-$FAPbI_3$ showed efficiencies and stabilities superior to those of devices fabricated without NHE.

6.1 Phase conversion kinetics

$FAPbI_3$ crystallizes as its equilibrium hexagonal non-perovskite phase (yellow color, δ-phase) at room temperature, and is transformed into its cubic perovskite polymorph (black color, α-phase) upon annealing at 150 ^oC through a soild-state phase conversion process [18,19]. In polycrystalline films, grain boundaries are at a higher energy state due to the additional contribution of surface (or interfacial) energy. Consequently, the grain boundaries act as heterogeneous nucleation sites where phase transition is first triggered. We introduced a hetero-interface at the grain boundaries by incorporating small amounts of layered perovskites into the precursor solution [15,20]. We varied both the amount and type of the layered perovskite to observe the effects of the hetero-interface (hereafter we define, control: bare $FAPbI_3$, 1P: $FAPbI_3$ with 1.67 mol% of PEA_2PbI_4, 3P: $FAPbI_3$ with 3.33 mol% of PEA_2PbI_4, and 3F: $FAPbI_3$ with 3.33 mol% of $FPEA_2PbI_4$). We expected the hetero-interface area to increase in the order control<1P<3P< 3F (please refer to **Figure A6.1** and **Figure A6.2** for discussion on the differences between PEA_2PbI_4 and $FPEA_4PbI_4$).

The layered perovskite/$FAPbI_3$ hetero-structured films were formed by spin-coating the precursor solutions, and the photographs of the films as a function of annealing time are presented in **Figure 6.1a**. As-spun films were semi-transparent yellowish irrespective of the added layered perovskite, indicating the formation of the hexagonal δ-phase. Upon annealing at 150 ^oC, the color of the control film rapidly converted to black within a minute, whereas the color change was retarded

with incorporation of the layered perovskites; 1P, 3P and 3F took approximately 2, 6, and 8 min, respectively. The slower color change is indicative of a slower phase conversion process. In **Figure 6.1b**, the phase conversion process was monitored by *in-situ* grazing incident wide angle X-ray scattering (GIWAXS) measurement of the corresponding films at 150 ^{o}C (under helium atmosphere on silicon substrate). Before heating at 150 ^{o}C, all the films showed a characteristic scattering peak around q=0.842 Å^{-1}, corresponding to the (010) orientation peak of the δ-$FAPbI_3$ phase. As the films were annealed at 150 ^{o}C, the peak disappeared with simultaneous occurrence of a new peak around q=0.996 Å^{-1}, attributed to the (001) orientation peak of the α-$FAPbI_3$ phase. The δ(010) peak of the control film almost abruptly disappeared after heating for 1 min with simultaneous appearance of the α(001) peak, and afterwards the α(001) peak maintained its initial shape and intensity. On the contrary, the δ(010) peak of the films with layered perovskite was retained for longer during the heat-treatment and gradually converted to the α(001) peak, indicating slower phase conversion with the layered perovskite. To analyze the phase conversion kinetics, we plotted isothermal transformation diagrams as in **Figure 6.1c**. The relative peak intensity (integrated area under the peaks) of α(001) to δ(010) was calculated from the *in-situ* GIWAXS patterns as a function of annealing time (upper panel in **Figure 6.1c**). A delayed phase transformation with incorporation of layered perovskite from control, to 1P, to 3P, and to 3F can be clearly seen. To quantitatively estimate the transformation kinetics, we fitted the phase conversion profiles using the simplified Johnson-Mehl-Avrami equation which describes the relationship between the fraction of transformed phase and the elapsed time. The extracted *k* values (**Table B6.1**) are seen to decrease from the control, 1P, 3P, to 3F films, suggesting that the nucleation and/or growth rates of the cubic phase were significantly retarded by the incorporation of the layered perovskite. We also confirmed that the phase transformation kinetics followed the same tendency for films on SnO_2-coated ITO substrates depending on the film composition by measuring the X-ray diffraction (XRD) patterns of the films with different heating times (**Figure A6.3** and the lower panel in **Figure 6.1c**). In addition to the different kinetics, the GIWAXS peak shapes also evolved differently for the films with layered perovskite as compared to the control film. The portion of the δ(010) peak with relatively lower q (higher d spacing, yellow arrows in **Figure 6.1b**) disappeared faster, whereas the portion of the α(001) peak with relatively higher q (lower d spacing, black arrows in **Figure 6.1b**) emerged faster. This feature became more pronounced as the phase conversion process retarded further, which implies the presence of strained phases and a consequent change in energetics and kinetics of the phase conversion process. We

speculated that the introduction of the hetero-interface between the $FAPbI_3$ and layered perovskite was probably associated with the observed strain and was responsible for retarding the phase conversion process.

6.2 Microstructure analysis and first-principles modeling

To observe the microstructure evolution during the phase conversion, *in-situ* transmission electron microscopy (TEM) measurement was conducted on the 3F film at an elevated temperature (**Figure 6.2a-d**). Upon heating the sample, nuclei of the cubic phase (bright spots indicated by arrows) formed simultaneously at both the bulk and boundaries of the grain (**Figure 6.2a**). However, the bulk nuclei were re-dissolved within a few minutes (**Figure 6.2b**), which is probably due to the relatively higher free energy barrier for stable nucleation. On the contrary, the grain boundary nucleus was stable and slowly grew towards the grain interior (**Figure 6.2c**). As the growth proceeded, we observed that the distinct grain boundary present before the phase conversion gradually became less distinguishable, and thus we speculated that the adjacent grains possibly merged during the phase transition (**Figure 6.2d**). In addition, the layered perovskites at the grain boundary region grew and reorientate/diffuse during the phase conversion process (**Figure A6.4a-d**). As a result, we observed aggregated layered perovskites along with blurred grain boundaries of the $FAPbI_3$ film from the cross-sectional TEM images of the sample after the phase conversion process (**Figure A6.4e, f**). We further noticed that the lattice of the as-formed α-$FAPbI_3$ seems to have aligned with the aggregated layered perovskites (**Figure A6.4g, h**). *Note: Since the in-situ measurement was carried out under vacuum on a sample with thickness <50 nm, the resulting microscopic morphology (grain size, layered perovskite distribution) may be different from that processed under ambient conditions.* High-resolution TEM images of the 3F film were further analyzed to investigate the microstructure of the hetero-interface between $FAPbI_3$ and the layered perovskite (**Figure 6.2e-j** and **Figure A6.5**). From the scanning transmission electron microscopy (STEM) images in **Figure A6.5a** and **b,** we identified the layered perovskite at the grain boundaries and surface of the $FAPbI_3$ grains before and after the heat-treatment with its characteristic interplanar spacing of around 7.25 Å corresponding to the (002) plane[21,22]. **Figure 6.2f** shows the magnified interface region between the layered perovskite and the δ-$FAPbI_3$ phase before the phase conversion process. From fast Fourier transform (FFT) analysis of the image in **Figure 6.2g**, we found that the (002) plane of the layered perovskite is aligned with the (010) plane

of the δ-$FAPbI_3$ phase. The measured interplanar distance of the δ-$FAPbI_3$ (7.25 Å) at the interface deviated from those measured from their bulk counterparts; 7.11 Å for (010) of δ-$FAPbI_3$, **Figure 6.2g** and **Figure A6.6a-c**. The larger interplanar spacing of the δ-$FAPbI_3$ indicates the presence of tensile strain at the interface with the layered perovskite. From the TEM images and corresponding FFT analysis after the phase conversion process (**Figure 6.2i, j**), a semi-coherent interface between the layered perovskite and the α-$FAPbI_3$ was observed. Despite of the semi-coherent interface, the (111) plane of the grown α-$FAPbI_3$ orientationally aligned with the (002) plane of the layered perovskite, which implies that heteroepitaxial growth of the α-$FAPbI_3$ crystals occurred during the phase conversion process. The measured interplanar spacing of 3.61 Å for the (111) plane of the α-$FAPbI_3$ at the interface region was slightly smaller than that measured from its bulk counterpart (3.65-3.71 Å, **Figure 6.2j** and **Figure A6.6a-f**), which implies the existence of compressive strain applied to the interfacial α-$FAPbI_3$ phase. From this observation, we assumed that the δ-$FAPbI_3$ phase (with its larger interplanar spacing) being converted to α-$FAPbI_3$ (with its smaller interplanar spacing) at the initial stage of the phase conversion (as shown in the *in-situ* GIWAXS measurements in **Figure 6.1b** with layered perovskite) was probably the $FAPbI_3$ at the interface with the layered perovskite. This indicates that the phase transition initiates at the hetero-interface, and the formed nuclei might grow towards the bulk of the grain.

To elucidate the origin of the different phase conversion kinetics, we performed first-principles density functional theory (DFT) calculations based on the observed strain and interfacial alignments as determined by the TEM studies (**Figure A6.7**). We initially postulated that two factors may have contributed to the change in phase conversion energetics: i) strain itself which can be directly responsible for increasing the phase conversion nucleation barrier as is well-known from conventional nucleation theory [23], and ii) change in entropy induced by the presence of strain, which was previously reported to be a crucial factor affecting the energetics of $FAPbI_3$ [19]. The phase conversion energetics without strain is presented in **Figure A6.8**. Firstly, to investigate the effect of strain, the energy barriers (ΔG_c) between the cubic and hexagonal phases with the lattice constants fixed to the given interlayer spacings are calculated as in **Figure 6.2k**. Solid lines indicate the energy barriers with strain applied to the transition states, whereas the dotted lines are the barriers with relaxed (unstrained) transition states (interlayer spacings of only the hexagonal and cubic phases are constrained to the given interlayer spacings). Overall, the energy barrier increases when strain is

applied to the transition state as expected from classical nucleation theory[23]. As the interlayer spacing decreases towards the 2D spacing, the compressive strain increases the cubic to hexagonal transformation barrier height by ~0.15eV in comparison to the value for the fully relaxed lattice (blue arrows in **Figure 6.2k** and second panel in **Figure 6.2l**), which will be beneficial for the thermodynamic stability of the cubic phase at $T<T_c$ (T_c is the critical temperature for phase conversion), correlating with previous experimental observations [9]. In the case of the phase transition from the hexagonal to cubic phase (δ→α), strain seems to less affect the ΔG_c value. However, we found that the contribution of entropy becomes more dominant. The activated rotation of the FA molecule at elevated temperatures contributes to the entropy of the system, which is known to be more significant in isotropic cubic structures and thus stabilizes the cubic phase over the hexagonal phase at a finite temperature [19]. The entropy contribution (S_{rot}) of a freely rotating FA^+ cation becomes more significant with an increasing temperature (T) as given by

$$S_{rot} = \frac{3}{2} k_B [1 + \ln\left(0.4786 k_B T \sqrt[3]{I_1 I_2 I_3}\right)]$$

where k_B and I_i are the Boltzmann constant and principal moments of inertia, respectively. The principal moments of inertia (I_i) of the FA^+ cation are 8.586, 48.851 and 57.436 uÅ^2, where the unified atomic mass unit, u, is 1.6605×10^{-27} kg [19]. The differences in the Gibbs free energy between the two phases are about -0.27eV at T=300 K and -0.47eV at T=500 K. As the free energy linearly decreases with T for the cubic phase, the relative stability between the two phases inverted above T_c while its contribution is negligible for the hexagonal phase (third panel in **Figure 6.2l**)[19]. On the other hand, the rotational entropy becomes a key contributor in stabilizing the strained hexagonal phase. Under the tensile strain, the interlayer spacing of the hexagonal phase increases significantly, and the activated isotropic rotation of the FA^+ cation also becomes accessible for the hexagonal phase. We confirmed a more than 50% decrease in the rotational barrier induced by the tensile strain, while the rotational barrier for the compressed cubic phase is not much affected (**Figure A6.9**). Consequently, the tensile strain applied to the hexagonal phase effectively increases the stability of the hexagonal phase at a finite temperature and contributes to slowing down the phase transformation process to the cubic phase (red arrow in the last panel in **Figure 6.2l**).

6.3 Effect of the bulk heteroepitaxy on film quality

The effect of the NHE on film quality was investigated by comparing the X-ray diffraction (XRD) patterns of the films before and after the phase conversion process. In **Figure 6.3a**, all the as-fabricated films showed characteristic peaks originating from the δ-$FAPbI_3$ phase with no significant difference in peak intensity, indicating that the added layered perovskites do not significantly alter the crystallization process of the hexagonal phase from the precursor solutions. On the contrary, the XRD patterns of the films after the phase conversion process were considerably different depending on the composition (**Figure 6.3b**). The intensity of the (001) and (002) peaks originating from the α-$FAPbI_3$ were systematically enhanced (control<1P<3P<3F) as the phase conversion became slower, which is also obvious in the high-resolution XRD patterns in **Figure 6.3c**. The enhancement of selective peaks of a specific orientation is indicative of an enhanced preferred orientation of the films. We confirmed the systematic enhancement of the preferred orientation of the films from pole figure measurements along the (001) orientation (**Figure 6.3d-g**). The more localized signal intensity at the center of the circle can be interpreted as a higher degree of preferred orientation of the films normal to the substrate. The degree of the (001) preferred orientation measured from the pole figures was well-correlated with the XRD patterns in **Figure 6.3b, c** (control<1P<3P<3F). The stronger preferred orientation indicates that heteroepitaxial growth of the α-$FAPbI_3$ became increasingly dominant with a larger hetero-interface area.

Closer inspection of the high resolution XRD patterns revealed that the full-width-half-maximums (FWHMs) of the normalized (002) peaks decreased as the peaks were gradually shifted toward higher angles in the same order, which indicates an incrementally increasing crystallite size and compressive strain (inset of **Figure 6.3c**). The crystallite size and lattice strain of the δ-$FAPbI_3$ films were further extracted from the full XRD patterns by using the Williamson-Hall method (**Figure A6.10**, **Table B6.2** and **Table B6.3**) [24,25]. Since the Williamson-Hall method is limited to crystallite sizes below 100 nm, for the α-$FAPbI_3$ crystallite sizes, we extracted the grain sizes of the films from the atomic force microscopy images in **Figure A6.11a-d** whose distribution is shown in **Figure A6.12**. The results are summarized in **Figure 6.3h**. The calculated strain of the films before phase conversion was closely correlated with the phase conversion kinetics, which confirms that the strain energy and resulting entropy change associated with the hetero-interface were likely responsible for the retarded phase conversion kinetics. The crystallite sizes before phase conversion were comparable irrespective of composition. Notably, the crystallite sizes were significantly

enlarged as the phase conversion became slower (from 43.5 nm to 160.4 nm for control, from 43.7 nm to 417.9 nm for 1P, from 40.6 nm to 520.8 nm for 3P, and from 65.4 nm to 675.0 nm for 3F). Based on the observations, we propose the following mechanism for the NHE (**Figure A6.13**). i) The added layered perovskite crystallizes at the grain boundaries with high surface energy, which would have otherwise triggered the initial nuclei formation. ii) The strain and resulting entropy change induced by the hetero-interface retards the phase transition and local epitaxial growth proceeds from the interface. iii) Owing to active reconstruction processes involving breakage and reformation of bonds during the phase transition [19,26], merger of the $FAPbI_3$ grains and layered perovskite sheets can be thermally activated. iv) Due to preferential orientation of the aggregated layered perovskite [27], the $FAPbI_3$ grains also orient with respect to the substrate. Our first-principles surface energy calculations support the suggested mechanism, where the surface energies of the δ(010) and α(111) facets are relatively higher than those of other facets (**Figure A6.14**), which might be the origin of the preferential alignment of the layered perovskite at the crystal facets.

Steady-state photoluminescence (PL) spectra of the films are presented in **Figure 6.3i**. The near-identical peak positions irrespective of film composition was correlated with the identical absorption onsets (inset of **Figure 6.3i** and **Figure A6.15**), which demonstrates that the bandgap of the films is unchanged from that of bulk $FAPbI_3$. The films with layered perovskite showed enhanced absorptions over the whole wavelength region as compared to the control film, which is probably due to the higher phase purity as observed in our previous study [20]. The peak PL intensity of 0.16×10^6 for the control film was significantly enhanced with NHE to 3.46×10^6, 4.49×10^6, and 5.34×10^6 for the 1P, 3P, and 3F films, respectively. Time-resolved PL decay profiles of the films are included in **Figure 6.3j** to elucidate the enhanced PL intensities. The measured data were fitted to a bi-exponential decay model, and the fitted parameters are summarized in **Table B6.4**. All films showed two decay regimes: a relatively faster initial decay (τ_1~ 3 ns), followed by a much slower decay (τ_2 >>10 ns). The faster decay component is generally assigned to charge carrier trapping caused by deep trap states originating from structural defects, whereas the slower decay is attributed to bimolecular radiative recombination of the free carriers [28,29]. It should be noted that the fast decay proportion (A_1) decreased from 39.1% for the control film to 38.2, 27.8, and 13.4% for the 1P, 3P, and 3F films, respectively. The decreased proportion of the faster decay implies reduced structural defects that constitute trap states, which is in line with the enlarged crystallite sizes. The reduced defect density

with NHE was also confirmed from space charge limited current (SCLC) measurements of the films (**Figure A6.16**), where the trap filling voltage (V_{TFL}) was gradually decreased from 0.618 to 0.445 to 0.415 to 0.332 V for the control, 1P, 3P, and 3F, respectively. Correspondingly, the estimated defect density of the films was significantly decreased from 1.08×10^{16} cm^{-3} for the control film to 5.80×10^{15} cm^{-3} for the 3F film. Moreover, the significantly elongated τ_2s from 32.0 ns of the control film to 1212.6 ns for 1P, 1509.1 ns for 3P, and 1862.1 ns for 3F is indicative of much longer charge carrier lifetimes in the bulk perovskite[30]. From the absorption and ultraviolet photoelectron spectroscopy (UPS) measurements, we found that $FPEA_2PbI_4$ forms a more ideal type I band alignment with larger energy offsets of the conduction band minimum (CBM) and valence band maximum (VBM) with respect to that of α-$FAPbI_3$, in comparison to the case with PEA_2PbI_4 (**Figure A6.17, 18**). This will more effectively repulse the carriers from the defective grain boundaries to elongate the carrier lifetime [15]. Consequently, the average PL lifetime (τ_{avg}) of the control film was significantly elongated from 20.6 ns to 750.8 ns for 1P, 1090.7 ns for 3P, and 1613.6 ns for 3F.

6.4 Proof-of-concept devices

This NHE approach to grow a high-quality α-$FAPbI_3$ film was not limited by substrate choice. Indeed, it can be replicated on different substrates such as glass, ITO, polyethylene naphthalate (PEN), SnO_2, fluorine-doped tin oxide (FTO), and silicon (**Figure A6.19**), which demonstrates its universality and applicability to be used for different device applications. We fabricated proof-of-concept solar cell and LED devices to show the versatility of the high-quality NHE-$FAPbI_3$ films. The thickness of the NHE-$FAPbI_3$ film is readily controlled in the range of few tenths of nanometers as demonstrated in **Figure A6.20**, facilitating optimization of device performance. It should be noted that our devices are altogether MA-free (including no MACl for crystallization control), Cs-free, Rb-free, and Br-free in the perovskite composition, which is beneficial to retain the inherently low bandgap of $FAPbI_3$ and operational stability of the devices.[31-33] **Figure 6.4a** shows schematics of the device structure and cross-sectional scanning electron microscopy (SEM) images of the solar cell device based on the NHE film (3F film). The large, single-crystalline grain size of the perovskite film perpendicular to the device direction is visible from the cross-sectional image. Current density-voltage (*J*-*V*) curves of the solar cell devices are shown in **Figure 6.4b**, and the photovoltaic parameters are summarized in **Table 1**. The device based on the control film showed a short-circuit current density (J_{SC}) of 23.69 mA/cm^2, open-

circuit voltage (V_{OC}) of 1.040 V, and fill factor (FF) of 0.649, corresponding to a power conversion efficiency (PCE) of 15.99%. Based on the NHE film, the PCE was significantly improved to 21.64% (35.3% improvement) with a J_{SC} of 24.93 mA/cm^2, V_{OC} of 1.101 V, and FF of 0.788. The measured PCE is competitive relative to previously reported devices based on MA-free, or MA- and Br-free perovskite compositions (**Table B6.5**). The improved J_{SC} was correlated with the improved external quantum efficiency (EQE) of the device, where the integrated J_{SC}s were calculated to be 21.55 and 24.07 mA/cm^2 for the control and NHE devices, respectively. The steady-state PCEs (SSPCEs) of the control and NHE devices were measured to be 15.12% and 20.87%, respectively (Inset of **Figure 6.4b**). The higher shunt resistance and lower series resistance of the device with 3F film calculated from the dark current measurement were correlated with the improvement in FF, whereas the lower ideality factor and saturation current were indicative of reduced non-radiative charge carrier recombination (**Figure A6.21**) [34], which contributed to the improved V_{OC} [35]. The LED with the NHE film as the emitting layer (EML) also demonstrated largely improved electroluminescent characteristics compared to the control device (**Figure 6.5d, e**). The normalized electroluminescence spectra of the devices based on the control and NHE films were almost identical (inset of **Figure 6.5d**), whereas the NHE device showed much greater radiance over the whole operating voltage range. The maximum radiance of the device substantially increased from ~70.78 W sr^{-1} m^{-2} for the control device to ~187.7 W sr^{-1} m^{-2} by using the NHE EML (165.2% improvement). The lower current density of the 3F device than that of the control is due to more effective charge blocking within the NHE EML, enabled by the grain boundary layered perovskite formation. (**Figure A6.22**). Consequently, the NHE LED device had a largely improved EQE, reaching ~8.28% at a low operating voltage (2.2 V), which is more than seven-fold enhanced compared to that of the control device (~1.11% at 2.4 V). The considerable performance enhancements for both the solar cell and LED devices can be mainly attributed to enhanced crystallinity and thus lower defect density of the perovskite films, which resulted in the suppressed non-radiative recombination of the charge carriers, which promoted effective charge carrier collection and enhanced radiative recombination in the solar cells and LEDs, respectively. Also, the grain boundary layered perovskite forming a type-I band alignment would additionally help to repulse the photo-generated or injected charge carriers from the defective grain boundaries, which will be helpful for the performance of both solar cells and LEDs.

The operational stabilities of the solar cells and LED devices were evaluated in **Figure 6.4f** and **G**, respectively. The stability of the solar cells was tested under 1 sun illumination (no UV filter) at open-circuit condition, where a more accelerated degradation is expected compared to the case of biasing the device at its actual maximum power point due to the stronger built-in potential and increased charge carrier recombination in the device [36]. Rapid initial decays in the SSPCEs of 20.3% and 8.6% were observed for the control and NHE devices, respectively. After the initial decay, a slower decay with an almost linear profile followed. After 650 h of continuous illumination, the SSPCE of the control device degraded to 63.4% of its initial value, while the NHE device retained 84.2% of its initial SSPCE. The T80 lifetimes (time at which the SSPCE degrades to 80% of its initial value) of the devices were then estimated with the assumption that the linear degradation profile is maintained. The T80 lifetime for the control device was estimated to be 733.4 h, and was significantly enhanced by 178% to 2040.4 h for the device based on the NHE film. To evaluate the operational stability of the LEDs, the radiance evolutions of the devices were recorded under a constant-voltage operation (constant voltage that initially emits radiance ~10 W sr^{-1} m^{-2}). The LED device based on the NHE film also showed a highly elongated lifetime as shown in **Figure 6.5g**. The T50 lifetime (time at which the radiance degrades to 50% of its initial value) of the devices was significantly enhanced from 5.7 min for the control device to 1042.4 min for the NHE device, respectively. Noting that the active migration of ionic defects in the perovskite is mainly responsible for degradation of the devices under operational conditions [37-40], we speculate that the higher crystallinity with lower defect density of the NHE films is the origin of the improved operational stabilities of the solar cells and LED devices. From temperature-dependent conductivity measurements in **Figure A6.23**, the activation energy for ion migration in the NHE films was determined to be 1.435 eV, which is much higher than that measured for the control films (0.516 eV), correlating with the retarded degradation dynamics. The much higher activation energy for ion migration in the NHE film can be attributed to significantly enhanced crystallinity and reduced defect density. We believe our approach will provide new insights to innovatively reduce the defect density in thin films of perovskite and other semiconducting materials using a simple, cheap and versatile method to further improve the stability and performance of the devices.

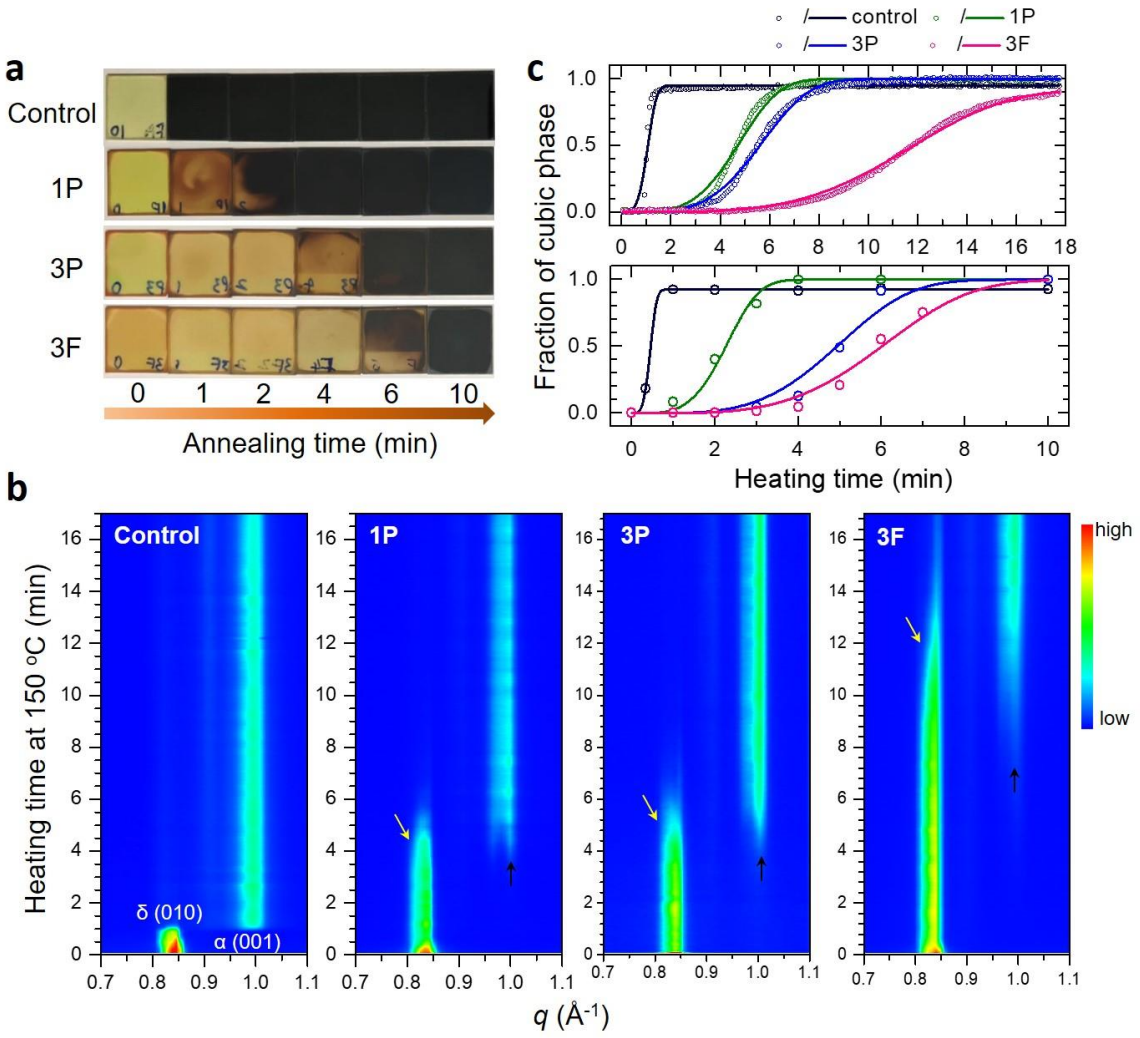

Figure 6.1. Phase conversion kinetics of formamidinium lead tri-iodide ($FAPbI_3$) perovskite with a hetero-interface at the grain boundaries. a, Photographs of $FAPbI_3$ films on SnO_2-coated ITO substrates with different annealing times at 150 °C. Control: bare $FAPbI_3$, 1P: $FAPbI_3$ with 1.67 mol% PEA_2PbI_4, 3P: $FAPbI_3$ with 3.33 mol% PEA_2PbI_4, and 3F: $FAPbI_3$ with 3.33 mol% $FPEA_2PbI_4$. **b**, *In-situ* grazing incident wide angle X-ray scattering (GIWAXS) measurements of corresponding films deposited on silicon wafer substrates. **c**, Isothermal transformation diagrams showing the evolution of the α-$FAPbI_3$ phase proportion in the films as a function of annealing time at 150 °C on silicon wafers (upper panel) and on SnO_2-coated ITO substrates (lower panel).

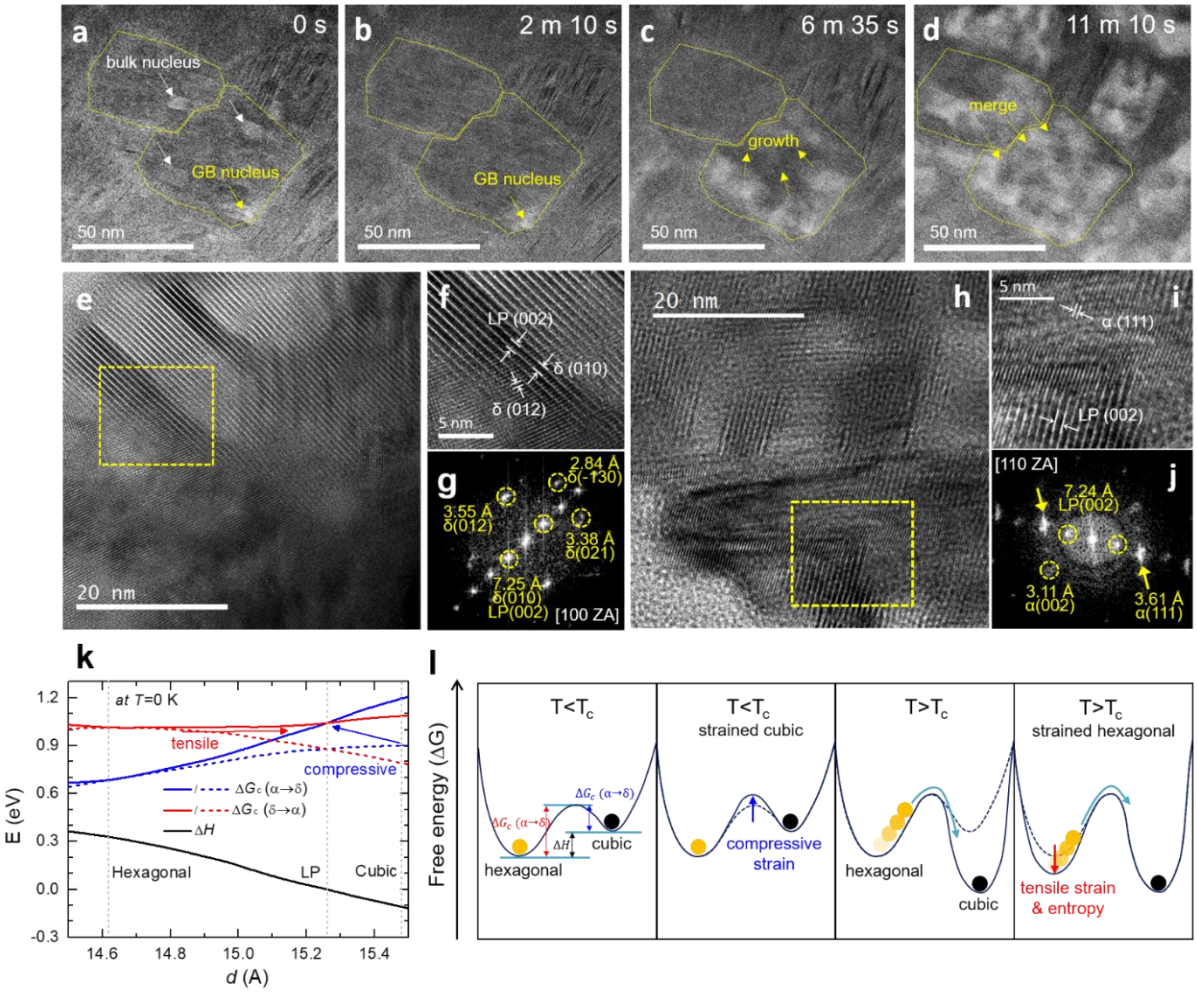

Figure 6.2. Transmission electron microscopy (TEM) images and density functional theory (DFT) calculations. a-d, *In-situ* TEM images of the δ-$FAPbI_3$ film annealed at the phase conversion temperature for different times. The relatively bright spots are the cubic phase nuclei transformed from the hexagonal phase. High-resolution TEM images of $FAPbI_3$ films incorporated with 3.33 mol% $FPEA_2PbI_4$ **e**, **f**, before and **h**, **i**, after the phase conversion process. **f** and **i** show magnified TEM images of the regions highlighted with yellow dashed boxes in **e** and **h**, respectively. **g** and **j** show corresponding fast Fourier transform (FFT) analysis of images **f** and **i**, respectively. Figure 6.2e-j are from samples prepared by scratching off the films from the substrate. **k**, DFT-calculated free energy barriers (ΔG_cs) for phase conversion from cubic to hexagonal (α→δ), from hexagonal to cubic (δ→α), and formation enthalpy of the cubic phase (ΔH) with respect to that of the hexagonal phase. Dashed lines and solid lines indicate ΔG_c without and with strain, respectively. The interlayer spacing of the strain-free hexagonal phase, layered perovskite and cubic phase are indicated with

gray colored dashed vertical lines (d-spacings of DFT optimized structures). **l**, Schematic free energy diagrams for the hexagonal and cubic phased $FAPbI_3$ at different temperatures and strain condition. T is temperature and T_c is the temperature for phase conversion.

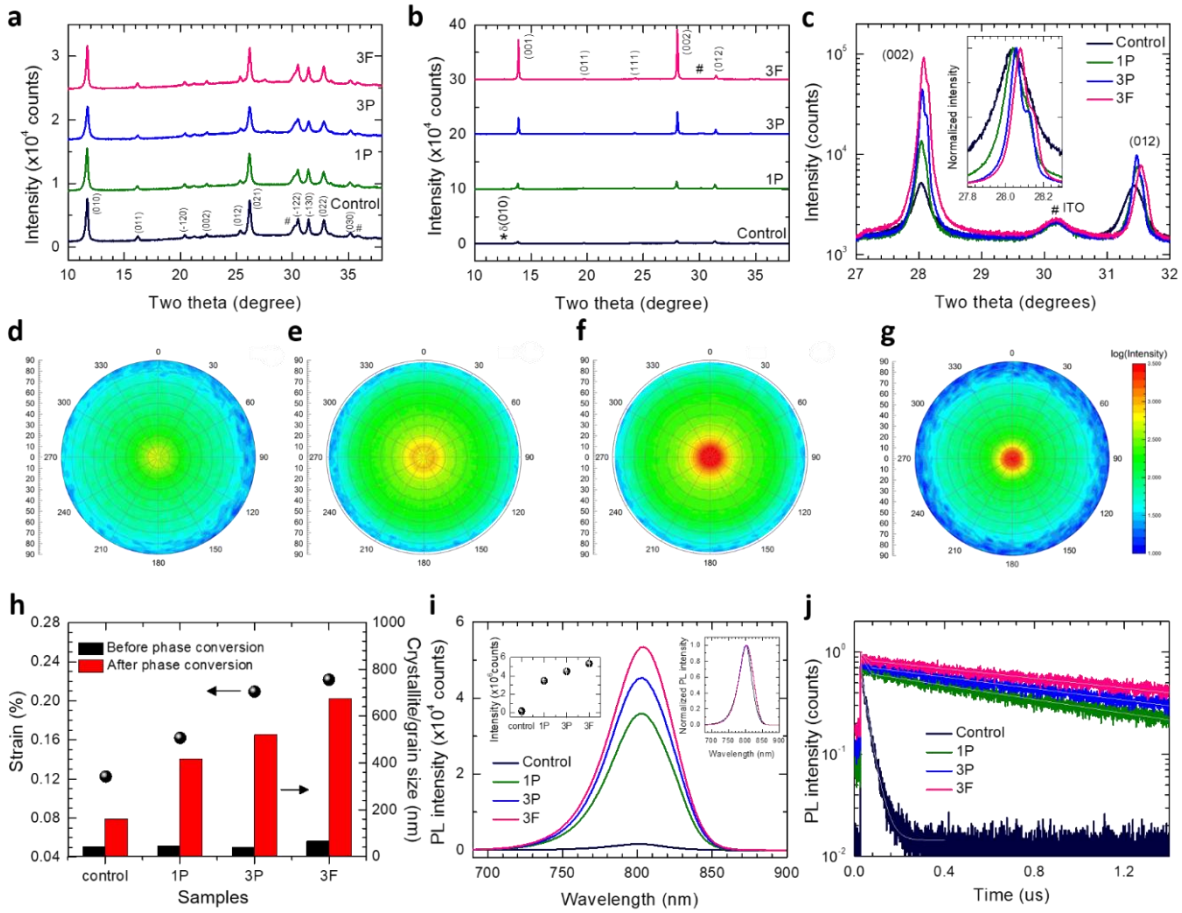

Figure 6.3. Crystallographic analyses before and after the phase conversion. X-ray diffraction (XRD) patterns of the films **a**, before and **b**, after the phase conversion process. **c**, High-resolution X-ray diffraction (XRD) patterns of the films after the phase conversion process. Inset shows the normalized (002) orientation peaks. **d**-**g**, XRD pole figure measurements along the (001) orientation of the **d**, control, **e**, 1P, **f**, 3P, and **g**, 3F films **h.** Composition-dependent strain before phase conversion and crystallite size of the films before and after the phase conversion process. The strain was calculated using the Williamson-Hall method from δ-$FAPbI_3$ films. The δ-$FAPbI_3$ crystallite sizes were calculated by the Williamson-Hall method, while the α-$FAPbI_3$ crystallite sizes were extracted from the AFM images. **i**, Steady-state photoluminescence (PL) and **j**, time-resolved PL decay profile measurements of the corresponding films. Insets of I show peak intensity

(left) and normalized PL spectra (right).

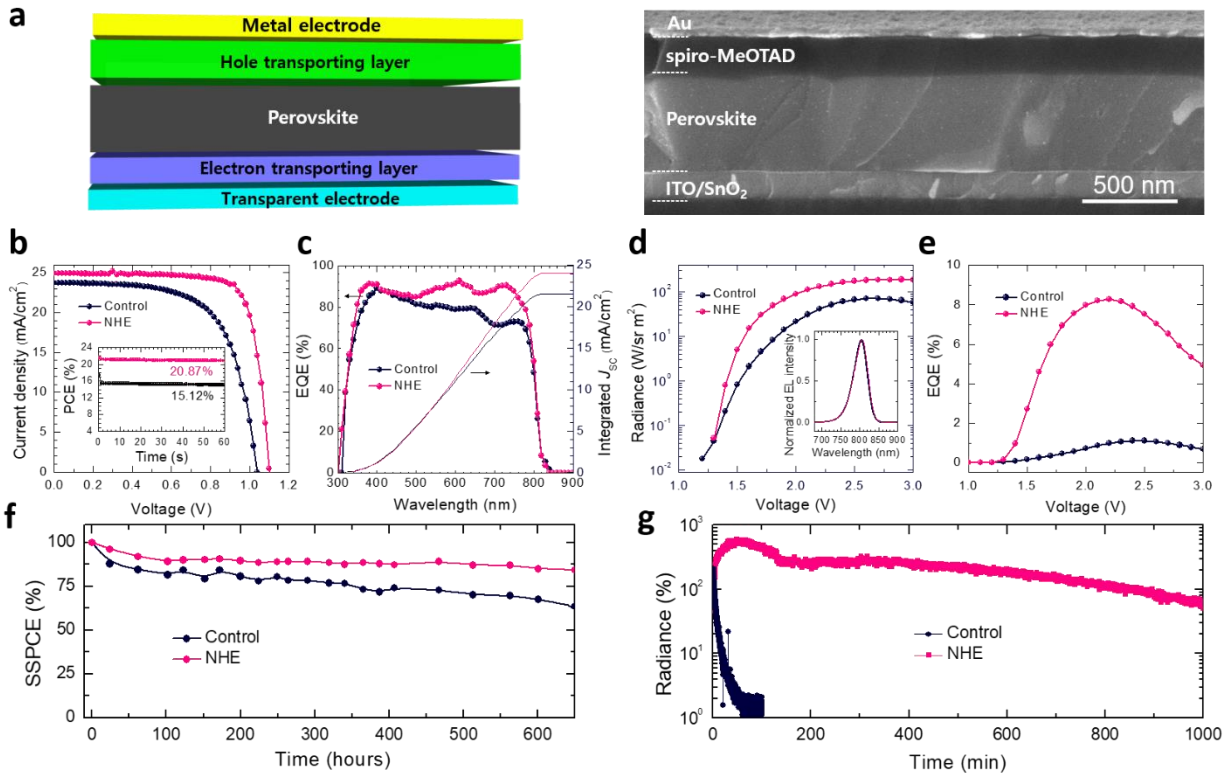

Figure 6.4. Proof-of-concept devices. a, Device structure schematics and corresponding cross-sectional scanning electron microscopy (SEM) images of the solar cell devices based on the $FAPbI_3$ film with nano heteroepitaxy (NHE, with 3.33 mol% $FPEA_2PbI_4$). **b**, Current density-voltage (J-V) and **c**, external quantum efficiency (EQE) curves of solar cell devices based on a bare $FAPbI_3$ film (control) and a $FAPbI_3$ film with NHE. Inset of **b** shows steady-state power conversion efficiencies (SSPCEs) measured at maximum power points. **d**, Voltage-radiance curves of the light emitting diode (LED) devices, and **e**, corresponding EQE curves of the LED devices based on the control and NHE films. Inset of **d** shows the electroluminescence spectra of the LED devices. Operational stability measurements of the **f**, solar cell (normalized SSPCE) and **g**, LED devices (normalized radiance) based on the control and NHE films.

Table 6.1. Measured performance parameters of perovskite solar cells and light-emitting diodes based on the control and NHE films. Short-circuit current density (J_{SC}), open-circuit voltage (V_{OC}), fill factor (FF), and power conversion efficiency (PCE) of the solar cells. Maximum radiance and external quantum efficiency (EQE) of the light-emitting diodes. The PCE values in parenthesis

are steady-state PCEs measured at maximum power points. The T80 and T50 lifetimes of the solar cells and light-emitting diodes were extracted from Figure 6.4f, g, respectively.

	Solar Cells					Light-emitting Diodes		
	J_{SC} (mA/cm^2)	V_{OC} (V)	FF	PCE (%)	T80 lifetime (h)	Maximum Radiance (W/sr m^2)	Maximum EQE (%)	T50 lifetime (min)
Control	23.69	1.040	0.649	15.99 (15.12)	726.3	70.78	1.11	5.7
NHE	24.93	1.101	0.788	21.64 (20.87)	2025.6	187.7	8.28	1042.4

References

1 Stringfellow, G. Epitaxy. *Rep. Prog. Phys.* **45**, 469 (1982).

2 Meyerson, B. S. Low-temperature silicon epitaxy by ultrahigh vacuum/chemical vapor deposition. *Appl. Phys. Lett.* **48**, 797-799 (1986).

3 Waltereit, P. *et al.* Nitride semiconductors free of electrostatic fields for efficient white light-emitting diodes. *Nature* **406**, 865 (2000).

4 Yoon, J. *et al.* GaAs photovoltaics and optoelectronics using releasable multilayer epitaxial assemblies. *Nature* **465**, 329 (2010).

5 Berger, C. *et al.* Electronic confinement and coherence in patterned epitaxial graphene. *Science* **312**, 1191-1196 (2006).

6 Shim, J. *et al.* Controlled crack propagation for atomic precision handling of wafer-scale two-dimensional materials. *Science* **362**, 665-670 (2018).

7 Walsh, A., Scanlon, D. O., Chen, S., Gong, X. & Wei, S. H. Self-regulation mechanism for charged point defects in hybrid halide perovskites. *Angew. Chem. Int. Ed.* **54**, 1791-1794 (2015).

8 Kelso, M. V., Mahenderkar, N. K., Chen, Q., Tubbesing, J. Z. & Switzer, J. A. Spin coating epitaxial films. *Science* **364**, 166-169, doi:10.1126/science.aaw6184 (2019).

9 Chen, Y. *et al.* Strain engineering and epitaxial stabilization of halide perovskites. *Nature* **577**, 209-215 (2020).

10 Jiang, J. *et al.* Carrier lifetime enhancement in halide perovskite via remote epitaxy. *Nat. Commun.* **10**, 1-12 (2019).

11 Shi, E. *et al.* Two-dimensional halide perovskite lateral epitaxial heterostructures. *Nature* **580**, 614-620 (2020).

12 Lee, J.-W. *et al.* A Bifunctional Lewis Base Additive for Microscopic Homogeneity in Perovskite Solar Cells. *Chem* **3**, 290-302 (2017).

13 Im, J.-H., Jang, I.-H., Pellet, N., Grätzel, M. & Park, N.-G. Growth of CH3NH3PbI3 cuboids with controlled size for high-efficiency perovskite solar cells. *Nat. Nanotech.* **9**, 927-932 (2014).

14 Lee, J.-W. *et al.* 2D perovskite stabilized phase-pure formamidinium perovskite solar cells. *Nature communications* **9**, 1-10 (2018).

15 Wang, Z. *et al.* Efficient ambient-air-stable solar cells with 2D–3D heterostructured butylammonium-caesium-formamidinium lead halide perovskites. *Nature Energy* **2**, 17135 (2017).

16 Han, T. H. *et al.* Surface-2D/Bulk-3D Heterophased Perovskite Nanograins for Long-Term-Stable Light-Emitting Diodes. *Advanced Materials* **32**, 1905674 (2020).

17 Min, H. *et al.* Efficient, stable solar cells by using inherent bandgap of α-phase formamidinium lead iodide. *Science* **366**, 749-753 (2019).

18 Lee, J. W., Seol, D. J., Cho, A. N. & Park, N. G. High-efficiency perovskite solar cells based on the black polymorph of HC (NH2) 2PbI3. *Adv. Mater.* **26**, 4991-4998 (2014).

19 Chen, T. *et al.* Entropy-driven structural transition and kinetic trapping in formamidinium lead iodide perovskite. *Sci. Adv.* **2**, e1601650 (2016).

20 Lee, J.-W. *et al.* 2D perovskite stabilized phase-pure formamidinium perovskite solar cells. *Nature Communications* **9**, 3021, doi:10.1038/s41467-018-05454-4 (2018).

21 Dou, L. *et al.* Atomically thin two-dimensional organic-inorganic hybrid perovskites. *Science* **349**, 1518-1521 (2015).

22 Kim, D. *et al.* Efficient, stable silicon tandem cells enabled by anion-engineered wide-bandgap perovskites. *Science*, eaba3433, doi:10.1126/science.aba3433 (2020).

23 Porter;, D. A., Easterling;, K. E. & Sherif;, M. Y. *Phase Transformations in Metals and Alloys*. 3 edn, (CRC Press, 1992).

24 Langford, J. I. & Wilson, A. Scherrer after sixty years: a survey and some new results in the determination of crystallite size. *J. Appl. Crystallogr.* **11**, 102-113 (1978).

25 Williamson, G. & Hall, W. X-ray line broadening from filed aluminium and wolfram. *Acta Metall.* **1**, 22-31 (1953).

26 Yadavalli, S. K., Zhou, Y. & Padture, N. P. Exceptional grain growth in formamidinium lead iodide perovskite thin films induced by the δ-to-α phase transformation. *ACS Energy Letters* **3**, 63-64 (2017).

27 Tsai, H. *et al.* High-efficiency two-dimensional Ruddlesden–Popper perovskite solar cells. *Nature* **536**, 312-316 (2016).

28 de Quilettes, D. W. *et al.* Impact of microstructure on local carrier lifetime in perovskite solar cells. *Science* **348**, 683-686 (2015).

29 Son, D.-Y. *et al.* Self-formed grain boundary healing layer for highly efficient CH3 NH3 PbI3 perovskite solar cells. *Nat. Energy* **1**, 16081 (2016).

30 Dong, Q. *et al.* Electron-hole diffusion lengths> 175 μm in solution-grown CH3NH3PbI3 single crystals. *Science* **347**, 967-970 (2015).

31 Lee, J. W. *et al.* Formamidinium and cesium hybridization for photo-and moisture-stable perovskite solar cell. *Advanced Energy Materials* **5**, 1501310 (2015).

32 Turren-Cruz, S.-H., Hagfeldt, A. & Saliba, M. Methylammonium-free, high-performance, and stable perovskite solar cells on a planar architecture. *Science* **362**, 449-453 (2018).

33 Syzgantseva, O. A., Saliba, M., Grätzel, M. & Rothlisberger, U. Stabilization of the perovskite phase of formamidinium lead triiodide by methylammonium, Cs, and/or Rb doping. *The journal of physical chemistry letters* **8**, 1191-1196 (2017).

34 Tress, W. *et al.* Interpretation and evolution of open-circuit voltage, recombination, ideality factor and subgap defect states during reversible light-soaking and irreversible degradation of perovskite solar cells. *Energy & Environ. Sci.* **11**, 151-165 (2018).

35 Zhao, D. *et al.* Efficient two-terminal all-perovskite tandem solar cells enabled by high-quality low-bandgap absorber layers. *Nat. Energy* **3**, 1093 (2018).

36 Domanski, K., Alharbi, E. A., Hagfeldt, A., Grätzel, M. & Tress, W. Systematic investigation of the impact of operation conditions on the degradation behaviour of perovskite solar cells. *Nat. Energy* **3**, 61 (2018).

37 Domanski, K. *et al.* Migration of cations induces reversible performance losses over day/night cycling in perovskite solar cells. *Energy & Environ. Sci.* **10**, 604-613 (2017).

38 Li, N. *et al.* Cation and anion immobilization through chemical bonding enhancement with fluorides for stable halide perovskite solar cells. *Nat. Energy* **4**, 408 (2019).

39 Yang, S. *et al.* Stabilizing halide perovskite surfaces for solar cell operation with wide-bandgap lead oxysalts. *Science* **365**, 473-478 (2019).

40 Saliba, M. Perovskite solar cells must come of age. *Science* **359**, 388-389 (2018).

41 Frisch, M. J. *et al.* Gaussian 09, Revision D. 01, Gaussian. *Inc.: Wallingford, CT* (2009).

42 Hirshfeld, F. L. Bonded-atom fragments for describing molecular charge densities. *Theor. Chim. Acta* **44**, 129-138 (1977).

43 Ritchie, J. P. Electron density distribution analysis for nitromethane, nitromethide, and nitramide. *J. Am. Chem. Soc.* **107**, 1829-1837 (1985).

44 Ritchie, J. P. & Bachrach, S. M. Some methods and applications of electron density distribution analysis. *J. Comput. Chem.* **8**, 499-509 (1987).

45 Singh, U. C. & Kollman, P. A. An approach to computing electrostatic charges for molecules. *J. Comput. Chem.* **5**, 129-145 (1984).

46 Besler, B. H., Merz Jr, K. M. & Kollman, P. A. Atomic charges derived from semiempirical methods. *J. Comput. Chem.* **11**, 431-439 (1990).

47 Matczak, P. A test of various partial atomic charge models for computations on diheteroaryl ketones and thioketones. *Computation* **4**, 3 (2016).

48 Wiberg, K. B. & Rablen, P. R. Atomic Charges. *J. Organic Chem.* **83**, 15463-15469 (2018).

49 Dennington, R., Keith, T. & Millam, J. GaussView, version 5. *Semichem Inc.: Shawnee Mission, KS* (2009).

50 Kresse, G. & Furthmüller, J. Efficient iterative schemes for ab initio total-energy calculations using a plane-wave basis set. *Phy. Rev. B* **54**, 11169 (1996).

51 Perdew, J. P., Burke, K. & Ernzerhof, M. Generalized gradient approximation made simple. *Phys. Rev. Lett.* **77**, 3865 (1996).

52 Perdew, J. P. *et al.* Restoring the density-gradient expansion for exchange in solids and surfaces. *Phys. Rev. Lett.* **100**, 136406 (2008).

53 Grimme, S., Antony, J., Ehrlich, S. & Krieg, H. A consistent and accurate ab initio parametrization of density functional dispersion correction (DFT-D) for the 94 elements H-Pu. *The Journal of chemical physics* **132**, 154104 (2010).

Appendix A. Supplementary Figures

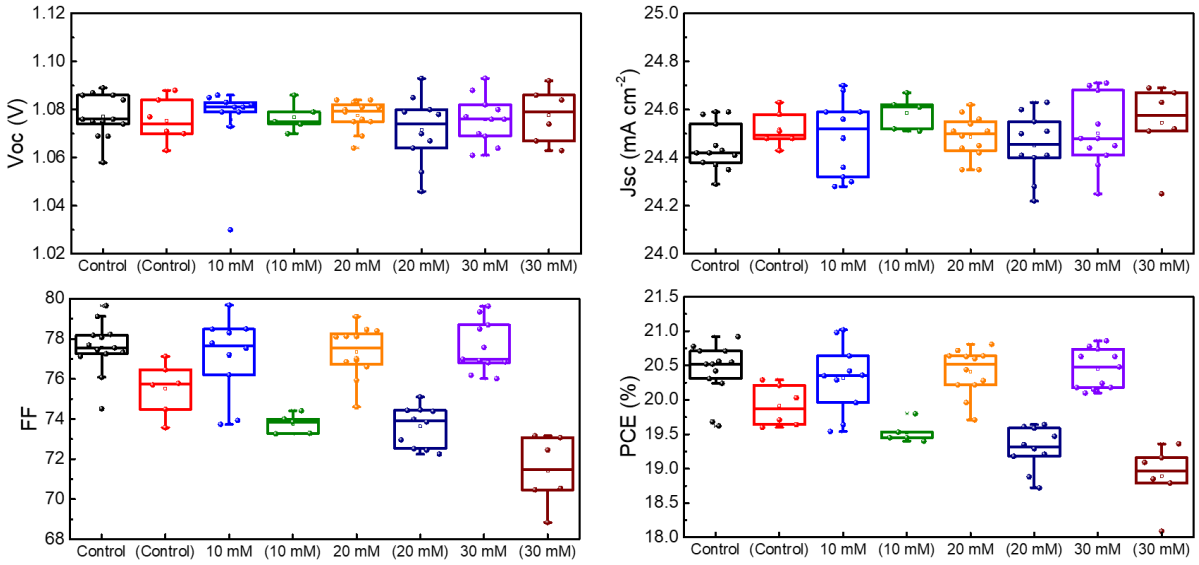

Figure A2.1. Photovoltaic parameters of control and treated devices. Box plots showing the distribution of the open-circuit voltage (V_{OC}), short-circuit current density (J_{SC}), fill factor (FF), and power conversion efficiency (PCE) of the control and treated devices. Parenthesis indicate parameters measured in forward scan.

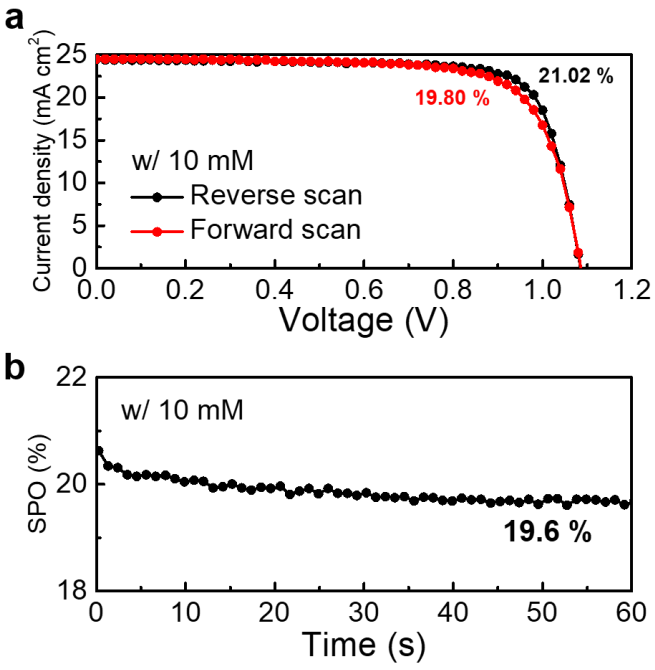

Figure A2.2. Photovoltaic performance of treated devices. a, Current density and voltage (*J-V*) curves of the champion devices in reverse (1.2 V to -0.1 V) and forward (-0.1 V to 1.2 V) scan and **b,** stabilized power output (SPO).

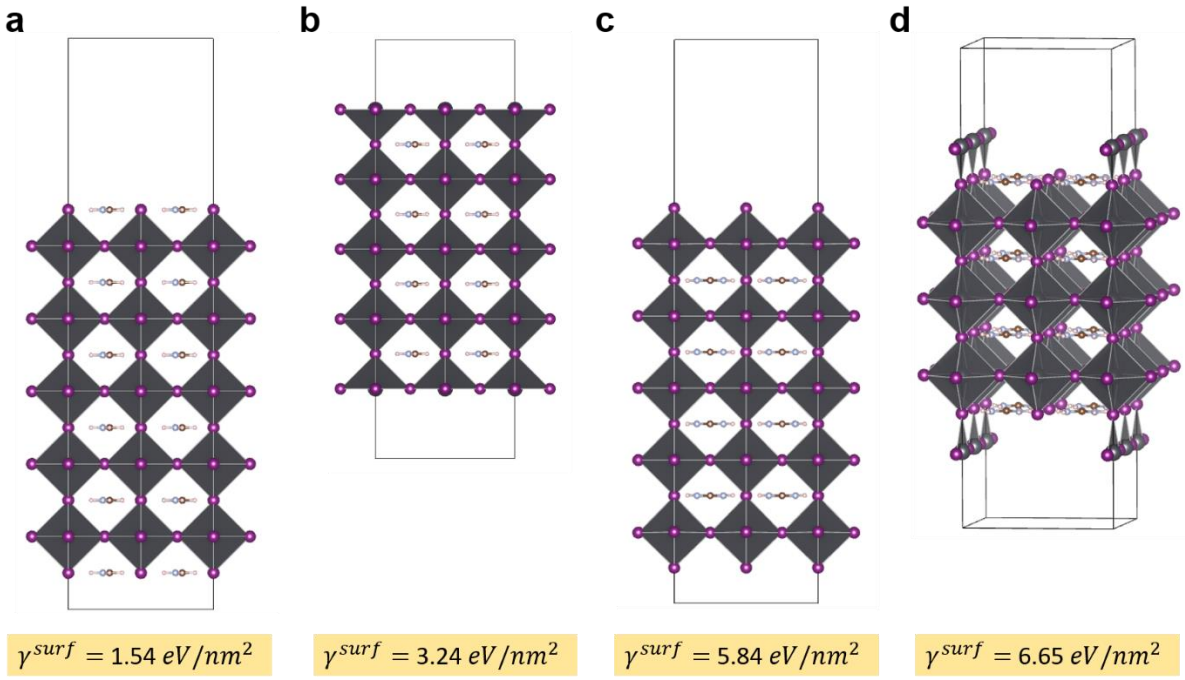

Figure A2.3. Theoretical slab models for first-principles calculations. (001) slab models of $FAPbI_3$ perovskite with **a**, FAI, **b**, PbI_2 (flat), **c**, FAI with evaporated FA, and **d**, vacant termination. Their calculated respective surface energies (γ^{surf}) are included.

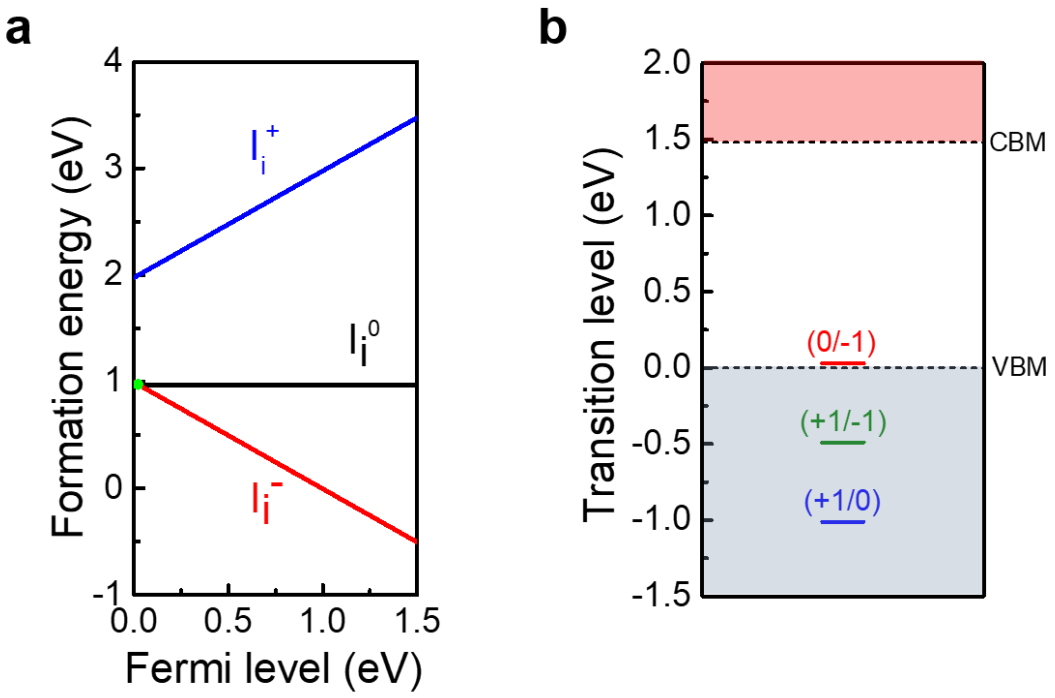

Figure A2.4. Fermi level (E_F) dependence of the surface formation energies. a, E_F dependence of the surface formation energies of neutral and charged iodine interstitial point defects. Transition levels are marked with green dots. $E_F = 0$ is set at the valence band maximum. **b**, charge transition levels of I_i in $FAPbI_3$. Red and grey shaded areas mark the conduction band and valence band, respectively.

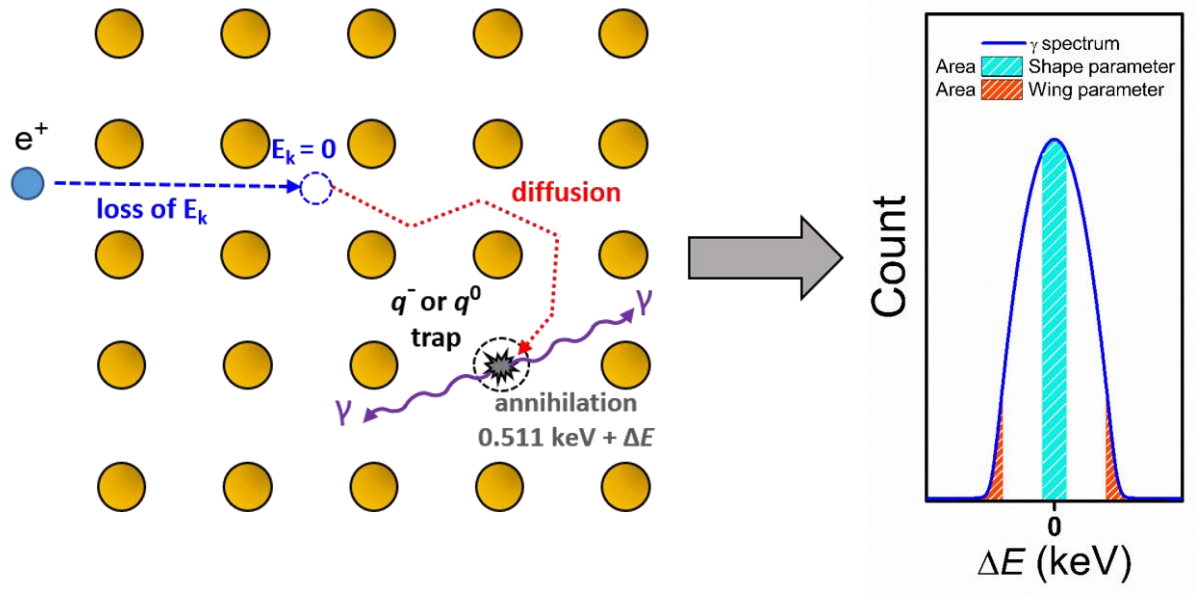

Figure A2.5. Positron Annihilation Spectroscopy (PAS). Schematic of the PAS technique.

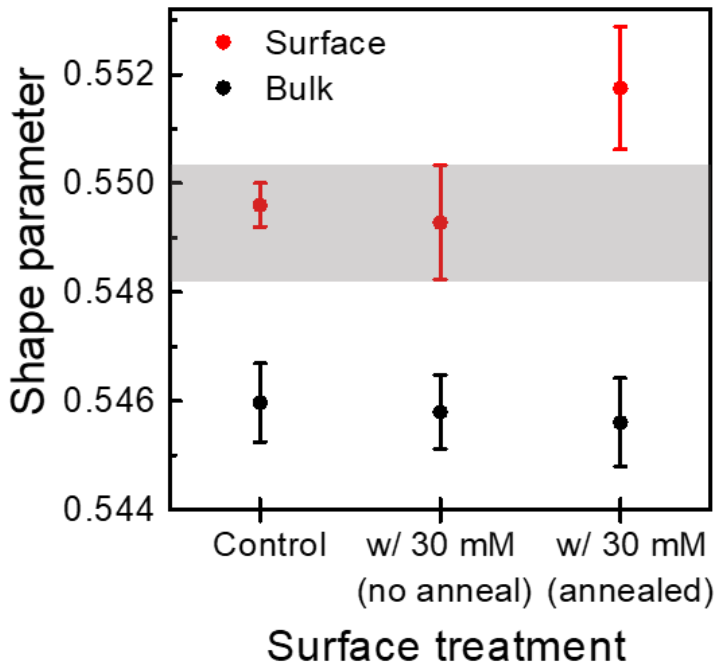

Figure A2.6. Shape parameters of the perovskite films. Surface and bulk shape parameters of the control and treated perovskite films on glass. Grey highlighted area demarcates the upper and lower bounds of the 'w/ 30 mM (no anneal)' condition.

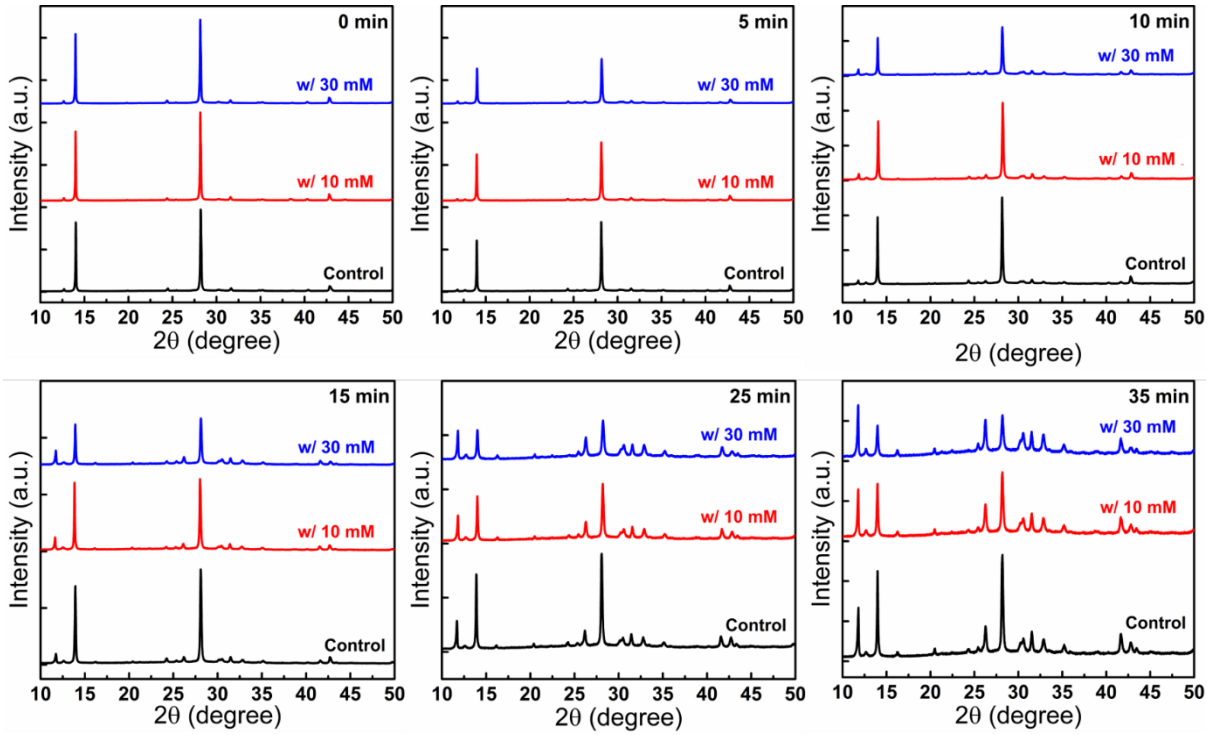

Figure A2.7. X-ray diffraction (XRD) measurements on the perovskite films. XRD diffractograms of the control and treated perovskite films after different exposure times to iodine vapour.

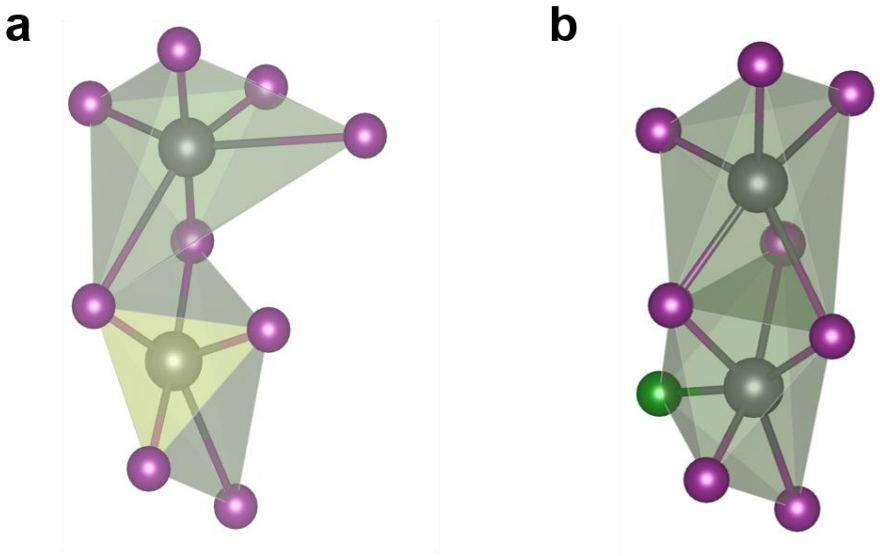

Figure A2.8. Atomic coordination structures. Transition state atomic coordination for the **a**, defect-free, and **b**, with iodine interstitial (in green) lattices. Atoms are expressed by spheres; iodine (purple), and lead (grey).

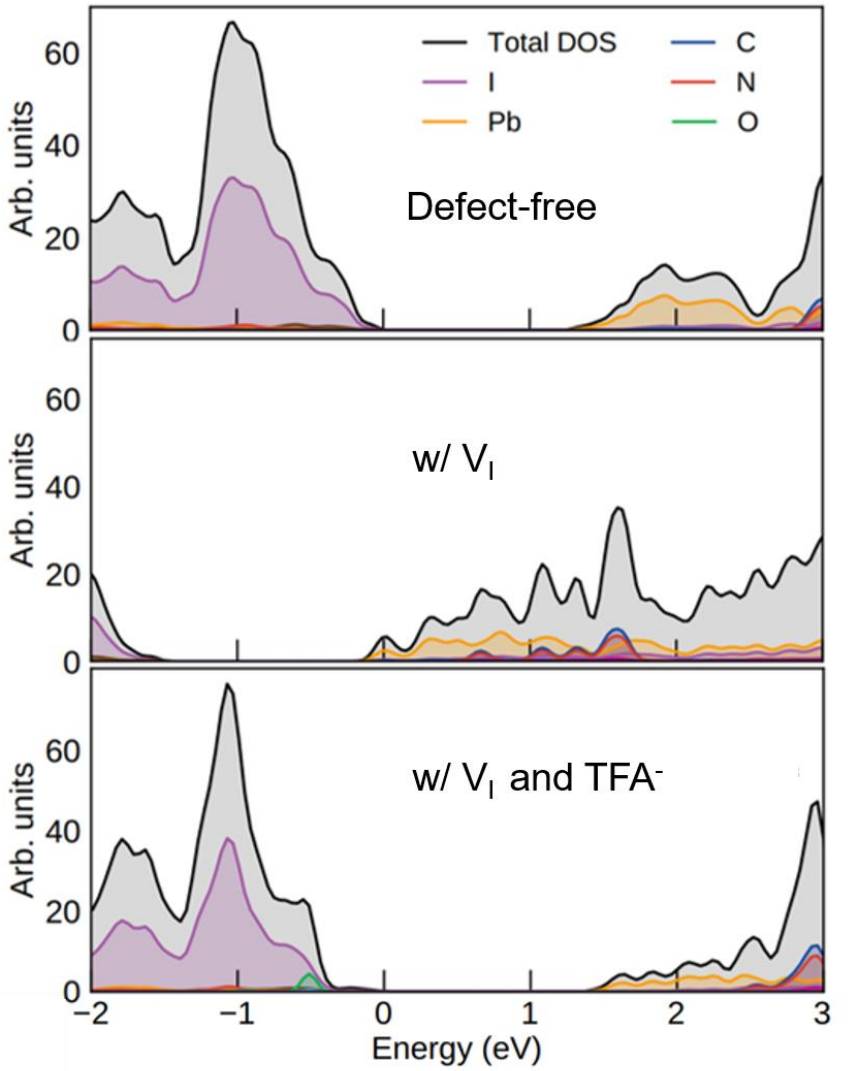

Figure A2.9. Density of states (DOS) simulated with first-principles calculations. DOS of the defect-free, defected and passivated FAI-terminated surfaces.

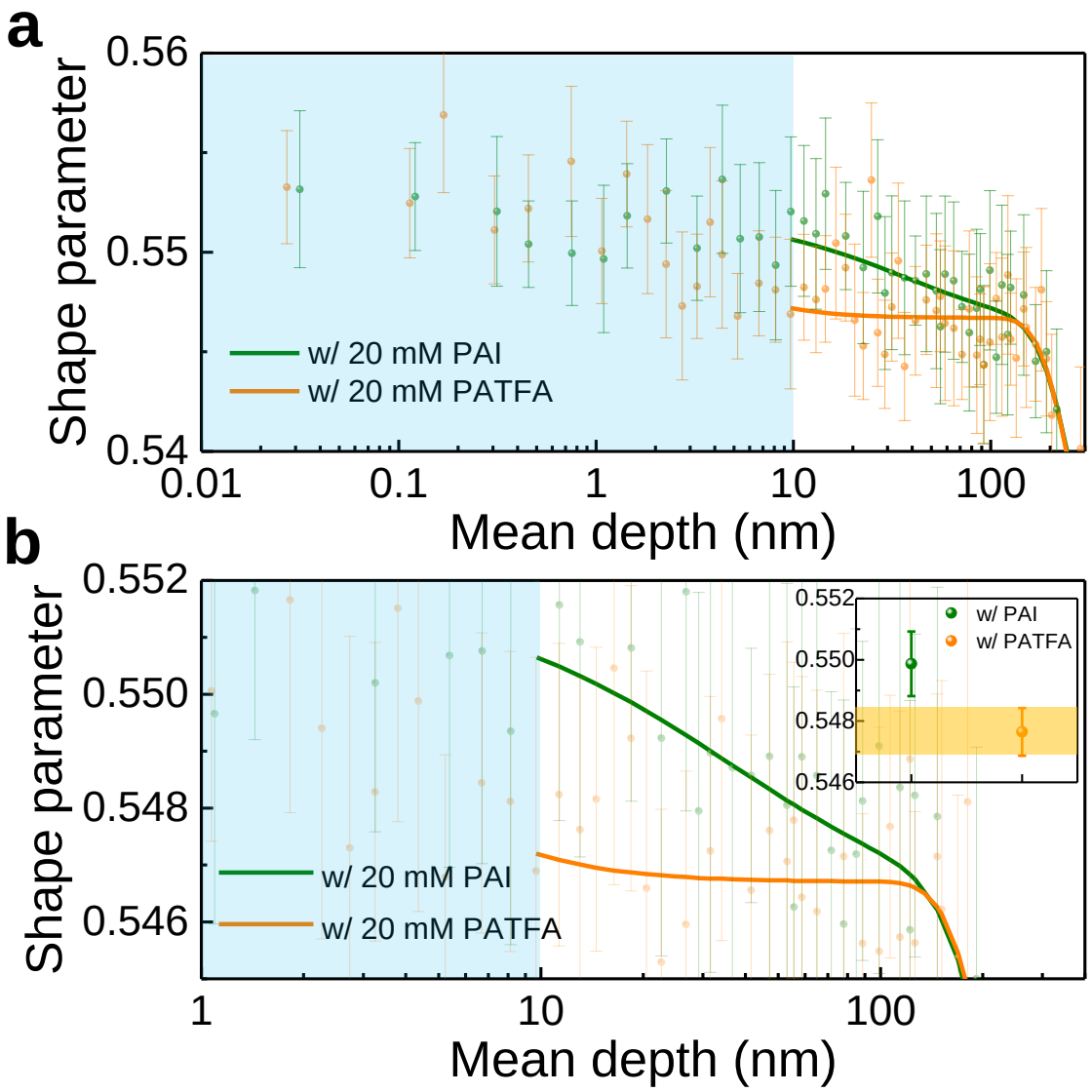

Figure A2.10. Positron Annihilation Spectroscopy on treated perovskite films. a, Shape parameter as function of depth of perovskite films on glass treated with 20 mM of either PAI or PATFA. Blue shaded area indicates assumed passivation layer thickness based on previous report.[2] Lines are fitted using dedicated software Vepfit. **b**, Magnified region of (a). Inset shows the averaged shape parameter from the raw data points from mean depth of 10 to 50 nm in a running average series. Yellow shaded area demarcate the upper and lower bounds for the film treated with PATFA.

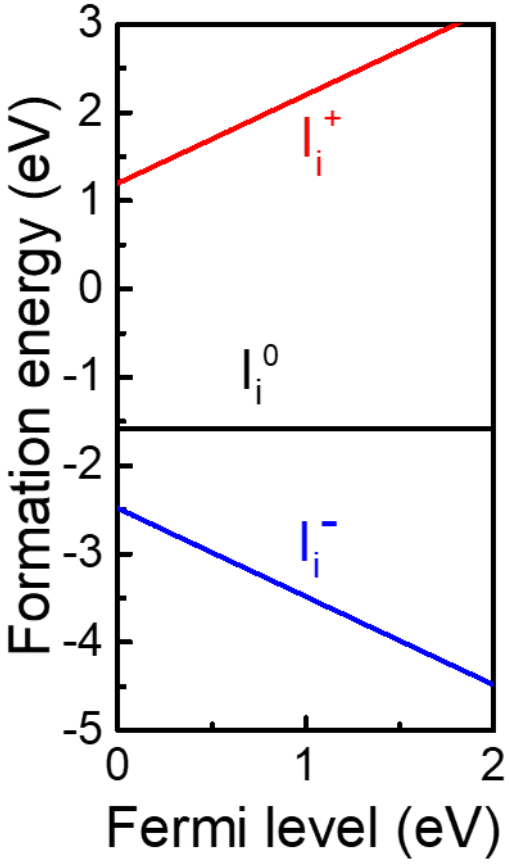

Figure A2.11. Fermi level (E_F) dependence of the surface formation energies. a, E_F dependence of the surface formation energies of neutral and charged iodine interstitial point defects, calculated for a FAI-terminated $FAPbI_3$ slab with PA^+ cation as the capping layer. $E_F = 0$ is set at the valence band maximum.

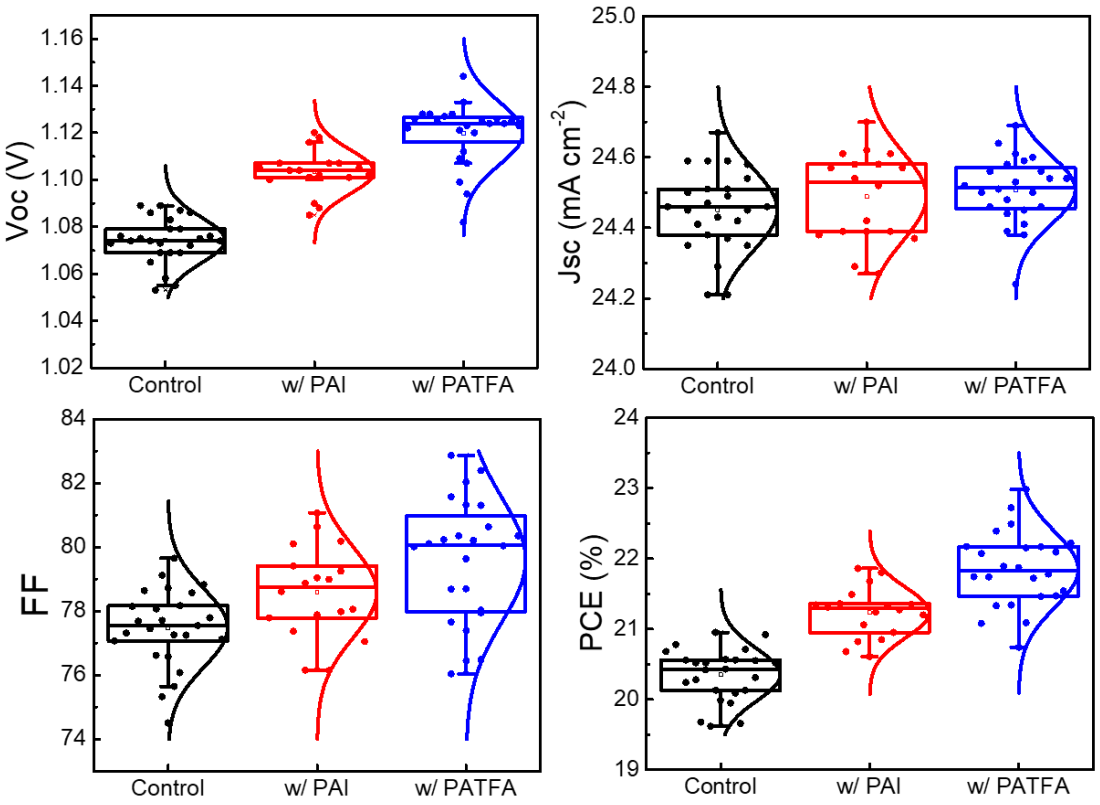

Figure A2.12. Photovoltaic parameters of control and treated devices. Box plots showing the distribution of the open-circuit voltage (V_{OC}), short-circuit current density (J_{SC}), fill factor (FF), and power conversion efficiency (PCE) of the control and treated devices.

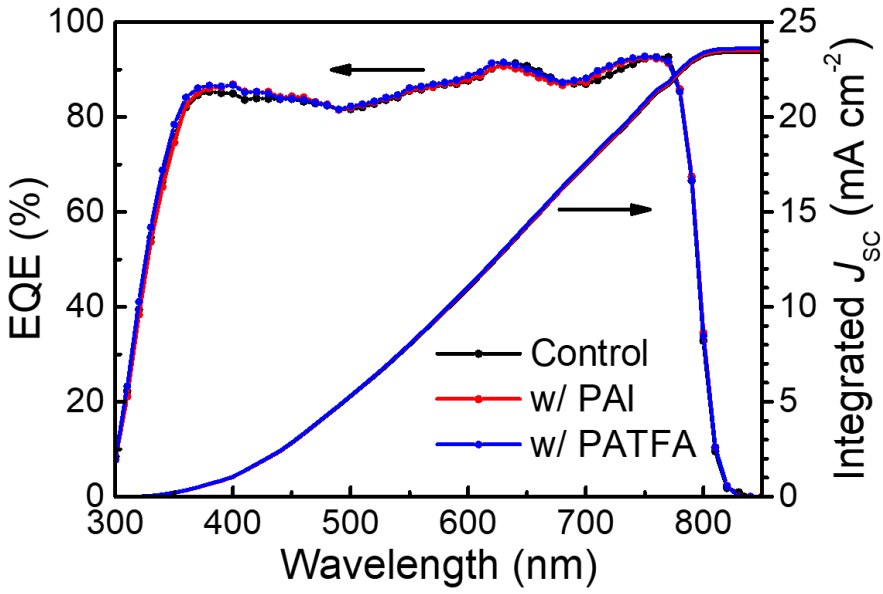

Figure A2.13. Device external quantum efficiency (EQE) spectra. EQE spectra and integrated J_{SC} of the control and treated devices.

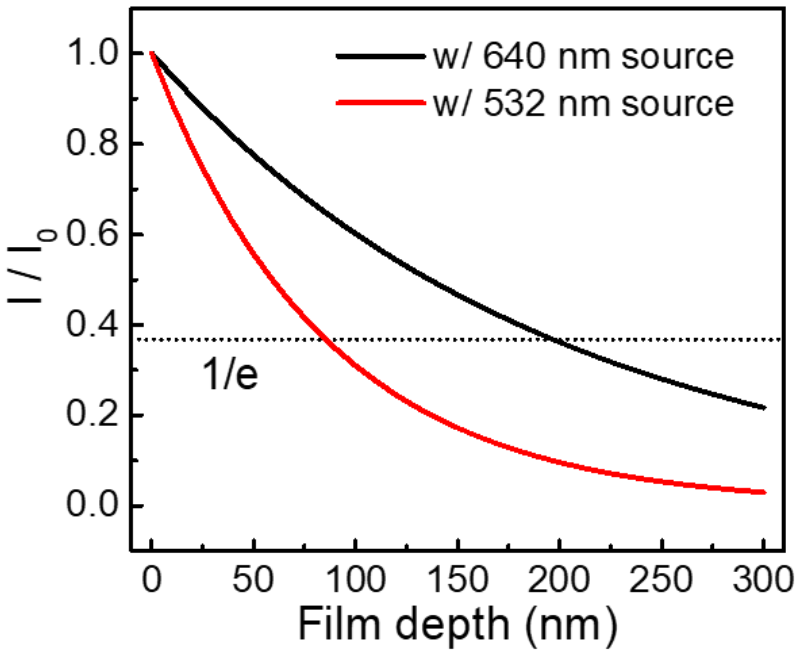

Figure A2.14. Excitation wavelength dependant penetration depth. Decay of the beam intensity according to Beer-Lambert's law with perovskite film depth with different excitation sources. The penetration depth is defined at the depth where the intensity decays to (1/e) of its initial value

(horizontal dashed line)

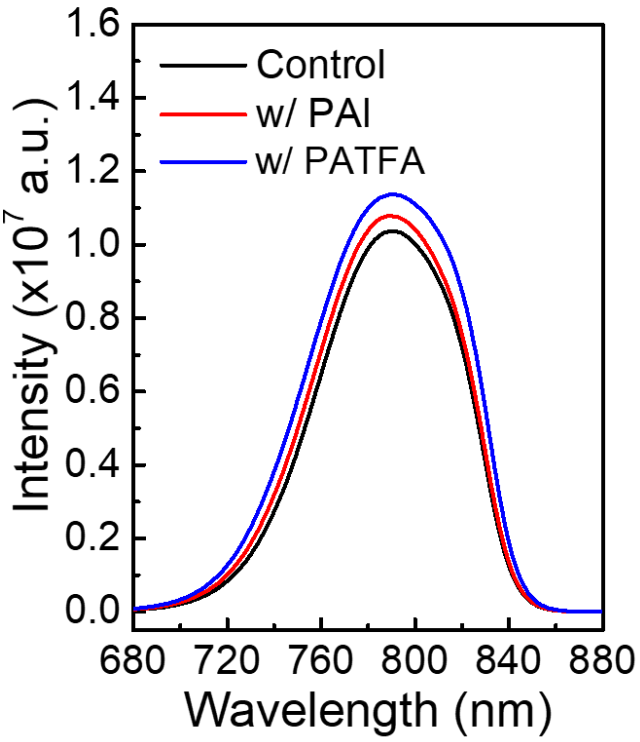

Figure A2.15. Steady-state photoluminescence (PL) spectra of the perovskite films. PL spectra of the control and treated perovskite films on glass probed with an excitation wavelength of 640 nm.

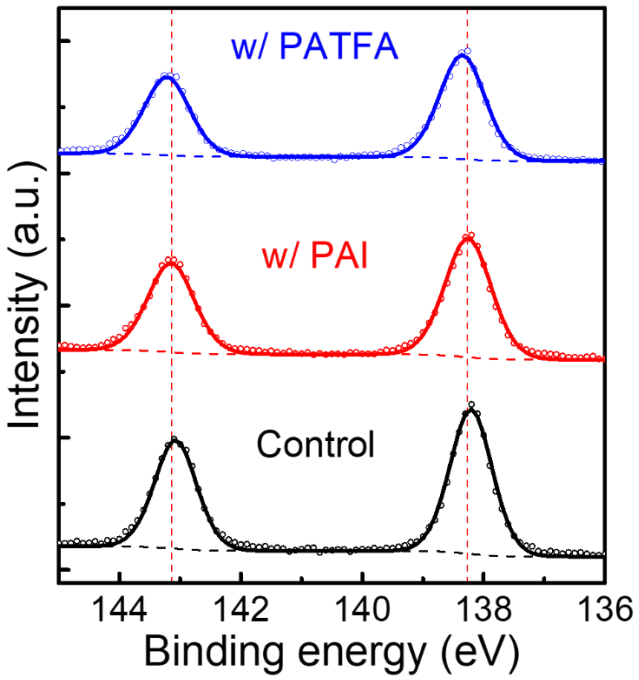

Figure A2.16. X-ray photoelectron spectroscopy (XPS) measurements on the perovskite films. High resolution XPS spectra of the Pb 4f 5/2 and Pb 4f 7/2 peaks of the control and treated perovskite films. Red vertical dashed lines demarcate the peak positions of the PAI treated film.

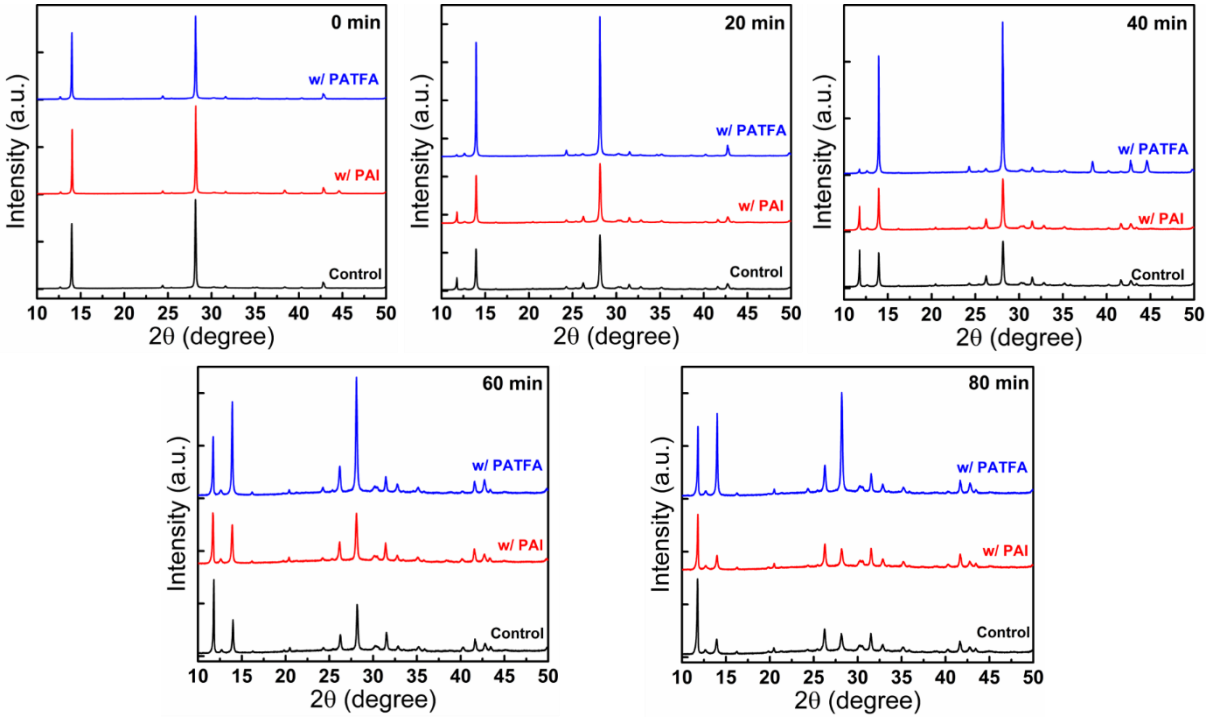

Figure A2.17. X-ray diffraction (XRD) measurements on the perovskite films. XRD diffractograms of the control and treated perovskite films after different exposure times to iodine vapour.

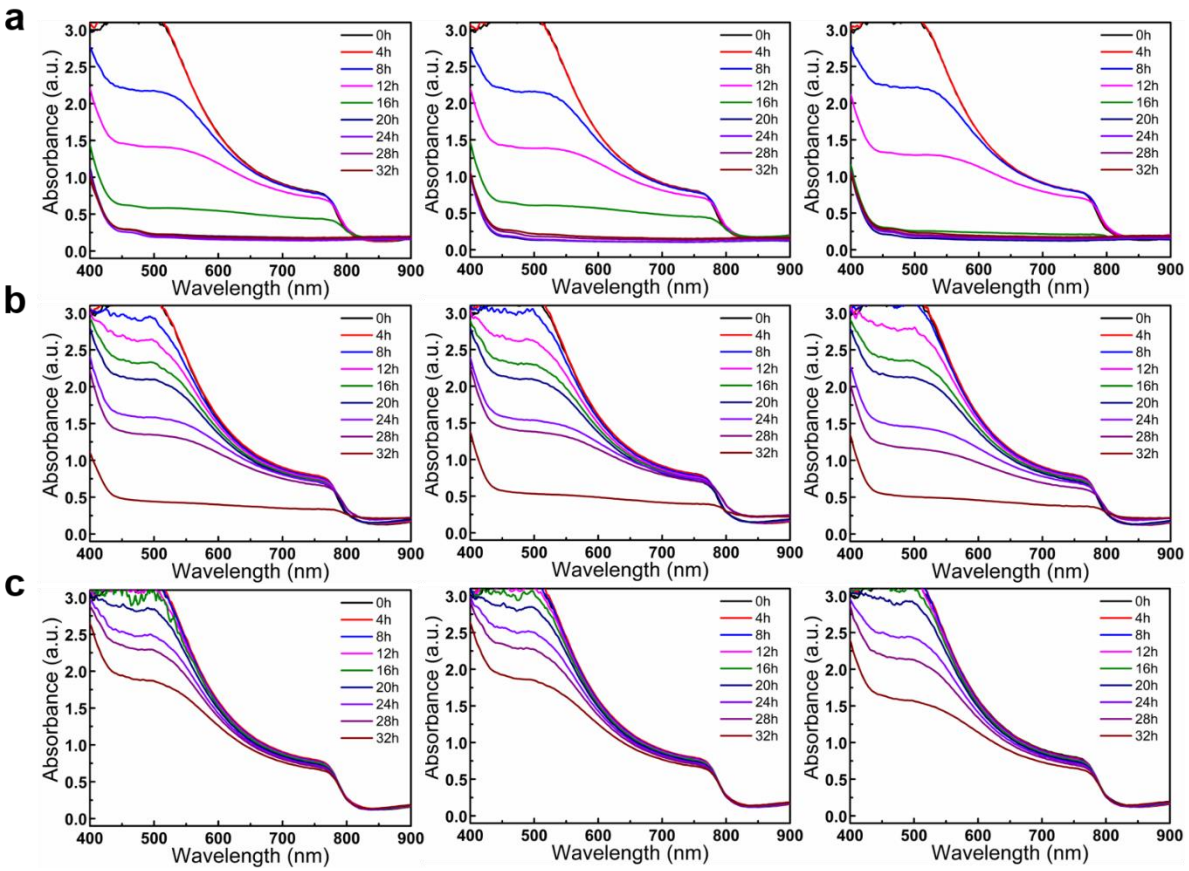

Figure A2.18. Ultraviolet-visible spectroscopy measurements on the perovskite films. a, control, **b**, w/ PAI and **c**, w/ PATFA treatment**.** Absorption spectra of the control and treated perovskite films after different exposure times to RH 75 ± 10 %.

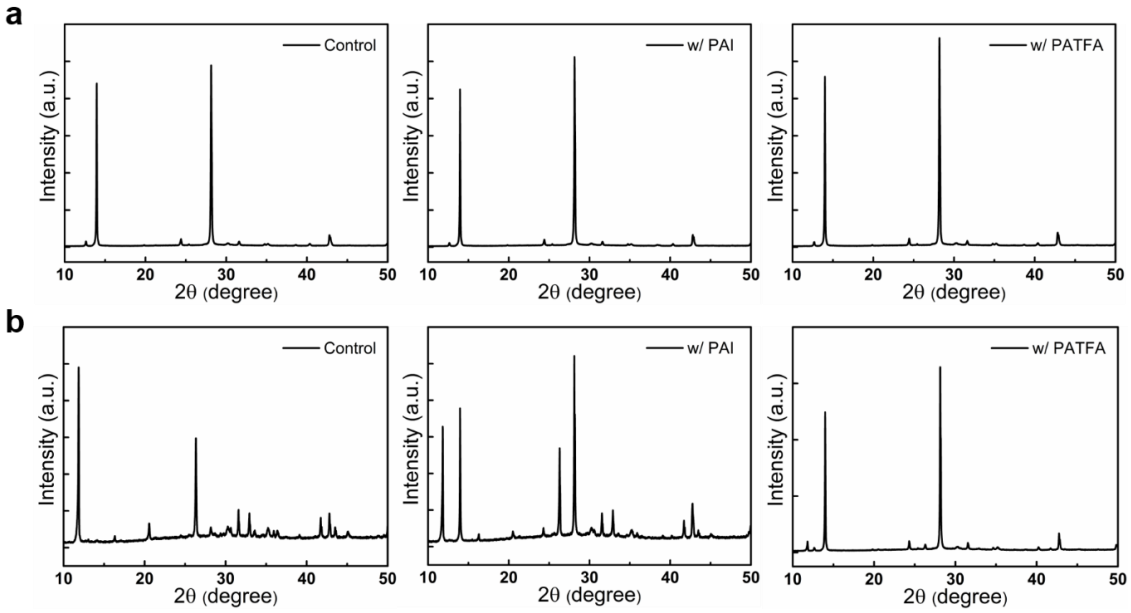

Figure A2.19. X-ray diffraction (XRD) measurements on the perovskite films. X-ray diffractograms of the control and treated perovskite films **a,** before and **b,** after exposure to RH 75 ± 10 % for 32 h.

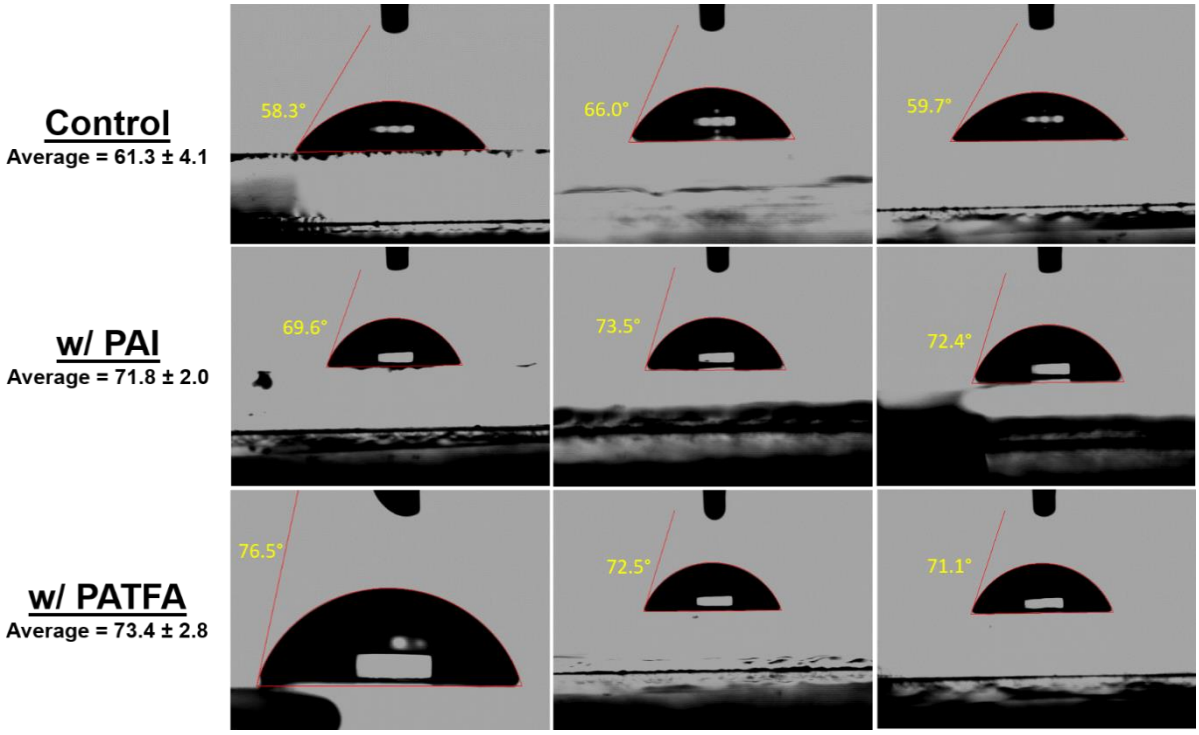

Figure A2.20. Contact angle measurements of the perovskite films. Water contact angles of the control and treated perovskite films. The averages for three films of each condition are included.

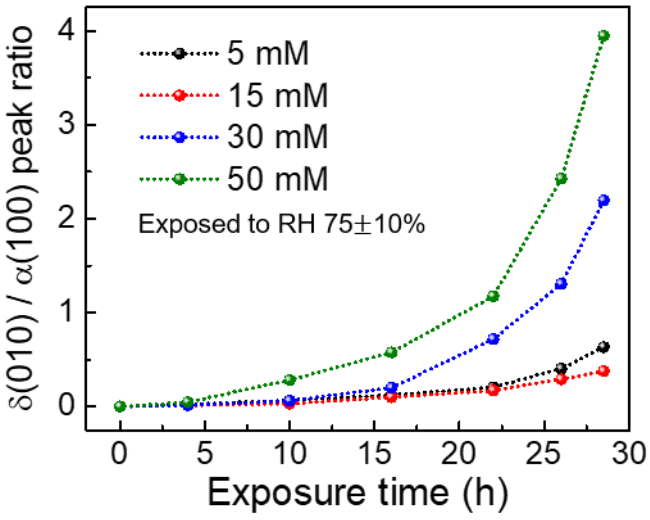

Figure A2.21. α-phase stability of films with different PAI concentration. Hexagonal δ(010)-to-cubic α(100) x-ray diffraction (XRD) peak intensity ratio of the perovskite films as a function of exposure time to RH 75 ± 10 %.

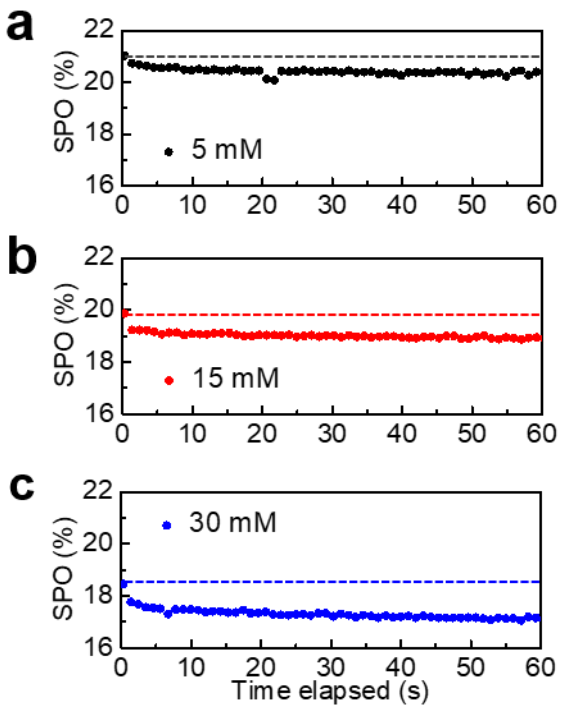

Figure A2.22. Stabilized power output (SPO) of devices with different PAI concentration. SPO of devices treated with **a**, 5 mM, **b**, 15 mM, and **c**, 30 mM of PAI. Horizontal dashed lines mark the initial SPO.

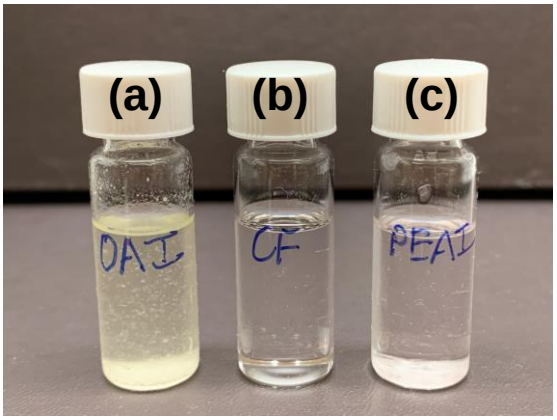

Figure A3.1. Photographs of ammonium salts in CF. Photographs of (a) 30 mmol OAI in CF, (b) pure CF, and (c) 30 mmol PEAI in CF. OAI formed a suspension in CF while PEAI remained

undissolved at the bottom of the vial in (c).

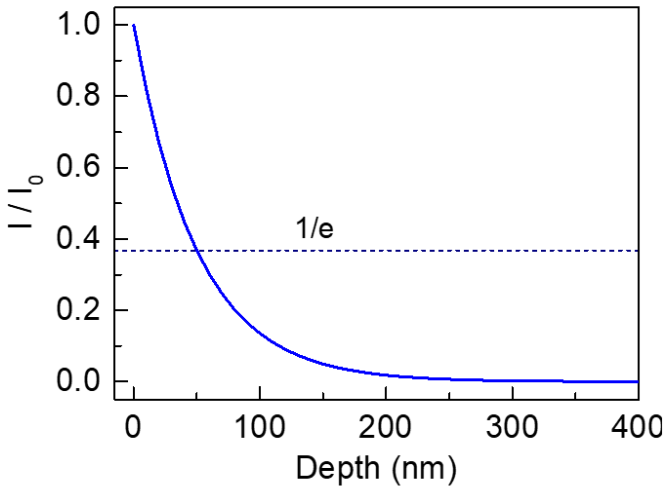

Figure A3.2. PL penetration depth estimation. Intensity decay calculated using the Beer-Lambert law. The absorption coefficient is assumed to be 2 x 10^5 cm^{-1} as was reported for α-$FAPbI_3$ thin films.[2] The penetration depth is defined as the depth by which the intensity decays to $\frac{1}{e}$ of its initial value.

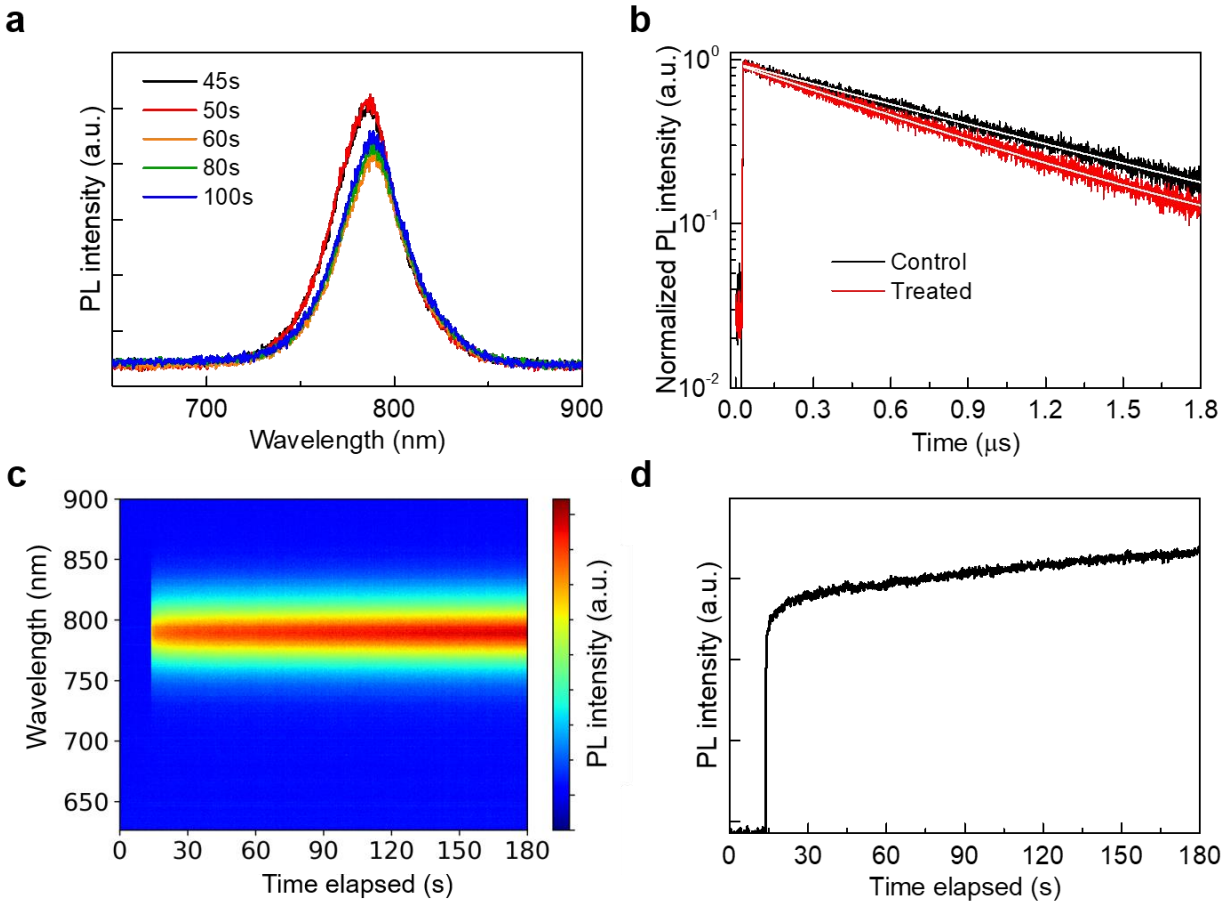

Figure A3.3. *In situ* and time-resolved PL spectra of the perovskite films. (a) Evolution of the raw PL spectra of the perovskite film undergoing treatment with IPA. (b) Normalized time-resolved PL spectra of the perovskite films on glass. Solid white lines are the fitted profiles using a mono-exponential decay function. (c) Contour plot and (d) evolution of the PL intensity of a perovskite film with time.

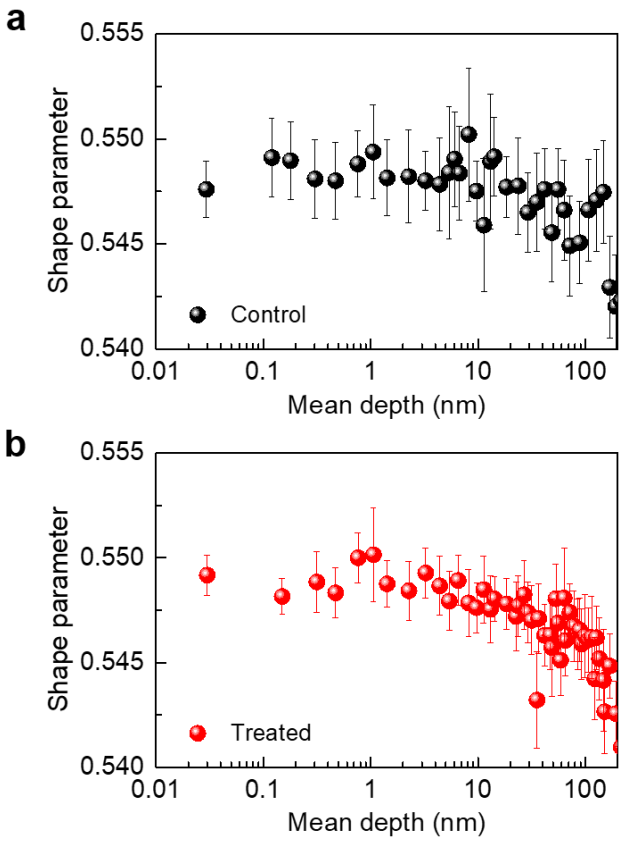

Figure A3.4. PAS profile of the perovskite films. PAS depth-profiling of the (a) control and (b) treated perovskite films.

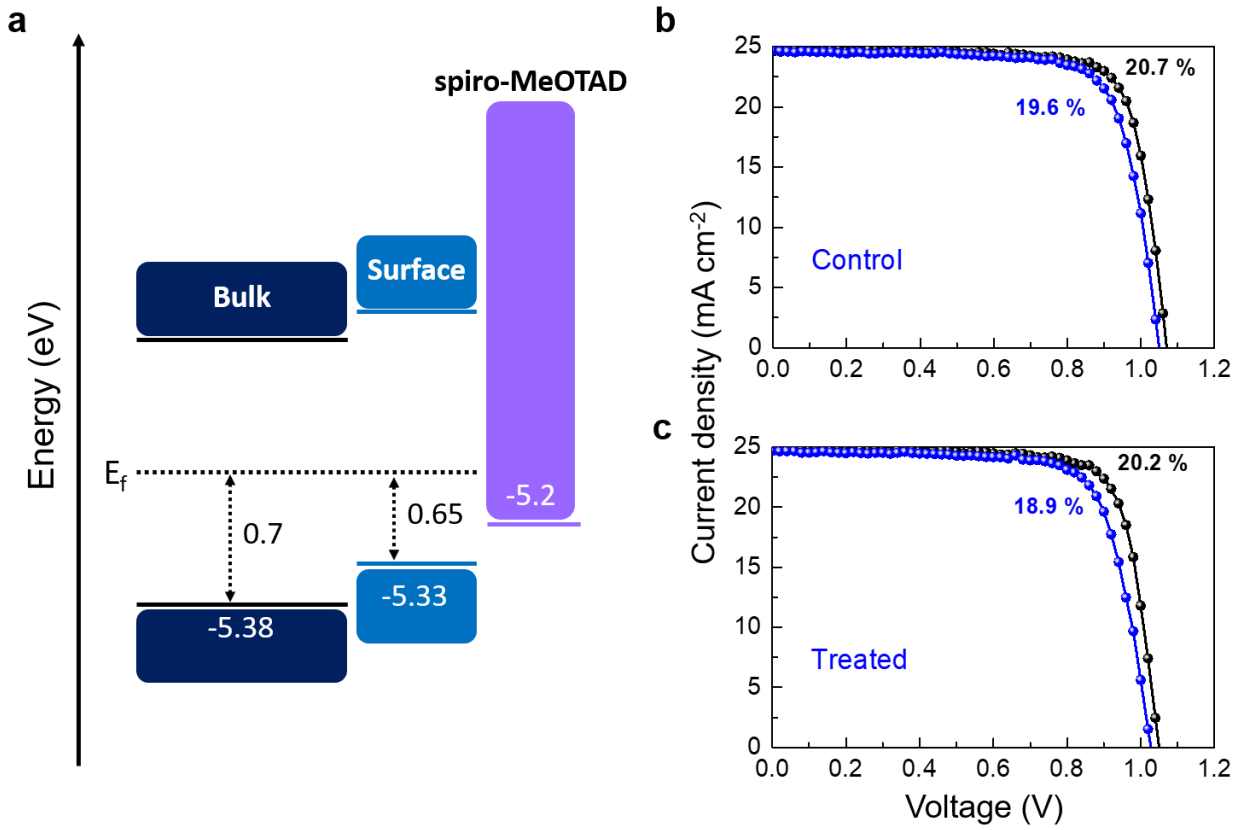

Figure A3.5. Device energy alignment and performance. (a) Schematic band diagram of the energy levels of the IPA treated perovskite film relative to the fermi level. Current density-voltage curves of the (b) control and (c) treated devices in reverse (in black) and forward (in blue) scans.

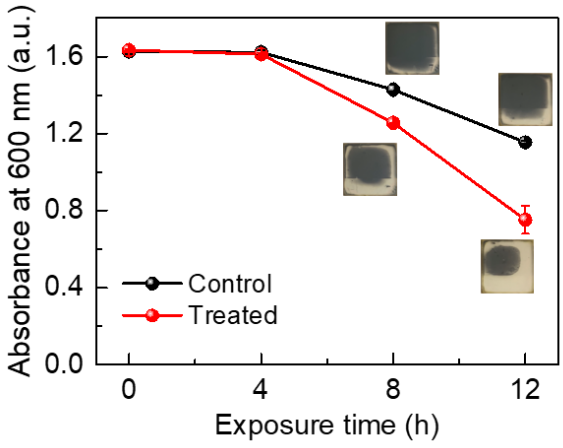

Figure A3.6. Humidity stability testing on the perovskite films. Absorbance at 600 nm of the perovskite films exposed to RH 75 ± 10% with time. Inset shows photographs of the films.

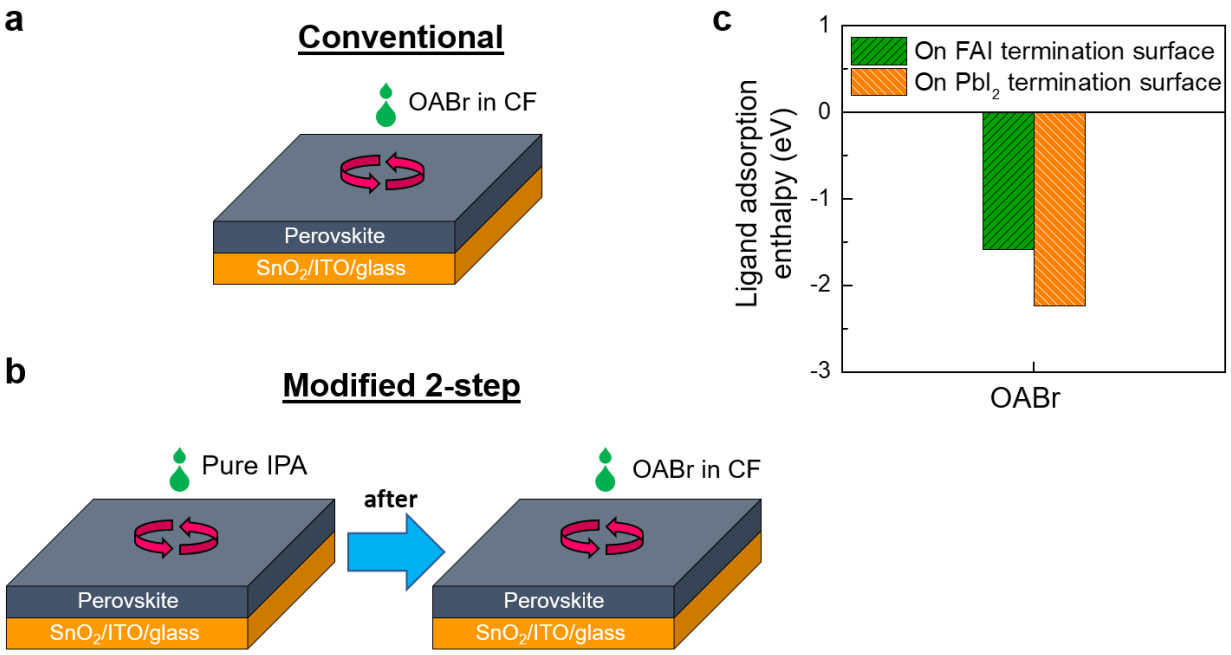

Figure A3.7. Modified surface treatment process. Schematic performance for the (a) conventional and (b) modified surface treatments procedures. (c) Enthalpy of adsorption of OABr on the surfaces.

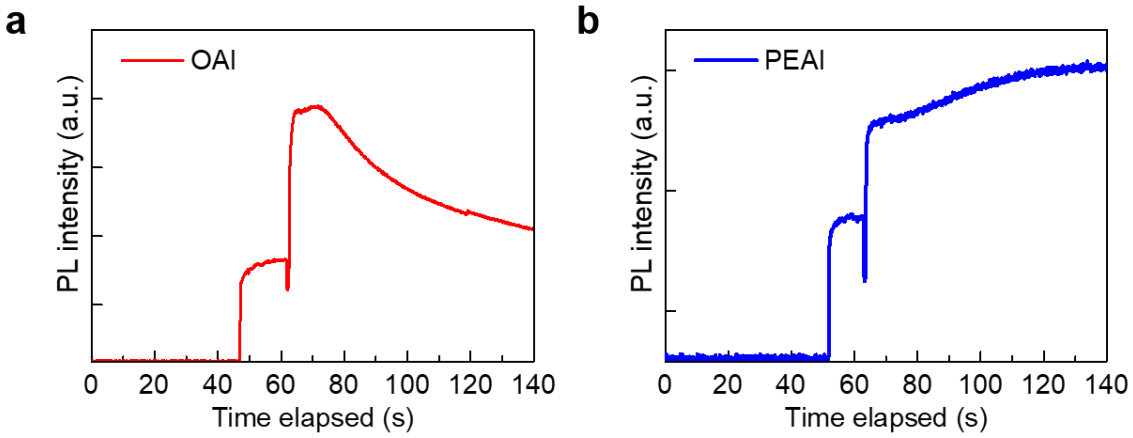

Figure A3.8. *In situ* PL of films undergoing surface treatment. Evolution of the PL intensity of films treated with (a) 10 mM OAI or (b) 10 mM PEAI as a function of time.

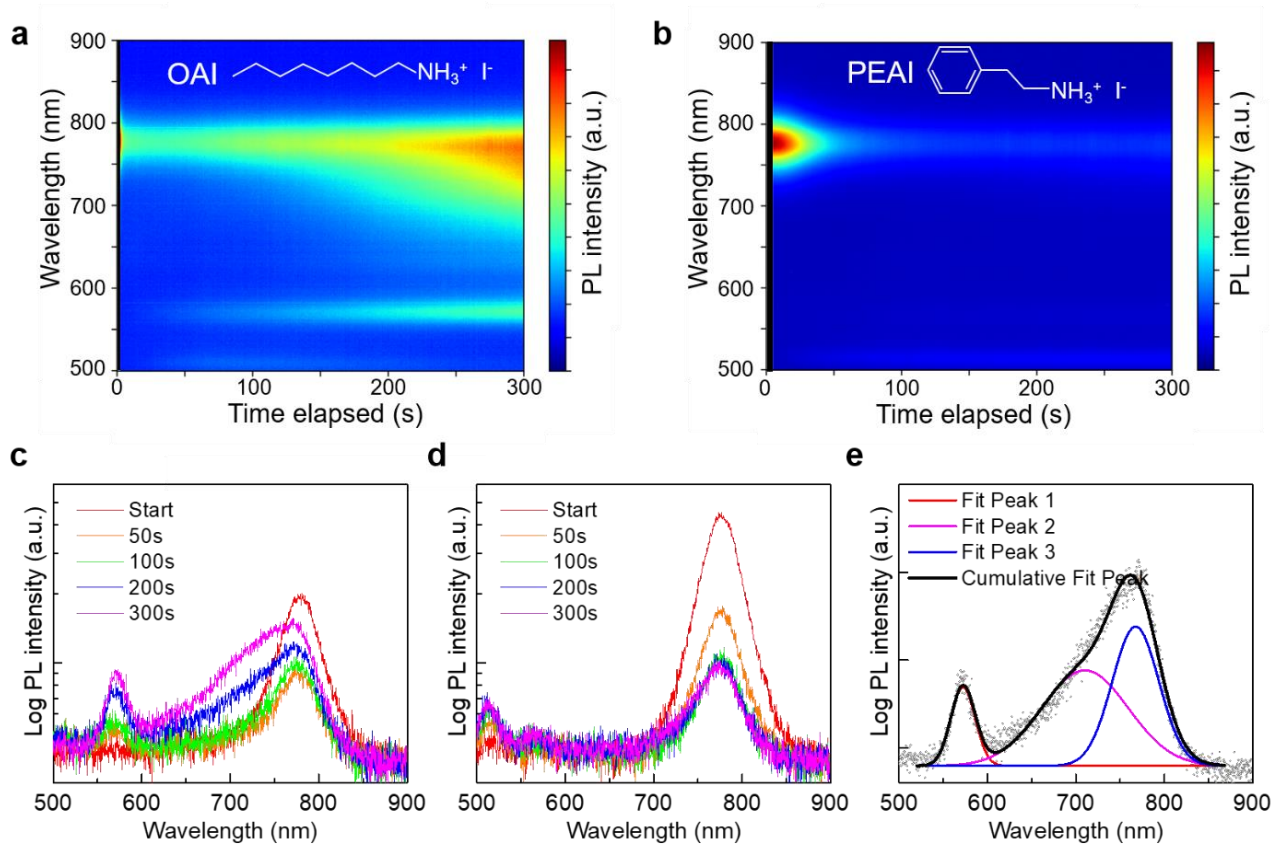

Figure A3.9. *In situ* PL of films undergoing post-annealing. Contour plots of perovskite films treated with (a) 25 mM OAI or (b) 25 mM PEAI in IPA undergoing post-annealing. Evolution with time of the raw PL spectra of the films treated with (c) 25 mM OAI or (d) 25 mM PEAI during post-annealing. (**E**) Deconvoluted peaks of the PL spectra at 300s for the OAI treated film.

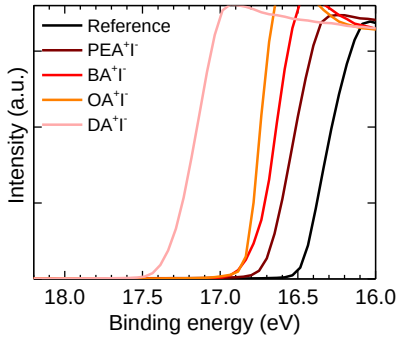

Figure A4.1. Work function change with ammonium iodide surface treatments. UPS secondary electron cut-offs of perovskite films treated with various ammonium iodide salts. Labels are PEA: phenylethylammonium, BA: butylammonium, OA: octylammonium, DA: dodecylammonium.

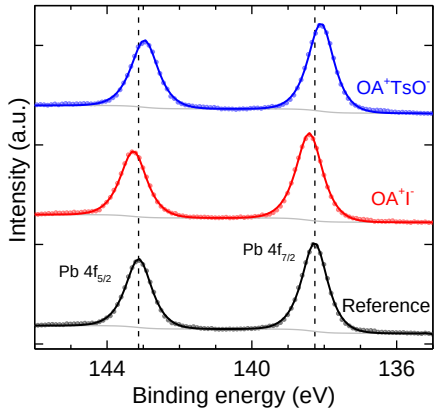

Figure A4.2. XPS characterization of the films. High-resolution Pb 4f spectra of the films. Dashed vertical lines demarcate the peak positions for the Reference film. The Pb 4f peaks of the OAI-treated film shifted to a higher binding energy relative to the Reference film, consistent with the interaction of alkylammonium iodides with Pb.[19] For the OATsO-treated film, the shift to lower binding energy is also consistent with the interaction of the $-SO_3^-$ group of $[TsO]^-$ with Pb.[20]

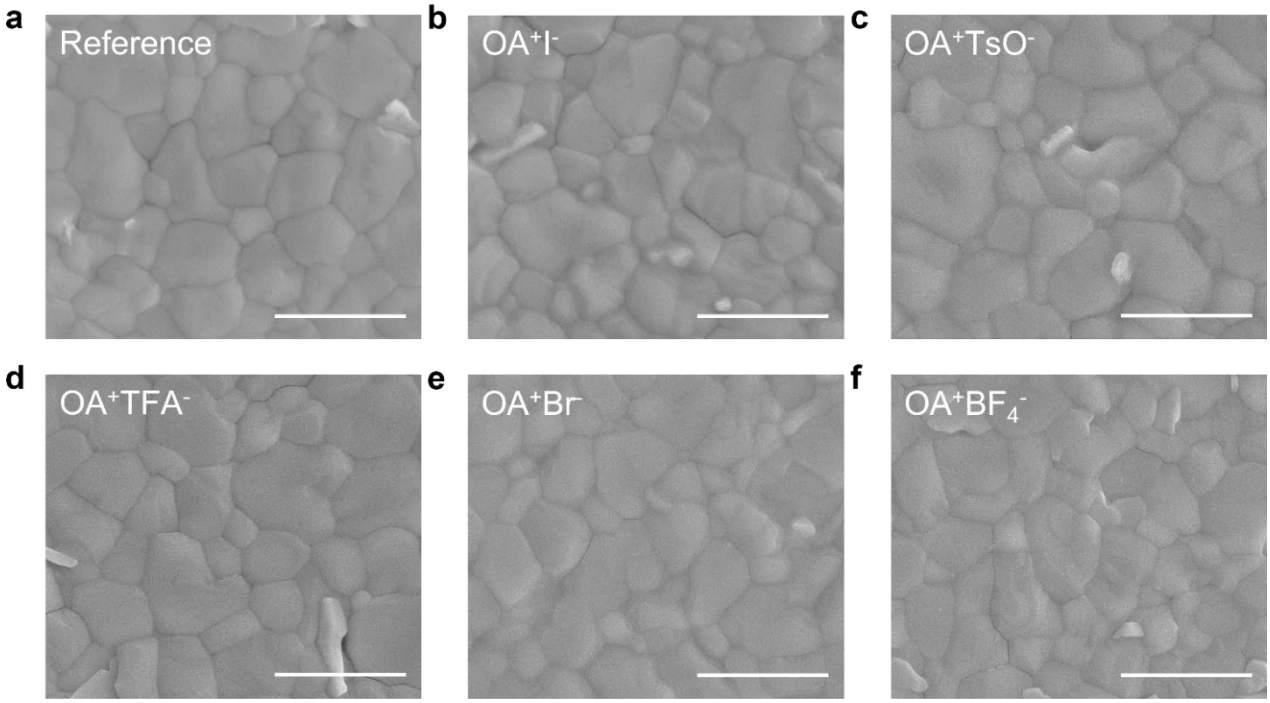

Figure A4.3. Morphology of the perovskite films. Surface morphology of the **a,** Reference, **b,** OAI-treated, **c,** OATsO-treated, **d,** OATFA-treated, **e,** OABr-treated, and **f,** $OABF_4$-treated perovskite films measured by SEM. All scale bars represent 2 μm. No obvious difference can be seen between the Reference and post-treated perovskite films.

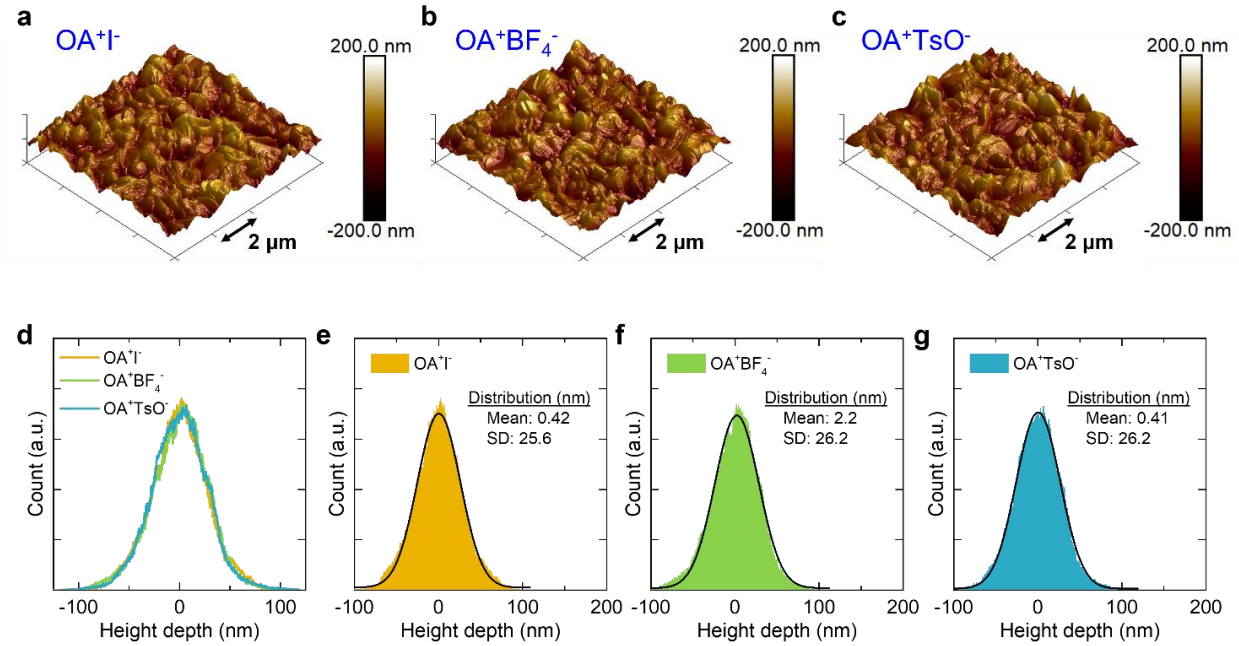

Figure A4.4. Topography of the passivated perovskite films. Representative 3D topography of the **a,** OAI-treated, **b,** $OABF_4$-treated, and **c,** OATsO-treated perovskite films measured by AFM. All scale bars represent 2 μm. **d,** Comparison of the height depth distribution of the films. Depth distribution histograms for the **e,** OAI-treated, **f,** $OABF_4$-treated, and **g** OATsO-treated perovskite films. Insets include the fitted statistical parameters. SD: standard deviation.

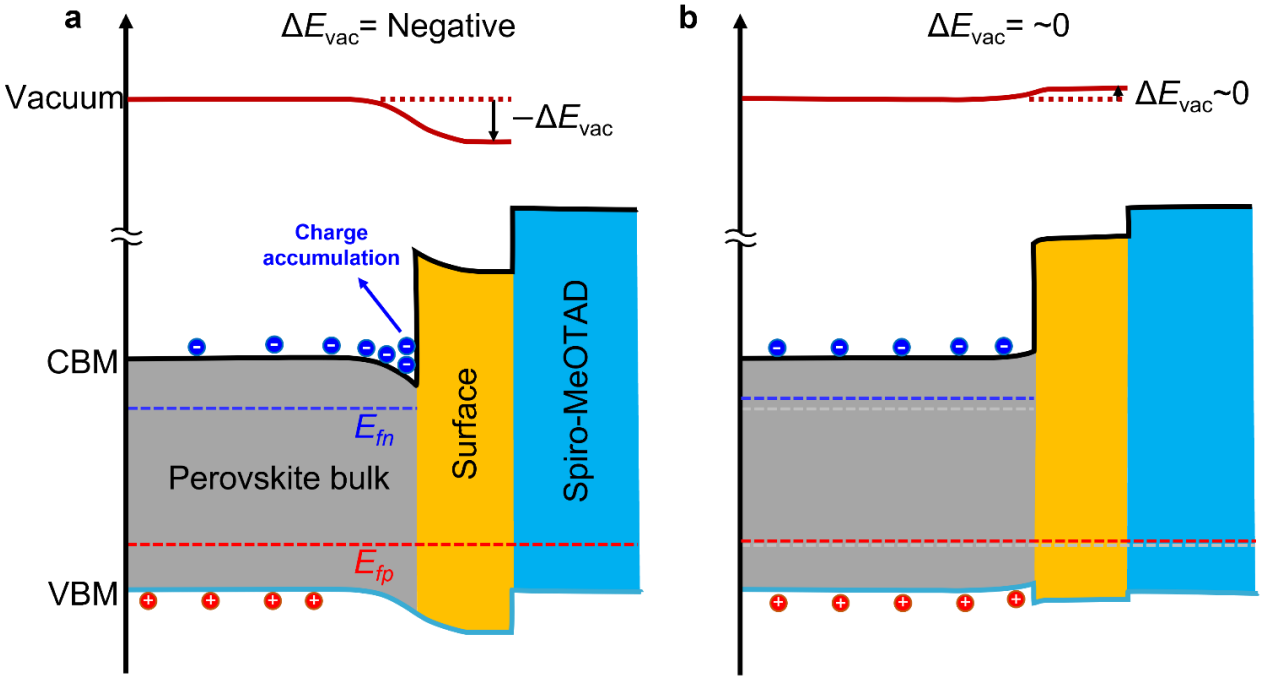

Figure A4.5. Heterointerface energy band diagrams. Schematic interpretation of the heterointerface band alignments of the **a,** OAI-treated and **b,** OATsO-treated devices under illumination in open-circuit condition. The band alignments are constructed based on the UPS results. CBM: conduction band minimum, VBM: valence band maximum, E_{fn}: electron quasi-fermi level, E_{fp}: hole quasi-fermi level. The dashed gray lines in (b) indicate E_{fn} and $E_{fp}$of the OAI-treated device from (a). The diagrams are not drawn to scale. Both surface treatments create a type I energy alignment at the heterointerface, but the vacuum level upshift of the OATsO-treated device minimized the potential well to mitigate the electron accumulation.

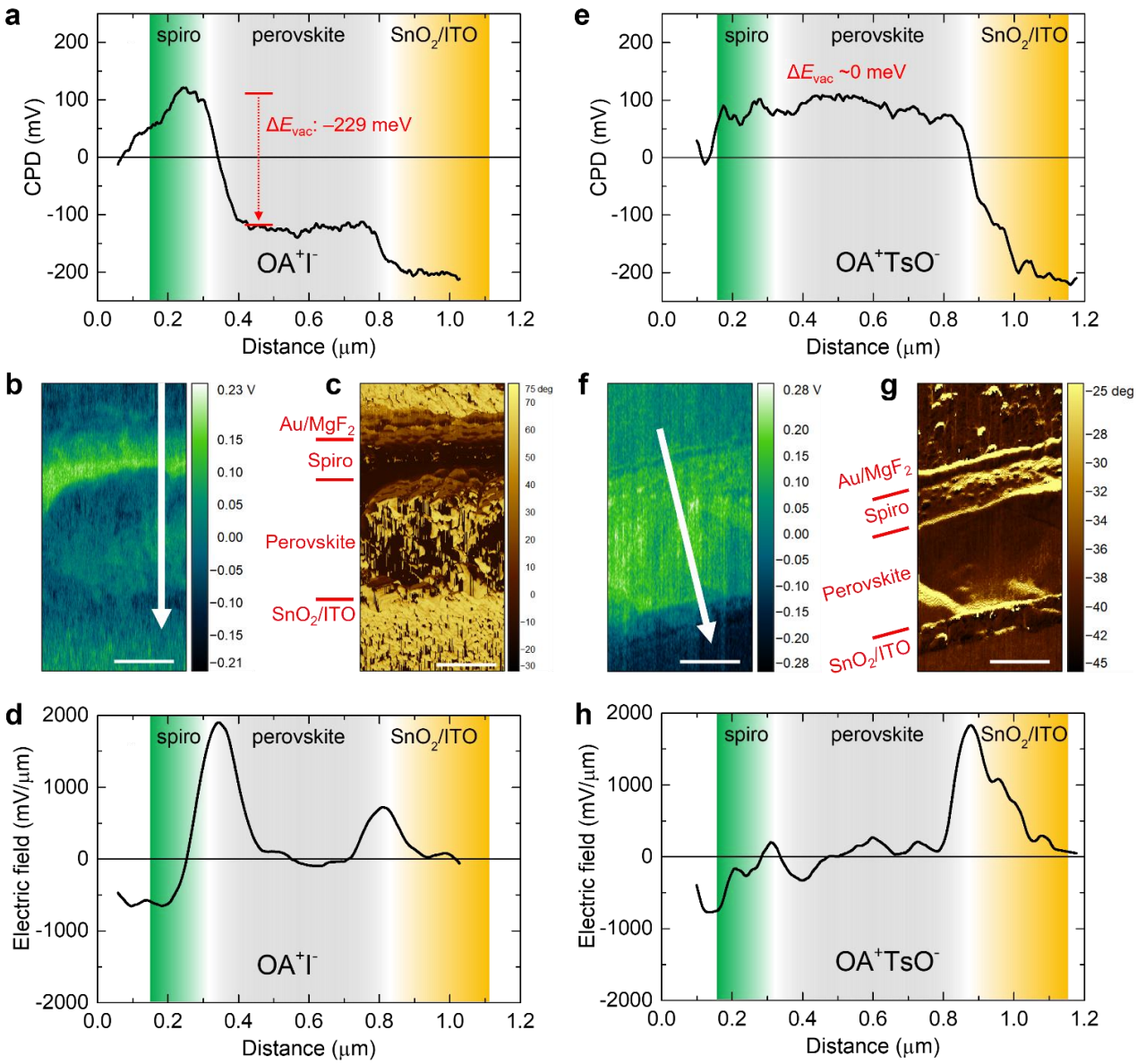

Figure A4.6. Device cross-sectional KPFM profiling. a, CPD profile, **b,** KPFM spatial mapping, **c,** corresponding AFM spatial mapping, and **d,** electric field distribution of the OAI-treated device. **e,** CPD profile, **f,** KPFM spatial mapping, **g,** corresponding AFM spatial mapping, and **h,** electric field distribution of the OATsO-treated device. Measurements were performed under illumination in open-circuit condition. All scale bars represent 300 nm. The CPD offsets were adjusted such that the CPD value of the buffer layer becomes zero. Note that this does not affect the electric field and charge displacement profiles, which calculate the derivatives of the CPD profiles. Although we do not expect the rough morphology seen in (c) to affect the KPFM signal, we cannot completely rule this out at this stage. Therefore, we have repeated the KPFM measurement on another separate OAI-treated device. As shown in Figure A4. 4. 4, we were able to reproduce the potential drop at the perovskite/spiro-MeOTAD heterointerface.

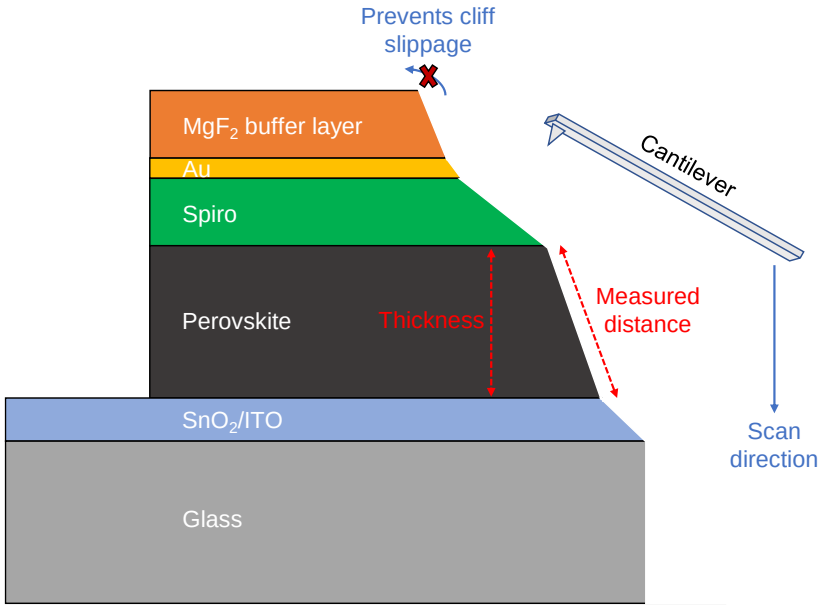

Figure A4.7. Cross-sectional KPFM schematic. Schematic illustrating the KPFM measurement setup and planar device structure of ITO/SnO_2/perovskite/spiro-MeOTAD/Au. The MgF_2 buffer layer prevents slippage of the cantilever tip at a "cliff". Often, the device cross-sections are not parallel, due to the uncontrollable nature of the mechanical cleaving process. Therefore, the measured distance may not represent the layer thickness. Note that we purposely avoided using FIB or mechanical polishing for the KPFM samples, as such processing may modify the properties of the exposed cross-sectional surface.[21]

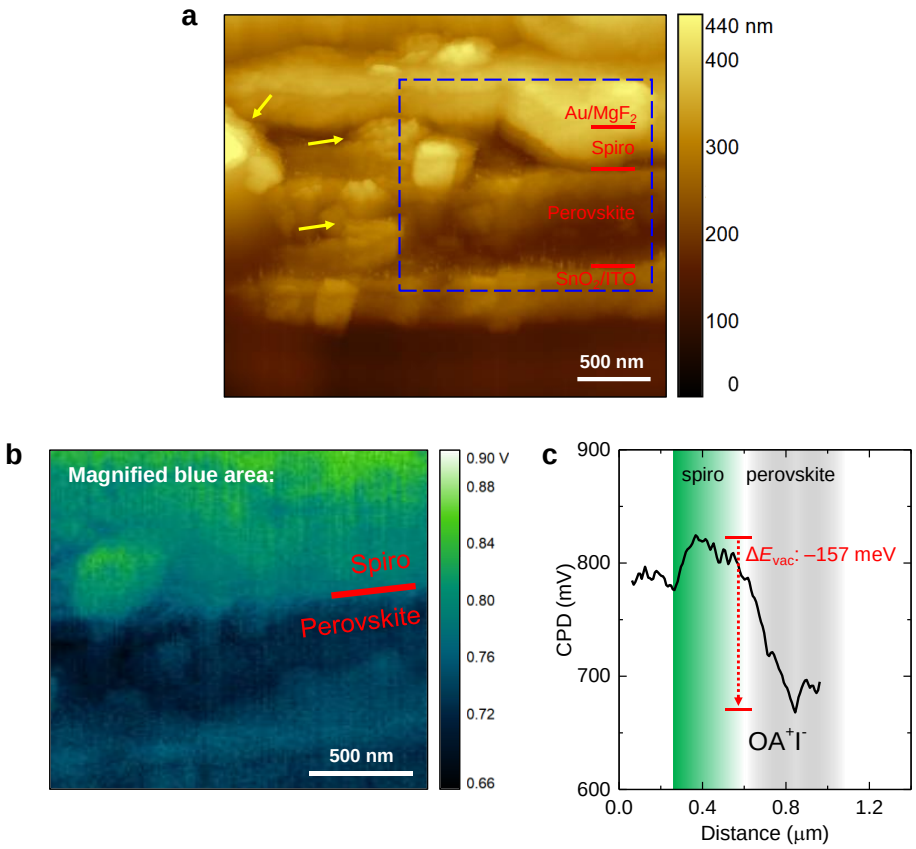

Figure A4.8. Cross-sectional KPFM profiling of another OAI-treated device. a, AFM spatial mapping of an OAI-treated device. Yellow arrows in (a) indicate damaged regions due to the mechanical cleaving process. **b,** KPFM spatial mapping, and **c,** CPD profile of the OAI-treated device. The magnified KPFM image in (b) spatially corresponds to the blue square region in (a). All scale bars represent 500 nm. The ΔE_{vac} value from the CPD profile matches those previously measured as shown in Figure A4. 4. 5.

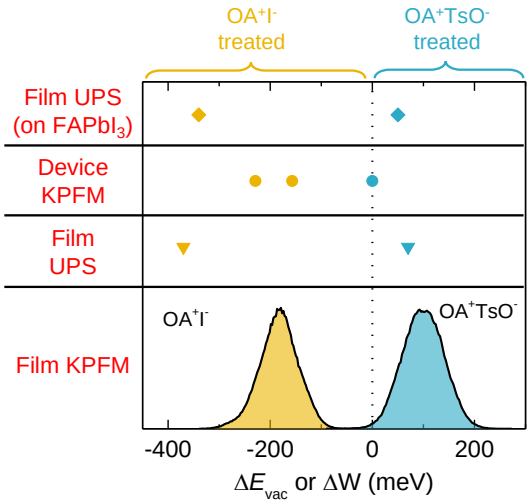

Figure A4.9. Different measurements of the vacuum level change. Comparison of the ΔE_{vac} or ΔW of the perovskite devices or films measured from KPFM or UPS.

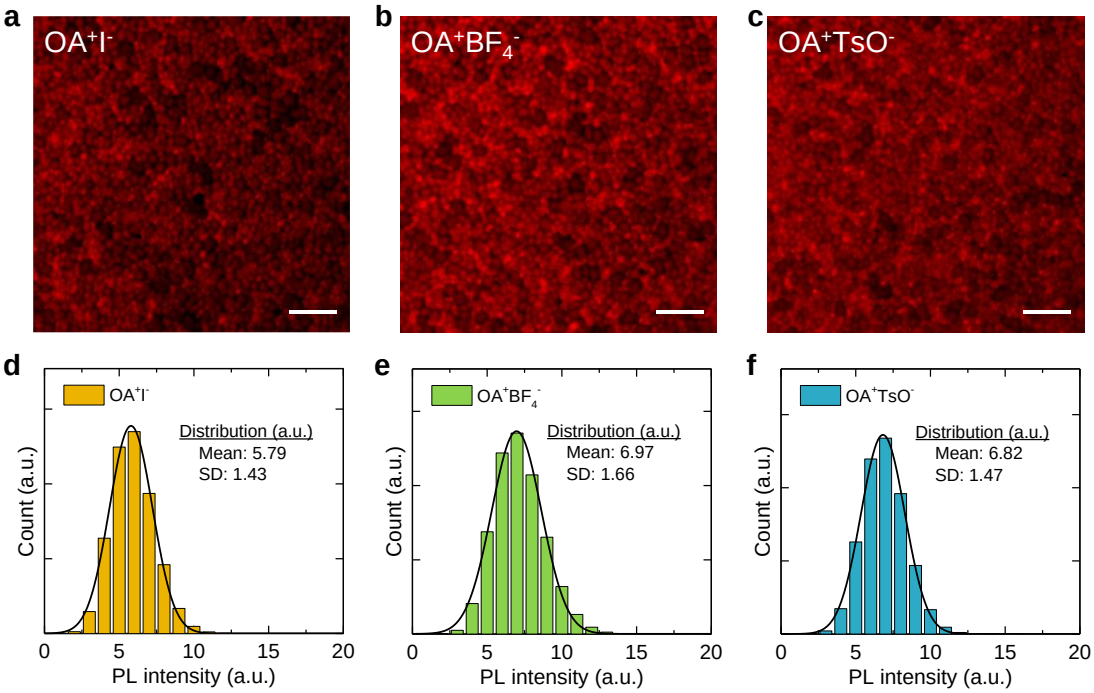

Figure A4.10. PL mapping of the passivated films. Representative confocal PL maps of the **a,** OAI-treated, **b,** $OABF_4$-treated, **c,** OATsO-treated perovskite films on glass. All scale bars represent 5 μm. PL intensity distribution histograms of the **d,** OAI-treated, **e,** $OABF_4$-treated, **f,** OATsO-treated perovskite films on glass. Insets include the fitted statistical parameters. SD: standard deviation.

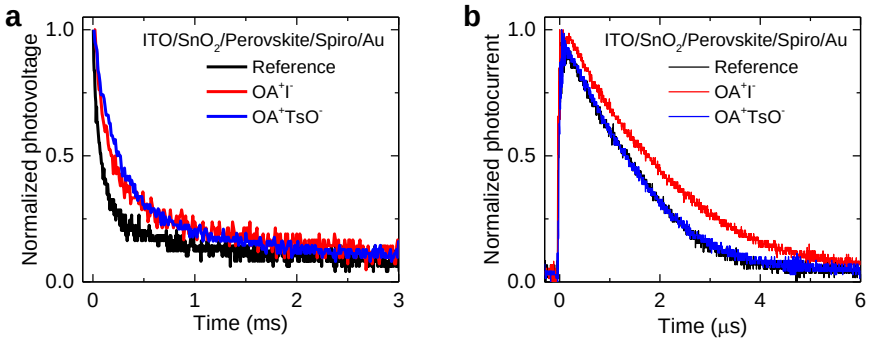

Figure A4.11. Photo-transient measurements of the complete devices. Normalized **a,** transient photovoltage decay and **b,** transient photocurrent decay of the complete devices.

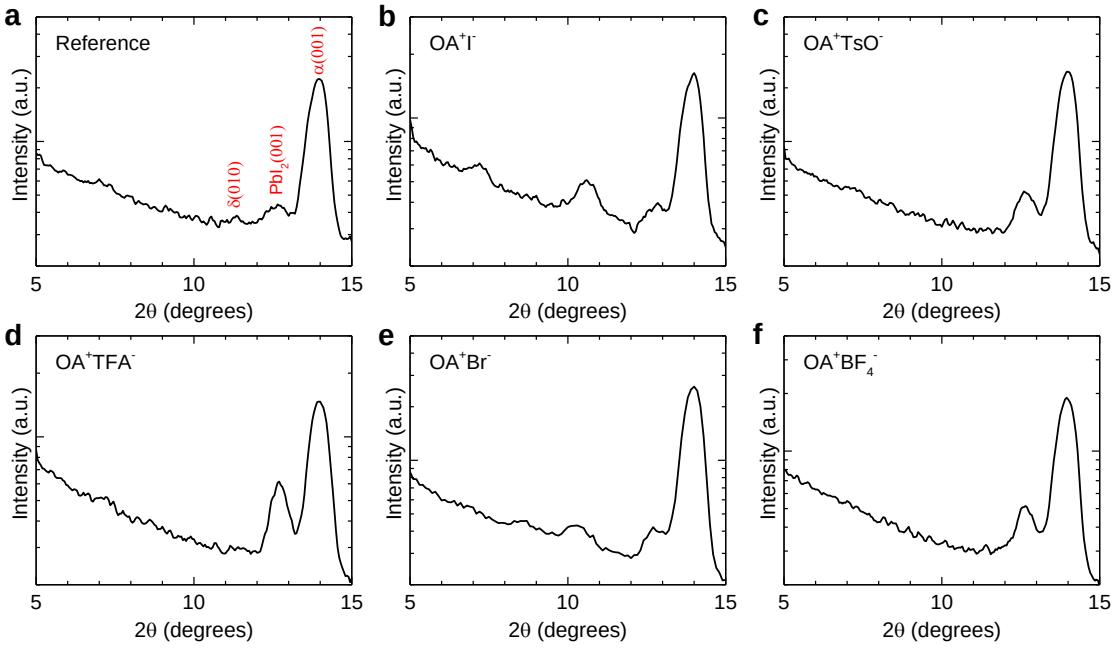

Figure A4.12. GIXRD characterization of the films. Grazing incidence X-ray diffraction (GIXRD) of the **a,** Reference, **b,** OAI-treated, **c,** OATsO-treated, **d,** OATFA-treated, **e,** OABr-treated, and **f,** $OABF_4$-treated perovskite films. Measurements were performed at an $\omega = 0.2°$, with an estimated penetration depth of <60 nm.

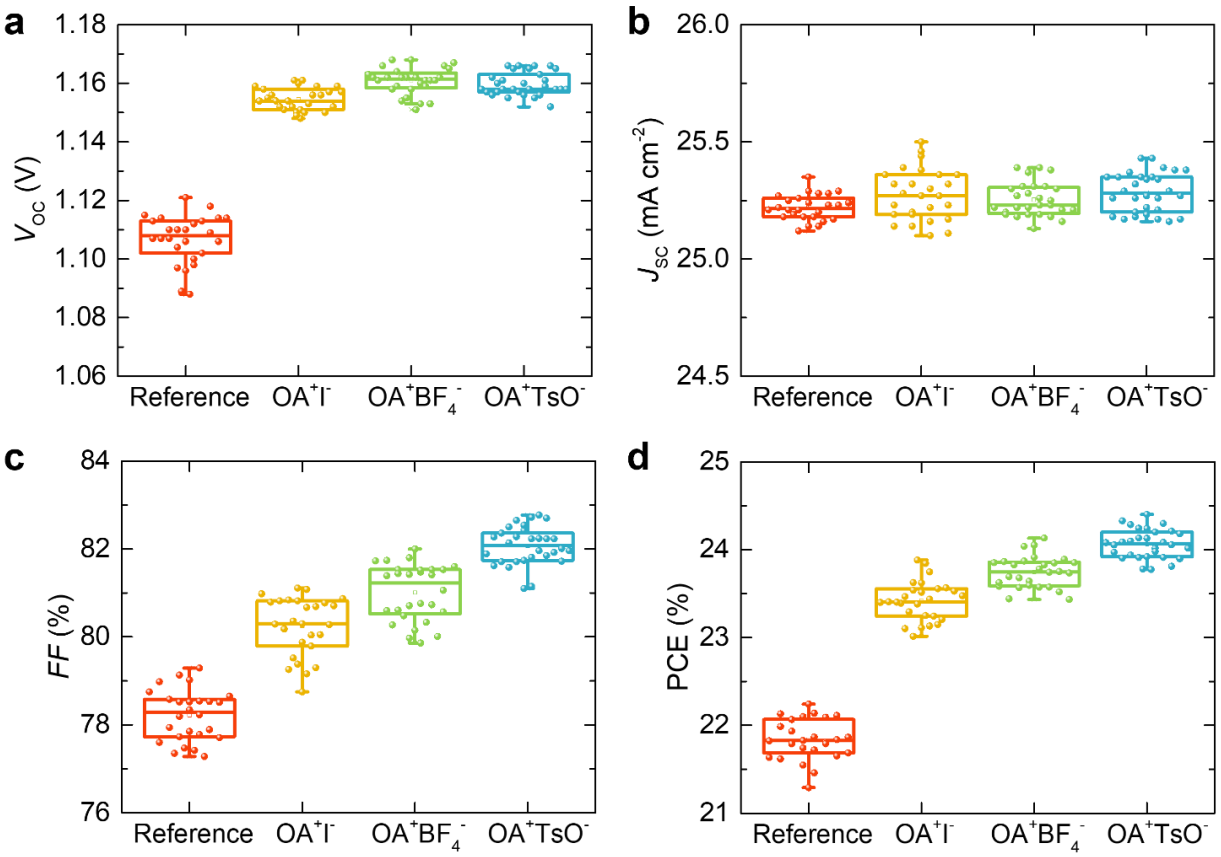

Figure A4.13. Device photovoltaic parameters. Box plots showing the distribution of the **a,** V_{OC}, **b,** J_{SC}, **c,** *FF*, and **d,** PCE of the devices. Center line: median, box limits: 25th and 75th percentile, whiskers: outliers.

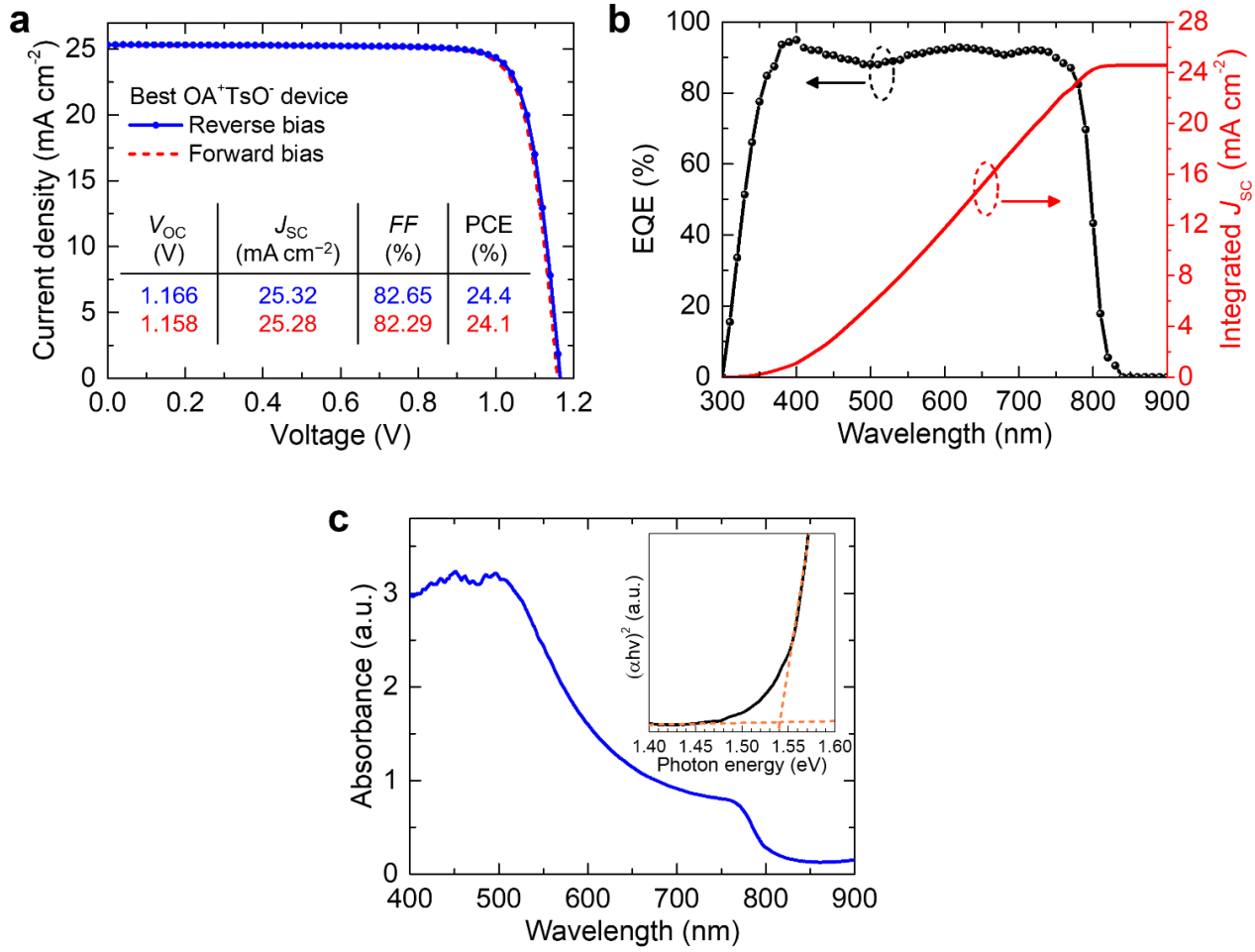

Figure A4.14. Characterization of the OATsO-treated devices. a, Current density-voltage curves of the best-performing OATsO-treated device, in reverse bias (blue line) and forward bias (red line). Inset includes the measured photovoltaic parameters. **b,** EQE spectrum and integrated J_{SC} of an OATsO-treated device. The integrated J_{SC} is 24.6 mA cm^{-2}, and therefore well-matched (<3% discrepancy) with the measured value. **c,** Absorbance profile of an OATsO-treated film on glass measured by UV-Vis spectroscopy. Inset includes a Tauc plot and linear fits to estimate the optical bandgap.

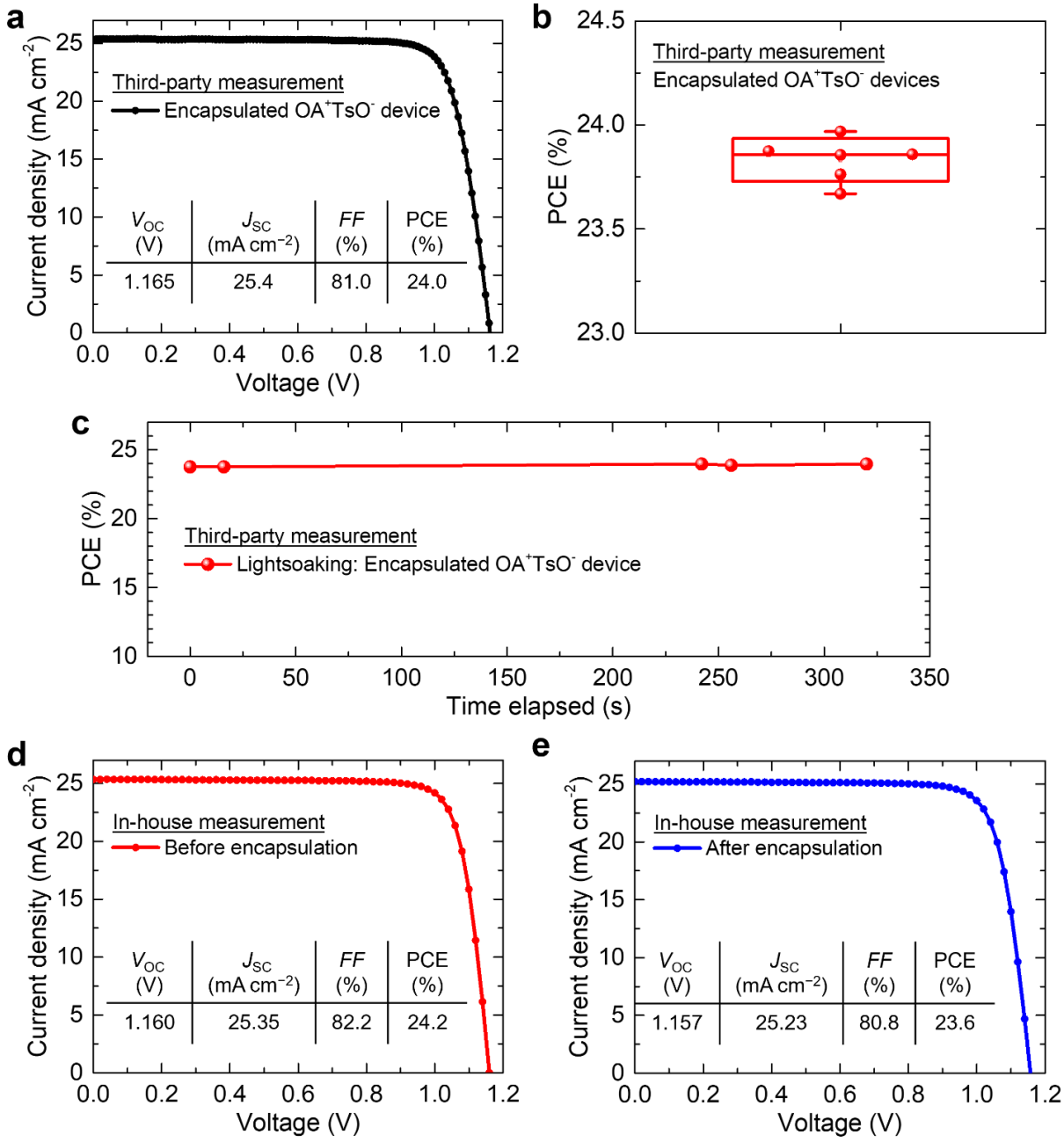

Figure A4.15. Third-party device performance measurements. a, Current density-voltage curve and **b,** box plot showing the PCE distribution of the encapsulated OATsO-treated devices. Since the measurements were fully done in ambient air (RH ~50%), all devices had to be encapsulated, which resulted in a drop in performance. **c,** PCE evolution with time under lightsoaking of an encapsulated OATsO-treated device. Current density-voltage curves of the same device **a,** before and **b,** after the encapsulation procedure, measured in-house.

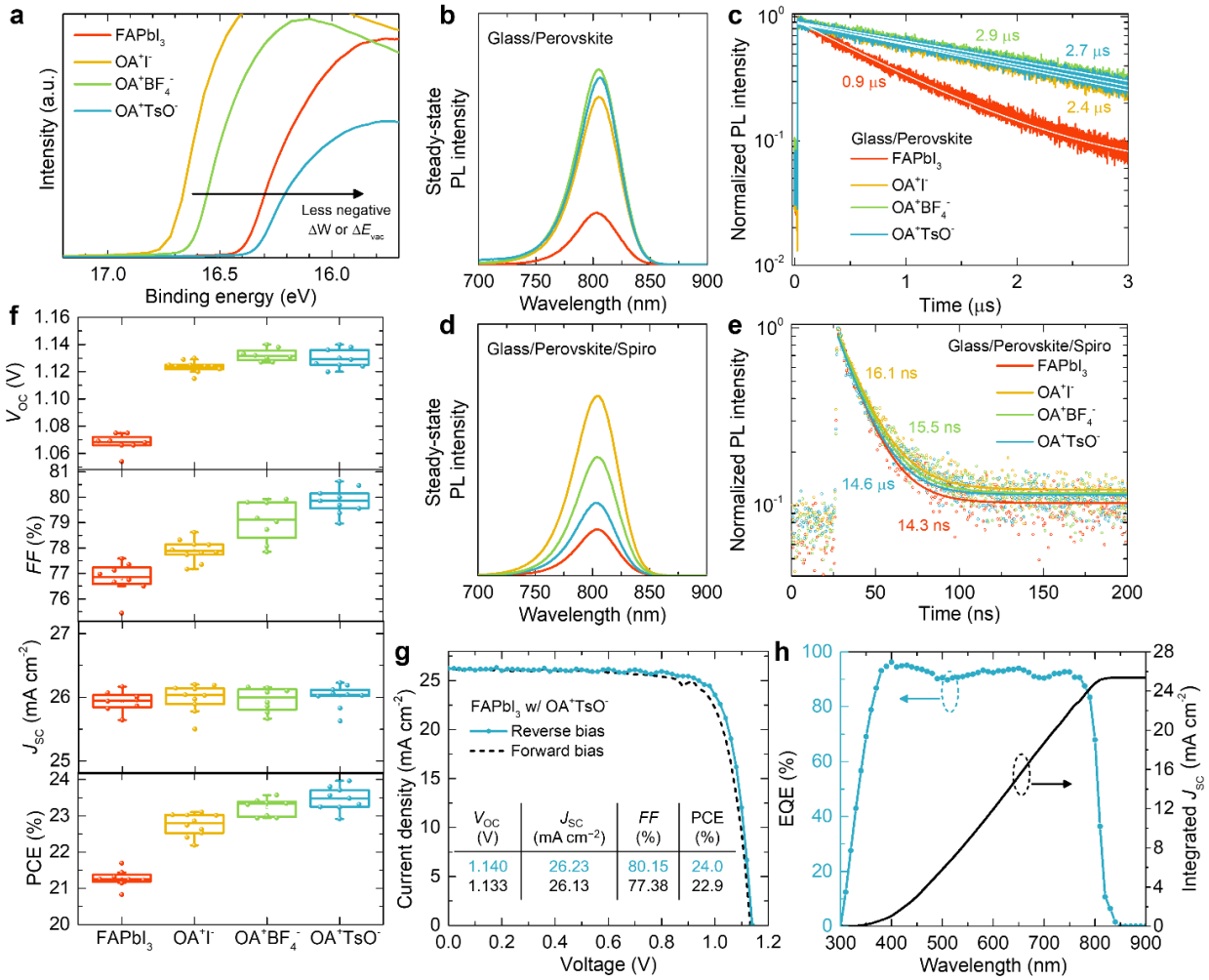

Figure A4.16. Universality verification on a $FAPbI_3$ composition.

a, UPS secondary electron cut-offs of the perovskite films. **b,** Steady-state and **c,** time-resolved PL spectra of the glass/perovskite films. **d,** Steady-state and **e,** time-resolved PL spectra of the glass/perovskite/spiro-MeOTAD films. The carrier lifetimes are fitted with a mono-exponential decay function. **f,** Box plots of the distribution of the device photovoltaic parameters. Center line: median, box limits: 25th and 75th percentile, whiskers: outliers. **g,** Current density-voltage curves and **h,** EQE spectrum and integrated J_{SC} of the best-performing device treated with OATsO. The integrated J_{SC} is 25.4 mA cm^{-2}, well-matched (~3% discrepancy) with the measured scan value.

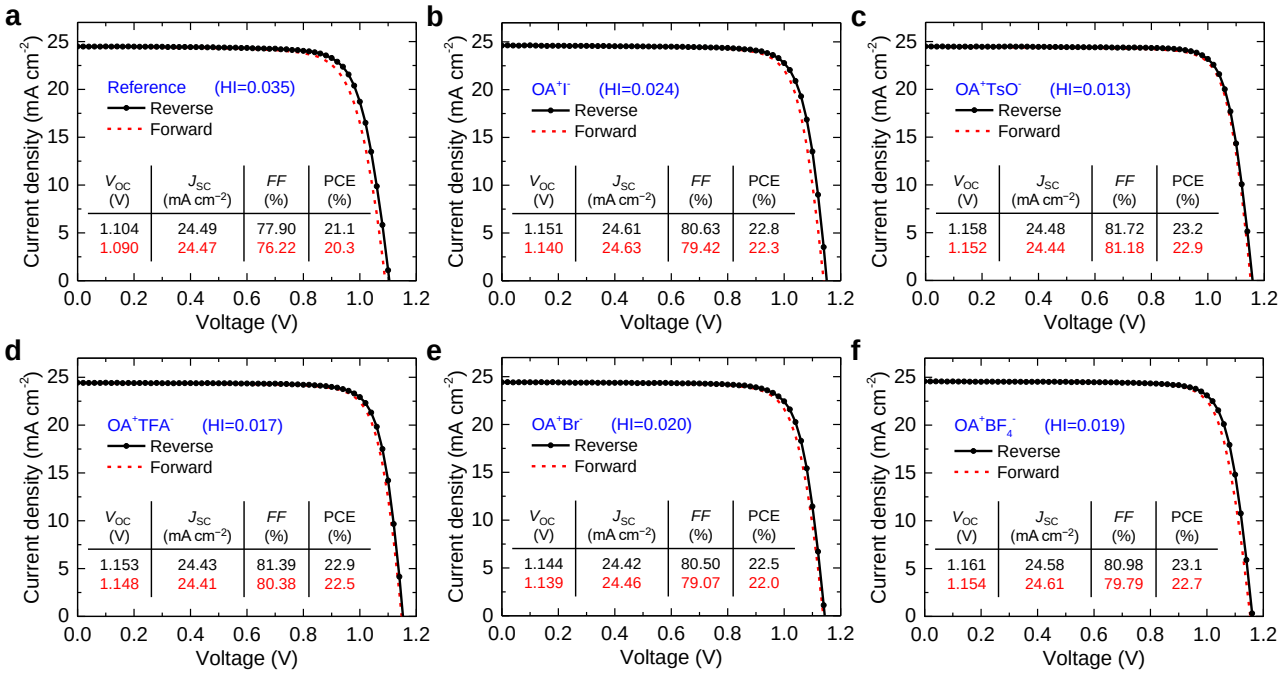

Figure A4.17. Device hysteresis behavior. a, Current density-voltage curve of the **a,** Reference, **b,** OAI-treated, **c,** OATsO-treated, **d,** OATFA-treated, **e,** OABr-treated, and **f,** $OABF_4$-treated devices, in reverse bias (black solid lines) and forward bias (red dashed lines). Insets include the measured photovoltaic parameters. We note that these devices did not have the MgF_2 anti-reflection coating. The hysteresis index (HI) is included in the insets.

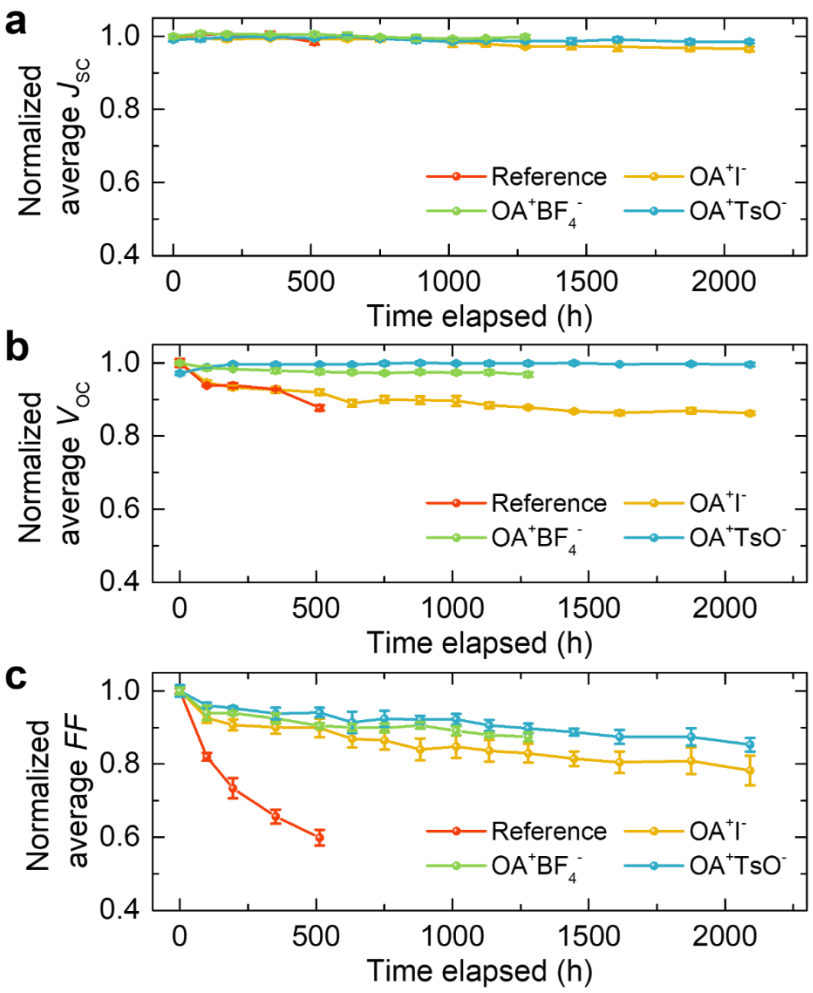

Figure A4.18. Open-circuit stability test device performance. Evolution with time of the normalized average **a,** J_{sc}, **b,** V_{OC}, and **c,** FF of the devices under continuous illumination with a metal halogen lamp. The encapsulated devices were aged in ambient atmosphere at RH ~ 40% and T ~ 40 °C in open-circuit condition. Error bars represent the standard deviation of four devices for each condition.

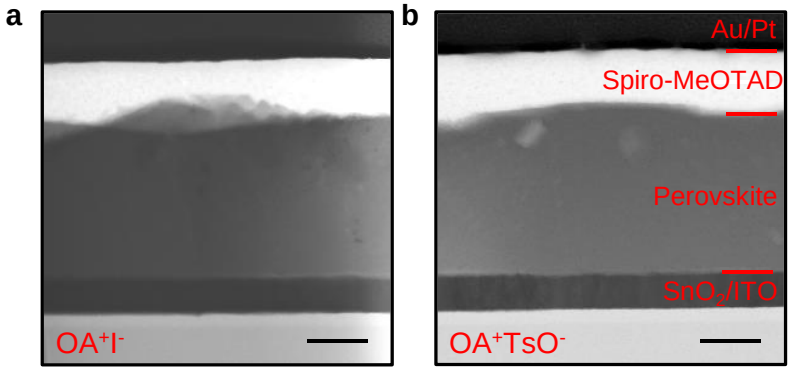

Figure A4.19. STEM images of the aged devices. STEM bright field images of the aged **a,** OAI-treated and **b,** OATsO-treated device cross-sections. All scale bars represent 200 nm.

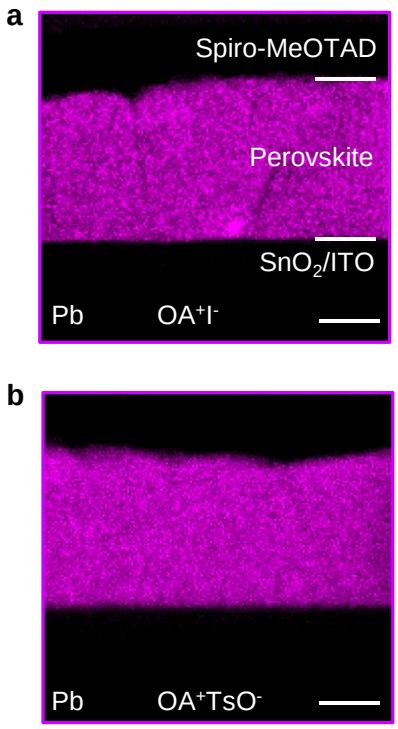

Figure A4.20. EDX analyses of the aged devices. EDX elemental maps of lead for the **a,** OAI-treated and **b,** OATsO-treated device cross-sections. All scale bars represent 200 nm.

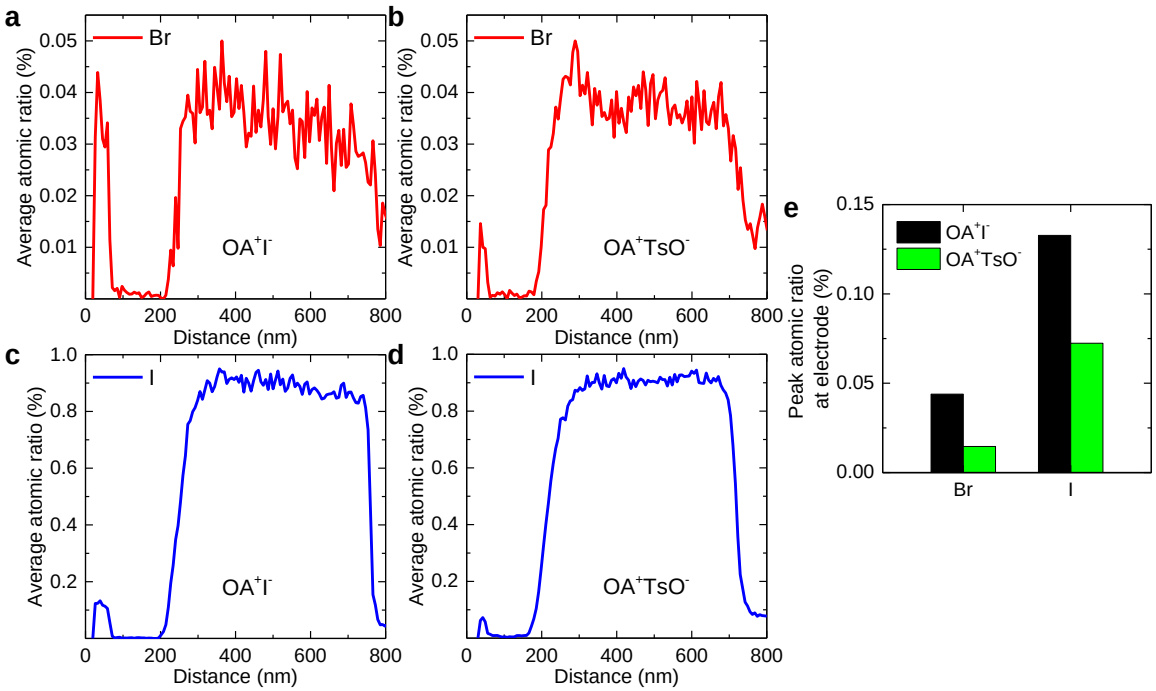

Figure A4.21. Halide distribution in the aged devices. Average atomic ratio distributions across the **a,** OAI-treated and **b,** OATsO-treated device cross-sections, and iodine for the **c,** OAI-treated and **d,** OATsO-treated device cross-sections. **e,** Peak values extracted from (a)-(d) at the electrode region. The average atomic ratios were calculated by simply multiplying the normalized signal intensity with the nominal perovskite stoichiometry.

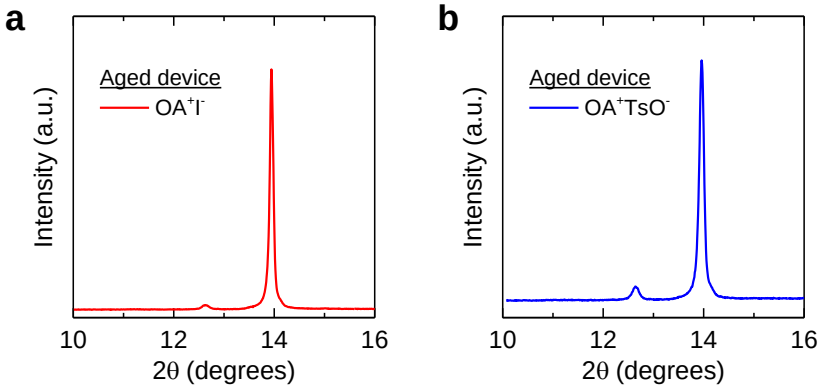

Figure A4.22. XRD analyses of the aged devices. XRD diffraction patterns measured with an ω-2θ setup of the aged **a,** OAI-treated and **b,** OATsO-treated devices. These were the same devices used for the STEM analyses, and were recovered after FIB milling. X-rays from the ω-2θ diffraction setup were able to penetrate through the top electrode and spiro-MeOTAD layers to probe the active layer itself. Concurrently, given the large penetration depth of ω-2θ XRD (>700 nm), it is not sensitive to the ultrathin 2D interlayer, which is only detectable by the GIXRD measurements.

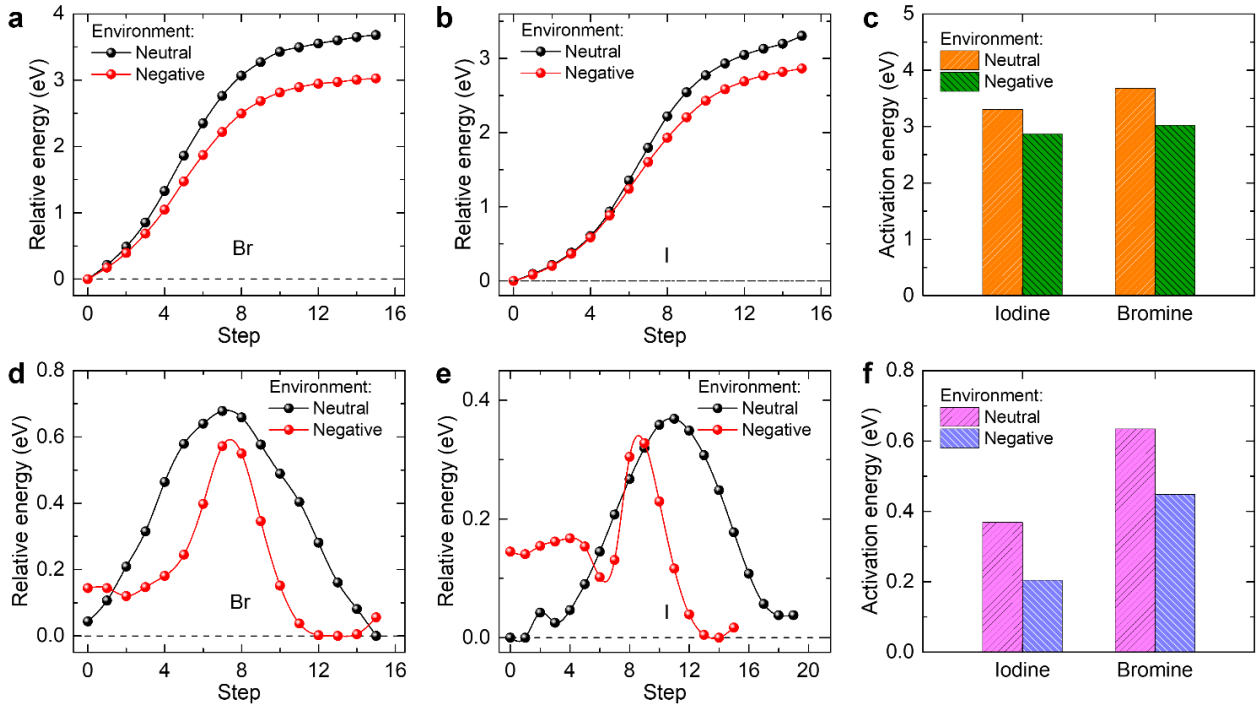

Figure A4.23. Activation energy for halide migration. Energy profiles for the extra-lattice migration of **a,** bromine and **b,** iodine in a neutral uncharged or negatively charged environment, and **c,** corresponding activation energy barriers. Energy profiles for the intra-lattice migration of **d,** bromine and **e,** iodine in a neutral uncharged or negatively charged environment, and **f,** corresponding activation energy barriers.

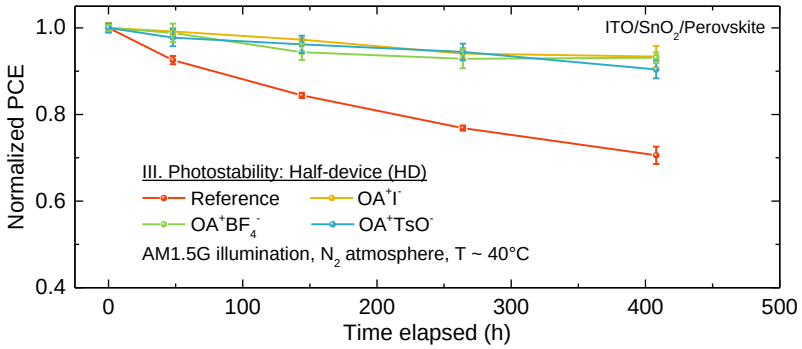

Figure A4.24. Half-device photostability test. Stability evolution with time of half-devices aged under continuous illumination in a nitrogen atmosphere. The time elapsed refers only to the time under illumination. Error bars represent the standard deviation of four devices for each condition.

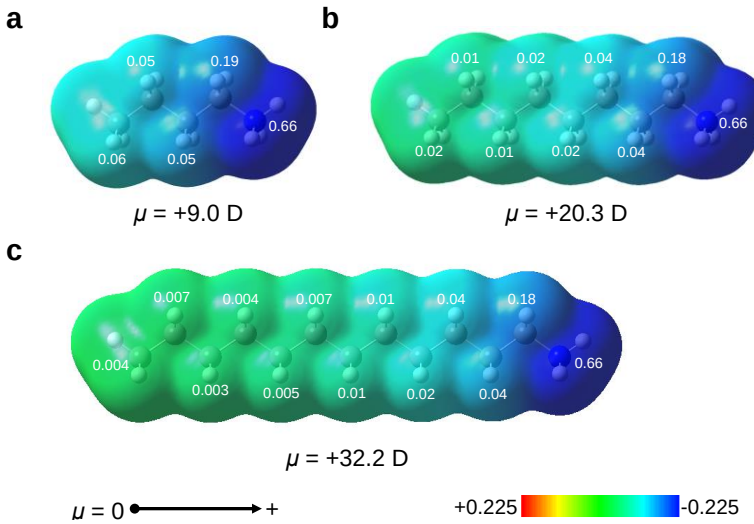

Figure A4.25. Electrostatic potentials of various cations. Electrostatic potential maps of **a,** $[BA]^+$, **b,** $[OA]^+$, and **c,** $[DA]^+$. Included are their respective dipole moments (μ).

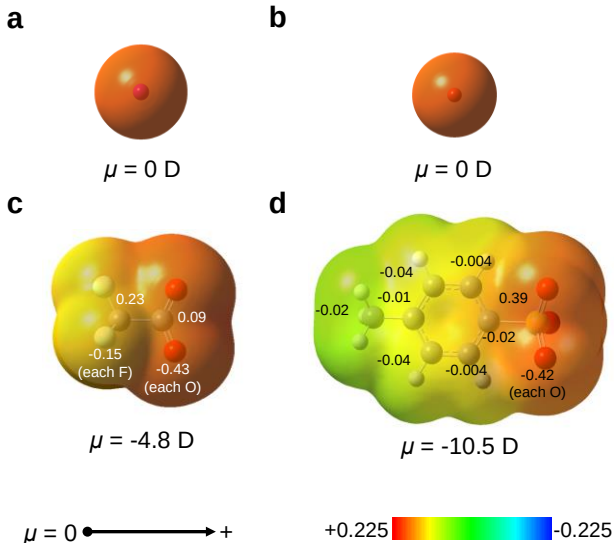

Figure A4.26. Electrostatic potentials of various anions. Electrostatic potential maps of **a,** $[I]^-$, **b,** $[Br]^-$, **c,** $[TFA]^-$, and **d,** $[TsO]^-$. Included are their respective dipole moments (μ).

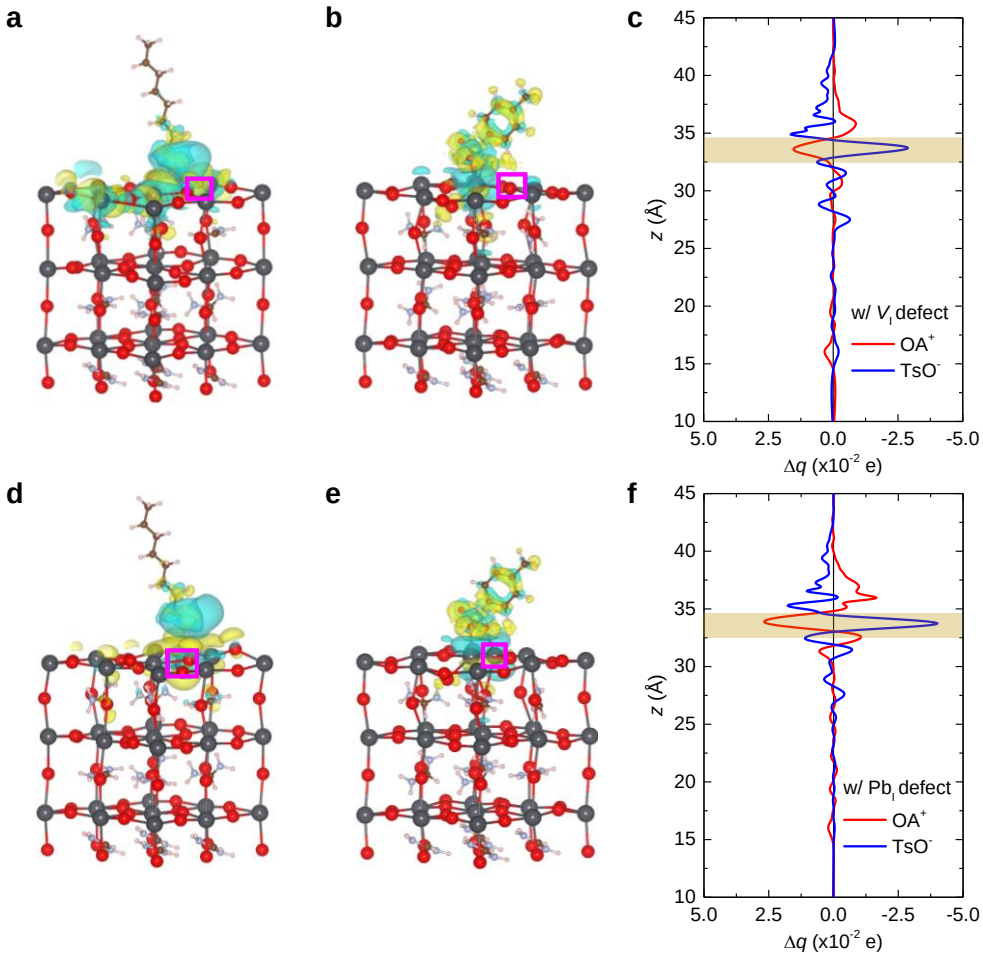

Figure A4.27. Surface states and charge displacement. Charge displacement with surface iodine vacancy defect (V_I) with **a,** $[OA]^+$ or **b,** $[TsO]^-$, and **c,** corresponding charge displacement profiles. Charge displacement with surface lead-iodine antisite defect (Pb_I) with **d,** $[OA]^+$ or **e,** $[TsO]^-$, and **f,** corresponding charge displacement profiles. Blue and yellow volumes on the slab models correspond to electron-depleted or electron-enriched regions, respectively. The point defects are marked by pink squares.

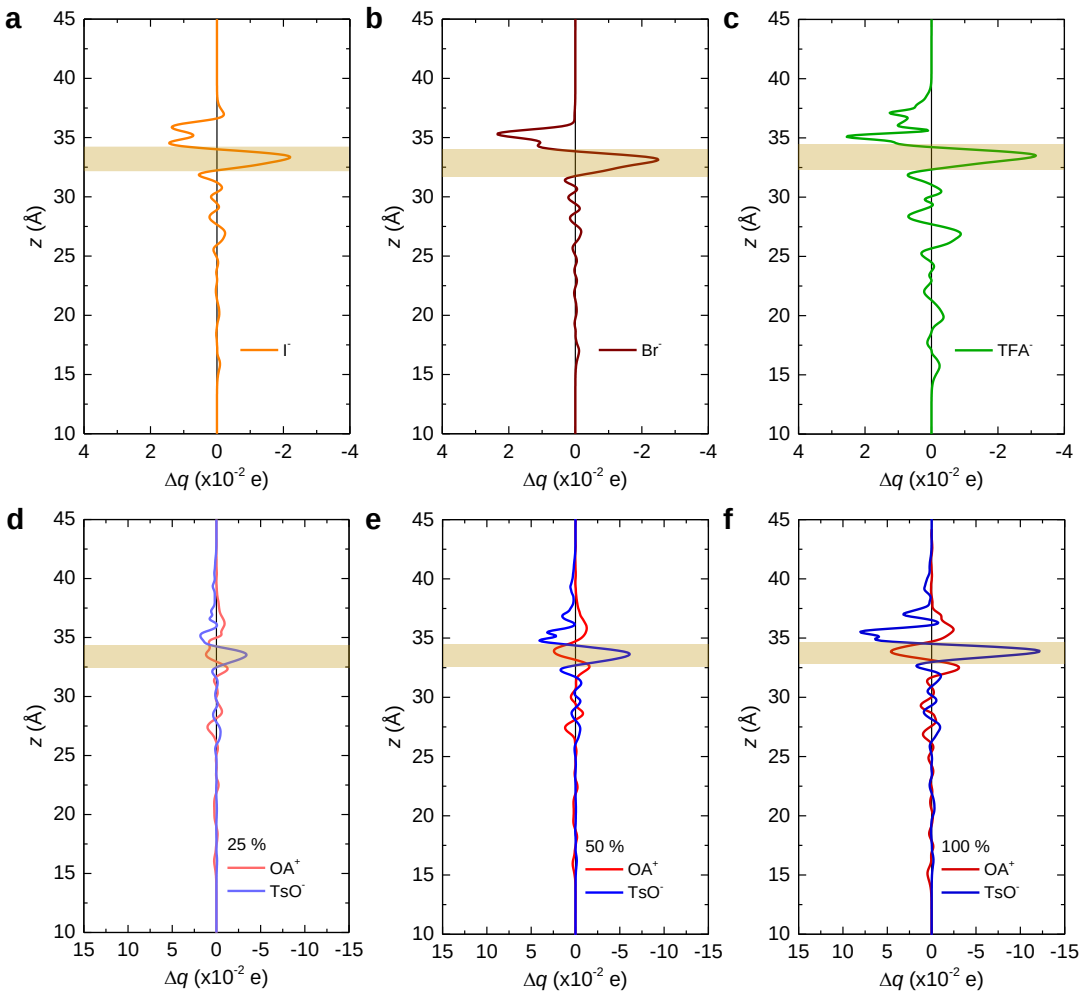

Figure A4.28. Charge displacement profiles with different anions and concentrations. Charge displacement profiles on defect-free surfaces with **a,** $[I]^-$, **b,** $[Br]^-$, and **c,** $[TFA]^-$. Charge displacement profiles on defect-free surfaces with increasing $[OA]^+$ or $[TsO]^-$ surface concentration from **d,** 25 %, to **e,** 50 %, and to **f,** 100 %.

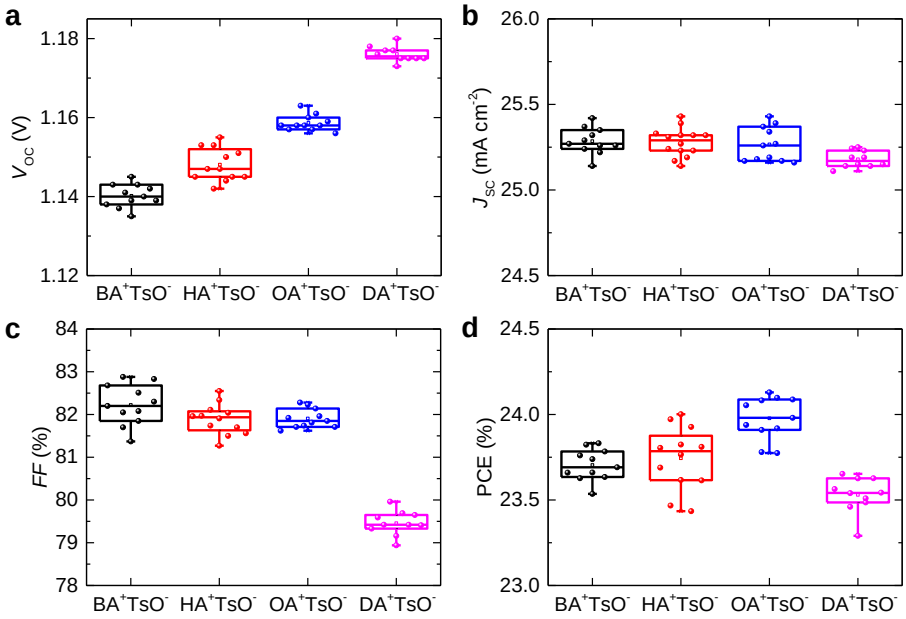

Figure A4.29. Device photovoltaic parameters with different tosylate-based salts. Box plots showing the distribution of the **a,** V_{OC}, **b,** J_{SC}, **c,** *FF*, and **d,** PCE of the devices. Center line: median, box limits: 25th and 75th percentile, whiskers: outliers.

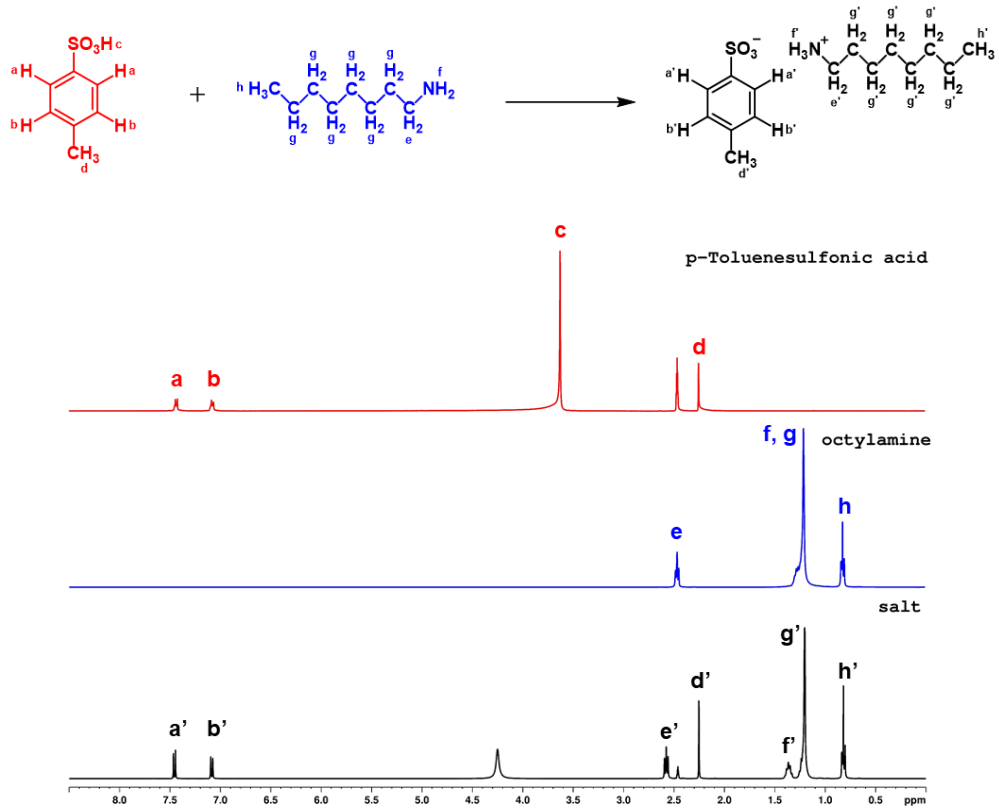

Figure A4.30. ^{1}H NMR spectra of p-Toluenesulfonic acid (red), octylamine (blue) and OATsO salt

(black) in DMSO-d_6. The chemical structures and reaction scheme are shown above the spectra. All atoms are labelled for identifying their corresponding peaks in the spectra.

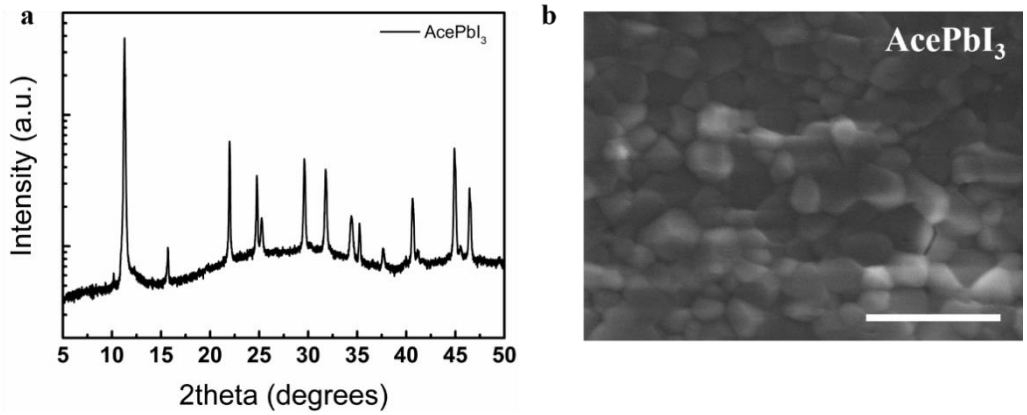

Figure A5.1. a) X-ray diffraction spectra in logarithmic scale and b) top surface scanning electron microscopy image of the $AcePbI_3$ film. Scale bar in b is 1 µm.

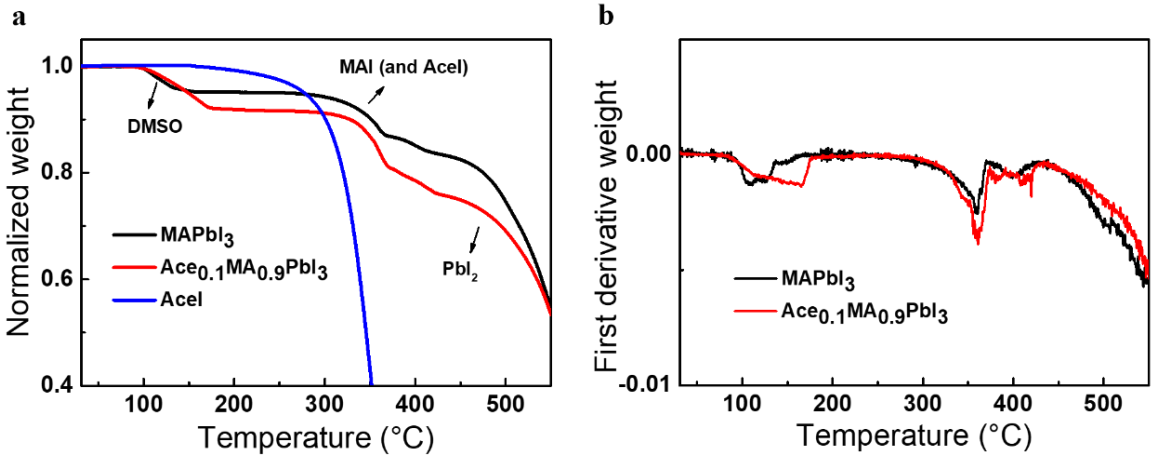

Figure A5.2. a) Weight loss and b) first derivative of weight loss as a function of temperature of the perovskite powders and AceI precursor measured using thermogravimetric analysis.

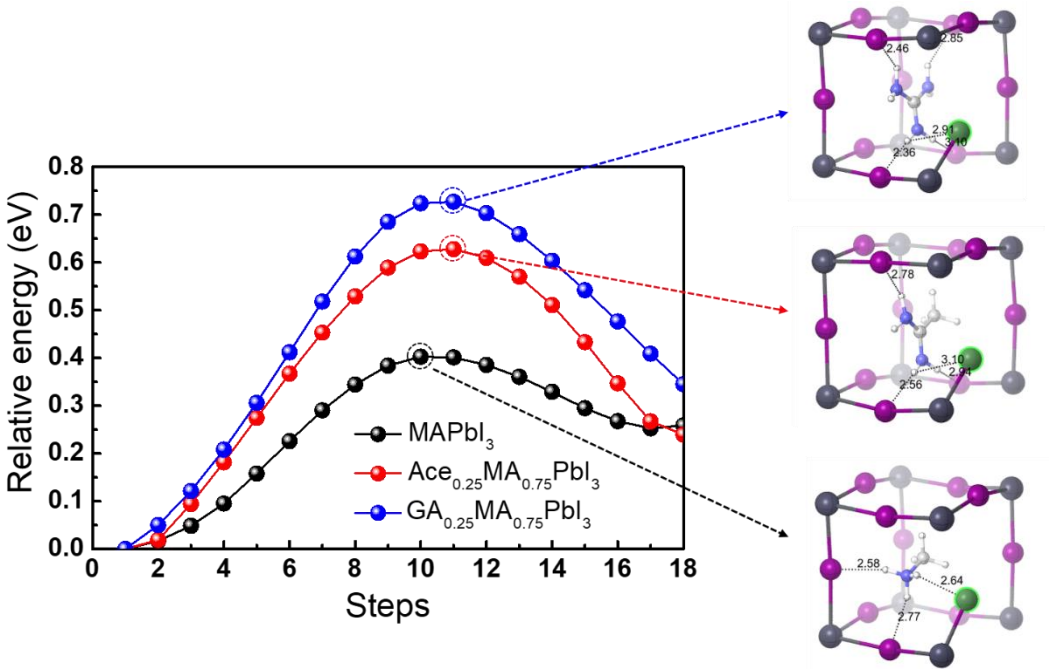

Figure A5.3. Iodide ion migration activation energy for $MAPbI_3$, $Ace_{0.25}MA_{0.75}PbI_3$ and $GA_{0.25}MA_{0.75}PbI_3$ calculated using DFT. Included are transition states corresponding to the maximum energy states, showing the hydrogen bond length between the migrating iodide ion (highlighted in green) and the nearest neighbouring hydrogen atom.

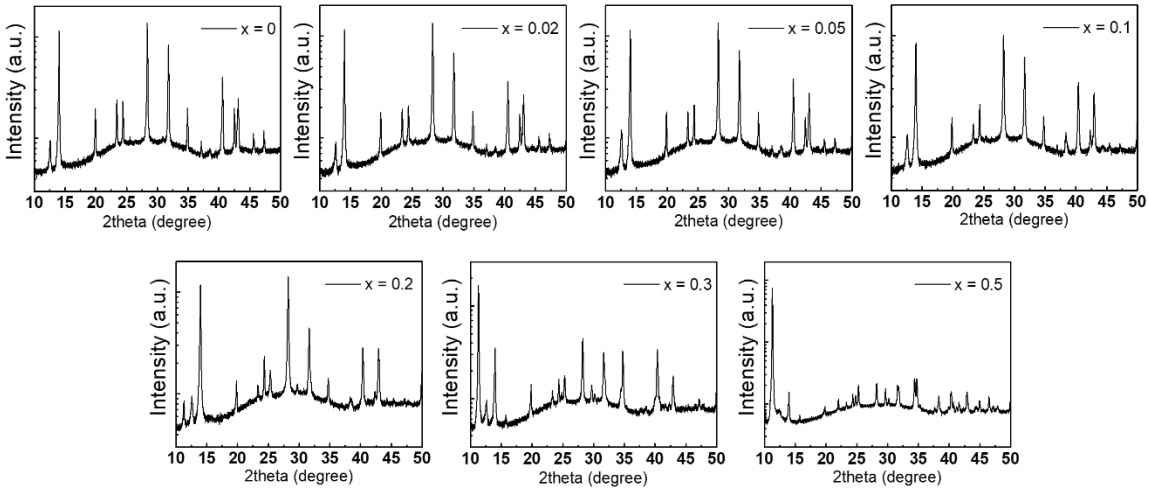

Figure A5.4. X-ray diffraction spectra in logarithmic scale of the $Ace_xMA_{1-x}PbI_3$ films with different values of x.

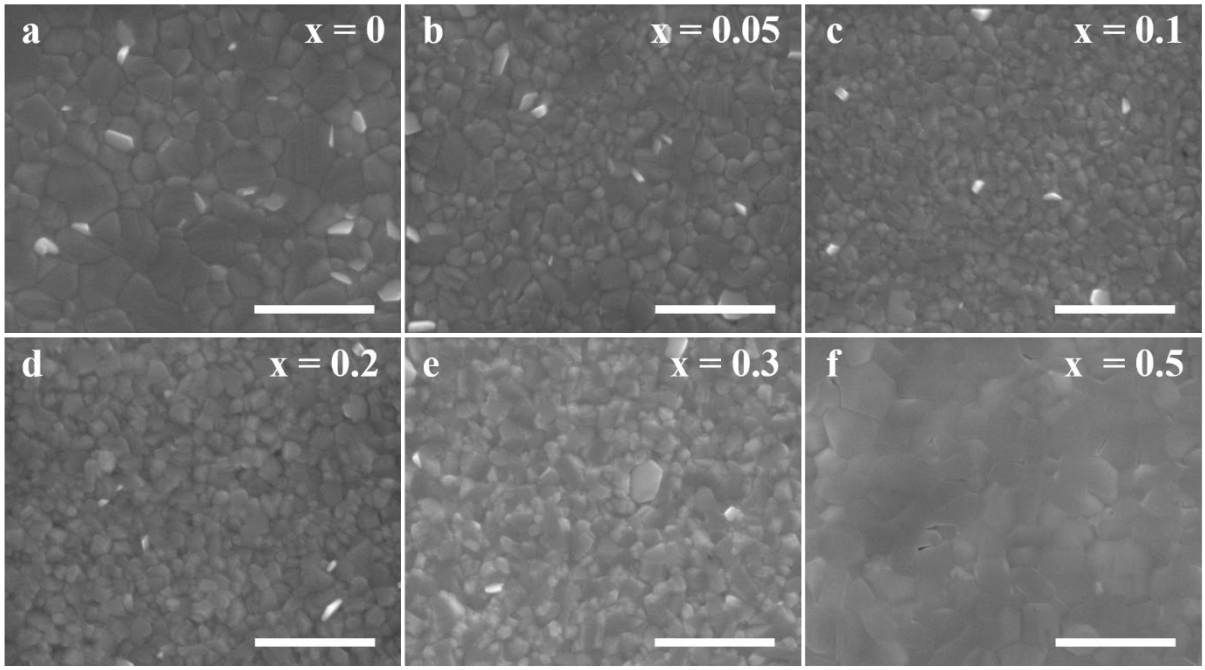

Figure A5.5. Top surface scanning electron microscopy images of the $Ace_xMA_{1-x}PbI_3$ films with different amounts of Ace substituted. Scale bar is 1 μm.

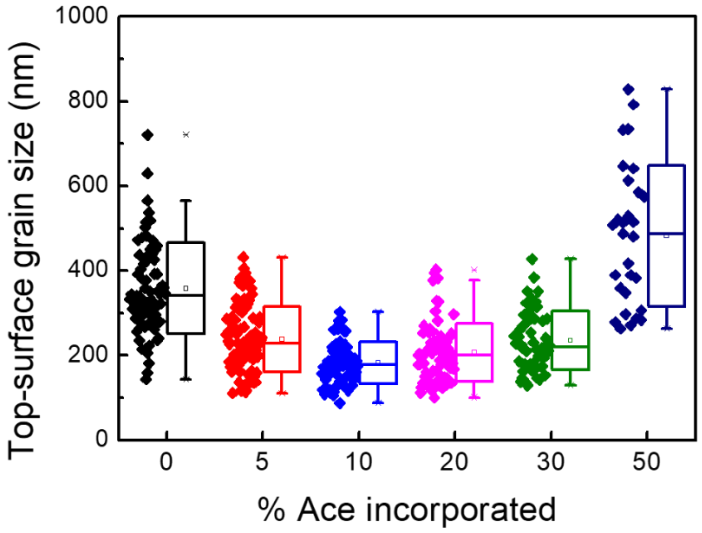

Figure A5.6. Apparent grain size of the $Ace_xMA_{1-x}PbI_3$ films with different amounts of Ace substituted determined from the top surface scanning electron microscopy images.

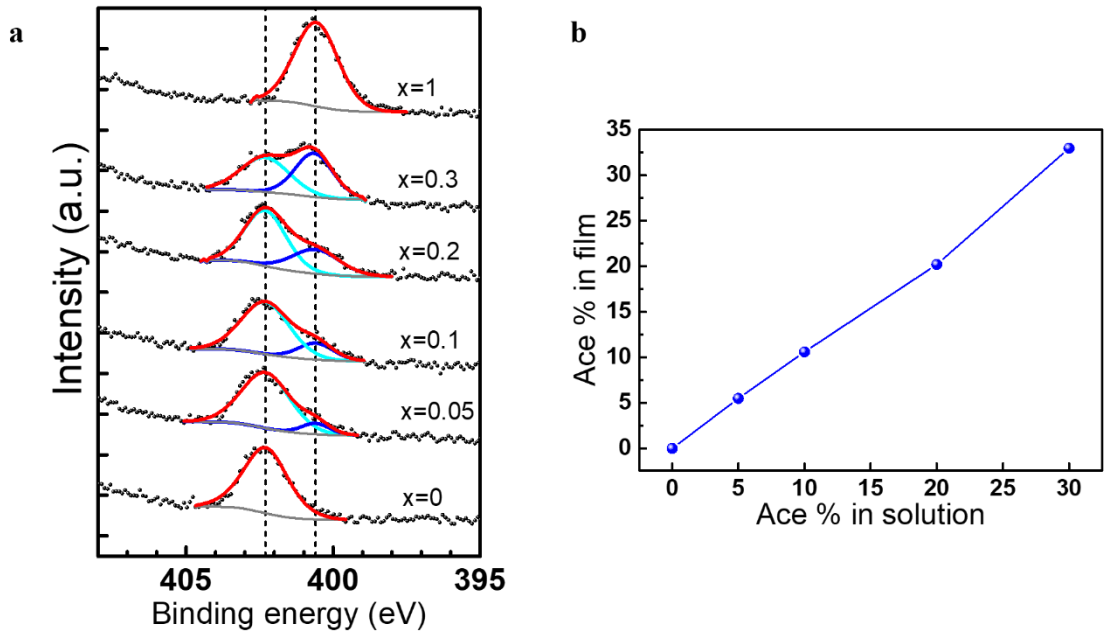

Figure A5.7. a) X-ray photoelectron spectroscopy (XPS) spectra of the $Ace_xMA_{1-x}PbI_3$ films with different amounts of Ace substituted, showing the fitted lines for the deconvoluted N 1s peaks from the NH_3^+ group in MA (cyan) and NH_2^+ group in Ace (blue), the convoluted peak (red), and the background (gray). The raw data is shown as empty circles. b) Comparison of the percentage Ace in the precursor solution versus the percentage in the perovskite film as determined from the XPS fitting.

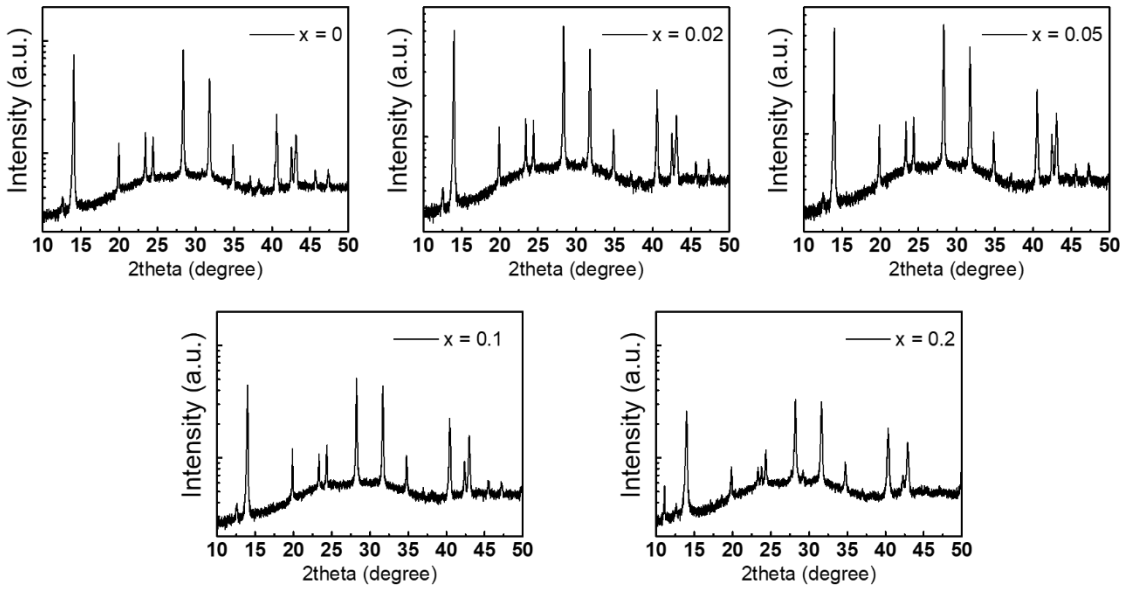

Figure A5.8. X-ray diffraction spectra in logarithmic scale of the $GA_xMA_{1-x}PbI_3$ films with different values of x.

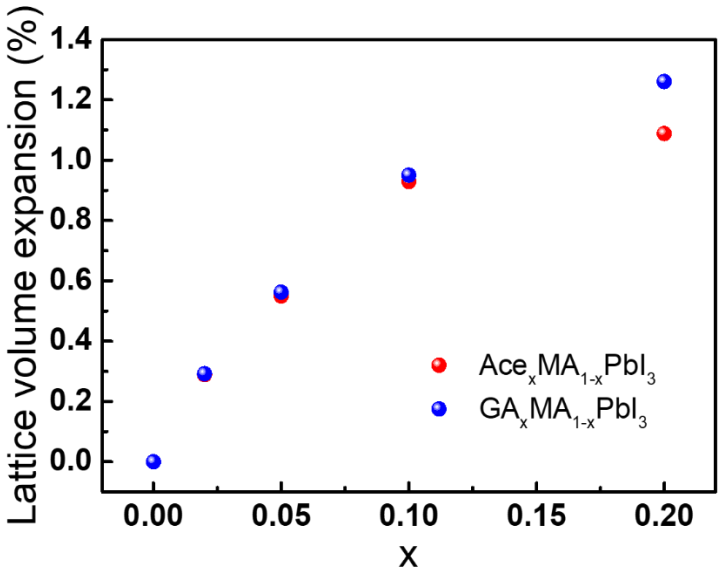

Figure A5.9. Lattice volume expansion of the $Ace_xMA_{1-x}PbI_3$ or $GA_xMA_{1-x}PbI_3$ films with different values of x with respect to $MAPbI_3$.

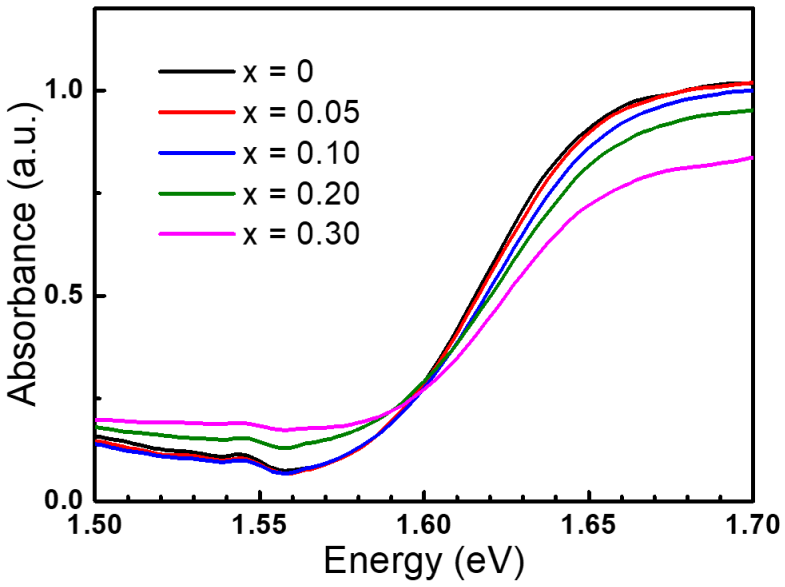

Figure A5.10. Absorption profile of the $Ace_xMA_{1-x}PbI_3$ films as a function of photon energy.

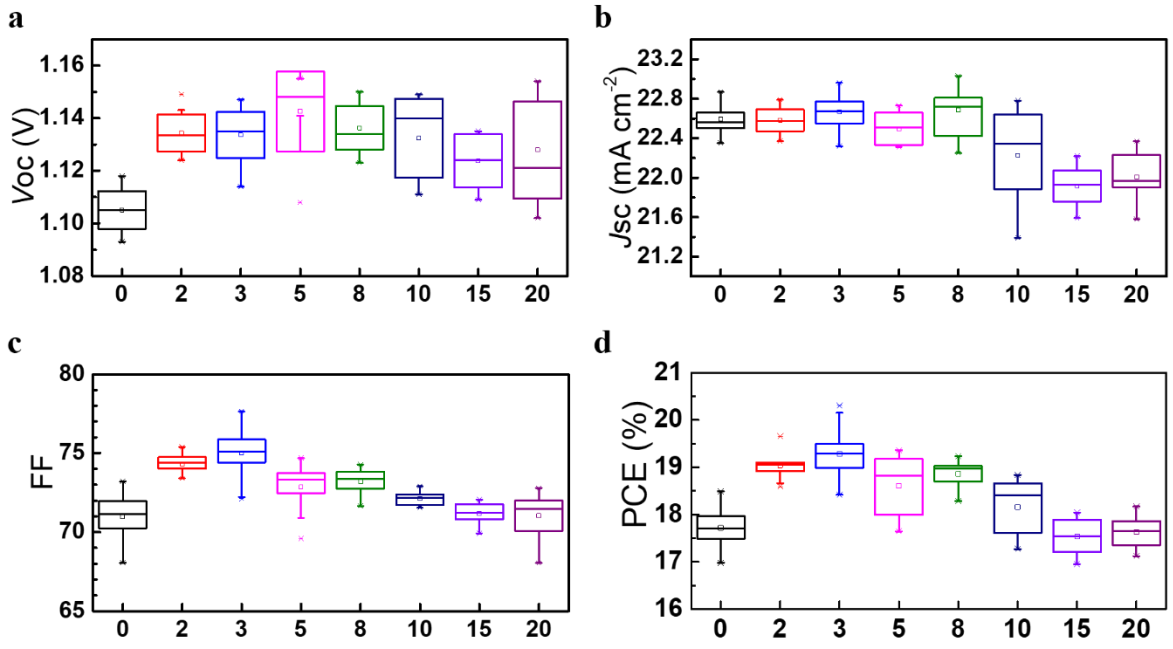

Figure A5.11. Box plots showing the distribution of the a) open-circuit voltage (V_{OC}), b) short-circuit current density (J_{SC}), c) fill factor (FF), and d) power conversion efficiency (PCE) of the $Ace_xMA_{1-x}PbI_3$ devices with different percentages of Ace substituted.

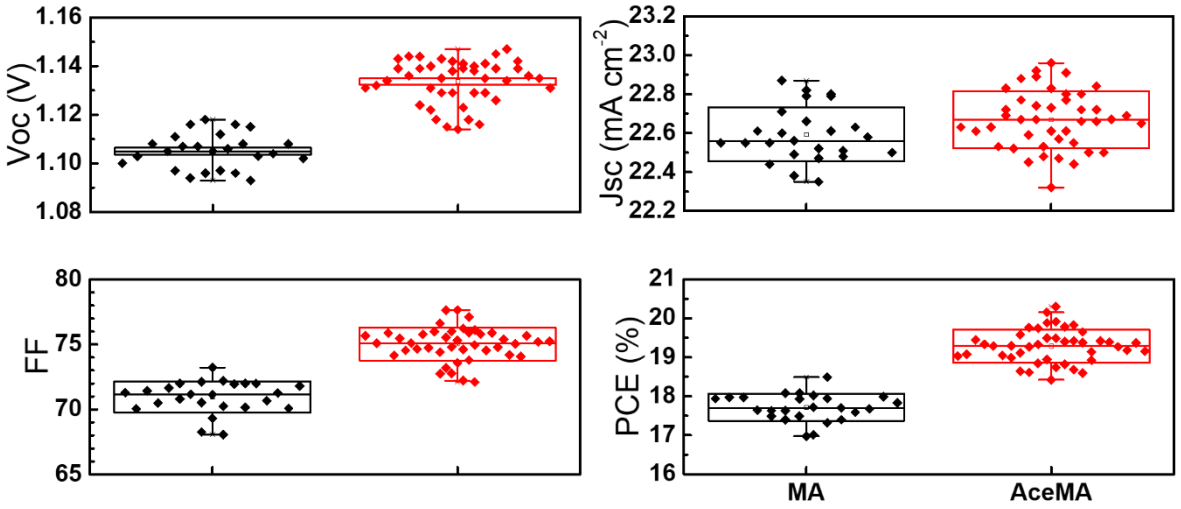

Figure A5.12. Box plots showing the distribution of the short-circuit current density (J_{SC}), open-circuit voltage (V_{OC}), fill factor (FF), and power conversion efficiency (PCE) of the $MAPbI_3$ and $Ace_{0.03}MA_{0.97}PbI_3$ devices.

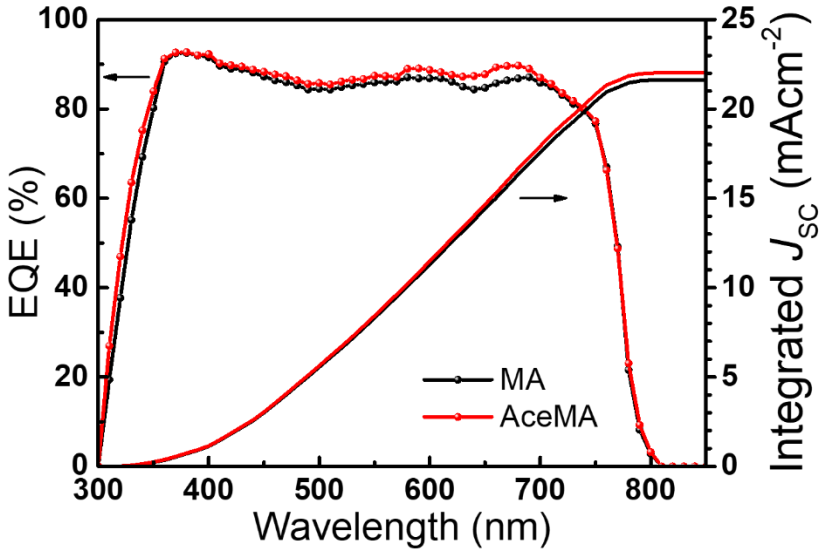

Figure A5.13. External quantum efficiency (EQE) spectra and integrated J_{SC} of the $MAPbI_3$ and $Ace_{0.03}MA_{0.97}PbI_3$ devices.

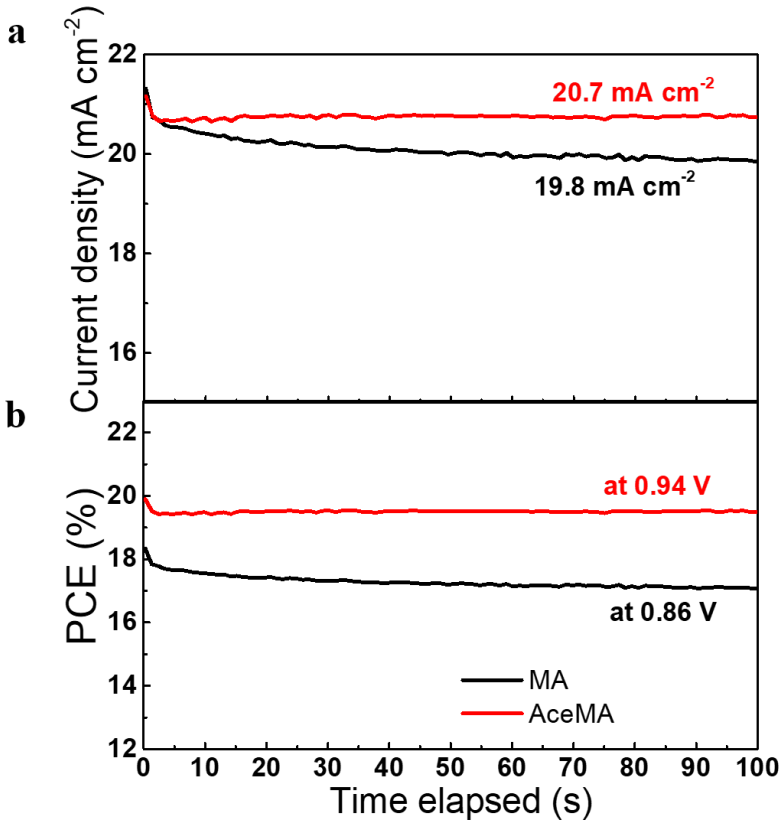

Figure A5.14. a) Current density and b) power conversion efficiency (PCE) of the champion $MAPbI_3$ and $Ace_{0.03}MA_{0.97}PbI_3$ devices as a function of time at a constant applied bias.

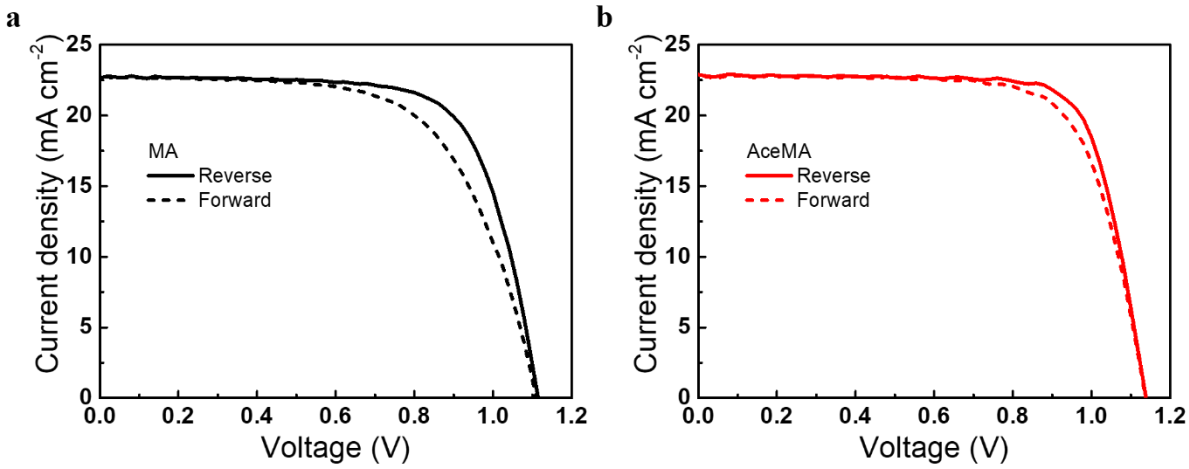

Figure A5.15. Current density and voltage (*J*-*V*) curves of the a) $MAPbI_3$ and b) $Ace_{0.03}MA_{0.97}PbI_3$ devices with different scan directions.

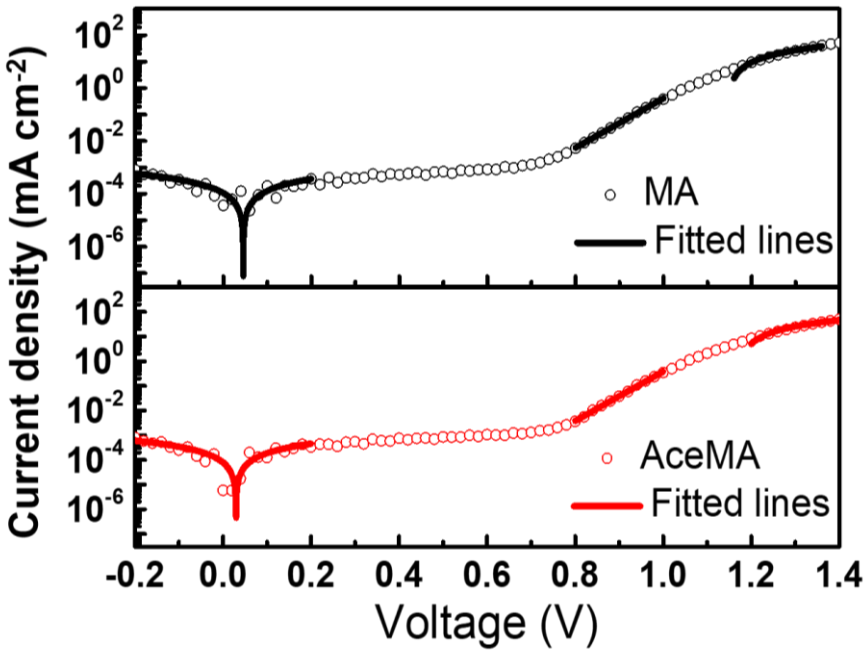

Figure A5.16. Dark current density and voltage (*J*-*V*) curves of the $MAPbI_3$ (MA) and $Ace_{0.03}MA_{0.97}PbI_3$ (AceMA) devices. Solid lines are fitted to extract the shunt (R_{sh}) and series (R_s) resistances, ideality factor (n) and dark current (J_0).

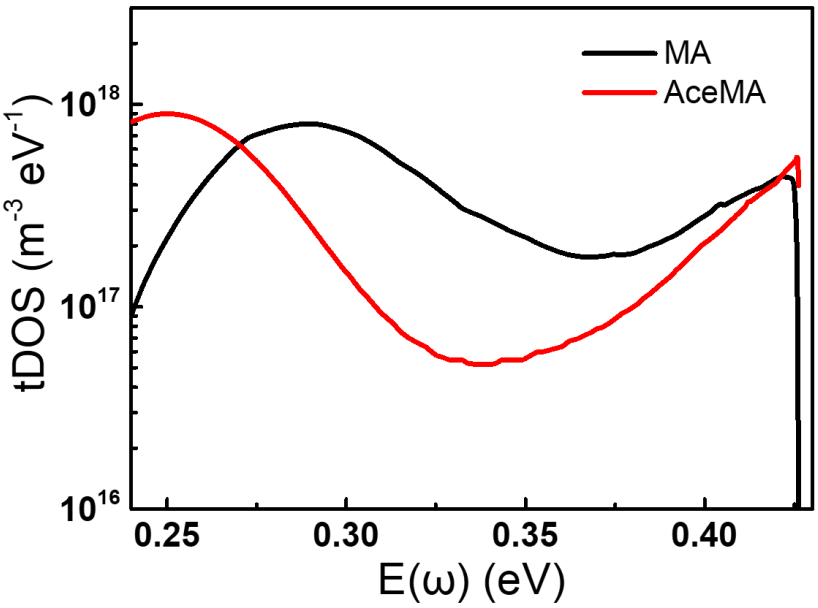

Figure A5.17. Trap density of states (tDOS) of the MA and AceMA devices measured using Thermal Admittance Spectroscopy.

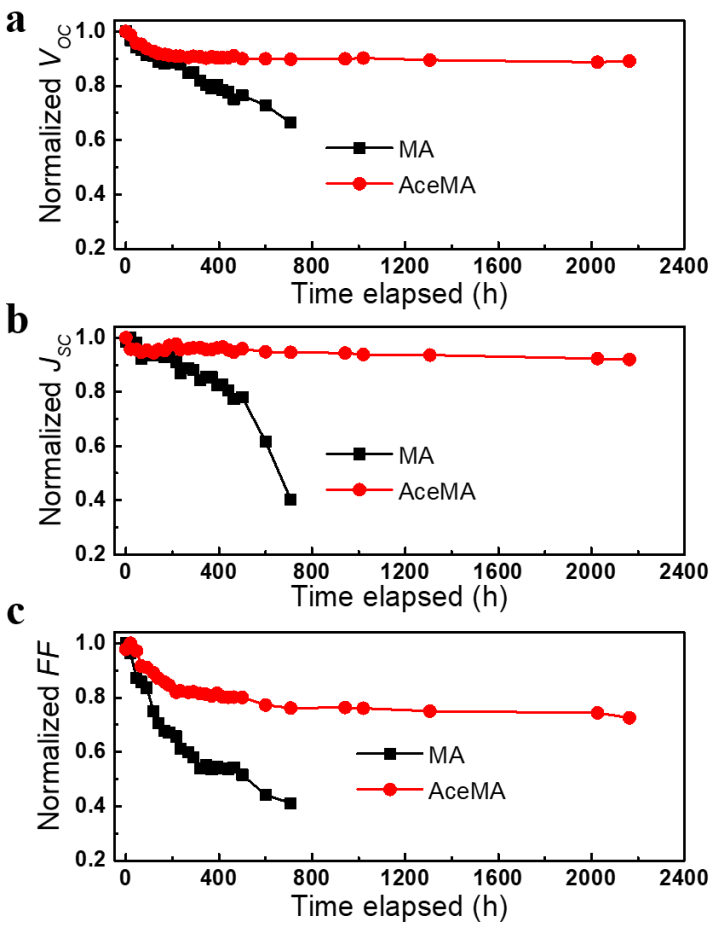

Figure A5.18. Degradation of the a) open-circuit voltage (V_{OC}), b) short-circuit current density (J_{SC}), and c) fill factor (FF) of the $MAPbI_3$ and $Ace_{0.03}MA_{0.97}PbI_3$ devices aged under continuous 1 sun intensity illumination at open-circuit conditions.

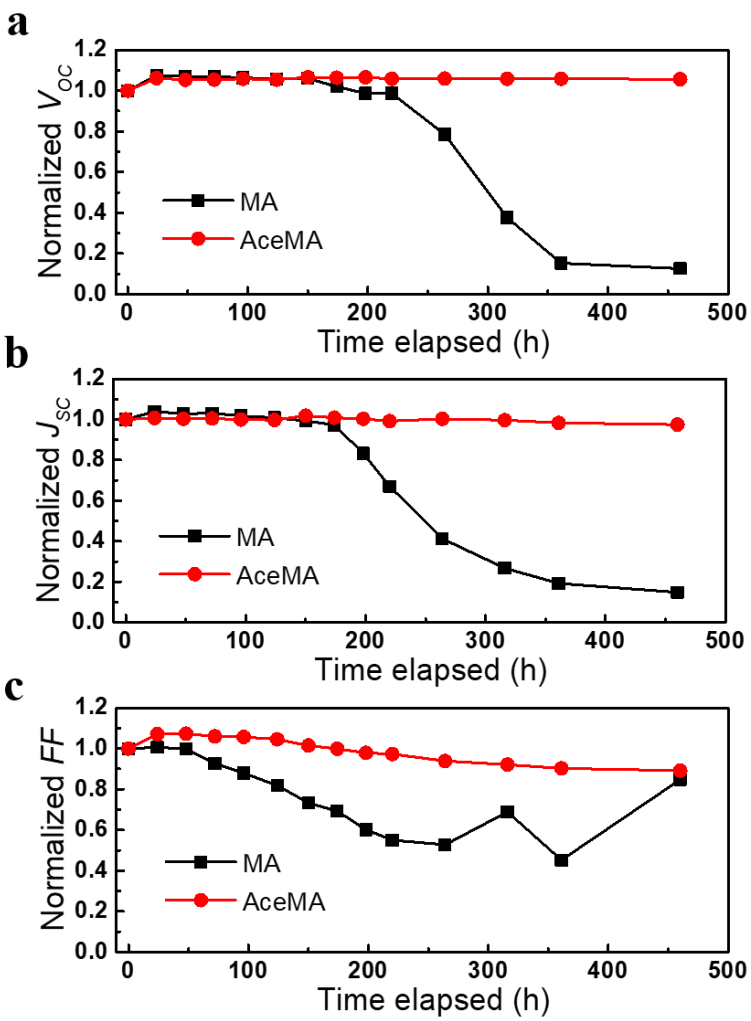

Figure A5.19. Degradation of the a) open-circuit voltage (V_{OC}), b) short-circuit current density (J_{SC}), and c) fill factor (FF) of the $MAPbI_3$ and $Ace_{0.03}MA_{0.97}PbI_3$ devices aged under continuous heating at 85 °C in a nitrogen atmosphere.

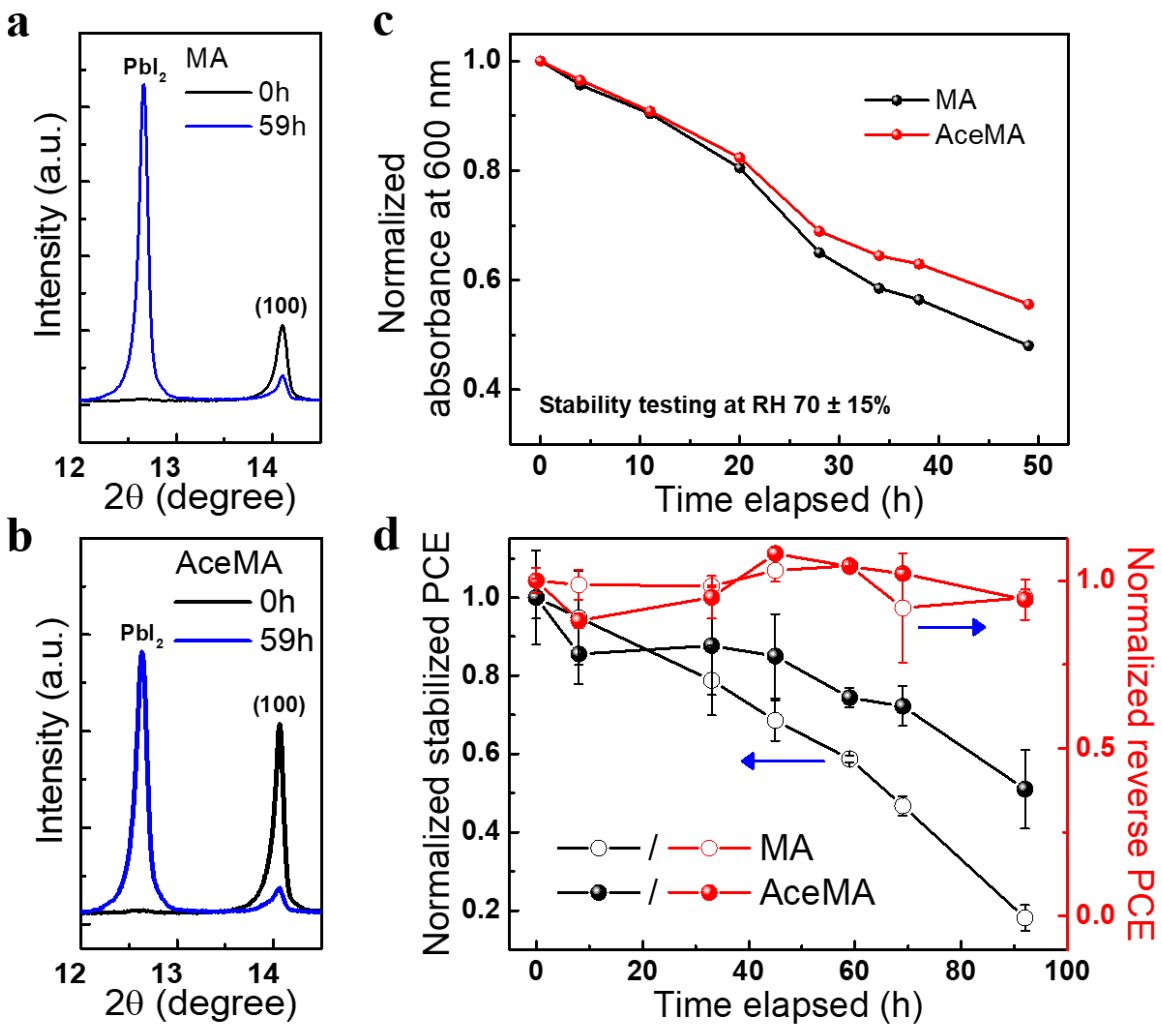

Figure A5.20. X-ray diffractogram of the a) $MAPbI_3$ and b) $Ace_{0.03}MA_{0.97}PbI_3$ films before and after the humidity (RH 70 ± 15%) aging. Degradation of the c) normalized absorbance at 600 nm and d) stabilized and reverse scan power conversion efficiency of the $MAPbI_3$ and $Ace_{0.03}MA_{0.97}PbI_3$ films and devices, respectively, aged under a humid environment (RH 70 ± 15%).

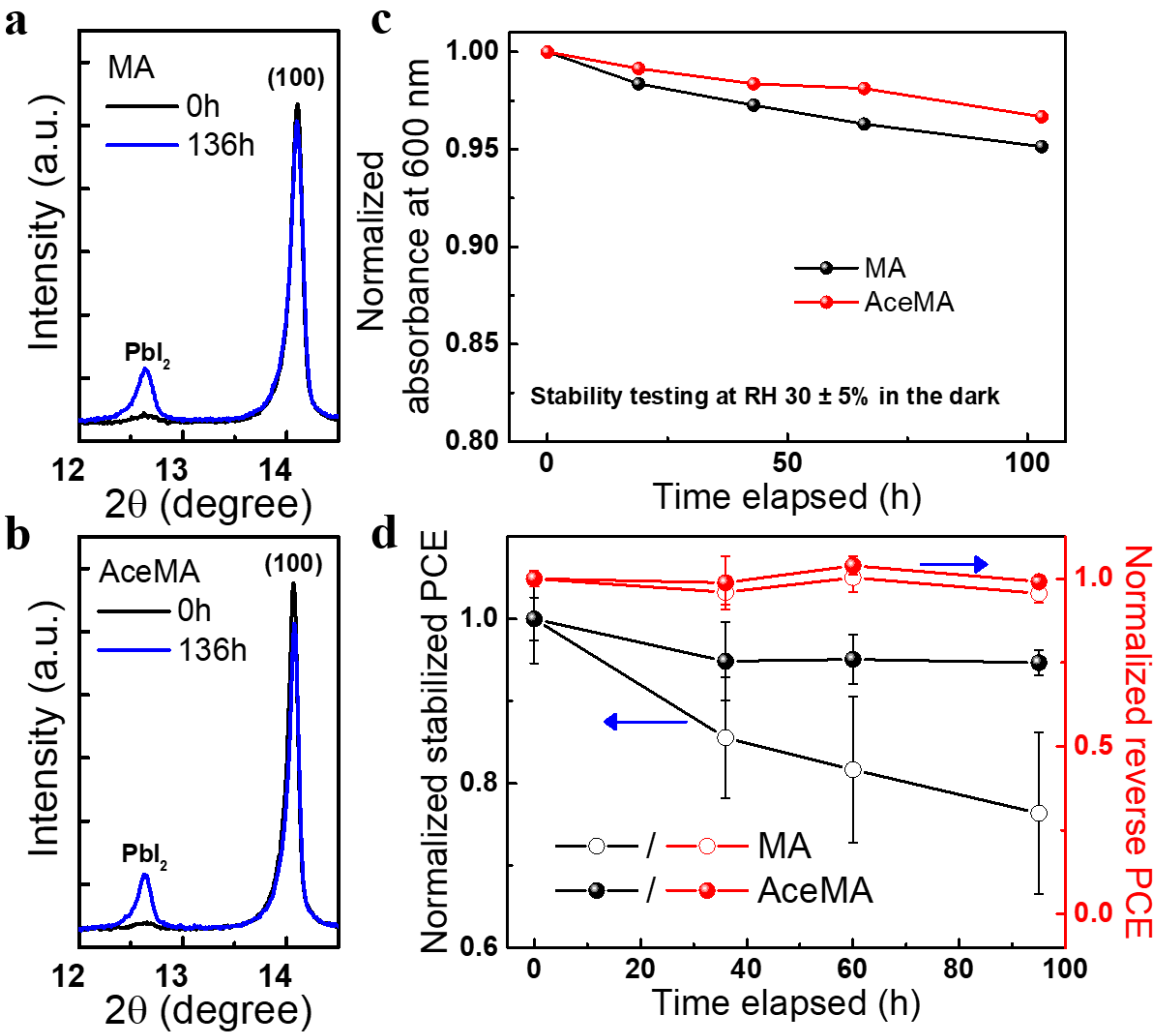

Figure A5.21. X-ray diffractogram of the a) $MAPbI_3$ and b) $Ace_{0.03}MA_{0.97}PbI_3$ films before and after the ambient (RH 30 ± 5%) aging. Degradation of the c) normalized absorbance at 600 nm and d) stabilized and reverse scan power conversion efficiency of the $MAPbI_3$ and $Ace_{0.03}MA_{0.97}PbI_3$ films and devices, respectively, aged under an ambient environment (RH 30 ± 5%).

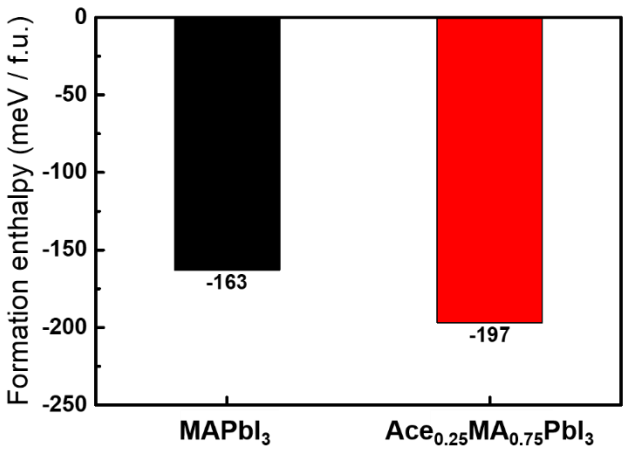

Figure A5.22. Formation enthalpy per formula unit of the $MAPbI_3$ and $Ace_{0.25}MA_{0.75}PbI_3$ compositions calculated using *ab initio* simulations.

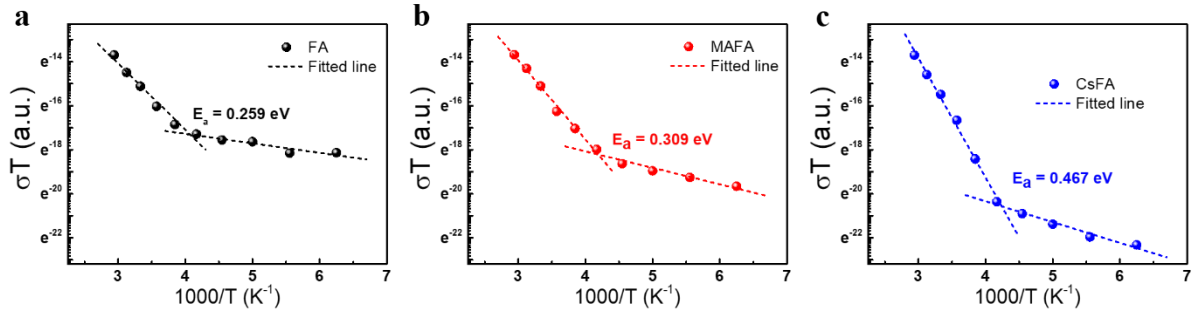

Figure A5.23. Temperature-dependent conductivity of the a) $FAPbI_3$ and b) $MA_{0.05}FA_{0.95}PbI_3$ and c) $Cs_{0.05}FA_{0.95}PbI_3$ lateral devices.

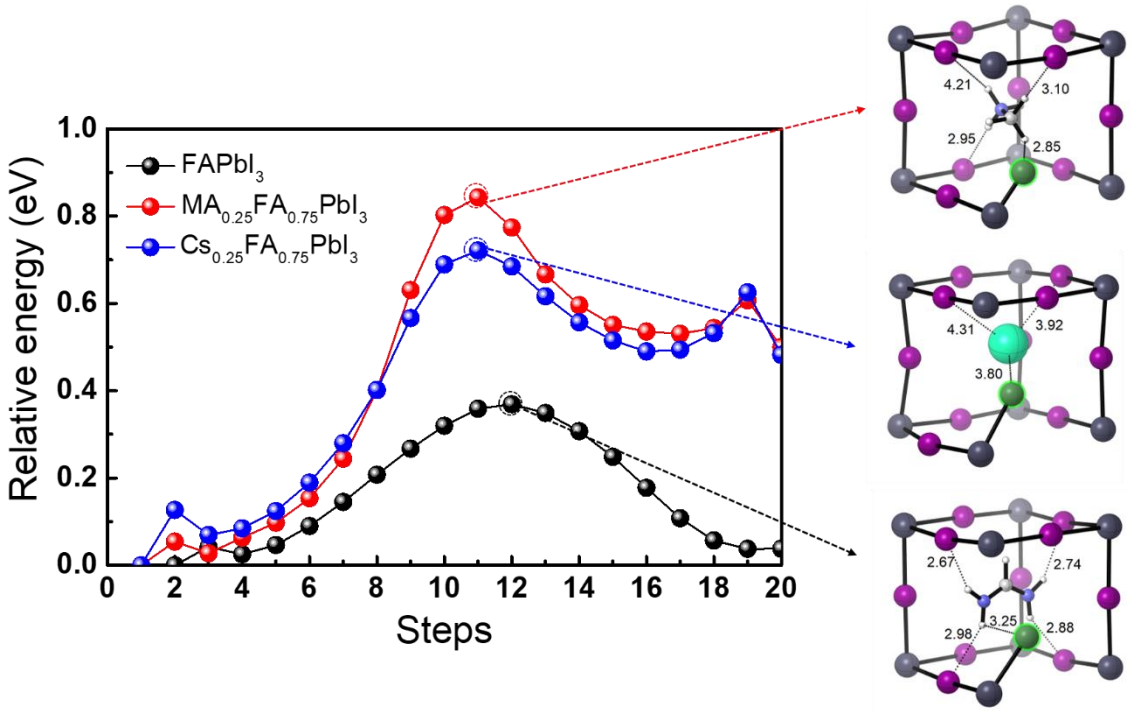

Figure A5.24. Iodide ion migration activation energy for $FAPbI_3$, $MA_{0.25}FA_{0.75}PbI_3$ and $Cs_{0.25}FA_{0.75}PbI_3$ calculated using DFT. Included are transition states corresponding to the maximum energy states, showing the bond length between the migrating iodide ion (highlighted in green) and the nearest neighboring atom.

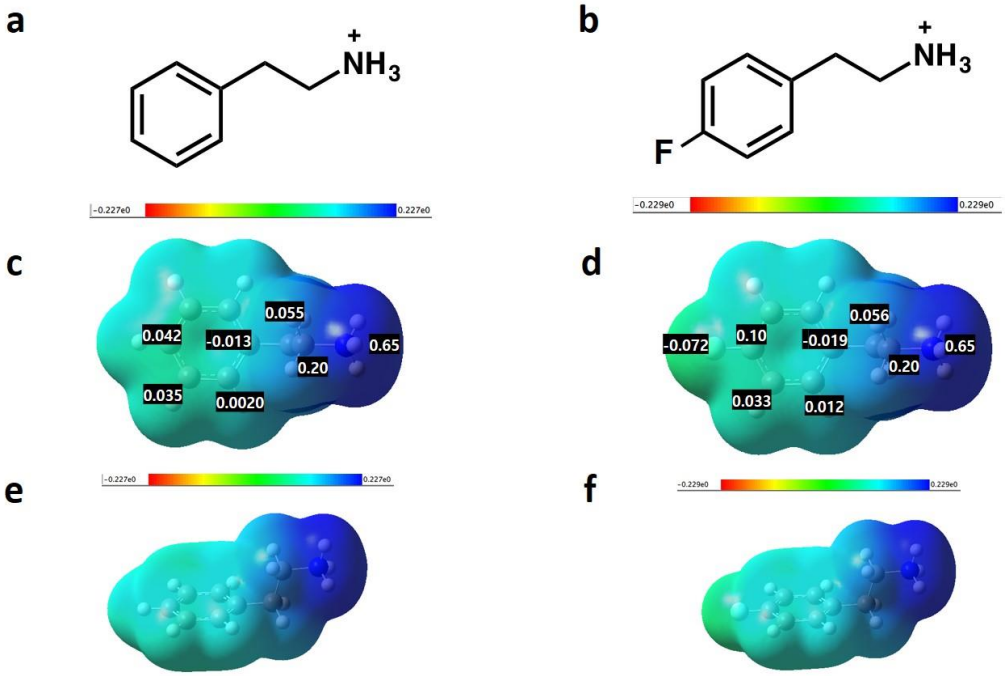

Figure A6.1. Charge distribution determined by density functional theory (DFT) calculation. Schematics showing molecular structure structure of a, phenethylammonium cation (PEA^+) and b, 4-fluoro-phenethylammonium cation ($FPEA^+$). Charge distribution of the c, e, PEA^+ and d, f, $FPEA^+$ molecules calculated by DFT calculation. c, d, top and e, f, cross sectional views

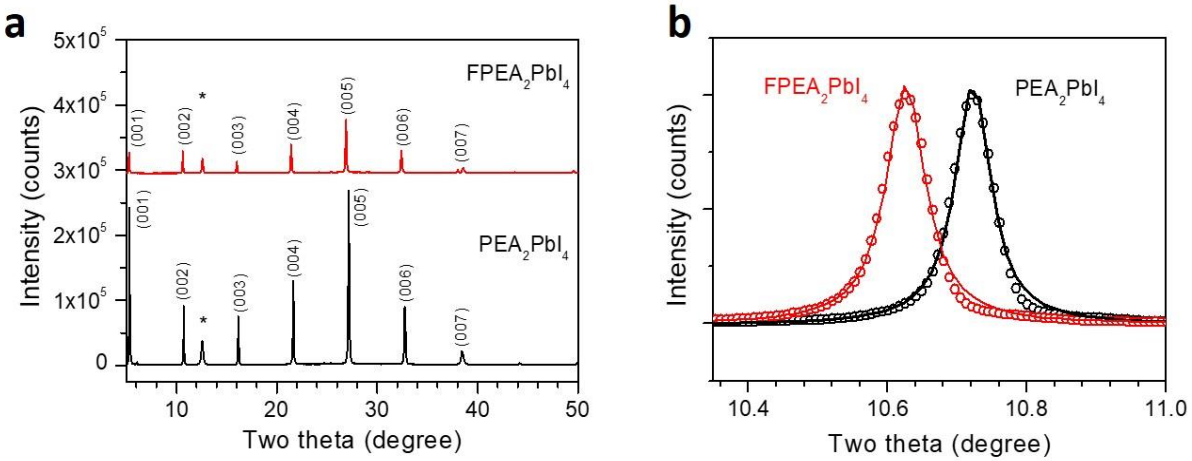

Figure A6.2. X-ray diffraction (XRD) patterns of PEA_2PbI_4 and $FPEA_2PbI_4$ films. a, XRD patterns of PEA_2PbI_4 and $FPEA_2PbI_4$ films on a glass substrate. The peaks indexed by * is from (001) orientation of PbI_2. b, The normalized (002) orientation peaks where the open circles are measured data and solid lines are the fitted curves using a Lorentzian distribution function.

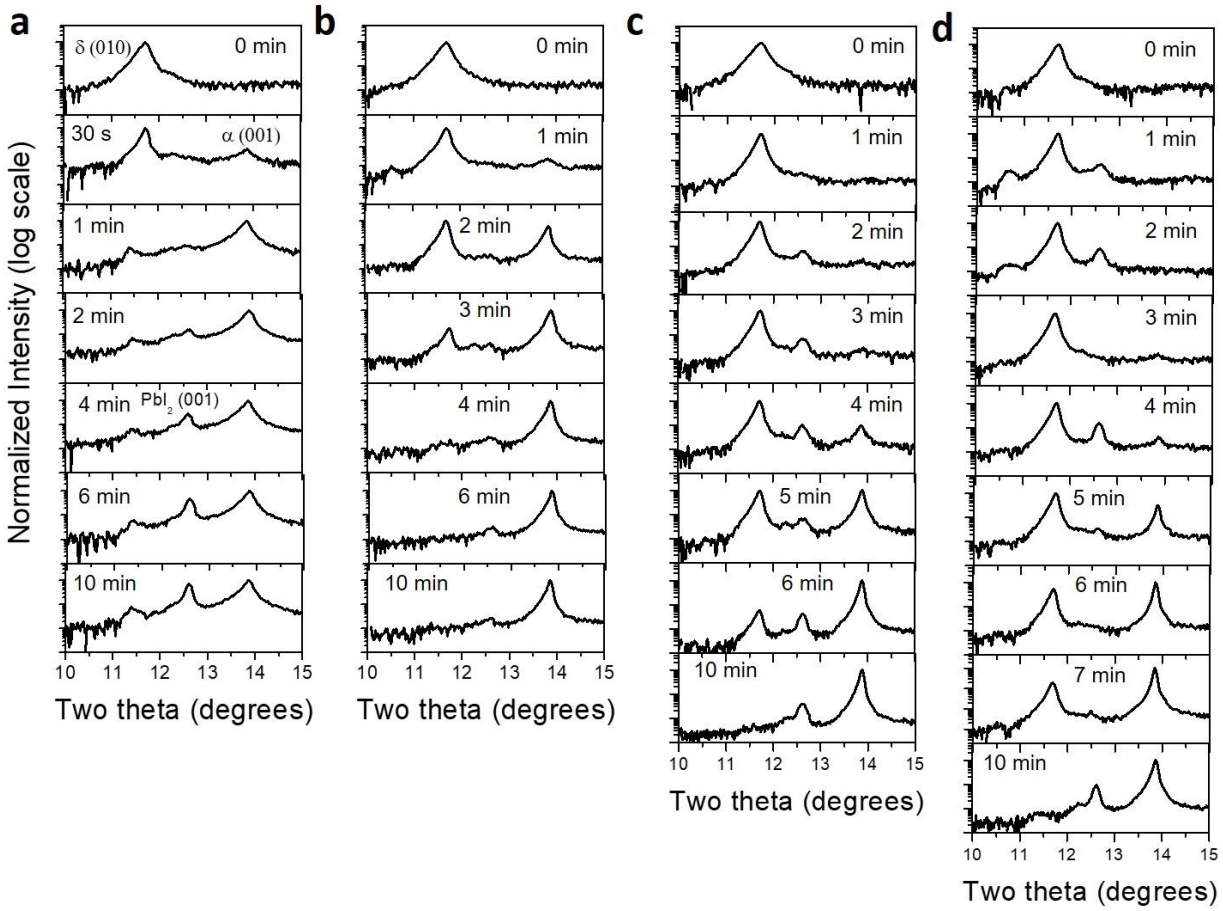

Figure A6.3. X-ray diffraction (XRD) patterns of $FAPbI_3$ films with different compositions and annealing time at 150 °C. a, control: bare $FAPbI_3$, b, 1P: $FAPbI_3$ with 1.67 mol% PEA_2PbI_4, c, 3P: $FAPbI_3$ with 3.33 mol% PEA_2PbI_4, and d, 3F: $FAPbI_3$ with 3.33 mol% $FPEA_2PbI_4$.

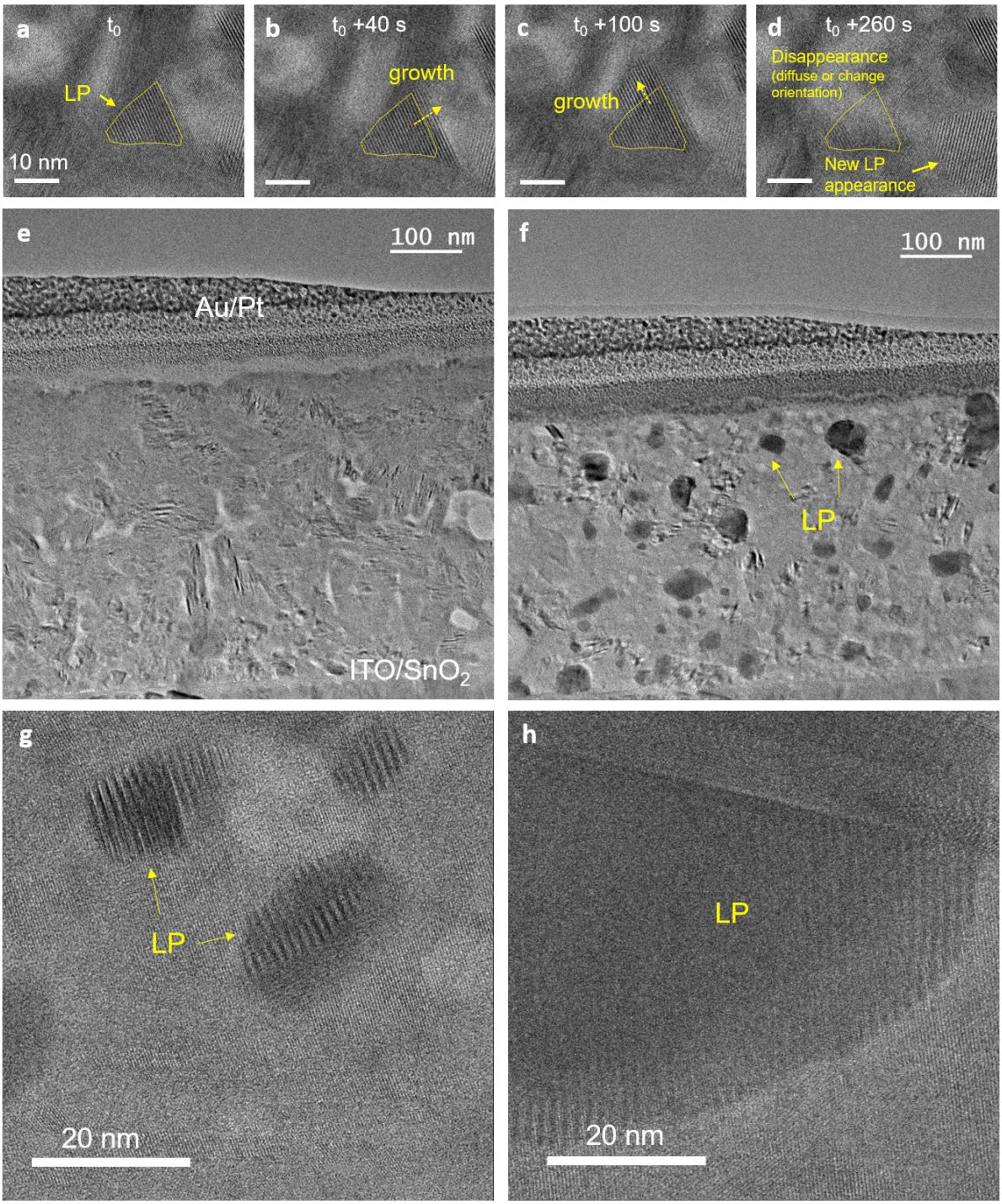

Figure A6.4. a-d, In-situ cross-sectional transmission electron microscopy (TEM) images of the layered perovskite (LP) in the $FAPbI_3$ film incorporated with 3.33 mol% $FPEA_2PbI_4$. The film was heated for different times to induce the phase transition of $FAPbI_3$ from its hexagonal phase to cubic polymorph. Cross sectional TEM images of $FAPbI_3$ films with 3.33 mol% $FPEA_2PbI_4$ e, before and f, after the in-situ measurement to induce the phase transition. Thickness of the sample

was around 50 nm. g,h, The magnified TEM images after the in-situ measurement, showing interface between LP phase and epitaxially grown $FAPbI_3$.

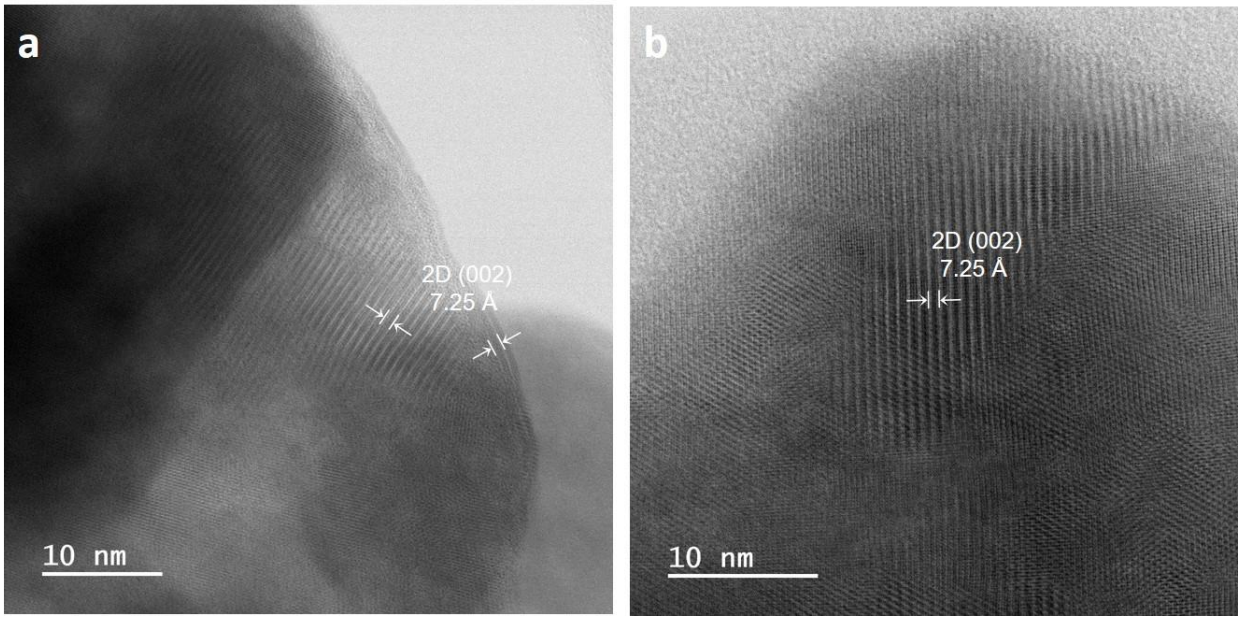

Figure A6.5. Scanning transmission electron microscopy images of $FAPbI_3$ films with 3.33 mol% $FPEA_2PbI_4$, a, before phase transition b, after phase transition. The samples were prepared by scratching off the films from the substrate.

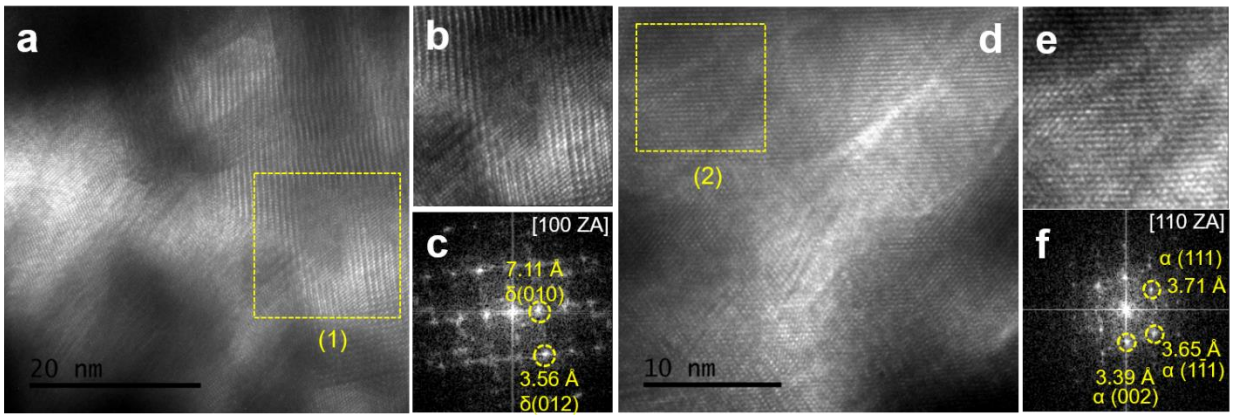

Figure A6.6. Transmission electron microscopic (TEM) analysis $FAPbI_3$ films. TEM images of the bare hexagonal a, b, and cubic d, e, $FAPbI_3$ film. b and e shows the magnified image of region 1 and 2, respectively. c and f show FFT analysis of the region 1 and 2 respectively. The samples were prepared by scratching off the films from the substrate.

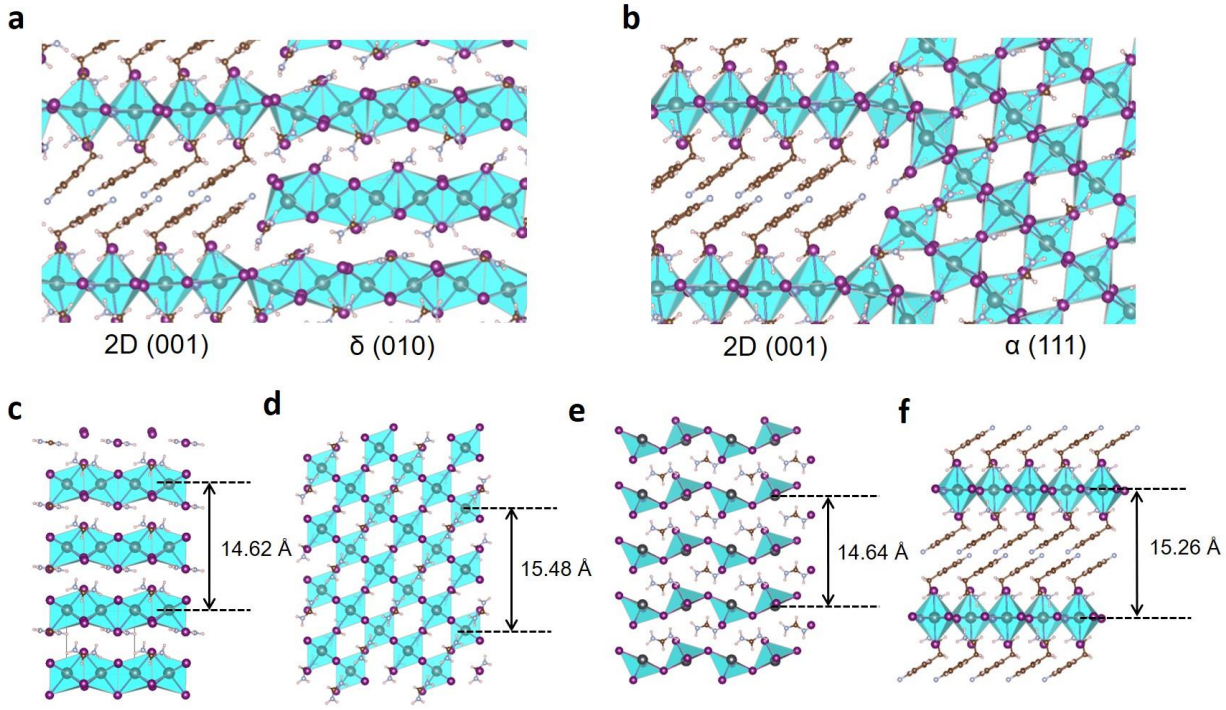

Figure A6.7. Schematics of perovskite crystal structure and their interfacial alignments. a, The interface between the hexagonal $FAPbI_3$ and $FPEA_2PbI_4$ crystals and b, the interface between the cubic $FAPbI_3$ and $FPEA_2PbI_4$ crystals determined by transmission electron microscopy studies. c-f, Density functional theory (DFT) optimized crystal configurations of $FAPbI_3$ and layered perovskite. δ-$FAPbI_3$ c, α-$FAPbI_3$ d, and transition state with the highest energy (saddle point, e) , and layered perovskite (f), where their interplanar distances are indicated in each figure. Purple spheres: iodine, black spheres: lead, brown spheres: carbon, white spheres: hydrogen

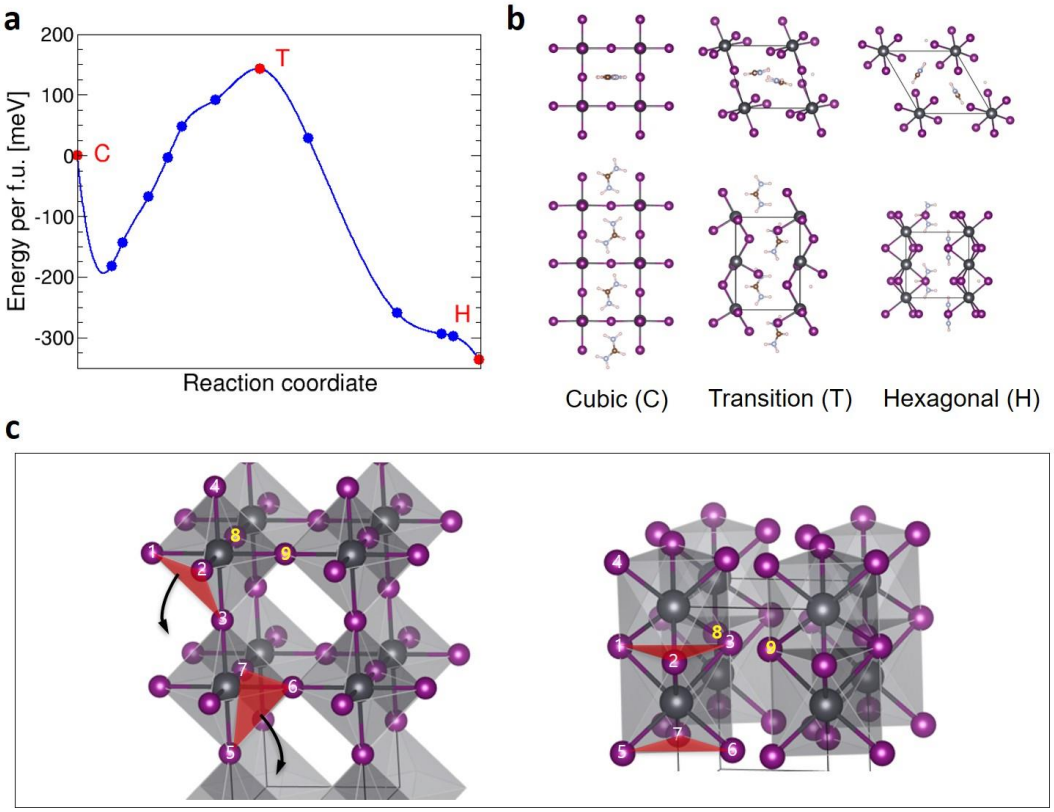

Figure A6.8. Phase conversion energetics without strain a, Energy landscape of the phase conversion of $FAPbI_3$. **b**, Atomic configurations of the cubic, hexagonal and transition state phases. **c**, Crystal models showing the phase conversion pathway where the atoms numbered to track their redistribution due to the phase conversion. Purple spheres: iodine, black spheres: lead, brown spheres: carbon, white spheres: hydrogen.

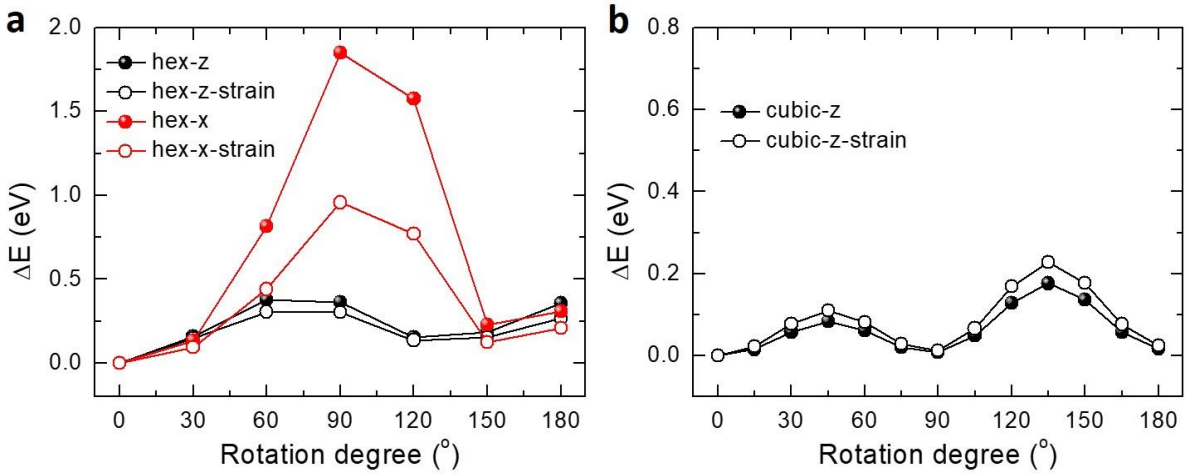

Figure A6.9. Calculated energy landscape for ratational motion of the FA^+ molecule. a, The energy landscape of the rotational motion of FA^+ in hexagonal phase without and with strain. Two different orientation was calculated (z and x axis). b, The energy landscape of the rotational motion of FA^+ in cubic phase without and with strain.

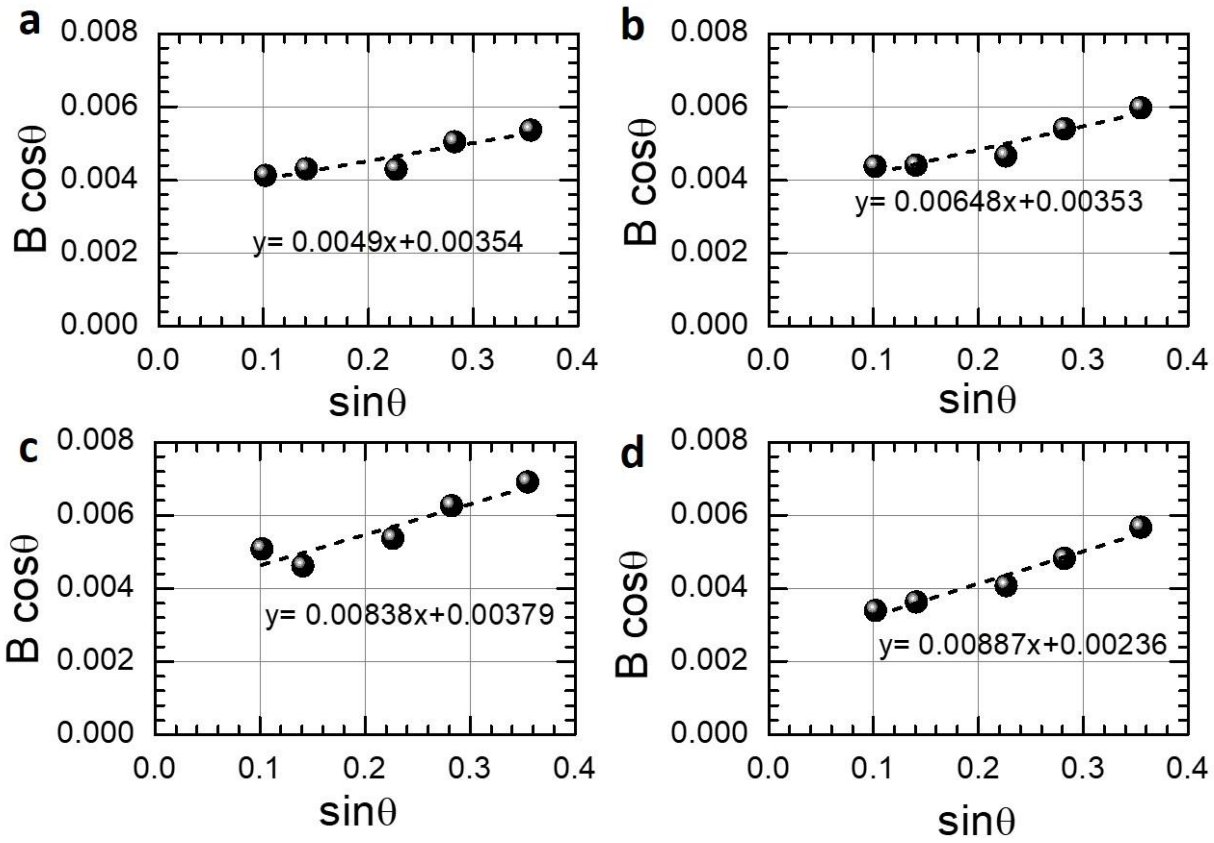

Figure A6.10. Willamson-Hall analysis of hexagonal $FAPbI_3$ films with different composition. a, control: bare $FAPbI_3$, b, 1P: $FAPbI_3$ with 1.67 mol% PEA_2PbI_4, c, 3P: $FAPbI_3$ with 3.33 mol% PEA_2PbI_4, d, 3F: $FAPbI_3$ with 3.33 mol% $FPEA_2PbI_4$. The filled curcles are measured data and dashed lines are fitted lines.

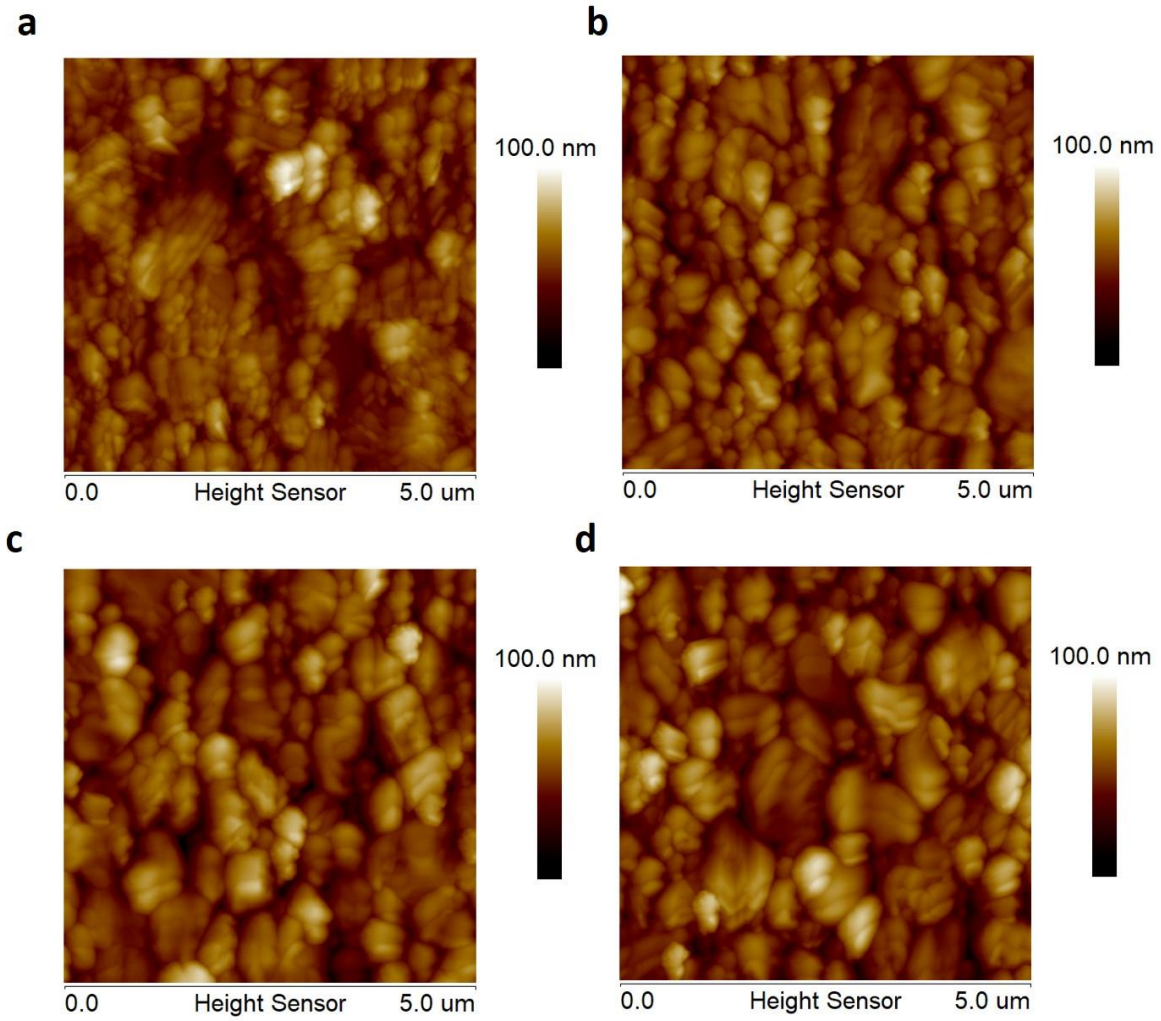

Figure A6.11. Atomic force microscopic (AFM) images of $FAPbI_3$ films. a, control: bare $FAPbI_3$, b, 1P: $FAPbI_3$ with 1.67 mol% PEA_2PbI_4, c, 3P: $FAPbI_3$ with 3.33 mol% PEA_2PbI_4, d, 3F: $FAPbI_3$ with 3.33 mol% $FPEA_2PbI_4$.

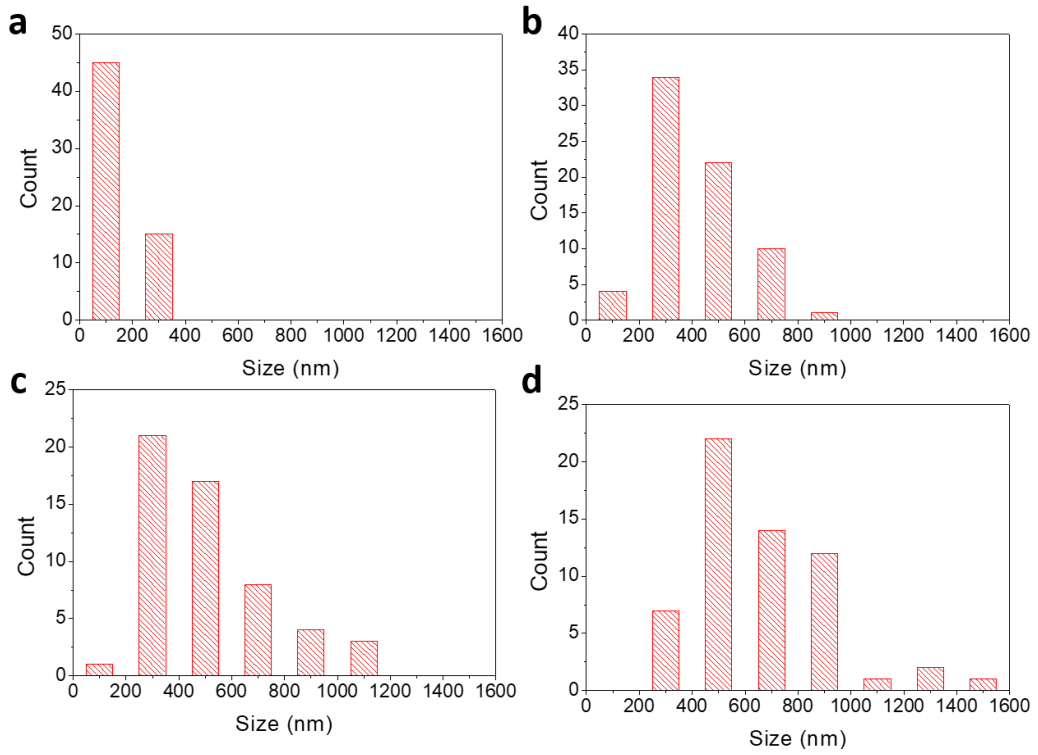

Figure A6.12. Grain size distribution extracted from the atomic force microscopy images. a, control: bare $FAPbI_3$, b, 1P: $FAPbI_3$ with 1.67 mol% PEA_2PbI_4, c, 3P: $FAPbI_3$ with 3.33 mol% PEA_2PbI_4, d, 3F: $FAPbI_3$ with 3.33 mol% $FPEA_2PbI_4$.

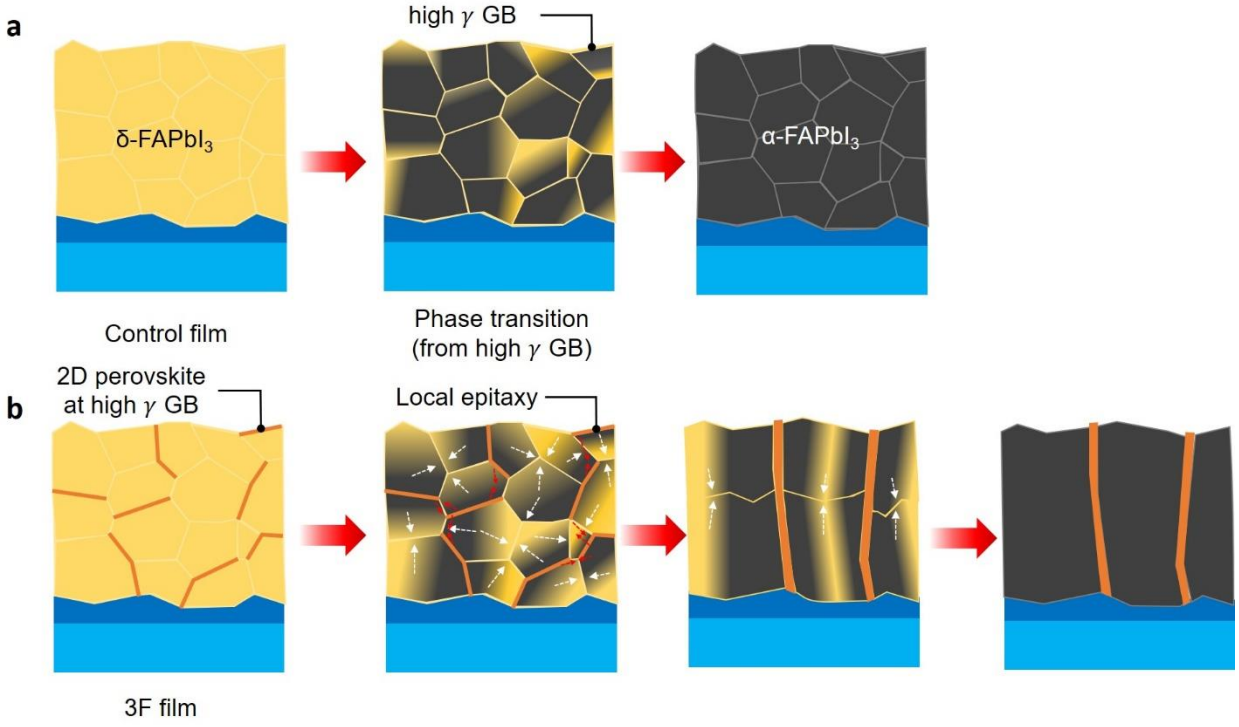

Figure A6.13. Proposed mechanism for the bulk heteroepitaxy process. a, Phase conversion process of the bare $FAPbI_3$ film. b, Phase conversion process of $FAPbI_3$ with added layered perovskite. GB: grain boundary, $\boldsymbol{\gamma}$: surface energy

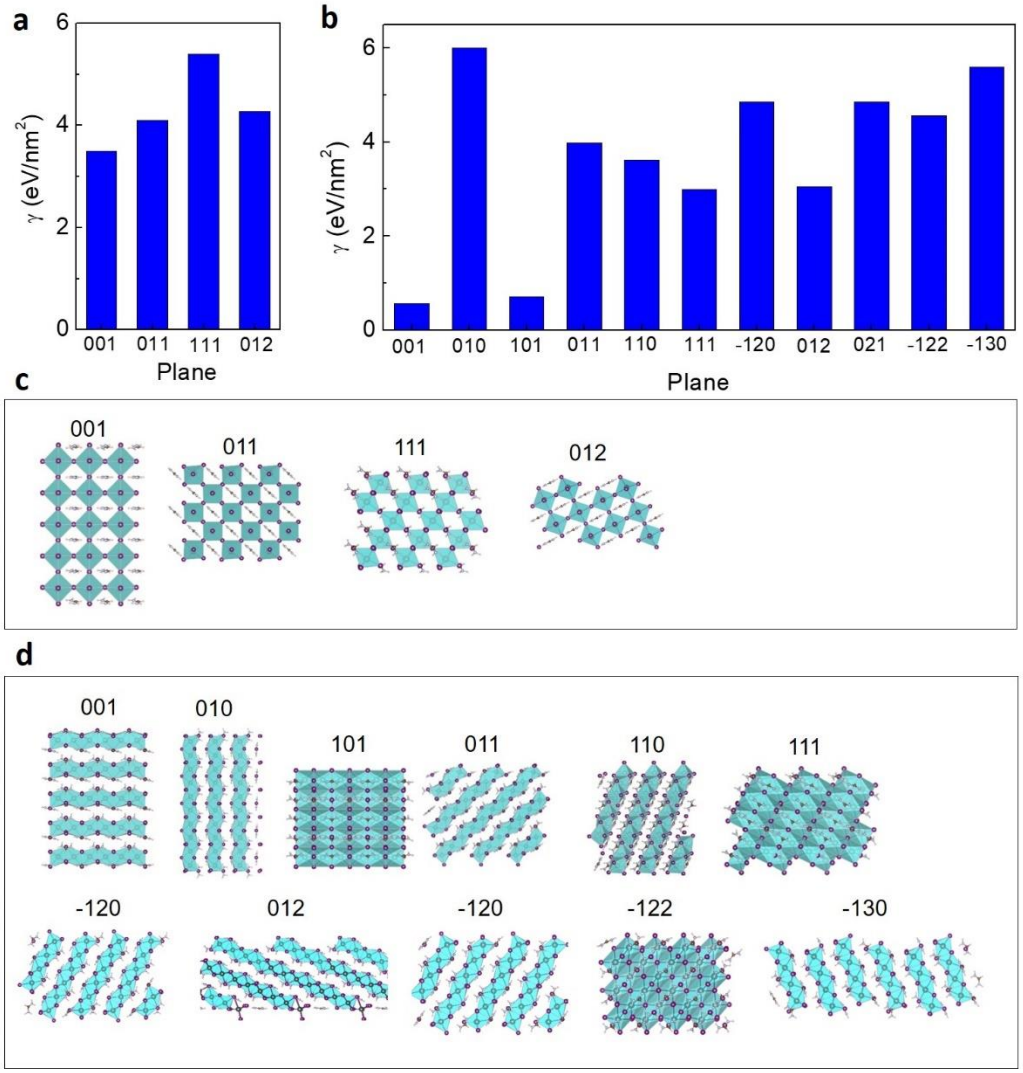

Figure A6.14. Calculated surface energies for **a**, α-$FAPbI_3$ and **b**, δ-$FAPbI_3$ **c, d**, Crystal configurations used for the calculations; **c**, α-$FAPbI_3$, **d**, δ-$FAPbI_3$.

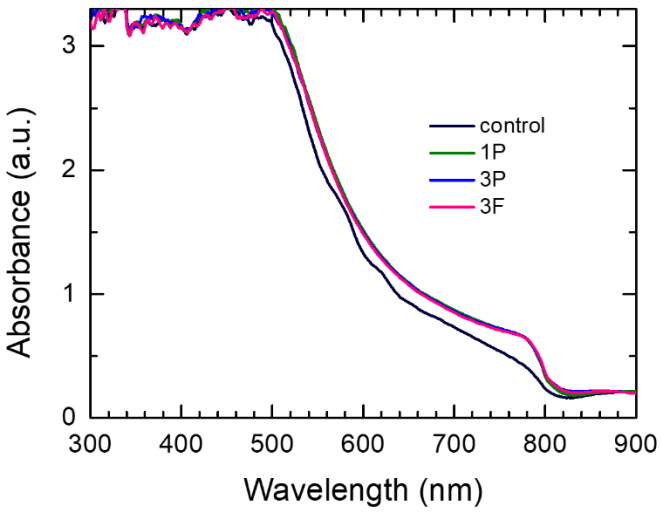

Figure A6.15. Absorption spectra of $FAPbI_3$ films. Control: bare $FAPbI_3$, 1P: $FAPbI_3$ with 1.67 mol% PEA_2PbI_4, 3P: $FAPbI_3$ with 3.33 mol% PEA_2PbI_4, 3F: $FAPbI_3$ with 3.33 mol% $FPEA_2PbI_4$.

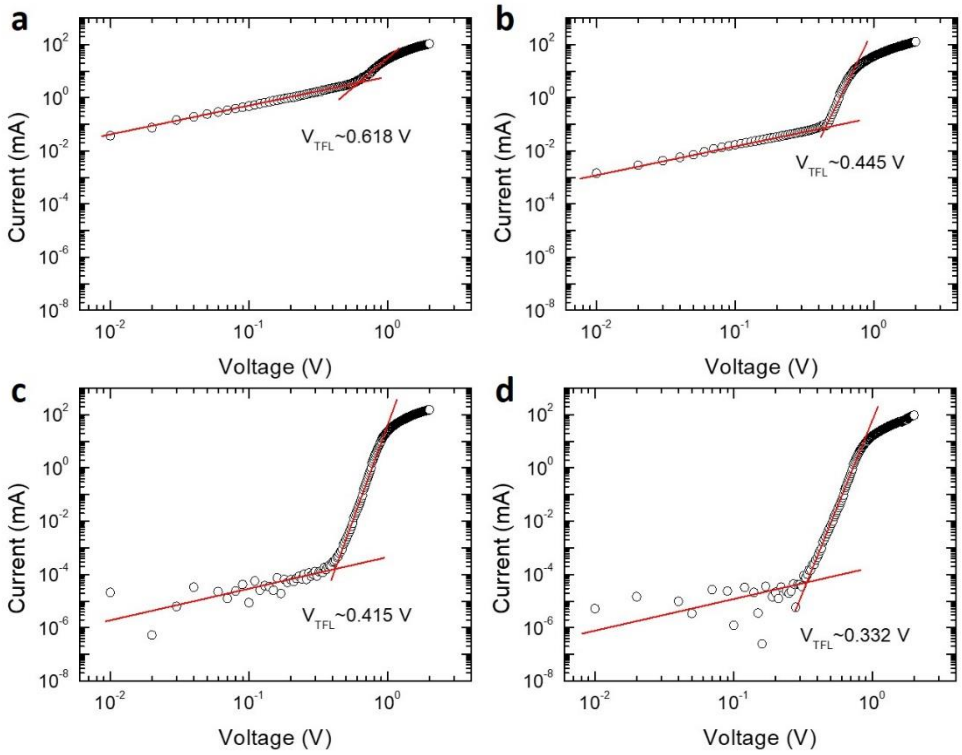

Figure A6.16. Space charge limited current (SCLC) measurement of the $FAPbI_3$ films. a, control: bare $FAPbI_3$, b, 1P: $FAPbI_3$ with 1.67 mol% PEA_2PbI_4, c, 3P: $FAPbI_3$ with 3.33 mol% PEA_2PbI_4, d, 3F: $FAPbI_3$ with 3.33 mol% $FPEA_2PbI_4$. Trap filling voltages (V_{TFL}) for each graph was determined from the linear intercept of the red lines where the characteristic current-voltage

relationship transfer from ohmic (I∝V) to trap-filling ($I \propto V^{n>3}$) regime.

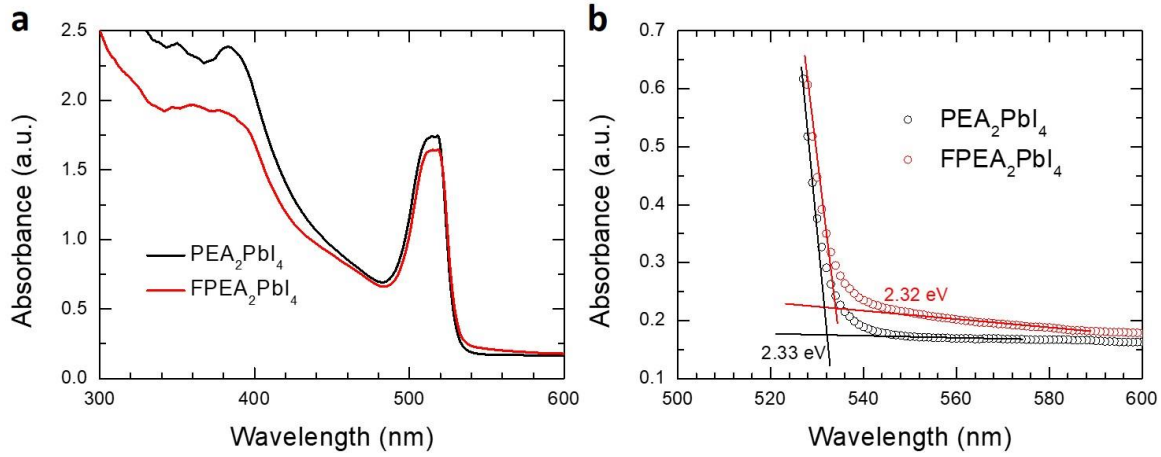

Figure A6.17. Determination of bandgap of layered perovskites. a, UV-vis absorption spectra of PEA_2PbI_4 and $FPEA_2PbI_4$ films on a glass substrate. b, Linear interpolation of absorption onset region and calculated bandgaps.

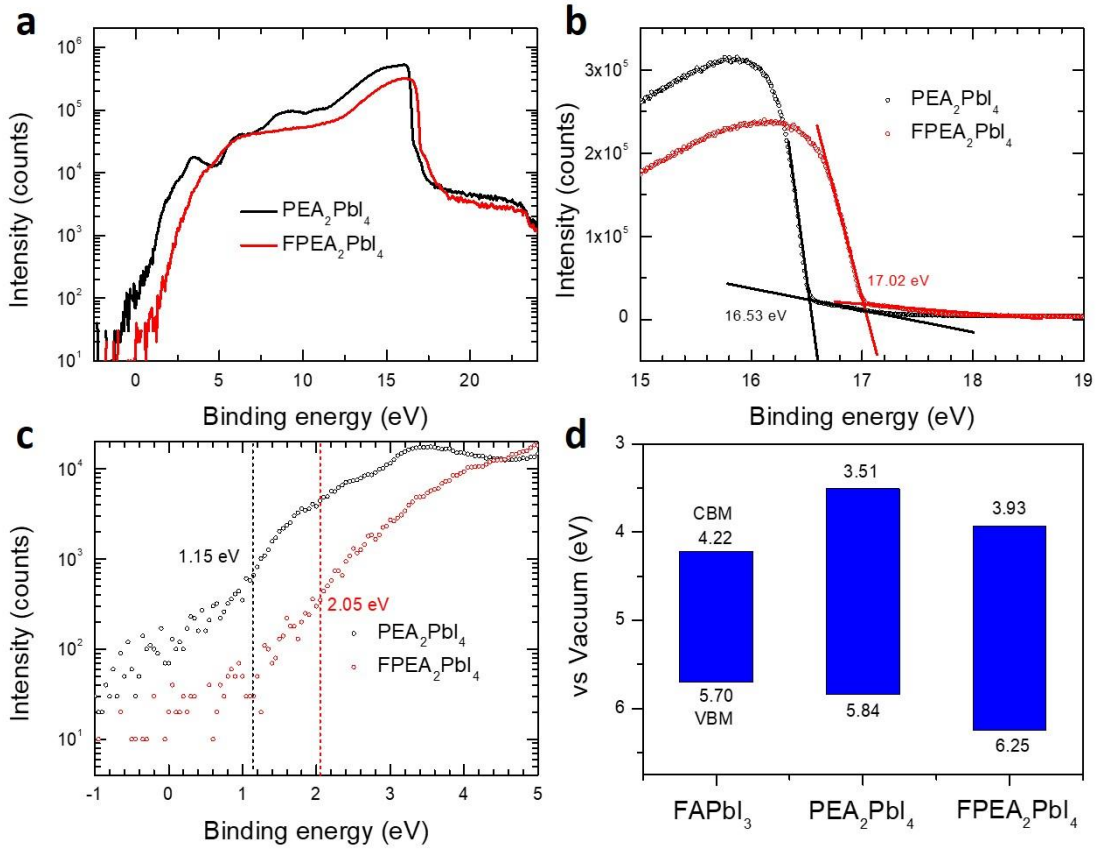

Figure A6.18. Ultraviolet photoelectron spectroscopy (UPS) measurement of layered perovskites. a, UPS spectra of PEA_2PbI_4 and $FPEA_2PbI_4$ films on a ITO substrate. b, cutt-off and c, onset regions of the spectra. d, Calculated band structure of the α-$FAPbI_3$, PEA_2PbI_4 and $FPEA_2PbI_4$. CBM and VBM stand for conduction band minimum and valence band maximum, respectively.

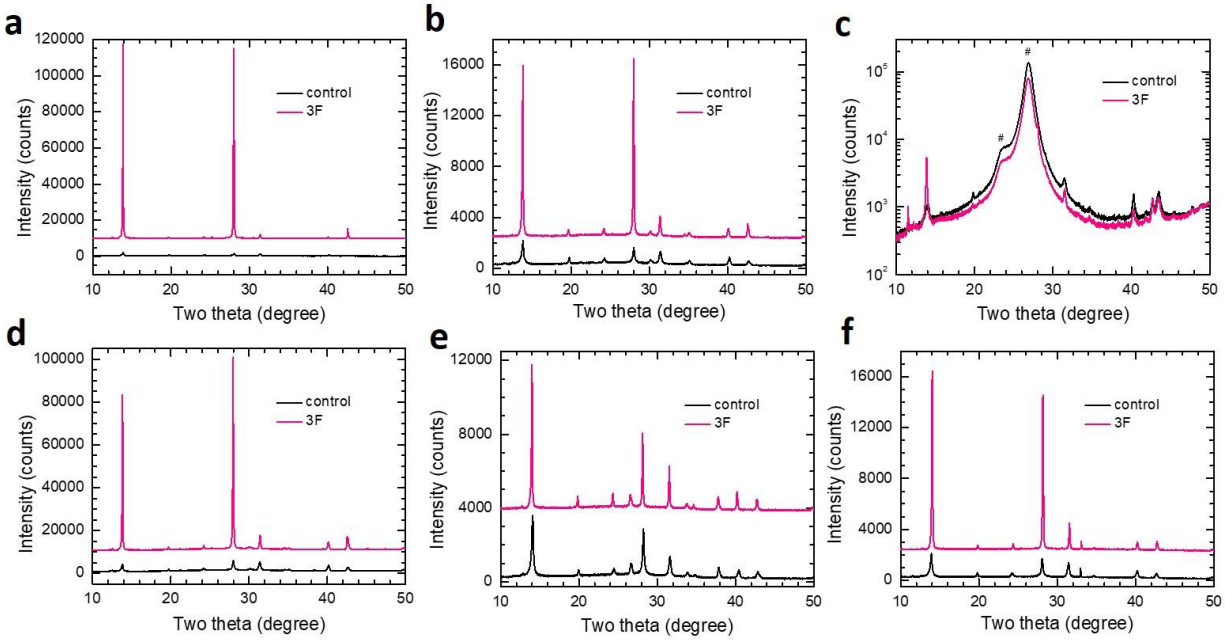

Figure A6.19. X-ray diffraction (XRD) patterns on different substrates. XRD patterns of bare $FAPbI_3$ (control) and $FAPbI_3$ with addition of 3.33 mol% $FPEA_2PbI_4$ (3F). a, Glass, b, ITO, c, polyethylene naphthalate (PEN), d, SnO_2, e, fluorine doped tin oxide (FTO), and f, silicon wafer. The data obtained on PEN substrate is plotted in logarithmic scale to distinguish the signal from $FAPbI_3$ from huge substrate peaks (#).

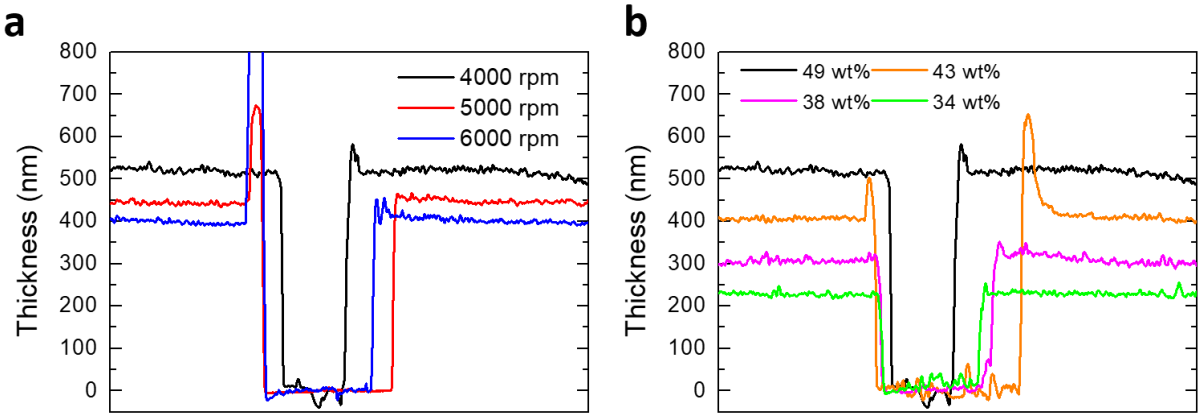

Figure A6.20. Thickness control of NHE-$FAPbI_3$ films. Film thickness control by tuning the initial deposition of δ-$FAPbI_3$ as a function of **a,** different spin-coating deposition rate (rpm) and **b.** perovskite precursor concentration. The spin-coated δ-$FAPbI_3$ is then regularly annealed to trigger the NHE phase conversion process, and the thickness is measured after the NHE process.

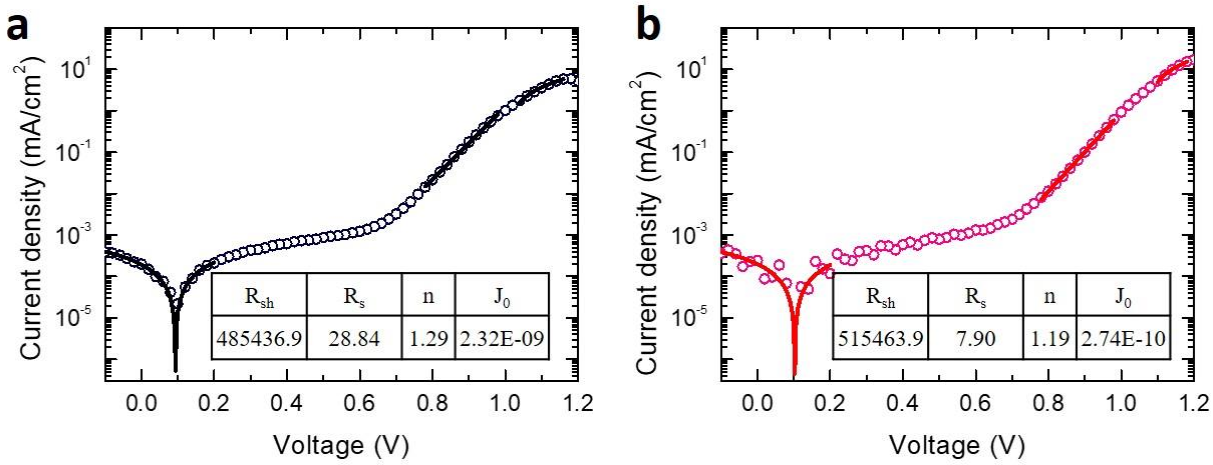

Figure A6.21. Dark current measurement of solar cell devices. Dark current density-voltage (J-V) curves of solar cell devices based on a a, bare $FAPbI_3$ film (control) and b, $FAPbI_3$ film with 3.33 mol% $FPEA_2PbI_4$ (target). Open circles indicate measured data while solid lines indicate fitted curves. The fitted shun resistance (R_{sh}), series resistance (R_s), ideality factor (n) and saturation current (J_0) are presented in the tables.

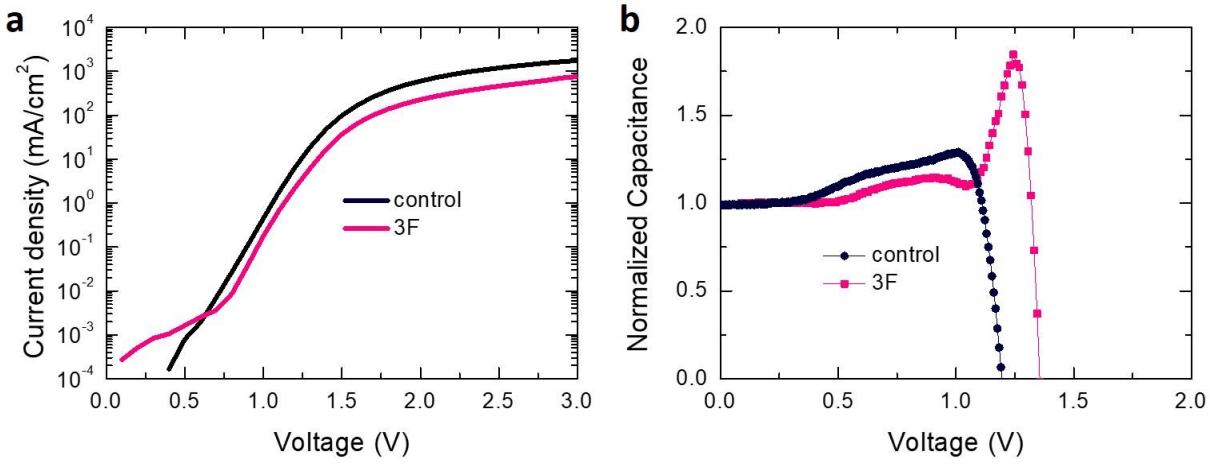

Figure A6.22. Current density-voltage (J-V) and capacitance-voltage (C-V) curves of light emitting diode (LED) devices. a, J-V and b, C-V curves of LED devices based on bare $FAPbI_3$ film (control) and $FAPbI_3$ film with 3.33 mol% $FPEA_2PbI_4$ (3F).

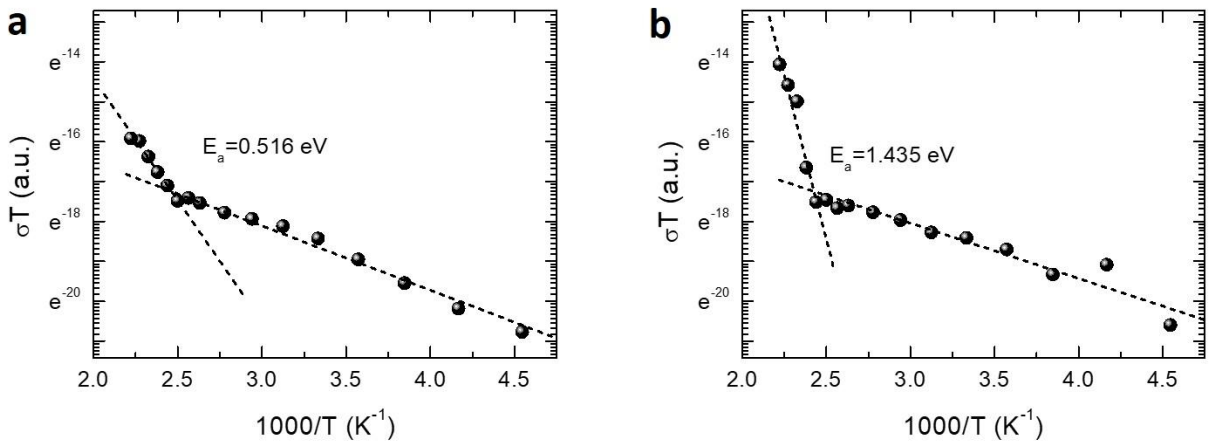

Figure A6.23. Measurement of activation energies for ion migration. Temperature dependent current-voltage curves of Au/Perovskite (100 μm)/Au lateral devices based on a, bare $FAPbI_3$ (control) and b, $FAPbI_3$ film with 3.33 mol% $FPEA_2PbI_4$ (3F) films. The σT (σ is conductivity) and temperature relationship was plotted. Dashed lines indicate linear fitting of the data to calculate the activation energy for ion migration (E_a).

Appendix B. Supplementary Tables

Table B2.1. Surface treatment with organic iodide based salts. Summary of organic iodide based salts and their deposition conditions used to surface treat perovskite solar cells.

	Concentration (relative to I^-)	Deposition condition	Further processing	Reference
Octylammonium iodide	15 mM in IPA	5000 rpm	100°C anneal for 5 min	[3]
Dodecylammonium iodide	15 mM in IPA	5000 rpm	100°C anneal for 5 min	[3]
Phenethylammonium iodide	15 mM in IPA	5000 rpm	Dried in a vacuum oven for 24 h	[3]
Imidazolium iodide	35.7 mM in IPA	6000 rpm	70°C for 10 – 15 min	[4]
Ethylammonium iodide	17.3 mM in IPA	6000 rpm	70°C for 10 – 15 min	[4]
Guanidinium iodide	26.7 mM in IPA	6000 rpm	70°C for 10 – 15 min	[4]
Phenylalanine iodide	6 mM in IPA	4000 rpm	100°C anneal for 10 min	[5]
Octylammonium iodide	11.7 mM in IPA	5000 rpm	100°C anneal for 5 min	[6]
Butylammonium iodide	11.7 mM in IPA	5000 rpm	100°C anneal for 5 min	[6]
Phenethylammonium iodide	20 mM in IPA	5000 rpm	None	[2]

Table B2.2. Photovoltaic parameters of control and treated devices. Average photovoltaic parameters of the control devices and devices treated with different ammonium cations.

	V_{OC} (V)	J_{SC} (mA cm^{-2})	FF	PCE (%)	Best PCE (%)
Control	1.077 ± 0.004	24.53 ± 0.08	0.771 ± 0.011	20.36 ± 0.36	20.95
PEAI	1.103 ± 0.004	24.51 ± 0.07	0.781 ± 0.002	21.10 ± 0.11	21.28
PEATFA	1.116 ± 0.004	24.49 ± 0.12	0.783 ± 0.003	21.41 ± 0.18	21.57
PAI	1.111 ± 0.006	24.45 ± 0.09	0.792 ± 0.012	21.50 ± 0.32	21.86

PATFA	1.124 ± 0.006	24.52 ± 0.08	0.796 ± 0.016	21.94 ± 0.45	22.72
OAI	1.106 ± 0.004	24.54 ± 0.14	0.772 ± 0.006	20.95 ± 0.23	21.42
OATFA	1.129 ± 0.005	24.47 ± 0.13	0.779 ± 0.009	21.51 ± 0.30	21.86

Table B2.3. Distribution of the device photovoltaic parameters measured in reverse scan for different concentrations of PAI. Abbreviations are open-circuit voltage (V_{OC}), short-circuit current density (J_{SC}), fill factor (FF), power conversion efficiency (PCE), and stabilized power output (SPO).

	V_{OC} (V)	J_{SC} (mA cm^{-2})	FF	PCE (%)
5 mM	1.104 ± 0.005	24.53 ± 0.11	0.783 ± 0.009	21.19 ± 0.26
15 mM	1.099 ± 0.006	24.42 ± 0.18	0.743 ± 0.010	19.93 ± 0.38
30 mM	1.095 ± 0.008	23.70 ± 0.19	0.691 ± 0.012	17.92 ± 0.39

Table B4.1. Energy levels of the perovskite films. The work function (WF) and (ionization energy (IE) – WF) values are based on the UPS measurements. The vacuum level shift (ΔE_{vac}) and valence band maximum (VBM) values are calculated based on an aligned Fermi level.

	WF (eV)	**IE - WF (eV)**	**ΔE_{vac} (eV)**	**Aligned VBM (eV)**
Reference	4.74	0.69	-	-5.43
PEA^+I^-	4.52	0.73	-0.22	-5.47
BA^+I^-	4.45	0.79	-0.29	-5.53
OA^+I^-	4.37	0.86	-0.37	-5.60
DA^+I^-	3.89	0.96	-0.85	-5.70
OA^+Br^-	4.43	0.92	-0.31	-5.66
$OA^+BF_4^-$	4.52	0.77	-0.22	-5.51
OA^+TFA^-	4.54	0.78	-0.20	-5.52
OA^+TsO^-	4.81	0.75	+0.07	-5.49

Table B4.2. Time-resolved photoluminescence decay parameters of the glass/perovskite/spiro-MeOTAD films, fitted with a bi-exponential decay model.

	A_1 (%)	τ_1 (ns)	A_2 (%)	τ_2 (ns)	τ_{ave} (ns)
Reference	100.0	3.0	0.0	15.2	3.0
OAI-treated	94.5	7.5	5.5	19.8	8.1
$OABF_4$-treated	99.1	4.7	0.9	17.4	4.8
OATsO-treated	99.9	3.5	0.1	17.7	3.5

Table B4.3. Energy levels of the $FAPbI_3$ perovskite films. The work function (WF) and (ionization energy (IE) – WF) values are based on the UPS measurements. The vacuum level shift (ΔE_{vac}) and valence band maximum (VBM) values are calculated based on an aligned Fermi level.

	WF (eV)	IE - WF (eV)	ΔE_{vac} (eV)	Aligned VBM (eV)
$FAPbI_3$	4.82	0.83	-	-5.65
OA^+I^-	4.48	1.02	-0.34	-5.84
$OA^+BF_4^-$	4.60	0.94	-0.22	-5.76
OA^+TsO^-	4.87	0.89	+0.05	-5.71

Table B4.4. Comparison of the device degradation at different time periods during the MPP stability test.

	PCE drop (%)		Degradation rate (%/h)	
	First 100 h	Next ~400 h	First 100 h	Next ~400 h
OAI-treated device	-6.4	-8.9	-0.064	-0.022
$OABF_4$-treated device	-2.9	-5.6	-0.029	-0.014
OATsO-treated device	~0	~0	-	-

Table B4.5. Activation energy for iodine or bromine migration in a neutral uncharged or negatively charged environment calculated from first-principles nudged elastic band (NEB) simulations.

	Neutral (eV)	Negative (eV)	Difference (%)
Intra-lattice			
I in $FAPbI_3$	0.335	0.205	- 38.7

Br in $FAPbBr_3$	0.634	0.448	- 29.4
Extra-lattice			
I in $FAPbI_3$	3.30	2.86	- 13.3
Br in $FAPbBr_3$	3.68	3.03	- 17.8

Table B4.6. Surface charge displacement, $\bar{q}$, with different species attached to defect-free surfaces.

	$\bar{q}$ (x10^{-2} *e*)
$[OA]^+$	+ 0.57
$[I]^-$	- 1.33
$[Br]^-$	- 1.40
$[TFA]^-$	- 1.97
$[TsO]^-$	- 2.19

Table B5.1. Fitted parameters from the dark current density and voltage (*J-V*) curves of the $MAPbI_3$ and $Ace_{0.03}MA_{0.97}PbI_3$ devices showing the extracted shunt (R_{sh}) and series (R_s) resistances, ideality factor (n) and dark current density (J_0).

	R_{sh} (Ω cm^2)	R_s (Ω cm^2)	J_0 (mA cm^{-2})	n
MA	1,029,866	5.62	1.81×10^{-10}	1.80
AceMA	1,334,579	4.78	3.70×10^{-11}	1.68

Table B6.1. Extracted *k* values from the *in-situ* Grazing Incidence Wide Angle X-ray Scattering and X-ray diffraction monitoring of the phase transformation.

	***in-situ* GIWAXS**		**X-ray diffraction**	
	n = 3 ***k***	**n = 4** ***k***	**n = 3** ***k***	**n = 4** ***k***
control	0.53818	0.5691	6.08	18.4
1P	7.04 x 10^{-3}	1.41 x 10^{-3}	6.45 x 10^{-2}	2.67 x 10^{-2}

3P	4.03 x 10^{-3}	7.01 x 10^{-4}	5.81 x 10^{-3}	1.17 x 10^{-3}
3F	3.68 x 10^{-4}	3.98 x 10^{-5}	3.15 x 10^{-3}	5.32 x 10^{-4}

Table B6.2. Fitted peak positions and full-width-half-maximums ($\boldsymbol{\beta_{total}}$) of the peaks extracted from the X-ray diffraction patterns of δ-$FAPbI_3$ films in Fig. 3a.

Hexagonal δ-phase				
Bragg peak	**R**	**1P**	**3P**	**3F**
(010)	2θ = 11.694° β_{total} = 0.23712°	2θ = 11.676° β_{total} = 0.25205°	2θ = 11.716° β_{total} = 0.29268°	2θ = 11.698° β_{total} = 0.19557°
(011)	2θ = 16.214° β_{total} = 0.24919°	2θ = 16.179° β_{total} = 0.25475°	2θ = 16.206° β_{total} = 0.26732°	2θ = 16.185° β_{total} = 0.20998°
(021)	2θ = 26.187° β_{total} = 0.25294°	2θ = 26.166° β_{total} = 0.27365°	2θ = 26.190° β_{total} = 0.31578°	2θ = 26.180° β_{total} = 0.23964°
(022)	2θ = 32.805° β_{total} = 0.30102°	2θ = 32.779° β_{total} = 0.32214°	2θ = 32.799° β_{total} = 0.37408°	2θ = 32.783° β_{total} = 0.28791°
(220)	2θ = 41.587° β_{total} = 0.32823°	2θ = 41.563° β_{total} = 0.36589°	2θ = 41.592° β_{total} = 0.42321°	2θ = 41.588° β_{total} = 0.34735°

Table B6.3. Fitted parameters for the data in Fig. A6.10a-d. The crystallite size and strain were calculated based on the function described in the table.

δ-$FAPbI_3$ phase					
	Function: $\beta_{total}\cos\theta = 4\varepsilon\sin\theta + \frac{\lambda}{L}$			**Crystallite size (Å)**	**Strain (%)**
	Slope	**Intercept**	**R^2 value**		
R	0.00490	0.00354	0.869	435	0.123
1P	0.00648	0.00353	0.910	437	0.162
3P	0.00838	0.00379	0.869	406	0.209
3F	0.00887	0.00236	0.962	654	0.222

Table B6.4. Fitted parameters for the time-resolved photoluminescence decay profiles in Fig. 3j. The data were fitted with a bi-exponential decay model. Control: bare $FAPbI_3$, 1P: $FAPbI_3$ with 1.67 mol% PEA_2PbI_4, 3P: $FAPbI_3$ with 3.33 mol% PEA_2PbI_4, and 3F: $FAPbI_3$ with 3.33 mol% $FPEA_2PbI_4$.

	Control	**1P**	**3P**	**3F**
A_1 (%)	39.1	38.2	27.8	13.4
τ_1 (ns)	2.8	3.0	3.0	3.0
A_2 (%)	60.9	61.8	72.2	86.6
τ_2 (ns)	32.0	1212.6	1509.1	1862.1
Average τ_{avg} (ns)	20.6	750.8	1090.7	1613.6